Journal of Sensors

Smart Sensing Technologies and their Applications in Civil Infrastructures

Guest Editors: Hong-Hu Zhu, Fei Dai, Zhenhua Zhu, Tuan Guo, and Xiao-Wei Ye

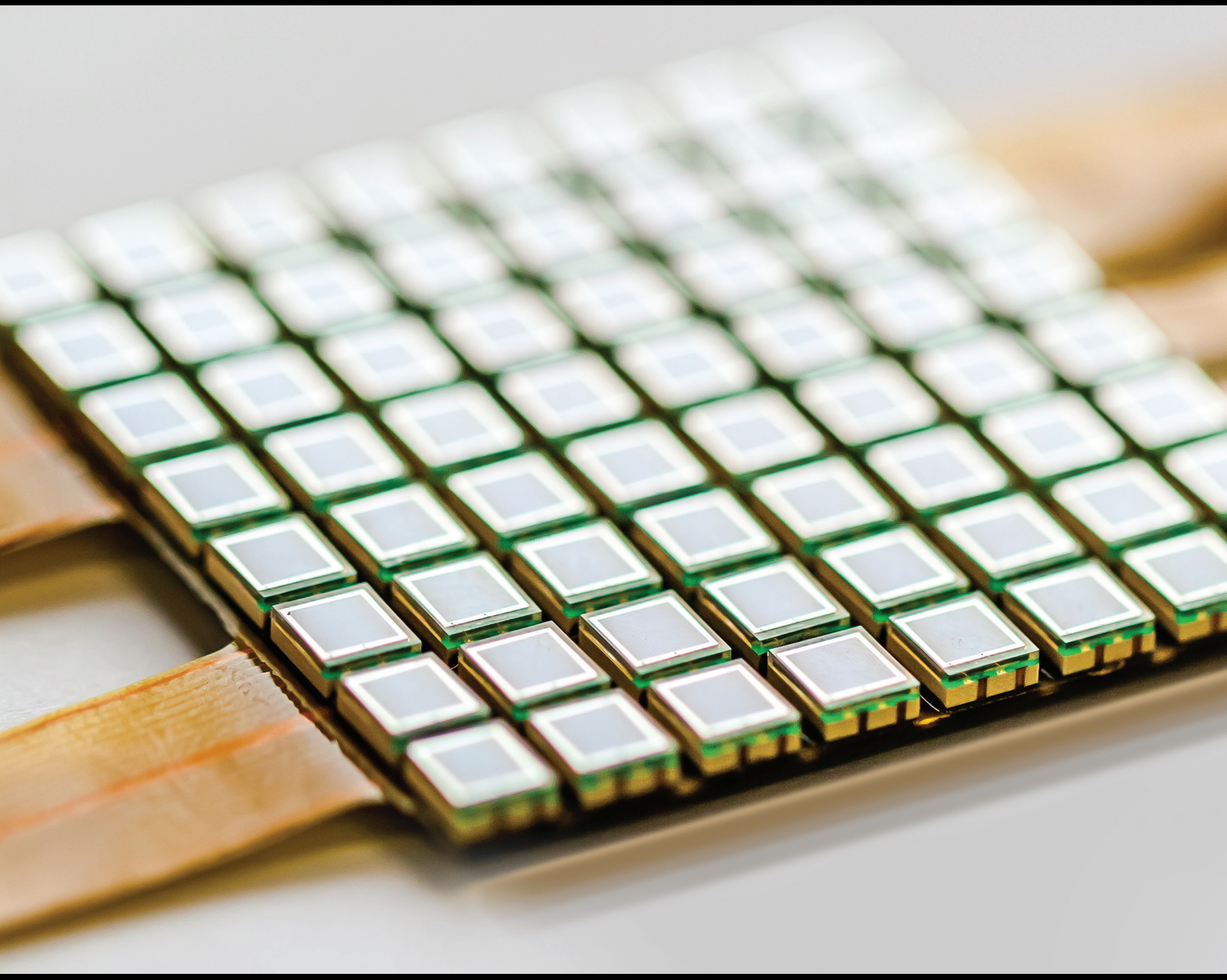

Smart Sensing Technologies and their Applications in Civil Infrastructures

Journal of Sensors

Smart Sensing Technologies and their Applications in Civil Infrastructures

Guest Editors: Hong-Hu Zhu, Fei Dai, Zhenhua Zhu, Tuan Guo, and Xiao-Wei Ye

Editorial Board

Contents

Hindawi Publishing Corporation
Journal of Sensors
Volume 2015, Article ID 265106, 1 page
http://dx.doi.org/10.1155/2015/265106

Editorial

Smart Sensing Technologies and Their Applications in Civil Infrastructures

Hong-Hu Zhu,[1] Fei Dai,[2] Zhenhua Zhu,[3] Tuan Guo,[4] and Xiao-Wei Ye[5]

[1]*School of Earth Sciences and Engineering, Nanjing University, Nanjing 210023, China*
[2]*Department of Civil and Environmental Engineering, West Virginia University, Morgantown, WV 26506, USA*
[3]*Department of Building, Civil and Environmental Engineering, Concordia University, Montreal, QC, Canada H3G 1M8*
[4]*Institute of Photonics Technology, Jinan University, Guangzhou 510632, China*
[5]*Department of Civil Engineering, Zhejiang University, Hangzhou 310058, China*

Correspondence should be addressed to Hong-Hu Zhu; zhh@nju.edu.cn

Received 27 April 2015; Accepted 27 April 2015

With the rapid development of urbanization in some developing countries such as China, India, and Brazil, numerous huge civil infrastructures have been built in recent years. The performance of these structures during construction, operation, maintenance, and repair becomes a major concern. In order to accurately assess the health condition of engineering structures and prevent potential failure, a variety of smart sensing technologies and methods have been successfully developed in the past few decades, such as fiber optic sensing (FOS), wireless sensor network (WSN), acoustic emission (AE), time domain reflectometry (TDR), microelectromechanical system (MEMS), global position system (GPS), particle image velocimetry (PIV), and laser scanning. Due to their inherent advantages, these technologies have played an increasingly important role in health monitoring of different types of civil infrastructures.

The aim of this special issue is to present original research articles on smart sensing technologies and their applications in civil infrastructures. The topics cover various aspects including novel smart sensing mechanisms and devices for civil infrastructures; applications of smart sensors and sensing systems in civil infrastructures; in-field implementation of structural health monitoring and diagnosis systems; supporting technologies and methodologies in monitoring civil infrastructures, such as real-time data acquisition and processing, data transferring, remote management, and performance evaluation; and typical case study of sensing applications and civil infrastructures monitoring.

The papers in this special issue are expected to provide in-depth insights into the development and applications of smart sensing technologies in civil infrastructures and be useful for civil engineering practitioners and researchers.

Acknowledgments

The guest editors of this special issue would like to express their sincere gratitude to all the authors and anonymous reviewers who have generously contributed to this special issue.

Hong-Hu Zhu
Fei Dai
Zhenhua Zhu
Tuan Guo
Xiao-Wei Ye

Hindawi Publishing Corporation
Journal of Sensors
Volume 2015, Article ID 610416, 14 pages
http://dx.doi.org/10.1155/2015/610416

Research Article

A Comparative Study on Frequency Sensitivity of a Transmission Tower

Peng-yun Li,[1] Bo Chen,[2] Wen-ping Xie,[1] and Xiang Xiao[3]

[1]*Guangdong Power Grid Corporation Co. Ltd., Guangzhou 510080, China*
[2]*Key Laboratory of Roadway Bridge and Structural Engineering, Wuhan University of Technology, Wuhan 430070, China*
[3]*School of Transportation, Wuhan University of Technology, Wuhan 430070, China*

Correspondence should be addressed to Bo Chen; cbsteven@163.com

Received 15 November 2014; Accepted 25 December 2014

Academic Editor: Fei Dai

Sensitivity analysis can take structural parameters as variable and achieve the relationship only with one time analysis, which will dramatically reduce the analytical work especially for large scale structures. The comparative study on frequency sensitivity of a transmission tower is actively carried out in this study. The three-dimensional analytical model of a transmission tower is established by using the finite element (FE) method. The sensitivity coefficients to natural frequencies are deduced based on the equation of motion of the tower. In addition, the expression of the frequency sensitivity to Young's modulus, density of material, the cross area of members, torsional stiffness, and bending moment inertia is proposed. A real transmission tower constructed in China is taken as an example to examine the feasibility and reliability of the proposed sensitivity computation approach. An intensive parametric study is conducted in detail in order to compare the sensitivity coefficients of different physical parameters. The work on an example structure indicated that the magnitudes of the sensitivity coefficients of Young's modulus, the density, and the cross area are much larger than those of the torsional stiffness and the bending moment inertia.

1. Introduction

To be a typical spatial steel structure, the transmission tower is widely used as electrical power infrastructures throughout the world. The transmission tower is a high-rise structure with small damping and is prone to strong dynamic excitations, such as earthquakes and wind loadings [1–3]. It is frequently reported across the world that the excessive vibration of a transmission tower under dynamic excitations may induce the structural damage and even failure [4–6]. Therefore, it is necessary to evaluate the structural performance of the transmission tower subjected to external dynamic excitations. Many theoretical and experimental investigations have been carried out during the past two decades for examining the performance of the transmission tower [7, 8]. With regard to the approaches and techniques used for performance evaluation, the transmission tower system is conventionally designed and constructed using appropriate design standards without considering the dynamic optimization effects. Therefore, the common approach does not provide deep insights into the structural transient behaviour under strong dynamic excitations, even though the consideration of dynamic effects may be important. Thus, the vibration-based structural health monitoring (SHM) approaches have been widely utilized in the performance evaluation of civil engineering structures across the world [9–11]. The SHM process needs to develop or improve a mathematical model of a physical system using measurement data to describe the input, output, and noise relationship [12, 13]. Various methods have been developed to improve the quality of the finite element model of a structure using measurement data [14]. Doebling et al. (1998) [15] gave a comprehensive review on SHM. With regard to the different SHM algorithm used, the effects of various physical parameters on the structural responses can be examined in detail to determine the crucial parameters for structural dynamic design and assessment.

For a transmission tower with determined parameters, it is troublesome to attain the relationship between dynamic characteristics and changed parameters by numerous recalculations which will be almost impossible for large

scale structures, while sensitivity analysis as an alternative approach can take structural parameters as variable and achieve the relationship only with one time analysis, which will dramatically reduce the analytical work especially for large scale structures [16]. The sensitivity analysis is a reasonable and powerful tool for investigating the effects of physical parameters on static and dynamic responses. The sensitivity analysis concerns the relationship between parameters available to the structural responses under dynamic excitations. The dependence of response measures, such as displacement, velocity, acceleration, stress, strain, natural frequency, mode shape, and frequency response, is implicitly defined through the governing equations of structural mechanics [17]. Dynamic sensitivity analysis is used to compute the rate of dynamic property change with respect to changes of structural physical parameters.

Current studies on the dynamic assessment of the transmission tower focus on the response computation and mitigation. Up to now, the sensitivity analysis of the transmission tower for dynamic assessment has been investigated rarely. To this end, the comparative study on frequency sensitivity of a transmission tower is actively carried out in this study. The three-dimensional model of a transmission tower is established by using the FE method. The differential sensitivity analysis approach is presented based on the differential sensitivity coefficient, the absolute sensitivity coefficient, and the relative sensitivity coefficient, respectively. The sensitivity coefficients to natural frequencies are deduced based on the equation of motion of the tower. In addition, the expression of the frequency sensitivity to the Young's modulus, density of material, the cross area of members, torsional stiffness, and bending moment inertia is proposed. A real transmission tower is taken as the example to investigate the effects of the structural parameters on the natural frequency through the detailed parametric study. An intensive parametric study is conducted to compare the sensitivity coefficients of different physical parameters. A real transmission tower constructed in China is taken as an example to examine the feasibility and reliability of the proposed sensitivity computation approach. The observations made indicate that the magnitudes of the sensitivity coefficients of the Young's modulus, the density and the cross area are much larger than those of the torsional stiffness and the bending moment inertia. The Young's modulus, the density and the cross area are important structural parameters affecting the dynamic properties of the transmission tower.

2. Model of Transmission Tower

A transmission tower is a typical truss structure constructed by using steel members, which can be commonly modelled by using beam elements based on the finite element (FE) method [18, 19]. For an Euler-Bernoulli beam element, stiffness matrix of the ith element of a transmission tower in the local coordinate system (LCS) $\mathbf{K}_i^e$ is

$$\mathbf{K}_i^e = \begin{bmatrix}
\frac{E_iA_i}{l_i} & & & & & & & & & & & \\
0 & \frac{12E_iI_z^i}{l_i^3} & & & & & & & & & & \\
0 & 0 & \frac{12E_iI_y^i}{l_i^3} & & & & & & \text{symmetry} & & & \\
0 & 0 & 0 & \frac{G_iI_x^i}{l_i} & & & & & & & & \\
0 & 0 & \frac{-6E_iI_y^i}{l_i^2} & 0 & \frac{4E_iI_y^i}{l_i} & & & & & & & \\
0 & \frac{6E_iI_z^i}{l_i^2} & 0 & 0 & 0 & \frac{4E_iI_z^i}{l_i} & & & & & & \\
\frac{-E_iA_i}{l_i} & 0 & 0 & 0 & 0 & 0 & \frac{E_iA_i}{l_i} & & & & & \\
0 & \frac{-12E_iI_z^i}{l_i^3} & 0 & 0 & 0 & \frac{-6E_iI_z^i}{l_i^2} & 0 & \frac{12E_iI_z^i}{l_i^3} & & & & \\
0 & 0 & \frac{-12E_iI_y^i}{l_i^3} & 0 & \frac{6E_iI_y^i}{l_i^2} & 0 & 0 & 0 & \frac{12E_iI_y^i}{l_i^3} & & & \\
0 & 0 & 0 & \frac{-G_iI_x^i}{l_i} & 0 & 0 & 0 & 0 & 0 & \frac{G_iI_x^i}{l_i} & & \\
0 & 0 & \frac{-6E_iI_y^i}{l_i^2} & 0 & \frac{2E_iI_y^i}{l_i} & 0 & 0 & 0 & \frac{6E_iI_y^i}{l_i^2} & 0 & \frac{4EI_y^i}{l} & \\
0 & \frac{6E_iI_z^i}{l_i^2} & 0 & 0 & 0 & \frac{2E_iI_z^i}{l_i} & 0 & \frac{-6E_iI_z^i}{l_i^2} & 0 & 0 & 0 & \frac{4E_iI_z^i}{l_i}
\end{bmatrix}. \quad (1)$$

The element stiffness matrix in the global coordinate system (GCS) $\mathbf{K}_i$ can be expressed as the multiple of the element stiffness matrix $\mathbf{K}_i^e$ in the LCS with the coordinate transformation matrix $\mathbf{T}_i^e$

$$\mathbf{K}_i = \mathbf{T}_i^{eT} \mathbf{K}_i^e \mathbf{T}_i^e. \tag{2}$$

The mass matrix of the ith element of a transmission tower in the LCS $\mathbf{M}_i^e$ can be constructed based on lumped mass assumption [20]:

$$\mathbf{M}_i^e = \frac{\rho_i A_i l_i}{2} \mathbf{m}_I = \frac{\rho_i A_i l_i}{2} \begin{bmatrix} \mathbf{I}_m & \mathbf{0} \\ \mathbf{0} & \mathbf{I}_m \end{bmatrix}, \tag{3}$$

where

$$\mathbf{I}_m = \begin{bmatrix} 1 & 0 & 0 & 0 & 0 & 0 \\ 0 & 1 & 0 & 0 & 0 & 0 \\ 0 & 0 & 1 & 0 & 0 & 0 \\ 0 & 0 & 0 & 0 & 0 & 0 \\ 0 & 0 & 0 & 0 & 0 & 0 \\ 0 & 0 & 0 & 0 & 0 & 0 \end{bmatrix}. \tag{4}$$

The element mass matrix of the ith structural member in the GCS $\mathbf{M}_i$ can be expressed as

$$\mathbf{M}_i = \mathbf{T}_i^{eT} \mathbf{M}_i^e \mathbf{T}_i^e. \tag{5}$$

The global mass matrix $\mathbf{M}$ and stiffness matrix $\mathbf{K}$ of the transmission tower can be expressed, respectively, as follows:

$$\begin{aligned} \mathbf{M} &= \sum_{i=1}^{ne} \mathbf{T}_i^T \mathbf{M}_i^e \mathbf{T}_i, \\ \mathbf{K} &= \sum_{i=1}^{ne} \mathbf{T}_i^T \mathbf{K}_i^e \mathbf{T}_i, \end{aligned} \tag{6}$$

where ne is the number of elements of a transmission tower; $\mathbf{T}_i$ is the freedom transform matrix from the LCS to the GCS.

3. Frequency Sensitivity Analysis

3.1. Differential Sensitivity Analysis. The performance assessment of complex structures to satisfy the dynamic responses restrictions is commonly hampered by the computational cost of dynamic analysis. There is a fundamental requirement for the information relating changes in the dynamic response quantities to changes in the structural parameters as well as a need for rapid reanalysis in structural performance evaluation. The sensitivity analysis of dynamic characteristics on structural parameters is very important and widely accepted in the structural design, optimization, and evaluation. Sensitivity coefficients are defined as the rate of change of a particular response quantity R with respect to a change in a structural parameter x. Sensitivity coefficients can be either evaluated as absolute, relative, or normalized relative values. Relative values are independent of the units of the parameter value while, in addition, normalized relative parameters are also normalized with respect to the response value.

A differential sensitivity coefficient is the slope of the response R_j with respect to parameter x_i, computed at a given state of the parameter. When this differential is computed for all selected responses with respect to the selected parameters, the element of the sensitivity matrix $\mathbf{S}$ is obtained:

$$S_{ji} = \frac{\partial R_j}{\partial x_i} \quad (j = 1, 2, \ldots, n;\ i = 1, 2, \ldots, m). \tag{7}$$

In which n is the number of the responses; m is the number of the structural parameter. The absolute sensitivity coefficient S_{ji} is the (j, i)th element in the sensitivity matrix $\mathbf{S}$.

The absolute sensitivity coefficients are computed by using the units of the response and parameter value. If sensitivities for different types of parameters are to be compared, the relative sensitivities can be adopted:

$$\mathbf{S}^r = \mathbf{S} \cdot \mathbf{P}, \tag{8}$$

where $\mathbf{P}$ is a diagonal, square matrix holding the parameter values. The relative sensitivity coefficient is given by

$$S_{ji}^r = \frac{\partial R_j}{\partial x_i} x_i \quad (j = 1, 2, \ldots, n;\ i = 1, 2, \ldots, m). \tag{9}$$

Relative sensitivities can be normalized with respect to the response value

$$\mathbf{S}^n = \mathbf{S}^r \cdot \mathbf{R} = \mathbf{S} \cdot \mathbf{P} \cdot \mathbf{R}, \tag{10}$$

where $\mathbf{R}$ is a diagonal, square matrix holding the response values. The normalized relative sensitivity coefficient is given by

$$S_{ji}^n = R_j^{-1} \frac{\partial R_j}{\partial x_i} x_i \quad (j = 1, 2, \ldots, n;\ i = 1, 2, \ldots, m). \tag{11}$$

3.2. Frequency Sensitivity. The eigenvalue equation of a MDOF transmission tower can be expressed as [21, 22]

$$\left(\mathbf{K} - \omega^2 \mathbf{M}\right) \boldsymbol{\varphi} = 0, \tag{12}$$

where $\mathbf{M}$, $\mathbf{K}$, and $\boldsymbol{\varphi}$ are the mass matrix, stiffness matrix and modal vector of the transmission tower respectively. The eigenvalue equation of the rth mode vibration is

$$\left(\mathbf{K} - \omega_r^2 \mathbf{M}\right) \boldsymbol{\varphi}_r = 0. \tag{13}$$

The mass matrix, stiffness matrix, and modal vector are the function of physical parameters. Thus, the first derivative of (13) to the parametric x_i of the ith structural member for the rth mode vibration results in

$$\left(\frac{\partial \mathbf{K}}{\partial x_i} - \frac{\partial \omega_r^2}{\partial x_i} \mathbf{M} - \omega_r^2 \frac{\partial \mathbf{M}}{\partial x_i}\right) \boldsymbol{\varphi}_r + \left(\mathbf{K} - \omega_r^2 \mathbf{M}\right) \frac{\partial \boldsymbol{\varphi}_r}{\partial x_i} = 0, \tag{14}$$

in which ω_r and $\boldsymbol{\varphi}_r$ are the rth circular frequency and modal vector of the system. Since the mass and stiffness matrices are a symmetric matrix, there exists

$$\boldsymbol{\varphi}_r^T \left(\mathbf{K} - \omega_r^2 \mathbf{M}\right) = \left[\left(\mathbf{K} - \omega_r^2 \mathbf{M}\right) \boldsymbol{\varphi}_r\right]^T = 0. \tag{15}$$

To pre-multiply the vector $\boldsymbol{\varphi}_r^T$ to (14) will yield

$$\frac{\partial \omega_r^2}{\partial x_i} = \frac{\boldsymbol{\varphi}_r^T \partial \mathbf{K}/\partial x_i - \omega_r^2 \left(\partial \mathbf{M}/\partial x_i\right) \boldsymbol{\varphi}_r}{\boldsymbol{\varphi}_r^T \mathbf{M} \boldsymbol{\varphi}_r}. \tag{16}$$

The relationship between the circular frequency ω_r and natural frequency f_r of the rth vibration mode can be written as

$$\begin{aligned} \frac{\partial \omega_r^2}{\partial x_i} &= 2\omega_r \frac{\partial \omega_r}{\partial x_i}, \\ \frac{\partial \omega_r}{\partial x_i} &= 2\pi \frac{\partial f_r}{\partial x_i}. \end{aligned} \tag{17}$$

The sensitivity of the frequency to the ith structural parameter x_i is

$$\frac{\partial f_r}{\partial x_i} = \frac{1}{8\pi^2 f_r} \cdot \frac{\boldsymbol{\varphi}_r^T \partial \mathbf{K}/\partial x_i - 4\pi^2 f_r^2 \left(\partial \mathbf{M}/\partial x_i\right) \boldsymbol{\varphi}_r}{\boldsymbol{\varphi}_r^T \mathbf{M} \boldsymbol{\varphi}_r}. \tag{18}$$

Equation (18) provides a way to calculate the sensitivity of the rth natural frequency to the change in the ith structural parameter x_i. Assuming that the transmission tower is linear and the change in natural frequency due to the change of structural parameter is small, the change in the rth natural frequency Δf_r, due to the variations of the structural parameter Δx_i, can be expressed as

$$\Delta f_r = \frac{\partial f_r}{\partial x_i} \Delta x_i. \tag{19}$$

3.3. Frequency Sensitivity of Structural Parameter. The sensitivity of the rth natural frequency to the structural parameter x_i can be rewritten by using the element stiffness matrix $\mathbf{K}_i^e$ and mass matrix $\mathbf{M}_i^e$ of the ith element in the GCS:

$$\frac{\partial f_r}{\partial x_i} = \frac{1}{8\pi^2 f_r} \cdot \frac{\boldsymbol{\varphi}_r^T \sum_{i=1}^{ne} \left(\partial \mathbf{K}_i^e/\partial x_i\right) - 4\pi^2 f_r^2 \sum_{i=1}^{ne} \left(\partial \mathbf{M}_i^e/\partial x_i\right) \boldsymbol{\varphi}_r}{\boldsymbol{\varphi}_r^T \mathbf{M} \boldsymbol{\varphi}_r}, \tag{20}$$

in which ne denotes the total number of the members of the transmission tower. The sensitivity of the rth natural frequency to the Young's modulus of the ith structural element E_i is given by

$$\frac{\partial f_r}{\partial E_i} = \frac{1}{8\pi^2 f_r} \cdot \frac{\boldsymbol{\varphi}_r^T \sum_{i=1}^{ne} \left(\partial \mathbf{K}_i^e/\partial E_i\right) \boldsymbol{\varphi}_r}{\boldsymbol{\varphi}_r^T \mathbf{M} \boldsymbol{\varphi}_r}, \tag{21}$$

where

$$\begin{aligned} \frac{\partial \mathbf{K}_i^e}{\partial E_i} &= \frac{\partial \mathbf{K}_i^e}{\partial \left(E_i A_i\right)} \cdot \frac{\partial \left(E_i A_i\right)}{\partial E_i} + \frac{\partial \mathbf{K}_i^e}{\partial \left(E_i I_z^i\right)} \cdot \frac{\partial \left(E_i I_z^i\right)}{\partial E_i} \\ &\quad + \frac{\partial \mathbf{K}_i^e}{\partial E_i I_y^i} \cdot \frac{\partial E_i I_y^i}{\partial E_i} + \frac{\partial \mathbf{K}_i^e}{\partial G_i} \cdot \frac{\partial G_i}{\partial E_i}. \end{aligned} \tag{22}$$

The sensitivity of the rth natural frequency to the density of the ith structural element ρ_i is

$$\frac{\partial f_r}{\partial \rho_i} = -\frac{f_r}{2} \cdot \frac{\boldsymbol{\varphi}_r^T \sum_{i=1}^{ne} \left(\partial \mathbf{M}_i^e/\partial \rho_i\right) \boldsymbol{\varphi}_r}{\boldsymbol{\varphi}_r^T \mathbf{M} \boldsymbol{\varphi}_r}. \tag{23}$$

Substituting (3) into (23) yields

$$\frac{\partial f_r}{\partial \rho_i} = -\frac{f_r \sum_{i=1}^{ne} A_i l_i}{4} \cdot \frac{\boldsymbol{\varphi}_r^T \mathbf{m}_I \boldsymbol{\varphi}_r}{\boldsymbol{\varphi}_r^T \mathbf{M} \boldsymbol{\varphi}_r}, \tag{24}$$

where A_i and L_i are the cross area and the length of the ith element, respectively. The sensitivity of the rth natural frequency to the cross area of the ith structural element A_i is

$$\frac{\partial f_r}{\partial A_i} = \frac{1}{8\pi^2 f_r} \cdot \frac{\boldsymbol{\varphi}_r^T \sum_{i=1}^{ne} \left(\partial \mathbf{K}_i^e/\partial A_i\right) - 4\pi^2 f_r^2 \sum_{i=1}^{ne} \left(\partial \mathbf{M}_i^e/\partial A_i\right) \boldsymbol{\varphi}_r}{\boldsymbol{\varphi}_r^T \mathbf{M} \boldsymbol{\varphi}_r}, \tag{25}$$

where

$$\begin{aligned} \frac{\partial \mathbf{M}_i^e}{\partial A_i} &= \frac{\rho_i l_i}{2} \mathbf{m}_I, \\ \frac{\partial \mathbf{K}_i^e}{\partial A_i} &= \frac{E_i}{l_i} \mathbf{A}_I = \frac{E_i}{l_i} \begin{bmatrix} \mathbf{I}_A & -\mathbf{I}_A \\ -\mathbf{I}_A & \mathbf{I}_A \end{bmatrix}, \\ \mathbf{I}_A &= \begin{bmatrix} 1 & 0 & 0 & 0 & 0 & 0 \\ 0 & 0 & 0 & 0 & 0 & 0 \\ 0 & 0 & 0 & 0 & 0 & 0 \\ 0 & 0 & 0 & 0 & 0 & 0 \\ 0 & 0 & 0 & 0 & 0 & 0 \\ 0 & 0 & 0 & 0 & 0 & 0 \end{bmatrix}. \end{aligned} \tag{26}$$

The sensitivity of the rth natural frequency to the moment of inertia I_x^i, I_y^i, and I_z^i of the ith structural element can be expressed as

$$\begin{aligned} \frac{\partial f_r}{\partial I_x^i} &= \frac{1}{8\pi^2 f_r} \cdot \frac{\boldsymbol{\varphi}_r^T \sum_{i=1}^{ne} \left(\partial \mathbf{K}_i^e/\partial I_x^i\right) \boldsymbol{\varphi}_r}{\boldsymbol{\varphi}_r^T \mathbf{M} \boldsymbol{\varphi}_r}, \\ \frac{\partial f_r}{\partial I_y^i} &= \frac{1}{8\pi^2 f_r} \cdot \frac{\boldsymbol{\varphi}_r^T \sum_{i=1}^{ne} \left(\partial \mathbf{K}_i^e/\partial I_y^i\right) \boldsymbol{\varphi}_r}{\boldsymbol{\varphi}_r^T \mathbf{M} \boldsymbol{\varphi}_r}, \\ \frac{\partial f_r}{\partial I_z^i} &= \frac{1}{8\pi^2 f_r} \cdot \frac{\boldsymbol{\varphi}_r^T \sum_{i=1}^{ne} \left(\partial \mathbf{K}_i^e/\partial I_z^i\right) \boldsymbol{\varphi}_r}{\boldsymbol{\varphi}_r^T \mathbf{M} \boldsymbol{\varphi}_r}. \end{aligned} \tag{27}$$

The sensitivity of the rth natural frequency to the Poisson's ratio of the ith structural element μ_i is

$$\frac{\partial f_r}{\partial \mu_i} = \frac{1}{8\pi^2 f_r} \cdot \frac{\boldsymbol{\varphi}_r^T \sum_{i=1}^{ne} \left(\partial \mathbf{K}_i^e/\partial \mu_i\right) \boldsymbol{\varphi}_r}{\boldsymbol{\varphi}_r^T \mathbf{M} \boldsymbol{\varphi}_r}, \tag{28}$$

where

$$\frac{\partial \mathbf{K}_i^e}{\partial \mu_i} = -\frac{I_x^i}{1 + \mu_i} \cdot \frac{\partial \mathbf{K}_i^e}{\partial I_x^i}. \tag{29}$$

4. Case Study

4.1. Description of an Example Transmission Tower. To examine the frequency sensitivity based on the proposed approach, a real transmission tower constructed in China is taken as the example structure. Figure 1 shows the elevation of a large transmission tower used for electric power transfer. The transmission tower with a height of 84.5 m is located in the southern coastal area in China. The structural members used in the transmission tower are made of Q235 steel with a yielding stress of 235 MPa. Young's modulus of the steel is 2.01×10^{11} N/m^2 and the density is 7800 kg/m^3. The vertical major members, the skew members, the cross arms, and the platform of the tower are formed as a spatial truss tower as shown in Figures 2(a), 2(b), and 2(c), respectively. Six platforms are connected to the vertical major members to form the tower body and the skew members are incorporated to increase the vertical and lateral stiffness of the entire tower. Two cross arms are constructed on top of the tower body for the connection of the transmission lines. A three-dimensional FE model is constructed based on the FE method with the aids of the commercial package.

A three-dimensional finite element model is established for the steel transmission tower using a commercial computer package. The model has a total of 1324 3D beam elements and 488 nodes with 6 degrees of freedom at each node. All the joints in the finite element model are assumed to be rigid. The movement of all the supports in the three orthogonal directions is restricted. For the sake of convenience in the subsequent discussion, the beam elements in each component of the transmission tower are numbered differently. The beam elements in the vertical major members are numbered from 1 to 80 (denote zc), the elements in the platforms are numbered from 81 to 408 (denote pt), the elements in the skew members are counted from 409 to 772 (denote xg), the elements in the lower cross arm are counted from 773 to 1072 (denote hd1), and the elements in the upper cross arm are counted from 1073 to 1324 (denote hd2). The number of vertical major members is only 6% of the total number of elements used in the structure while the number of skew members is 24.7% of the total number of elements used in the structure. Except that the vertical major members are of hollow circular section, all the other members are of angle section.

4.2. Dynamic Characteristics of the Transmission Tower. The dynamic characteristics analysis is conducted based on the established finite element model of the steel transmission tower. The first eight natural frequencies and vibration modes of the tower are depicted in Table 1 and Figure 3, respectively. The first natural frequencies of the transmission tower for the out-of-plane and in-plane vibration are 1.736 Hz and 1.759 Hz, respectively. It is seen that the first and second vibration modes are the global vibration mode in the x direction and y direction, respectively. The third vibration mode is a global torsional vibration mode in the x-y plane due to the tower rotation. The fourth to sixth vibration modes are the high order translational and torsional vibration modes of the tower. The first eight natural frequencies computed indicate that the natural frequencies of the structure are not closely spaced. The dynamic responses of the first three mode shapes are the major parts of the entire dynamic responses of the transmission tower.

Table 1: Dynamic properties of the transmission tower.

Number	Natural frequency (Hz)	Properties of the mode shape
f_1	1.736	1st global vibration mode in the x direction
f_2	1.759	1st global vibration mode in the y direction
f_3	2.63	1st global torsional vibration mode
f_4	3.541	2nd global vibration mode in the x direction
f_5	3.961	2nd global vibration mode in the y direction
f_6	4.26	2nd global torsional vibration mode
f_7	4.849	Local vibration mode of the platform
f_8	5.767	3rd global vibration mode in the x direction

4.3. Frequency Sensitivity of the Transmission Tower. Figure 4 shows the sensitivities of the first eight natural frequencies to Young's modulus of each member. It is seen from the first two figures that the first two natural frequencies are more sensitive to Young's modulus change of members in the vertical major members (zc) than other members. The curves in the third figure indicate that the sensitivity coefficients of the first torsional frequency of the skew members are much larger than those of the other members. All the higher natural frequencies of the global vibration are more sensitive to Young's modulus change of both vertical major members and the skew members. This is consistent with the structural configuration and the modes of vibration; the first two translational modes of vibration are mainly due to the deformation of the vertical major members and the first torsional mode is due to the deformation of the skew members. However, the higher modes of vibration are mainly due to the movement combination of both vertical major members and the skew members. The seventh vibration mode is the local vibration of the platform number 1 and thereby the seventh natural frequency is clearly sensitive to Young's modulus of the platform number 1. To compare the magnitude of the sensitivity coefficients in Figure 4, one can find that Young's modulus of the vertical major members plays an important role in the first two vibration modes in comparison with all the other vibration modes. The sensitivity coefficients of the skew members are slightly smaller than those of the vertical major members.

Displayed in Figure 5 is the sensitivity of the first eight natural frequencies to the density of the material. It is well known that the natural frequencies decrease with

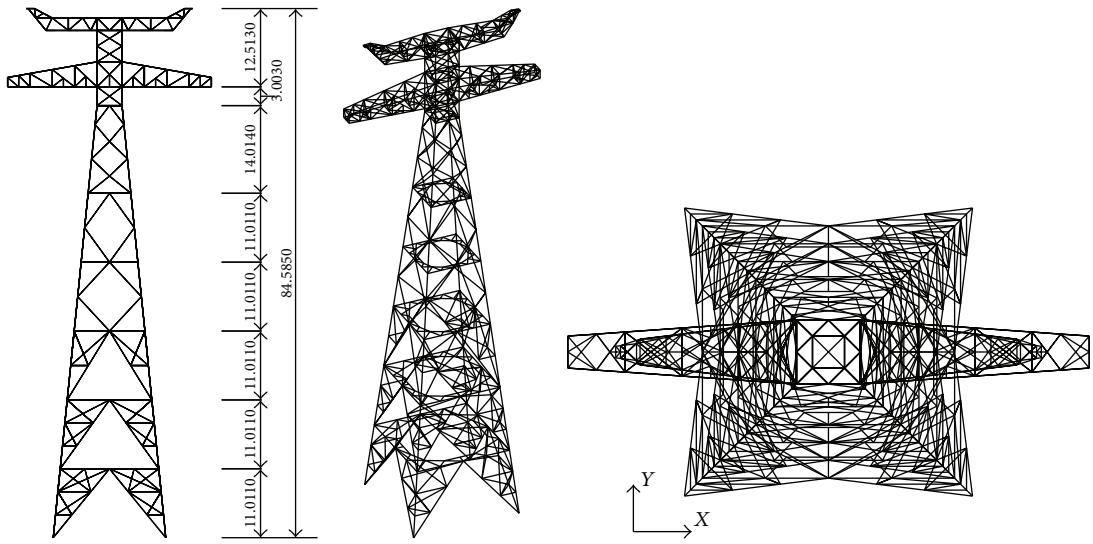

(a) Elevation (b) 3D model (c) Plane view

Figure 1: Analytical model of the example transmission tower.

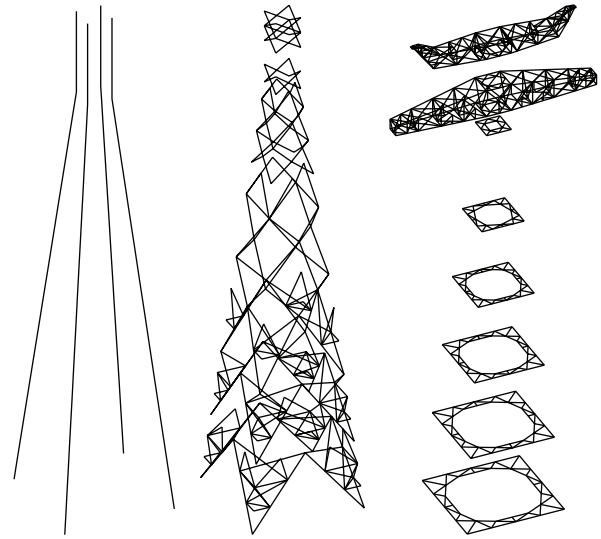

(a) Vertical major members (zc) (b) Skew members (xg) (c) Cross arm (hd) and platform (pt)

Figure 2: Configuration of the example transmission tower.

the increasing material density. Therefore, it is indicated from Figure 5 that the sensitivity coefficients are negative. It is seen that the sensitivity coefficients of the natural frequencies to the density are quite different to those of Young's modulus. The first two figures demonstrate that the first two natural frequencies are more sensitive to the density change of members in the vertical major members (zc) and cross arms. However, the density sensitivity coefficients of the skew members and platforms are much smaller. The curves in the third figure indicate that the sensitivity coefficients of the first torsional frequency of the two cross arms are much larger than those of the other members. This is because the third mode is the torsional vibration of the two cross arms. The second-order translational frequencies of both the out-of-plane vibration and in-plane vibration, namely, the fourth and fifth frequencies, are dominantly sensitive to the density change of the vertical major members. Similar observations can be made from the density sensitivity of the second order torsional modes (e.g., the sixth mode) because this mode is the torsional vibration of the tower body. Regarding

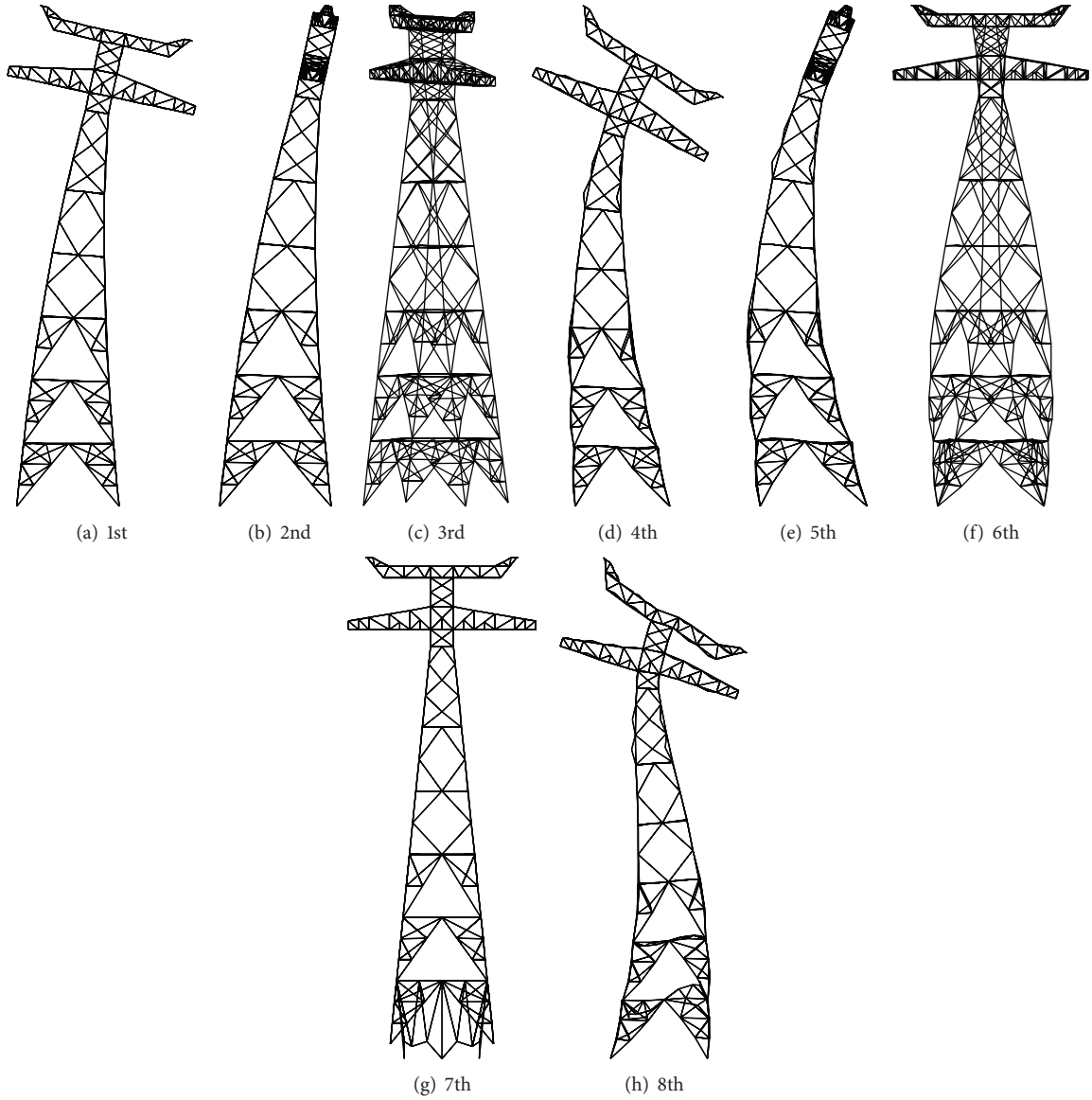

Figure 3: First eight mode shapes of the example transmission tower.

the higher order translational modes, the density of skew members may have slight effects on the sensitivity coefficients as shown in the eighth figures in Figure 5.

Figure 6 indicates the sensitivities of the first eight natural frequencies to the cross area of each member. It is clear that the sensitivity coefficients of the cross area are quite different to those of Young's modulus and density. The increase of member cross area does not always cause the increment of the structural natural frequencies. It is seen from the first two figures that the first two natural frequencies are more sensitive to the cross area change of the vertical major members than other members. As far as the first two natural frequencies are concerned, the increase in cross area of most of the vertical major members may induce the increment of the natural frequencies. On the contrary, the increase in the member cross areas of the two cross arms may lead to the increase of the global mass instead of the stiffness. Therefore, the structural natural frequencies may decrease to some extents. As displayed in the third figure, the skew members can be strengthened by increasing the cross areas and the third natural frequency, corresponding to the first order torsional mode, can be increased. Similar observations can be found from the sensitivity coefficients of the other higher natural frequencies. It is seen that the sensitivity coefficients of Young's modulus and the cross area are similar to great extents. The stiffness matrix of the ith element of a transmission tower in the local coordinate system $\mathbf{K}_i^e$ is expressed in (1). It can be found that both Young's modulus E and cross area A have an important contribution to the axial stiffness EA/l of a single member. In addition, Young's modulus also makes the contribution to the member bending stiffness EI/l^3. Therefore, the comparison between

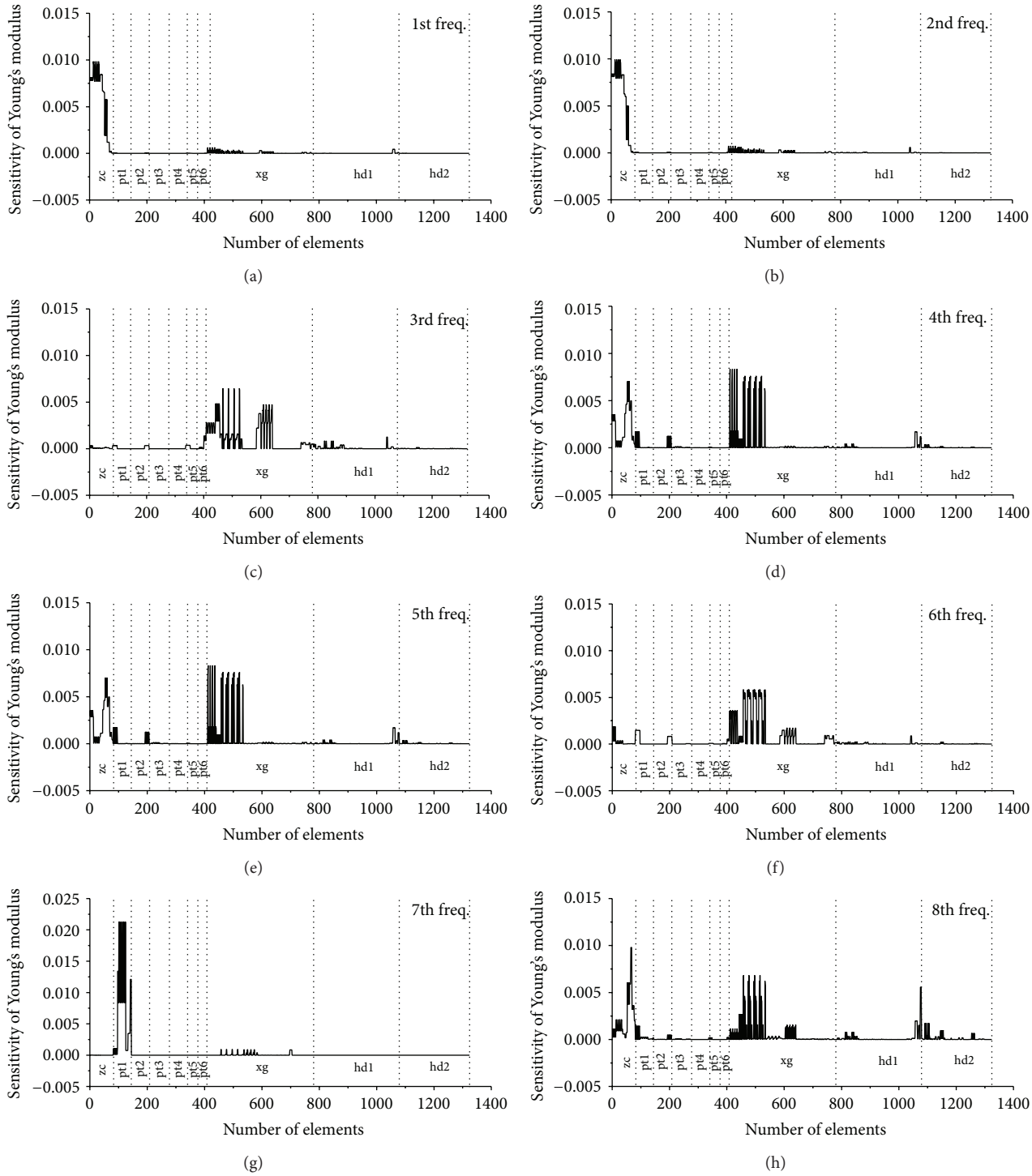

Figure 4: Sensitivity of first eight natural frequencies to the Young's modulus.

Figures 4 and 6 indicates that the magnitudes of the sensitivity coefficients of Young's modulus are slightly larger than those of the cross area.

Sensitivity of the first eight natural frequencies to the torsional stiffness I_x is displayed in Figure 7. It is seen from the third figure that the sensitivity coefficients of the third frequency to the torsional stiffness are much larger than those of the all the other frequencies. Therefore, the frequency sensitivity coefficients to the torsional stiffness are substantially smaller than those of Young's modulus, the density, and the cross area. The torsional stiffness of structural members may have a certain level of effects on the torsional

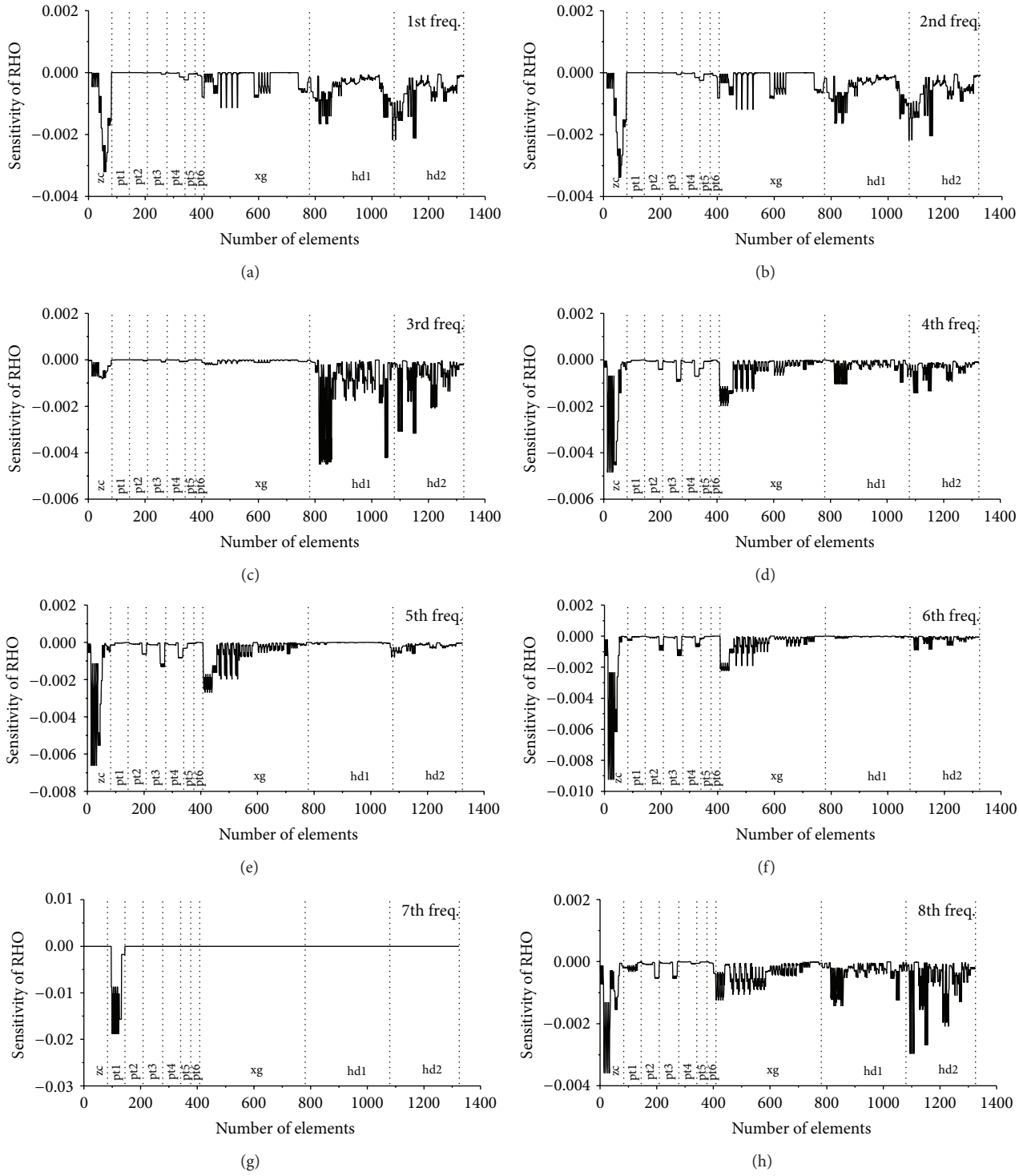

Figure 5: Sensitivity of first 8 natural frequencies to the density of material.

vibration modes of the transmission tower. The sensitivity of first eight natural frequencies to the bending moment of inertia I_y and I_z are indicated in Figures 8 and 9, respectively. Similarly, the frequency sensitivity coefficients to the bending moment stiffness are also remarkably smaller than those of Young's modulus, the density, and the cross area. It is found that the sensitivity coefficients of the major vertical members are much larger than those of the other members for the first five natural frequencies. This observation means that the effects of the bending moment inertia of the major vertical

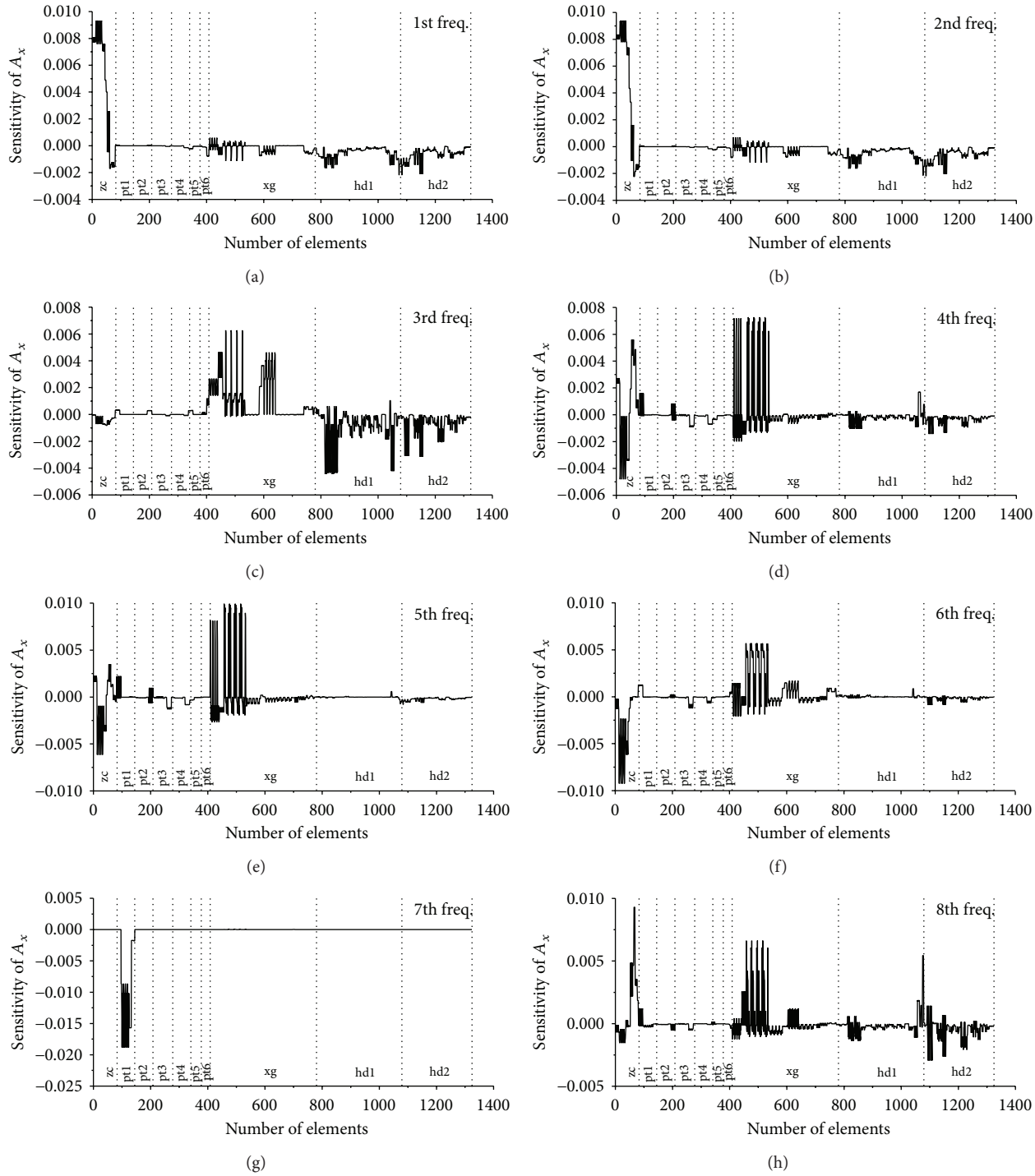

Figure 6: Sensitivity of first eight natural frequencies to the cross area.

members on structural modal properties are more obvious in comparison with other members.

5. Concluding Remarks

The feasibility of evaluating the parametric effects of a transmission tower based on the frequency sensitivity analysis is actively carried out in this study. The 3D analytical model of a transmission tower is first constructed by using the FE method. The differential sensitivity analysis approach is presented based on the differential sensitivity coefficient, the absolute sensitivity coefficient, and the relative sensitivity coefficient, respectively. The sensitivity coefficients to natural frequencies are deduced based on the equation of motion of the tower. In addition, the expression of the frequency

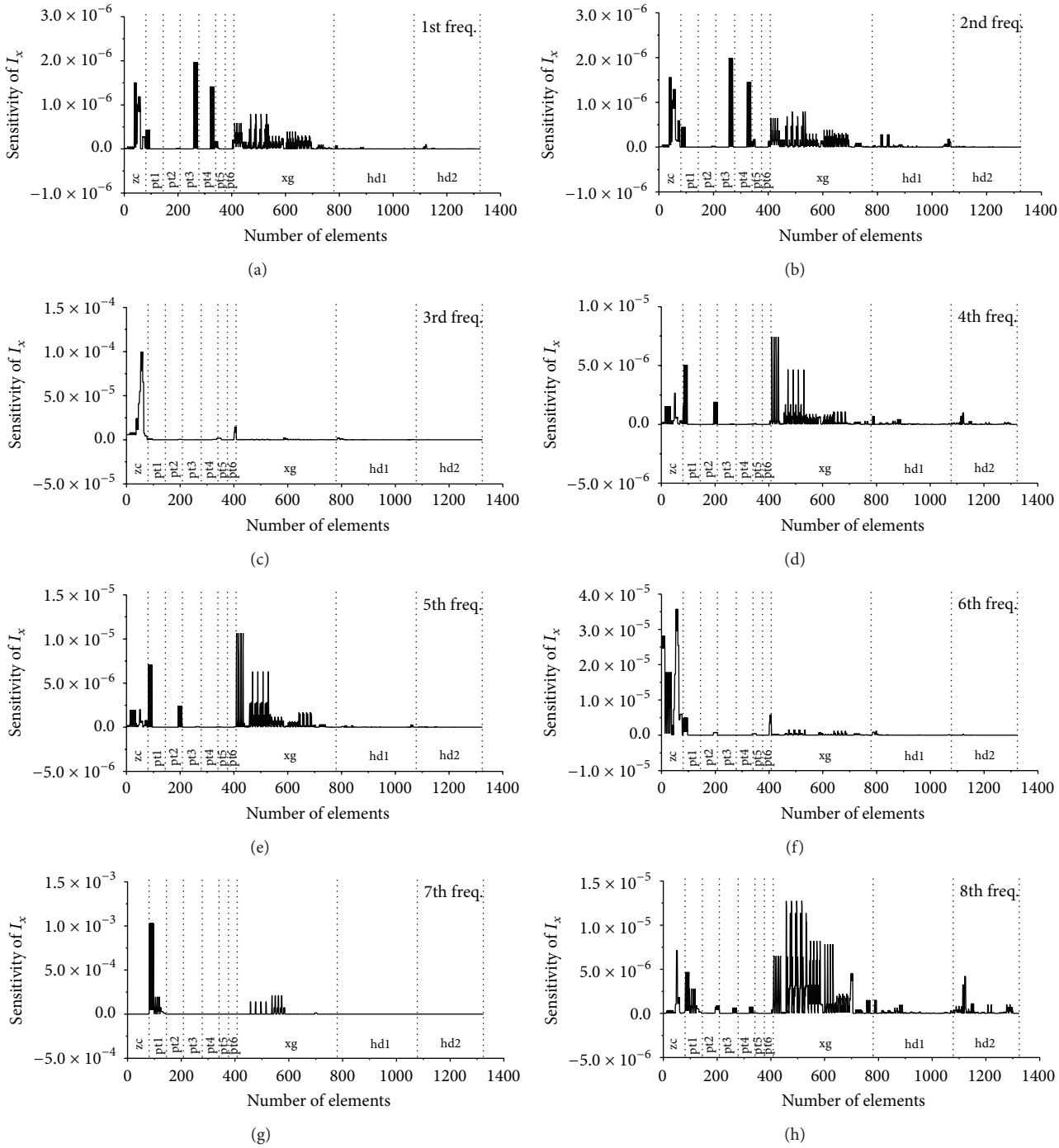

Figure 7: Sensitivity of first eight natural frequencies to the torsional stiffness I_x.

sensitivity to Young's modulus, density of material, the cross area of members, torsional stiffness, and bending moment inertia is proposed. A real transmission tower-line system is taken as the example to investigate the effects of the structural parameters on the natural frequency through the detailed parametric study.

The observations made demonstrate that Young's modulus of the vertical major members plays an important role in the first two vibration modes in comparison with all the other vibration modes. The sensitivity coefficients of the skew members are slightly smaller than those of the vertical major members. The sensitivity coefficients of the natural frequencies to the density are different to those of Young's modulus because the natural frequencies decrease with the increasing material density. The sensitivity coefficients of the cross area are quite different to those of Young's modulus and

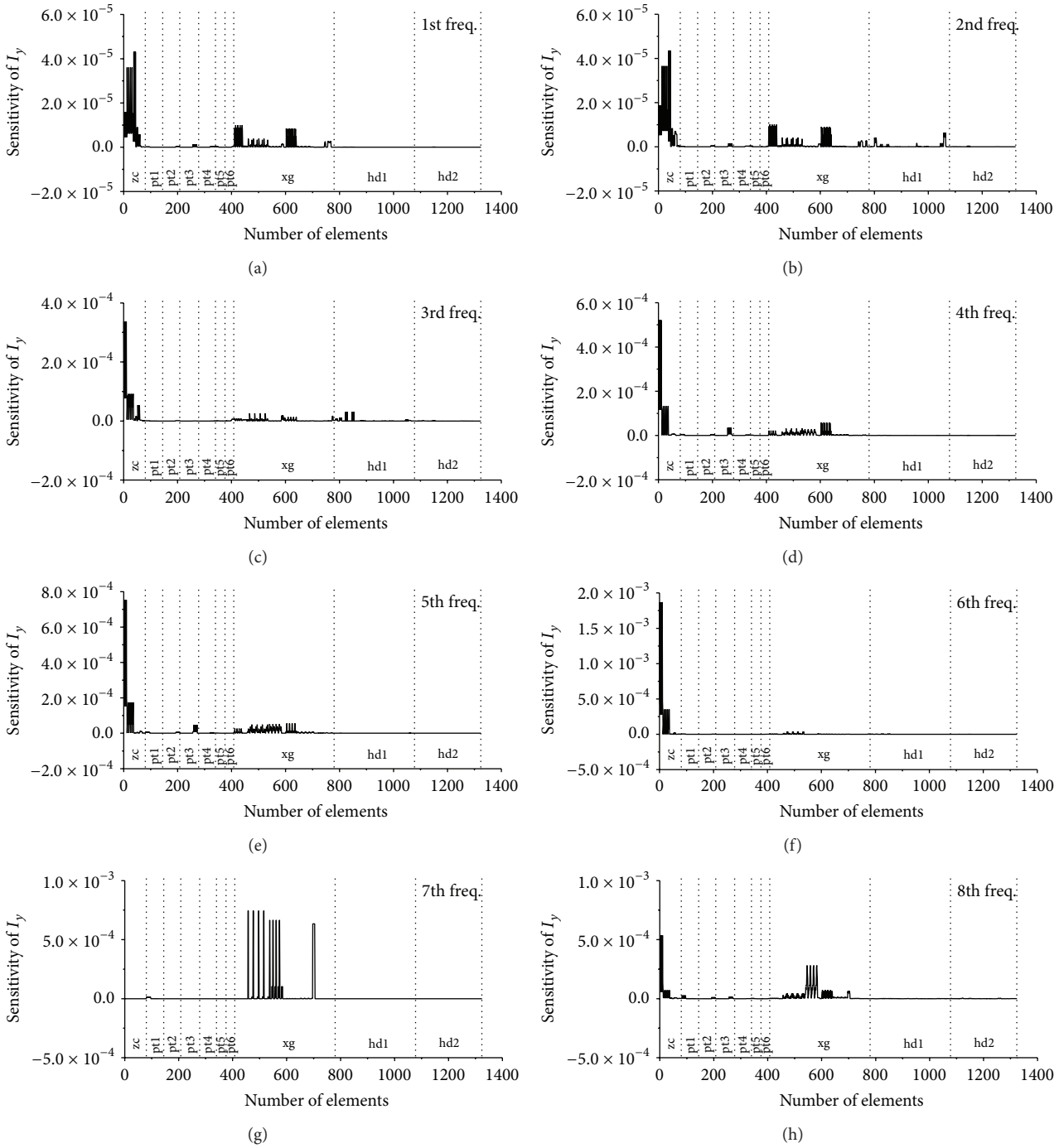

Figure 8: Sensitivity of first eight natural frequencies to the bending moment of inertia I_y.

density. The increase of member cross area does not always cause the increment of the structural natural frequencies. The frequency sensitivity coefficients to the torsional stiffness and the bending moment stiffness are substantially smaller than those of Young's modulus, the density, and the cross area. To compare the magnitudes of the sensitivity coefficients, one can find that Young's modulus, the density, and the cross area are more important structural parameters in assessing the dynamic performance of the transmission tower.

Conflict of Interests

The authors declare that there is no conflict of interests regarding the publication of this paper.

Acknowledgments

The writers are grateful for the financial support from the Technological Project of the Chinese Southern Power Grid

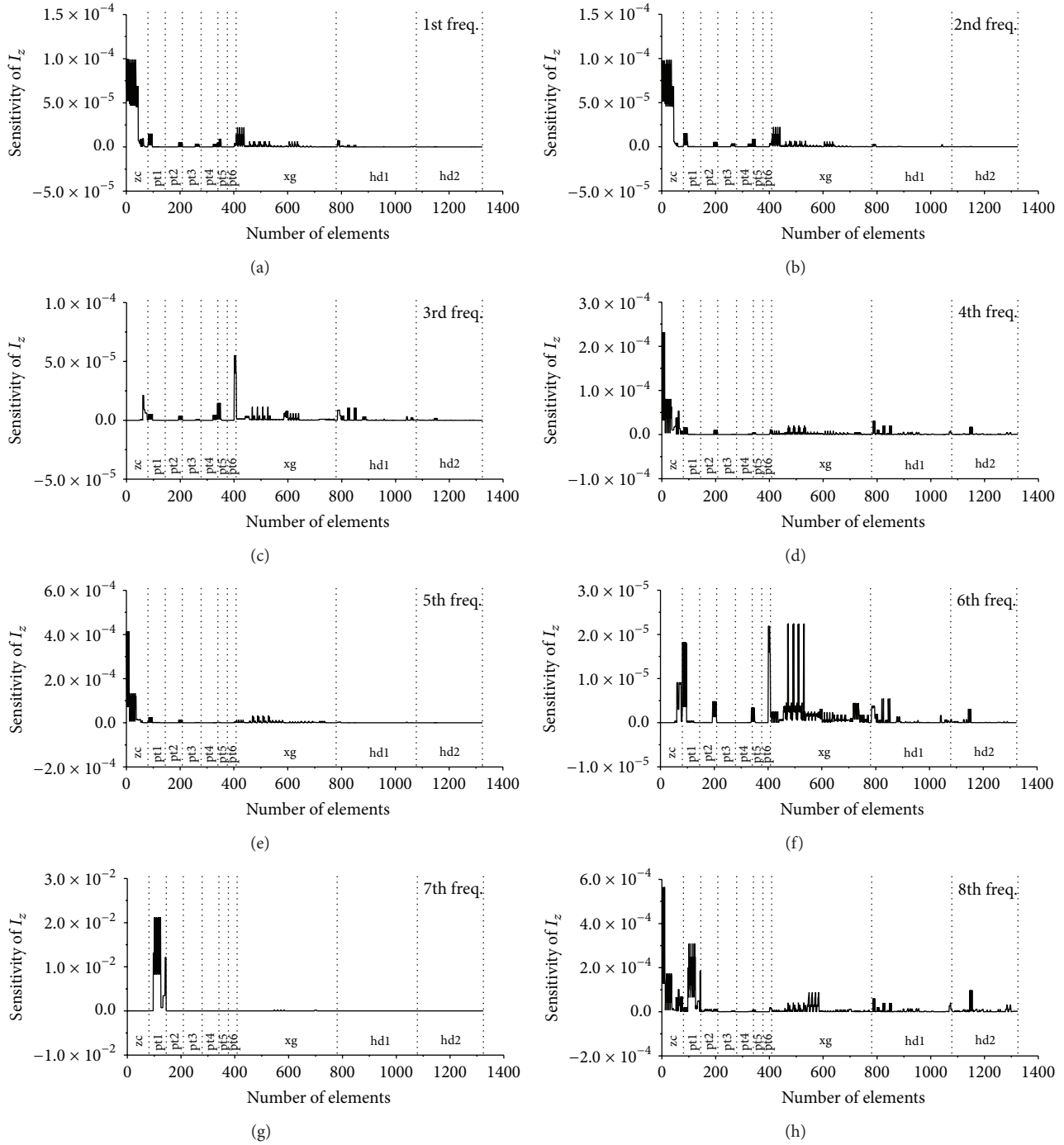

Figure 9: Sensitivity of first eight natural frequencies to the bending moment of inertia I_z.

Co. Ltd. (K-GD2013-0783), the Natural Science Foundation of Hubei Province (2014CFA026), and the Fok Ying-Tong Education Foundation (131072).

References

[1] E. Savory, G. A. R. Parke, M. Zeinoddini, N. Toy, and P. Disney, "Modelling of tornado and microburst-induced wind loading and failure of a lattice transmission tower," *Engineering Structures*, vol. 23, no. 4, pp. 365–375, 2001.

[2] B. Chen, J. Zheng, and W. L. Qu, "Control of wind-induced response of transmission tower-line system by using magnetorheological dampers," *International Journal of Structural Stability and Dynamics*, vol. 9, no. 4, pp. 661–685, 2009.

[3] E. Simiu and R. Scanlan, *Wind Effects on Structures*, John Wiley & Sons, New York, NY, USA, 3rd edition, 1996.

[4] Q. Xie and L. Sun, "Failure mechanism and retrofitting strategy of transmission tower structures under ice load," *Journal of Constructional Steel Research*, vol. 74, pp. 26–36, 2012.

[5] R. C. Battista, R. S. Rodrigues, and M. S. Pfeil, "Dynamic behavior and stability of transmission line towers under wind forces," *Journal of Wind Engineering and Industrial Aerodynamics*, vol. 91, no. 8, pp. 1051–1067, 2003.

[6] H. N. Li, S. Y. Tang, and T. H. Yi, "Wind-rain-induced vibration test and analytical method of high-voltage transmission tower," *Structural Engineering and Mechanics*, vol. 48, no. 4, pp. 435–453, 2013.

[7] P.-S. Lee and G. McClure, "Elastoplastic large deformation analysis of a lattice steel tower structure and comparison with full-scale tests," *Journal of Constructional Steel Research*, vol. 63, no. 5, pp. 709–717, 2007.

[8] T. Okamura, T. Ohkuma, E. Hongo, and H. Okada, "Wind response analysis of a transmission tower in a mountainous area," *Journal of Wind Engineering and Industrial Aerodynamics*, vol. 91, no. 1-2, pp. 53–63, 2003.

[9] H. Sohn, C. R. Farrar, F. M. Hemez, D. D. Shunk, D. W. Stinemates, and B. R. Nadler, "A review of structural health monitoring literature :1996–2001," Los Alamos National Laboratory Report LA-13976-MS, 2003.

[10] B. Chen, S.-L. Zhao, and P.-Y. Li, "Application of Hilbert-Huang transform in structural health monitoring: a state-of-the-art review," *Mathematical Problems in Engineering*, vol. 2014, Article ID 317954, 22 pages, 2014.

[11] B. Chen, Y. L. Xu, and X. Zhao, "Integrated vibration control and health monitoring of building structures: a time-domain approach," *Smart Structures and Systems-An International Journal*, vol. 6, no. 7, pp. 811–833, 2010.

[12] Y. Q. Ni, X. W. Ye, and J. M. Ko, "Monitoring-based fatigue reliability assessment of steel bridges: analytical model and application," *Journal of Structural Engineering*, vol. 136, no. 12, pp. 1563–1573, 2010.

[13] X. W. Ye, Y. H. Su, and J. P. Han, "Structural health monitoring of civil infrastructure using optical fiber sensing technology: a comprehensive review," *The Scientific World Journal*, vol. 2014, Article ID 652329, 11 pages, 2014.

[14] M. L. Friswell and J. E. Mottershead, *Finite Element Model Updating in Structural Dynamics*, Kluwer Academic, Norwell, Mass, USA, 1995.

[15] S. W. Doebling, C. R. Farrar, M. B. Prime, and D. W. Shevitz, "A review of damage identification methods that examine changes in dynamic properties," *Shock and Vibration Digest*, vol. 30, no. 2, pp. 91–105, 1998.

[16] B. Chen, Y. L. Xu, and W. L. Qu, "Evaluation of atmospheric corrosion damage to steel space structures in coastal areas," *International Journal of Solids and Structures*, vol. 42, no. 16-17, pp. 4673–4694, 2005.

[17] B. Chen and Y. L. Xu, "A new damage index for detecting sudden change of structural stiffness," *International Journal of Structural Engineering and Mechanics*, vol. 26, no. 3, pp. 315–341, 2007.

[18] K. J. Bathe, *Finite Element Procedures*, Prentice-Hall, Englewood Cliffs, NJ, USA, 1996.

[19] H. M. Irvine, *Cable Structure*, The MIT Press, New York, NY, USA, 1981.

[20] R. W. Clough and J. Penzien, *Dynamic of Structures*, McGraw-Hill, New York, NY, USA, 3rd edition, 2003.

[21] Y. L. Xu and B. Chen, "Integrated vibration control and health monitoring of building structures using semi-active friction dampers: part I-methodology," *Engineering Structures*, vol. 30, no. 7, pp. 1789–1801, 2008.

[22] B. Chen and Y. L. Xu, "Integrated vibration control and health monitoring of building structures using semi-active friction dampers: part II—numerical investigation," *Engineering Structures*, vol. 30, no. 3, pp. 573–587, 2008.

Hindawi Publishing Corporation
Journal of Sensors
Volume 2015, Article ID 610473, 6 pages
http://dx.doi.org/10.1155/2015/610473

Research Article

Distributed Measurement of Temperature for PCC Energy Pile Using BOFDA

Lei Gao,[1] Baoquan Ji,[1] Gangqiang Kong,[1] Xu Huang,[1] Mingkun Li,[1] and Ali H. Mahfouz[2,3]

[1]*Key Laboratory of Geomechanics and Embankment Engineering, Ministry of Education, Hohai University, Nanjing 210098, China*
[2]*Faculty of Petroleum and Mining Engineering, Suez University, Suez 34721, Egypt*
[3]*Engineering College, Jazan University, Jazan 45142, Saudi Arabia*

Correspondence should be addressed to Lei Gao; taiyang360@gmail.com

Received 16 November 2014; Revised 15 December 2014; Accepted 16 January 2015

Academic Editor: Fei Dai

PCC energy pile is a new technology for sustainable development of urban areas. Learning and understanding the temperature variation of PCC energy pile are very important to its development and application. In this study, the Brillouin optical frequency domain analysis (BOFDA) technology is firstly used to measure the temperature variation of PCC energy pile from a model test. The aim is to provide an optical fiber sensing method for monitoring the temperature distribution of PCC energy pile. When the temperatures of circulating water are 70°C, 60°C, 50°C, and 40°C, the result shows that the temperatures of PCC energy pile under different conditions are measured well by the optical fiber sensor. It will help to master the temperature distribution and thermomechanical characteristic of PCC energy pile. It can also provide the important scientific and theoretical basis for the design and application of PCC energy pile.

1. Introduction

The solar energy and geothermal energy on the surface of earth which are restored in the shallow soil can be absorbed by ground source heat pump which will provide the energy to the building. It is a double system of heating and cooling in the energy-efficient way, less pollution, and environment protection based on the principle of heat pump. For the reasons above, ground source heat pump is widely used in engineering application. In recent years, the underground space is on the fast exploitation. The energy pile technology combined with the ground source heat pump and pile foundation is proposed by the civil engineers. Various shapes of heat exchanger units are laid in the pile foundation. The low temperature geothermal energy can be transferred in the shallow layer soil. It will meet the conventional mechanical function and realize the heat exchange of the shallow geothermal energy. It plays a dual role of pile foundation and ground source heat pump. The cast-in-place concrete large-diameter pipe pile (PCC pile) is a new type of foundation reinforcement technology developed by Hohai University with independent intellectual property rights, which has strong applicability in construction. It is very convenient to use in the soft soil reinforcement and control the quality of construction. Besides, the PCC pile has a very high capacity with low cost and the depth of reinforcement can be up to 25 m or more. According to the characteristics of PCC pile, a novel energy pile technology called PCC energy pile is developed (see Figure 1), which has the features of efficient circulation of energy, less amount of concrete, high capacity of pile, space saving, and so on. The temperature variation of PCC energy pile is very important to optimize the design and construction of PCC energy pile. However, the little research has been done to the variation of temperature for this new kind of PCC energy pile. Now, the resistive sensor is commonly used to monitor the temperature of pile, but it is very easy to damp and is vulnerable to electromagnetic; it also needs to connect excessive data lines. The data obtained by the resistive sensor is often lost in the project. So the new temperature measurement technology and method should be used to monitor the temperature of PCC energy pile; it will show great significance for the development of PCC energy pile.

The Brillouin frequency domain analysis (BOFDA) is a new technology for temperature and strain measurement. Using this type of distributed sensing technology, the parameters can be measured as a function of the length optical fiber sensor [1–8]. The strain and temperature distribution information of the entire optical fiber can be continuously measured and real-time display by BOFDA technology. Meanwhile, the optical fiber sensor is a medium and a transmission channel with the characteristics of small size, light weight, geometric shape, and strong adaptability, antielectromagnetic interference, electrical insulation, high sensitivity, and so on. The distributed optical fiber sensor is easy to implement and perform remote monitoring; it can be widely used to monitor the deformation and temperature precisely in geotechnical engineering project [9–13]. In this paper, the new optical fiber sensing technology based on BOFDA is firstly used to monitor the real-time temperature variation of PCC energy pile. The layout of the optical fiber sensor and the PCC energy pile model test are proposed; the temperature data of PCC energy pile are obtained and analyzed.

2. Principle of BOFDA

The new distributed optical fiber sensing technology based on BOFDA was proposed in 1996 by Garus and the related experiments were carried out. The accuracy of spatial resolution of 3 m, temperature resolution of 5°C, and strain resolution of 0.01% was obtained [2]. The transfer function based on the location detection of the measuring point is achieved; its complex amplitude of the probe and pump light transmission are in full consideration. The temperature and strain distribution of optical fiber sensor can be obtained by calculating the impulse response function.

A fully distributed system can be realized by using the phenomenon called stimulated Brillouin scattering (SBS) in silica optical fiber. The SBS can be seen as the interaction of two counter propagating light waves with an acoustic wave within the optical fiber. There will be a frequency shift of the backscattered light and it depends on the strain and temperature distribution along the optical fiber sensor. The BOFDA analyzer calculates the complex transfer function by comparing with the optical signals in amplitude and phase. This function is converted by the inverse fast Fourier transform. In Figure 2, a bunch of narrow-line width continuous pump light is injected into a single-mode optical fiber sensor from one side and a bunch of narrow-line width continuous probe light is injected into the optical fiber from the other side. The frequency of the probe light is adjusted to a value that is lower than that of the pump light. The frequency difference between them is approximately equal to the Brillouin frequency shift. A variable frequency f_m with a sinusoidal signal is to detect the amplitude of modulated light. The detector is used to determine the intensity value of the signal at each frequency of probe light and pump light. The output signal of detector is input to the network analyzer instrument that is based on the light baseband transmission function. The output signal $h(t)$ of network analyzer converted by the inverse fast Fourier transform

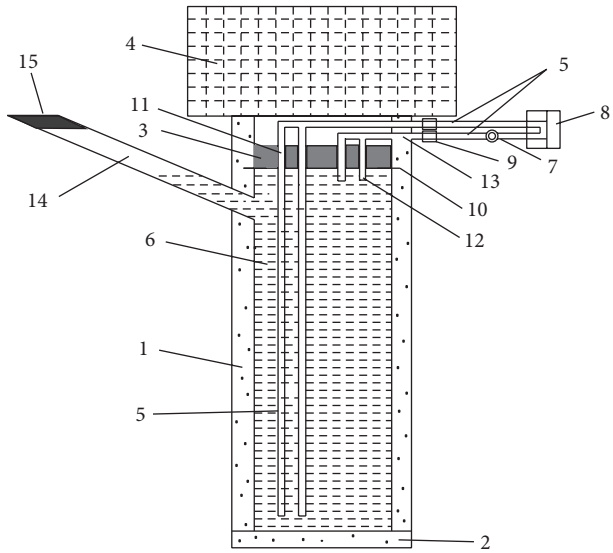

(1) PCC pile
(2) Base plate
(3) Cover plate
(4) Superstructure
(5) Heat pipe
(6) Thermal fluid
(7) Geothermal heat pump
(8) Collectors
(9) Removable contact
(10) Dowel
(11) Inlet hole
(12) Out hole
(13) Preformed hole
(14) Check passage
(15) Seal plate

Figure 1: Design of PCC energy pile [14].

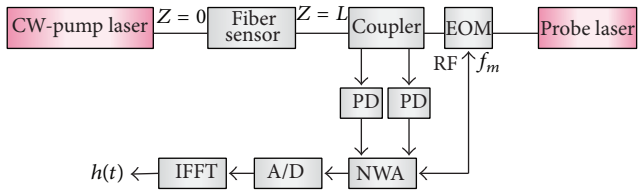

Figure 2: Principle of BOFDA [8].

contains the strain or temperature distribution information along the optical fiber sensor [6–8]. Figure 2 shows the principle of BOFDA system.

3. Model Test of PCC Energy Pile

3.1. Instrument. The BOFDA instrument used in this study is fTB2505 produced by a German company called fibrisTerre GmbH. The instrument can be used for the continuous, long-distance strain and temperature monitoring by the optical fiber. It is also used to monitor the early damage of geotechnical structures, fatigue strength of bridges, tunnels, dams, high-precision strain of oil pipeline, and so on. The fTB2505 has the measure accuracy of less than 2 $\mu\varepsilon$ and temperature measurement accuracy of less than 0.1°C. It can achieve the spatial resolution of 0.5 m within the range of

(a) Instrument (b) Software

Figure 3: Test instrument and software.

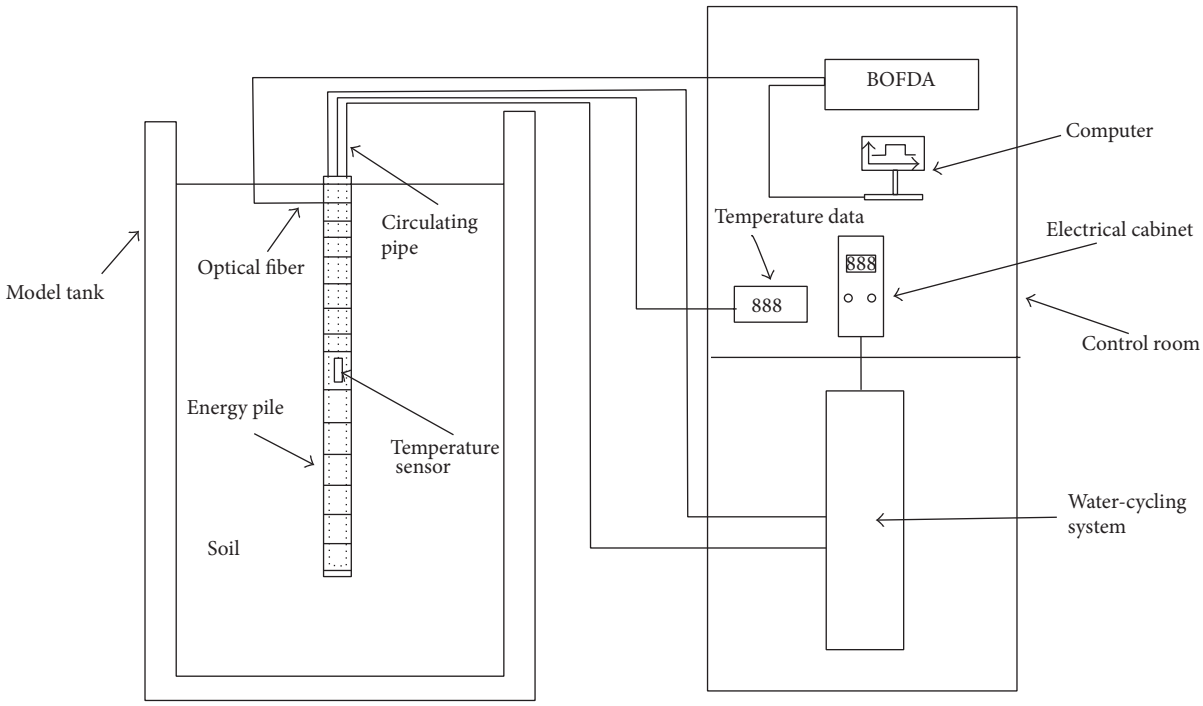

Figure 4: Diagram of model test for PCC energy pile.

25 km. The parameters of BOFDA with the type of fTB2505 are shown in Tables 1 and 2.

The fTB2505 is a readout unit for the distributed temperature and strain measurement using the optical fiber sensor. It can realize long-range, continuous sensing and structural health monitoring, which is very useful for the civil and geotechnical engineering project. The measurement system includes the monitoring software FTView, FTB readout unit, and a computer. The instrument and software can be seen in Figure 3.

3.2. Test Equipment. In order to simulate the actual work state of PCC energy pile, a PCC energy pile model test based on BOFDA is proposed. The test equipment mainly includes a PCC energy pile, soil, a heating device, and an optical sensing fiber sensor. Figure 4 is the diagram of model test for PCC energy pile based on BOFDA. The model can also be used to study the temperature variation of different type of energy pile. The size of model tank used in the test is 2 m×1 m×1.5 m.

Table 1: Parameters of fTB2505.

Label	Parameters	Label	Parameters
Fiber model	Standard single-mode optical fiber	Distance	25 km
Connector type	E-2000/APC	Spatial resolution	0.5 m
Detection form	Double-end detection	Monitoring mode	Single, continuous, custom
Spatial accuracy	0.05 m	Size	$L \times W \times H$ 495 × 482 × 145

Table 2: Indices of fTB2505.

Label	Index			Label	Index	
Dynamic range	>10 dB			Weight	13 kg	
Measurement object	Brillouin frequency shift, temperature, strain			Temperature	5–40°C	
Accuracy range	Accuracy		Fluctuation range	Typical acquisition time	0.2 km	20 s
	Strain	<2 $\mu\varepsilon$	±3%		2 km	1 min
	Temperature	<0.1°C	−273 to 1000°C		10 km	8 min
	Brillouin frequency shift	<100 kHz	10–13 GHz		25 km	25 min

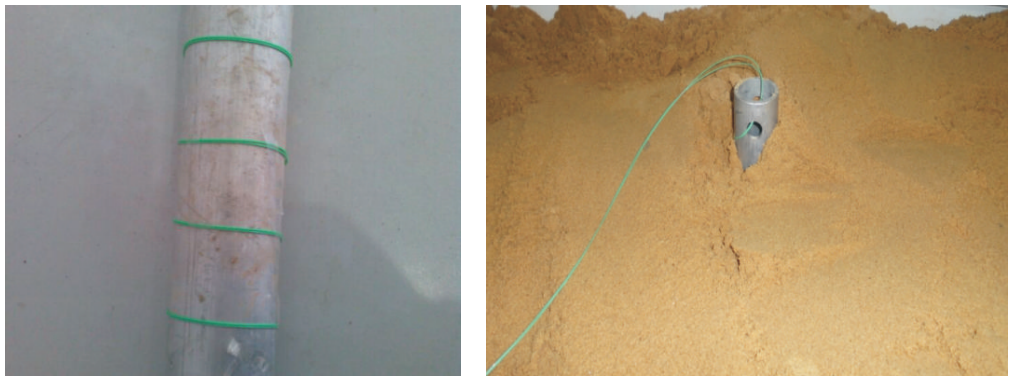

(a) Installation of optical fiber sensor (b) Pile and soil

Figure 5: Photos of model test for PCC energy pile.

The heater provides the heat to the model of PCC energy pile. The heater consists of four parts: thermostat control panel, heating pipe, pump, and circulating water. The heater uses circulating hot water as heat transfer medium; the water is heated by using electricity. It has a touch control electric cabinet which is easy to operate. Meanwhile, it also has the characteristics of fast heating and cooling, high accuracy, stability, and unique heat design with power. The single-mode optical fiber sensor is used as the temperature sensor in this test shown in Figure 5(a). The optical fiber sensor responds quickly and can be monitored remotely to the long distance which can ensure the safety of person and equipment in the project. The optical sensing fiber sensor is laid helically as shown in Figure 5(b); it should be examined in case there is some damage produced during the installation process.

3.3. Result and Discussion. The model of PCC energy pile has the diameter of 5 cm and the length of 1.0 m. An optical fiber sensor is fixed along the pile. The temperatures of circulating water are 70°C, 60°C, 50°C, and 40°C; the temperatures of PCC energy pile under different conditions are measured. It can be seen in Figure 6 that the temperature of the optical fiber sensor along with PCC energy pile can be obtained during the measurement time that lasts for 180 seconds, and the temperature of the optical fiber sensor shows a decreasing trend with time. The temperature distribution of PCC energy pile with 70°C, 60°C, 50°C, and 40°C is shown in Figures 6(a), 6(b), 6(c), and 6(d), respectively. It indicates that the temperature of PCC energy pile decreases when the water temperature decreases. When the water temperature decreases to 40°C which is equal to the temperature of PCC energy pile, there will be very small variation of temperature for the pile. The results indicate that the model test of PCC energy pile based on BOFDA is successfully developed to simulate the working state and monitor the temperature variation of PCC energy pile. The optical sensing fiber sensor is used to obtain a lot of useful data and good results for the pile.

PCC energy pile is a new pile; the reinforcement cost of PCC energy pile is low and very close to a flexible pile, while it has an effect of rigid reinforcement. The PCC energy pile can be used in the clay, sand, and silt soil area. In order to master the temperature distribution and thermomechanical characteristics of PCC energy pile, a PCC energy pile model test based on BOFDA is developed; the model test system is very good for the testing. The temperature of PCC energy pile is often measured by the resistive sensor. But the resistive sensor is easily destroyed; it also needs to connect excessive data lines and have only one piece of data for each monitoring point; the data is often lost in the project; it cannot obtain all the temperature information of PCC energy pile. So the new BOFDA technology is used to monitor the temperature of PCC energy pile in this test system; the result shows that the BOFDA technology can measure the temperature of PCC energy pile well and the optical fiber sensor is used to measure the temperature of every point for the pile. In the future, the strain of PCC energy pile should also be measured by the optical fiber sensor; this will show great significance for the development of PCC energy pile.

4. Conclusions

(1) PCC energy pile is a new type of pile, which has the advantages of energy saving and environmental

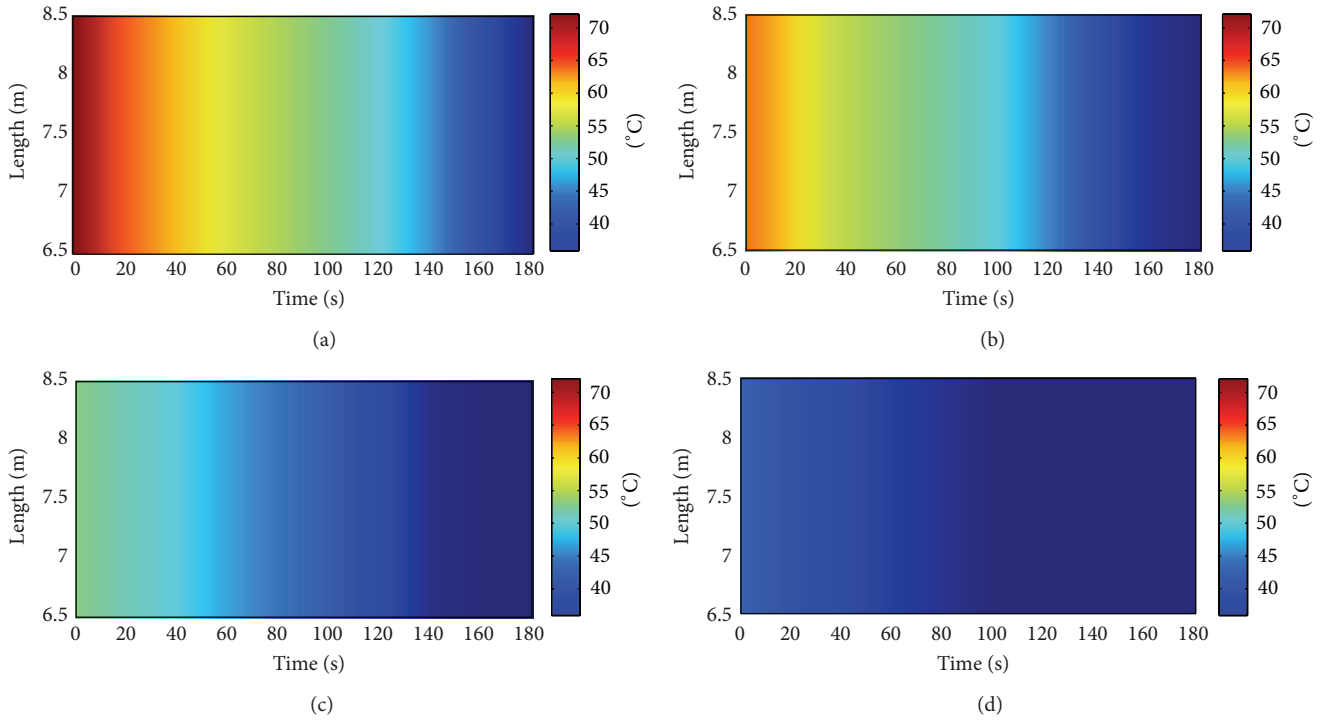

Figure 6: Variation of temperature for PCC energy pile.

protection. The cost of PCC energy pile is low; it can be used in the clay, sand, and silt soil area and will have a very broad prospect.

(2) As a new technology, the BOFDA monitoring technology is firstly used to measure the temperature of PCC energy pile; it shows that the optical fiber has the advantages of simple layout, high survival rate, and high precision.

(3) A PCC energy pile model test based on BOFDA is developed. The temperature variation of PCC energy pile can be effectively monitored by using BOFDA technology; the temperature information of PCC energy pile is obtained and the model test achieves good results.

Conflict of Interests

The authors declare that there is no conflict of interests regarding the publication of this paper.

Acknowledgments

Financial supports from the Fundamental Research Funds for the Central Universities of Hohai University (no. 2014B04914), China Postdoctoral Science Foundation (nos. 2012M511193 and 2014T70468), Ph.D. Programs Foundation of Ministry of Education of China (no. 20120094120015), the Natural Science Foundation of Jiangsu Province (no. BK20130832), and the National Natural Science Foundation of China (no. 51378178) are gratefully appreciated.

References

[1] D. Garus, T. Gogolla, K. Krebber, and F. Schliep, "Brillouin optical-fiber frequency-domain analysis for distributed temperature and strain measurements," *Journal of Lightwave Technology*, vol. 15, no. 4, pp. 654–662, 1997.

[2] R. Bernini, A. Minardo, and L. Zeni, "An accurate high-resolution technique for distributed sensing based on frequency-domain brillouin scattering," *IEEE Photonics Technology Letters*, vol. 18, no. 1, pp. 280–285, 2006.

[3] X. Bao and L. Chen, "Recent progress in distributed fiber optic sensors," *Sensors*, vol. 12, no. 7, pp. 8601–8639, 2012.

[4] F. Wang, C. Li, X. Zhao, and X. Zhang, "Using a Mach-Zehnder-interference-based passive configuration to eliminate the polarization noise in Brillouin optical time domain reflectometry," *Applied Optics*, vol. 51, no. 2, pp. 176–180, 2012.

[5] X. Zhang, Y. Lu, F. Wang, H. Liang, and Y. Zhang, "Development of fully-distributed fiber sensors based on brillouin scattering," *Photonic Sensors*, vol. 1, no. 1, pp. 54–61, 2011.

[6] Y. Yao, Y. Lu, X. Zhang, F. Wang, and R. Wang, "Reducing trade-off between spatial resolution and frequency accuracy in BOTDR using cohen's class signal processing method," *IEEE Photonics Technology Letters*, vol. 24, no. 15, pp. 1337–1339, 2012.

[7] R. Bernini, A. Minardo, and L. Zeni, "Distributed sensing at centimeter-scale spatial resolution by BOFDA: measurements and signal processing," *IEEE Photonics Journal*, vol. 4, no. 1, pp. 48–56, 2012.

[8] C. A. Galindez-Jamioy and J. M. López-Higuera, "Brillouin distributed fiber sensors: an overview and applications," *Journal of Sensors*, vol. 2012, Article ID 204121, 17 pages, 2012.

[9] H.-H. Zhu, A. N. L. Ho, J.-H. Yin, H. W. Sun, H.-F. Pei, and C.-Y. Hong, "An optical fibre monitoring system for evaluating

the performance of a soil nailed slope," *Smart Structures and Systems*, vol. 9, no. 5, pp. 393–410, 2012.

[10] Y. Lu, B. Shi, G. Q. Wei, S. E. Chen, and D. Zhang, "Application of a distributed optical fiber sensing technique in monitoring the stress of precast piles," *Smart Materials and Structures*, vol. 21, no. 11, Article ID 115011, 2012.

[11] X. Weng, H.-H. Zhu, J. Chen, D. Liang, B. Shi, and C.-C. Zhang, "Experimental investigation of pavement behavior after embankment widening using a fiber optic sensor network," *Structural Health Monitoring*, vol. 14, no. 1, pp. 46–56, 2015.

[12] H.-H. Zhu, B. Shi, J.-F. Yan, J. Zhang, C.-C. Zhang, and B.-J. Wang, "Fiber Bragg grating-based performance monitoring of a slope model subjected to seepage," *Smart Materials and Structures*, vol. 23, no. 9, Article ID 095027, 2014.

[13] H.-H. Zhu, B. Shi, J. Zhang, J.-F. Yan, and C.-C. Zhang, "Distributed fiber optic monitoring and stability analysis of a model slope under surcharge loading," *Journal of Mountain Science*, vol. 11, no. 4, pp. 979–989, 2014.

[14] H. L. Liu, G. Q. Kong, and W. W. N. Charles, "Applications of energy piles and technical development of PCC energy piles," *Chinese Journal of Geotechnical Engineering*, vol. 36, no. 1, pp. 176–181, 2014.

Hindawi Publishing Corporation
Journal of Sensors
Volume 2015, Article ID 908956, 16 pages
http://dx.doi.org/10.1155/2015/908956

Research Article

Toward Collinearity-Avoidable Localization for Wireless Sensor Network

Xiaoyong Yan,[1,2] Aiguo Song,[2] Jimin Yu,[1] and Zhong Yang[1]

[1]*School of Intelligence Science and Control Engineering, Jinling Institute of Technology, Nanjing 211169, China*
[2]*School of Instrument Science and Engineering, Southeast University, Nanjing 210096, China*

Correspondence should be addressed to Aiguo Song; a.g.song@seu.edu.cn

Received 16 June 2014; Revised 10 November 2014; Accepted 11 November 2014

Academic Editor: Xiaowei Ye

In accordance with the collinearity problem during computation caused by the beacon nodes used for location estimation which are close to be in the same line or same plane, two solutions are proposed in this paper: the geometric analytical localization algorithm based on positioning units and the localization algorithm based on the multivariate analysis method. The geometric analytical localization algorithm based on positioning units analyzes the topology quality of positioning units used to estimate location and provides quantitative criteria based on that; the localization algorithm based on the multivariate analysis method uses the multivariate analysis method to filter and integrate the beacon nodes coordinate matrixes during the process of location estimation. Both methods can avoid low estimation accuracy and instability caused by multicollinearity.

1. Introduction

Wireless sensor network (WSN) [1–3] refers to a sort of wireless network comprised of large amounts of static or mobile sensor network nodes in forms of self-organization and multihop. The aim of such network is to cooperatively detect, process, and transmit targets' monitoring information within the coverage area of the network, as well as report the information to users. As a new pattern of obtaining information, it possesses many advantages such as low cost, easy deployment, self-organization, and flexibility, so it has been widely applied in various domains, such as national defense and military affairs [4], environment inspection [5], traffic management [6], long-distance control of dangerous region [7], and so on. WSN has shown its significance and capability in application.

In many application problems related to sensor network, location information of nodes is of great importance to the monitoring activity of the whole network, which plays a critical role in many applications. Monitoring data without nodes' location information is often of no use. 80% of information provided by sensor nodes to users related with the monitored area is connected with location [8].

Generally, the localization process can be roughly divided into two phases [9, 10]: distance measurement phase and location estimation phase. In distance measurement phase, sensor nodes communicate with neighbors to estimate distance between pairs of devices. In location estimation phase, a localization method is used based on previous estimated distance, and sensor nodes can finally estimate their physical locations in the form of coordinates. "Zero error" is the eternal pursuit of localization algorithm. Owing to the limited computing capacity of sensor and complexity in the network environment, each stage would generate some errors that have significant influence on the final coordinate estimation. Therefore, the final estimated locations of the unknown nodes are mainly affected by the distance measurement between the nodes and the relative location of reference nodes. Most researchers carried out studies for the measurement accuracy [11–13] and have achieved some results, especially in recent years, for further development of robust estimation, making use of this advanced technology to the localization accuracy and algorithm design of localization mechanism. However, when it is used as the reference nodes for location estimation, in other words, when the topological shape between beacon nodes is collinear or approximately collinear, that is, there

is multicollinearity [14, 15], the localization accuracy of surrounding unknown nodes is poor, which can even reduce the localization accuracy of the whole monitoring area. At present, most localization methods conduct research in accordance with the ranging error during the localization process, and seldom consideration had been given to the impact of beacon nodes on localization accuracy.

The research object of this paper is the impact of the relative location between beacon nodes on localization accuracy, and the discussion is divided into two parts: the first part starts from analysis of the topology quality of beacon nodes; firstly, the multicollinearity problem caused by poor localization units under two-dimensional and three-dimensional localization environment will be analyzed. Then, the shape of poor localization units will be provided, which will also be quantified, the quality determination standard will be provided, and last but not the least, the impact of multicollinearity problem caused by collinear or approximately collinear localization units on the localization accuracy will be solved; the second part starts from the coordinate matrix of localization units; the dimensionality reduction method in multivariate analysis is used to reconstruct the beacon nodes used in location estimation, and by eliminating the data with low SNR (signal to noise ratio), the noise is reduced and the data with multicollinearity is eliminated.

The rest of the paper is organized as follows. In Section 2, we analyze two-dimensional and three-dimensional localization unit topological qualities. In Section 3, we formulate a series of newly developed localization algorithms based on the geometry analysis of the localization unit and describe these WSN localization algorithms. In Section 4, we make use of multivariate analysis to analyze the localization unit and formulate our localization algorithm based on multivariate analysis. In Section 5, we give justification of the applicability and effectiveness of our approaches in WSN location. Section 6 gives the conclusion.

2. Topological Analysis of Beacon Nodes

In general, the more beacon nodes are chosen by the unknown node, the more accurate the estimated location is [9, 16]. But, in fact, the topology of beacon nodes and the topological structure formed between beacon nodes and the unknown node will greatly affect unknown node's estimation result. Localization algorithm in the two-dimensional space requires a minimum of three reference nodes within the whole operational field [16]; however, in a three-dimensional space, due to increase of one dimensionality, it requires at least four beacon nodes to estimate the location of an unknown node [16]. Without loss of generality, a localization unit (LU) is defined as a beacon node group which can determine at least one unknown node and directly affect the final localization result. In a two-dimensional plane, when the distance between each beacon node and the unknown node in a LU is calculated, the trilateration or multilateration can be used to determine the location of the unknown node. However, during calculation of the distance between the unknown node and beacon node, there generally exists certain error, which makes the three circles fail to meet at one point during the trilateral positioning, so the estimation method should be used to determine the location of unknown node. When three beacon nodes spread approximated on a straight line, that is, the three nodes are of collinearity, the location of unknown nodes may not be able to be estimated with ordinary least-squares estimation method, and the error rate can be up to 200% [17, 18]. See Figure 1. The distance between node A and each beacon node $L1$, $L2$, and $L3$ has been given. As the three beacon nodes are almost on a straight line, that is, the three nodes are approximately of collinearity, the location of unknown node A may be A or A'. As for this, A's practical location cannot be figured out under such circumstance.

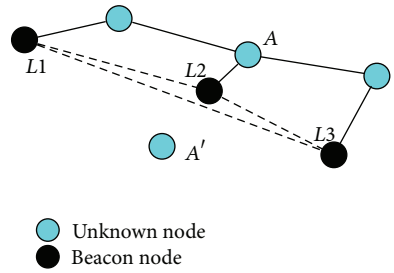

Figure 1: Collinearity of beacon nodes.

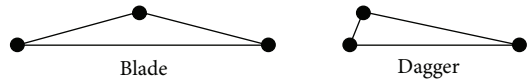

Figure 2: The poor-quality of LU in two-dimensional space.

Because in a two-dimensional space, the three beacon nodes that constitute the LU form a triangle, there are two kinds of collinearity phenomena: when the three points of triangle are in a straight line, the location process has complete collinearity, which is rare in reality; more often, approximate collinearity tends to occur; the LU with approximate collinearity has at least one small angle, and the formed triangle has a big aspect ratio. In other words, the triangle has at least one small angle, and three vertices of triangle are approximately collinear. It is also easy for us to know there are two types of triangle (as shown in Figure 2): one type has no short edge and is called blade; the other type has one short edge and is called dagger [19, 20].

During three-dimensional location estimation, if a certain beacon node is known, and the distance between the undetermined unknown node and this node can be observed, then this undetermined track is a sphere. In order to determine the location of the undetermined node, its distances to at least four known nodes should be determined; create four positioning spheres with the four known nodes as the centers of sphere and with the observed four distances as radiuses, two spheres can intersect at one space curve, and four spheres can intersect at one point. Because it requires at least four beacon nodes to conduct three-dimensional localization, so a tetrahedron determines the LU of three-dimensional localization. Similar to the two-dimensional space, the topology quality of tetrahedron also affects the localization accuracy

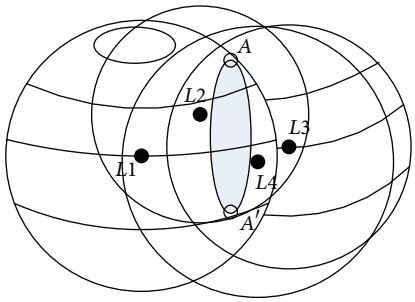

Figure 3: Four coplanar beacons in three-dimensional space.

of unknown node with it as the reference. Similarly, the distance error is inevitable in an actual environment, which causes that the four spheres in the localization not necessarily have an intersection point. When the relative locations of four beacon nodes are approximately coplanar, four spheres have two intersection points, so it is difficult to estimate the location of unknown node. As shown in Figure 3, if the geometric distributions of beacon nodes $L1$, $L2$, $L3$, and $L4$ are completely coplanar, when using the traditional location estimation method, unknown node's estimated coordinate may be A or A', in which case node A's physical coordinate cannot be estimated and the errors also will be up to 200%. If the deployment environment noise is large, the estimated location of the unknown node A will be far away from its true location.

It is generally believed that tetrahedron is the expansion of triangle in the three-dimensional space, and therefore, there are two situations in which collinearity phenomenon occurs: when the volume of tetrahedron is close to zero, it is equal to occurrence of approximately collinear phenomenon; when the volume of tetrahedron is zero, it is equal to occurrence of complete collinear phenomenon. The researchers found that when tetrahedral volume is equal to zero or tends to zero, the composition of the tetrahedron triangle always contains one or more triangles with a large aspect ratio [19, 21]. Cheng et al. [19, 22] made detailed study on the tetrahedrons, proposing nine kinds of poor-quality tetrahedron whose structures are shown in Figure 4.

3. Localization Method Based on the Geometrical Analysis of LU

3.1. Geometrical Analysis of Two-Dimensional LU. In order to solve the impact of collinearity phenomenon on localization accuracy in the two-dimensional space, the researchers have proposed multiple solutions based on analysis of LU in different scenarios. In accordance with the fact that the LU has a triangular form in the two-dimensional space, Poggi and Mazzini [23] proposed the concept of collinearity (also called degree of collinearity, DC). They used the smallest value of the three heights of triangle as the DC's parameter of a triangle and used it to measure the topology quality of LU; the more the three beacon nodes that constitute the LU are close to be collinear, the lower its DC is, and otherwise the higher the DC is. Their experimental result also shows that the more the LU are close to be collinear (i.e., low DC), the higher the location error of unknown node is, which might even be nonlocalized; the more the LU are close to equilateral triangle, the higher the localization accuracy of unknown nodes is. Later, Wu et al. [24, 25] proposed another standard of DC, that is, the biggest cosine value of the interior angles of triangle. Similarly, for the DC by using the method proposed by them the lower the value is, the worse the estimation result is; the higher the DC is, that is, the more the LU are close to equilateral triangle, the better the positioning result is. The literature [25] also provides another definition of DC: assuming the longest side length of the triangle formed by three random points in the plane is $l_{\max}$, the corresponding height of this length is $h_{\min}$, the ratio $2\sqrt{3}/3$ between $h_{\min}$ and $l_{\max}$ is defined as the collinearity of this triangle, and when the three nodes are collinear, the collinearity is 0. In this way, the value range of DC is $[0, 1]$, and the smaller the collinearity is, the closer to be collinear these three nodes are. The several DC determination methods mentioned above are actually used to measure the quality of triangle unit. Many years ago, researchers [20] had studied in detail the measurement criterion for the quality of triangle unit and provided various scientific judgment and quality evaluation methods from different perspectives. They believed that the measurement criterion for the quality of triangle positioning unit should satisfy the following principle: the translation, rotation, inverse, reflection, and uniform scaling of triangle unit should change its measured value; when and only when the triangle is an equilateral triangle, use the biggest measured value; when the triangle area is close to zero, its measured value is also close to zero. Based on the standard mentioned above, the researchers provided various methods to determine the topology quality of triangle: the smallest angle measurement method; the longest and shortest side measurement method; area-side length measurement method; inner and external radius measurement method; inner radius-shortest side measurement method; shortest height-longest side measurement method. The quality determination method mentioned above has the following definition formula:

(1) the smallest angle measurement method

$$q_{\alpha\min} = \frac{3\alpha_{\min}}{\pi}, \tag{1}$$

(2) the longest and shortest side measurement method

$$q_{Ll} = \frac{l_{\min}}{l_{\max}}, \tag{2}$$

(3) area-side length measurement method

$$q_{ALS} = \frac{4\sqrt{3}A}{l_1^2 + l_2^2 + l_3^2}, \tag{3}$$

(4) inner and external radius measurement method

$$q_{Rr} = \frac{2r}{R}, \tag{4}$$

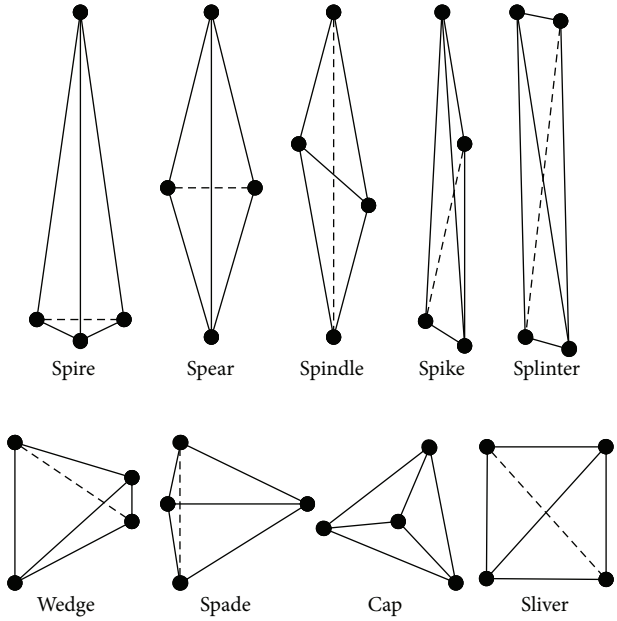

Figure 4: The poor-quality of LU in three-dimensional space.

(5) inner radius-shortest side measurement method

$$q_{Lr} = \frac{2\sqrt{3}r}{l_{\max}}, \tag{5}$$

(6) shortest height-longest side measurement method

$$q_{Lh} = \frac{2h_{\min}}{\sqrt{3}l_{\max}}, \tag{6}$$

where $\alpha_{\min}$ is the smallest inner angle; $l_{\min}$ and $l_{\max}$ are the length of the shortest and longest edge, respectively; l_1, l_2, and l_3 are the length of the three sides of the triangle; A is the area of the triangular element; r is the inradius of a triangle; R is the circumradius of a triangle; and $h_{\min}$ is the minimum height of the triangle.

Literatures also demonstrate that the formulas above are equivalent [20, 26]; the formulas all tend to zero in the case that the triangles mesh's area tends to zero; metric formula value tends to one in the case that the triangles mesh tends to an equilateral triangle mesh.

3.2. 2D Localization Algorithm Based on Determination of the Geometrical Shape of LU. The unknown node obtains its "distance" to the beacon nodes through various methods such as RSSI, ToA, TDoA, and AoA, relative distance or skip distance, and after it has communicated with more than three surrounding beacon nodes, the unknown node can use trilateration or multilateration to estimate the unknown node. Because the quality of LU has a huge impact on the final estimation result, during the estimation process, the quality of LU should be determined, and the six criterions mentioned in the previous section are approximately equivalent. Therefore, by refereeing to the DC determination criterion, the concept of degree of multicollinearity (DM) is proposed in this paper as the measurement criterion for LU quality and then develops its corresponding novel location algorithm in the two-dimensional space, called two-dimensional location estimation-shape analysis (2D LE-SA). Assume there are n nodes in total in the monitoring area; their actual coordinate is $\{\mathbf{x}_i\}_{i=1}^{n}$, the first m are beacon nodes, and their coordinates are known; after obtaining the distance matrix $\mathbf{D}$ between nodes, see Algorithm 1 for the location estimation method of unknown node.

3.3. Geometrical Analysis of Three-Dimensional LU. For location estimation in the three-dimensional space, Zhou et al. [27, 28] proposed the optimized selection principle of beacon nodes, and by establishing the error area of four beacon nodes, it could improve the localization accuracy and provide better localization service through certain distribution of the four beacon nodes. However, during the solving process, the tangent plane was used to replace the sphere for signal propagation, which caused the idea that the signal could not reach certain part in the built model, and the obtained solution needs further discussion. In addition, there is another three-dimensional localization algorithm based on elevation-type reference nodes [29]. By installing each beacon node is equipped with an omnidirectional antenna that can be raised up and lowered down when needed. Using its movable antenna makes it possible for the beacon nodes to send signal at different heights, and after determining the height of unknown node, the method of projection is used to project the unknown node to the two-dimensional plane and the trilateration method is used to obtain its two-dimensional coordinate. This method uses the lifting equipment to obtain the vertical coordinate of node; after obtaining the projection, the two-dimensional coordinate relation can be skillfully

Input: **D**: distance matrix between nodes; $\{x_1, x_2, \ldots, x_m\}(m \geq 3)$: coordinate of beacon nodes.
Output: $\{\widehat{x}_{m+1}, \widehat{x}_{m+2}, \ldots, \widehat{x}_n\}$: estimated location of the non-beacons.

(1) Divide the beacon nodes collected by the unknown node into a series of LU groups in accordance with their IDs and by obtaining the combinatorial number, and calculate the DM value of each subgroup. Any one of Formulas (1)–(6) can be used to calculate the DM value.

(2) Compare the DM value of each positioning unit with the set DM threshold value, eliminate the subgroups with poor unit quality (low measured value), only keep the subgroups with good quality, and record the DM value of the kept positioning units and corresponding estimated locations obtained by using trilateration or multilateration.
It can be believed that the bigger the DM value is, the better the quality of positioning unit, and it has bigger contribution to the accuracy of final positioning result. Assume there is such a multicollinearity weight after the positioning units with poor quality have been eliminated, and its expression is as the following:

$$W_i = \frac{\mathrm{DM}_i}{\sum_i \mathrm{DM}_i}$$

(3) At last, multiply the obtained weight with the estimated location of corresponding positioning unit, and add the corresponding products to obtain the final estimated location.

Algorithm 1: 2D LE-SA.

obtained, so the algorithm has low complexity, but the nodes have a high deployment cost, and the application scope is small.

In the three-dimensional space, it requires at least four beacon nodes to form the positioning unit; these four nodes form a tetrahedron, and the tetrahedron can be regarded as the expansion of triangle in the three-dimensional space, so they have a certain connection. It is generally believed that tetrahedron mesh's quality criteria include the following: the metric will not change in the case of tetrahedron mesh cells' translation, rotation, reflection, and equal scaling; the metric unit reaches the maximum in the case of a regular tetrahedron and tends to zero in the case that its volume tends to zero. Based on the criteria, researchers have proposed many criteria for measurement of which the most common ones include the minimum solid angle θ, radius ratio ρ, coefficient Q, and coefficient γ. They are, respectively, defined as follows [19, 21, 26]:

(1) the minimum solid angle θ

$$\theta = \min\left(\theta_1, \theta_2, \theta_3, \theta_4\right), \tag{7}$$

where θ_1 is given by $\sin(\theta_1/2) = 12V/(\prod_{2\leq j<j\leq 4}[(l_{1i} + l_{1j})^2 - l_{ij}^2])^{0.5}$. $\theta_2, \theta_3, \theta_4$ can be obtained by rotation of indices;

(2) radius ratio ρ

$$\rho = \frac{3r}{R}, \tag{8}$$

where r and R are the inradius and circumradius of the tetrahedron mesh, respectively;

(3) coefficient Q

$$Q = C_d \frac{V}{\left[\sum_{1\leq i<j\leq 4} l_{ij}\right]^3}, \tag{9}$$

where the coefficient $C_d = 1832.8208$ is applied so that the highest value of Q (for equilateral element) is equal to 1;

(4) coefficient γ

$$\gamma = \frac{72\sqrt{3}V}{\left[\sum_{1\leq i<j\leq 4} l_{ij}^2\right]^{1.5}}. \tag{10}$$

In the above expression, V denotes the volume of tetrahedron mesh with vertexes P_1, P_2, P_3, P_4, l_{ij} representing the length of the edge joining P_i and P_j.

Literatures [30] also demonstrate that the formulas above are equivalent; the formulas all tend to zero in the case that the tetrahedron mesh's volume tends to zero; metric formula value tends to one in the case that the tetrahedrons mesh tends to a regular tetrahedron mesh.

3.4. 3D Localization Algorithm Based on Determination of the Geometrical Shape of LU. Similar to positioning in the two-dimensional environment, in the three-dimensional monitoring area, the unknown node obtains more than four surrounding beacon nodes and its distances to these beacon nodes to conduct localization. Due to the impact of the LU formed by beacon nodes on location estimation, during the localization process, it requires quality determination of these LU. The four criterions mentioned in the above section are approximately equivalent, and we can choose any one out of Formulas (7)–(10) as the criterion to measure the quality of three-dimensional tetrahedron and then develop its corresponding novel location algorithm in the three-dimensional space, called three-dimensional location estimation-shape analysis (3D LE-SA), and see Algorithm 2 for the detailed procedure.

4. Localization Algorithm Based on Multivariate Analysis

4.1. Multicollinearity Problem during the Localization Process. In accordance with the literature, we know that the equation set of the distance between unknown node and beacon node can be transformed into the form of $\mathbf{Ax} = \mathbf{b}$

Input: **D**: distance matrix between nodes; $\{x_1, x_2, \ldots, x_m\}$ $(m \geq 4)$: coordinate of beacon nodes.
Output: $\{\widehat{x}_{m+1}, \widehat{x}_{m+2}, \ldots, \widehat{x}_n\}$: estimated location of the non-beacons.

(1) Divide the beacon nodes collected by the unknown node into a series of LU groups in accordance with their IDs and by obtaining the combinatorial number, and calculate the DM value of each subgroup. Any one of Formulas (7)–(10) can be used to calculate the DM value.

(2) Compare the DM value of each positioning unit with the set DM threshold value, eliminate the subgroups with poor unit quality (low measured value), only keep the subgroups with good quality, and record the DM value of the kept positioning units and corresponding estimated locations obtained by using trilateration or multilateration.
It can be believed that the bigger the DM value is, the better the quality of positioning unit, and it has bigger contribution to the accuracy of final positioning result. Assume there is such a multicollinearity weight after the positioning units with poor quality have been eliminated, and its expression is as the following:

$$W_i = \frac{\mathrm{DM}_i}{\sum_i \mathrm{DM}_i}$$

(3) At last, multiply the obtained weight with the estimated location of corresponding positioning unit, and add the corresponding products to obtain the final estimated location.

Algorithm 2: 3D LE-SA.

[31, 32]. Because the deployment environment has various interference sources, noise within the node, and rounding off caused by quantification of signal, error exists in the distance measurement, and the actual equation set generally exists in the form of $\mathbf{Ax} = \mathbf{b} + \xi$, in which ξ refers to the error. In order to obtain the optimal solution of location estimation, and also considering the convenience of computation, the square of error is generally used as the criterion, and in order to obtain the optimal solution, calculate the partial derivative of loss equation and set it as zero; that is,

$$\frac{\partial \|\xi\|^2}{\partial \mathbf{x}} = -2\mathbf{A}^T\mathbf{b} + 2\mathbf{A}^T\mathbf{Ax} = 0. \tag{11}$$

The formula (11) can be recast as

$$\mathbf{A}^T\mathbf{b} = \mathbf{A}^T\mathbf{Ax}. \tag{12}$$

If the beacon nodes that constitute the LU are not in a straight line, that is, square matrix $\mathbf{A}^T\mathbf{A}$ is reversible, then, for the equation, the common least square method can be used to obtain the estimated coordinate of unknown node: $\widehat{\mathbf{x}} = (\mathbf{A}^T\mathbf{A})^{-1}\mathbf{A}^T\mathbf{b}$. If the beacon nodes that constitute the LU are or are approximately in a straight line, at this moment, there will be multicollinearity phenomenon in the estimation; if forced implementation of least square method continues, it will cause instability to the estimated value, and under severe situation, the multicollinearity might even cause abnormality in the signal of estimated value, which makes the estimated result lose all its meanings. When the LU are completely collinear, matrix $(\mathbf{A}^T\mathbf{A})^{-1}$ does not exist, which makes it impossible to use the least square method to estimate the location of unknown node; when the LU are approximately collinear, $|\mathbf{A}^T\mathbf{A}| \approx 0$, it results in big diagonal element of matrix $(\mathbf{A}^T\mathbf{A})^{-1}$, which increases the variance of the parameter estimated value, and the estimated value becomes invalid.

The concept of multicollinearity in multivariate analysis was firstly proposed by Frisch in 1934 [33], and its initial meaning is that some independent variables in the regression model are linear dependent, and for the location estimation algorithm, it means at least two columns in **A** matrix have liner relation; that is, columns $\mathbf{a}_1, \mathbf{a}_2, \ldots, \mathbf{a}_n$ in matrix **A** have relational expression:

$$k_1\mathbf{a}_1 + k_2\mathbf{a}_2 + \cdots + k_n\mathbf{a}_n = 0, \tag{13}$$

where not all of the constants $k_1, k_2, \ldots, k_n$ are zero. Obviously, the linear relation of columns in matrix **A** has caused the abnormality of matrix $\mathbf{A}^T\mathbf{A}$, which makes the algorithm of location estimation completely invalid. However, in actual application, this kind of situation is rare. Under most circumstances, certain data columns in matrix **A** can be approximately expressed by other data columns, not completely; in other words, columns $\mathbf{a}_1, \mathbf{a}_2, \ldots, \mathbf{a}_n$ in matrix **A** have

$$k_1\mathbf{a}_1 + k_2\mathbf{a}_2 + \cdots + k_n\mathbf{a}_n + \xi = 0, \tag{14}$$

where ξ is a stochastic error. At this moment, it can be called nearly collinearity, and complete collinearity and nearly collinearity together are called multicollinearity. If there is multicollinearity problem, it is not treated and location estimation continues. Although sometimes nearly collinearity can be used to calculate the location of unknown node, it will increase the variance of estimated value; the estimated value is unstable, its confidence interval is increased, and the estimation accuracy is reduced, and under severe situation, it might cause the estimated location and actual location to have a mirror-image relation along the straight line formed by beacon nodes.

4.2. Detection and Remedies for Multicollinearity Problem. During the location estimation process, because the positioning units have a collinear or approximately collinear geometrical relationship, it results in the fact that the columns in matrix **A** constituted by LU also have a collinear or approximately collinear relation. These collinear or nearly collinear relations result in an unstable model during the estimation computation, and under severe circumstance, it

may even affect the accuracy of location estimation. Methods like variance inflation factor (VIF), condition index (CI), and variance proportions (VP) are usually used to diagnose multicollinearity [34–36]. In accordance with the literature [36], if VIF > 10, it is generally believed that the model has a strong multicollinearity relation; if the CI is between 10 and 30, there is weak multicollinearity relation, if it is between 30 and 100, there is medium multicollinearity relation, and if is bigger than 100, there is strong multicollinearity relation; among the big CI, the variable subset consisting of independent variables with a variance proportion bigger than 0.5 is regarded as related variable set.

At present, in theory and practical engineering applications, there are also various methods that can be used to overcome the impact of multicollinearity. Researchers have proposed various detection methods and remedial measures, but different methods have different effects in engineering application. Ridge regression (RR) and principal component regression (PCR) are the most common remedial measures for multicollinearity problem [35, 37, 38] used by researchers. RR was proposed by Ae [38] in 1962, by introducing offset k (also known as "ridge parameter"), and the estimated unbiasedness is sacrificed for significant decrease of variance in the estimated value, in order to realize the final purpose of increasing estimation accuracy and stability. For the estimation model $\mathbf{A}^T\mathbf{A}\mathbf{x} = \mathbf{A}\mathbf{b}$, after introducing the ridge parameter k, a new estimation model $(\mathbf{A}^T\mathbf{A} + k\mathbf{I})\mathbf{x} = \mathbf{A}^T\mathbf{b}$ can be obtained. Due to introduction of the ridge parameter k, the location estimation is no longer unbiased, but the multicollinearity problem is solved, which reduces the variance in the estimated value, and in the meantime, the estimation becomes stable. RR is easy and feasible, and in a certain degree, it overcomes the impact of multicollinearity on the estimated value, so it has been widely applied in the engineering practices. The key of RR is how to choose appropriate ridge parameter k, and ridge parameter k does not have specific meaning, which causes that the selection of k is too subjective. In accordance with Formula (14), we can see that most multicollinearity is caused by noise, while ridge regression reduces variance in the estimated value only by adding k, and the RR method retains all variables, so the ridge regression method does not apply to the scenario with severe noises.

According to statistics and the maximum entropy principle, the information in signal data set generally refers to the variation of data in this set, while the variation can be measured by the total variances; the bigger the variance is, the more information is contained in the data and the smaller variance the noise has, and the signal to noise ratio is actually the variance ratio between signal and noise [39]. Therefore, when choosing the data that can best explain the system, the values with big variances in multiple observations are actually chosen, and this kind of data is called principal components (PCs). Principal component analysis (PCA) [33, 40] is a method which uses a small amount of PCs to disclose the internal structure of multiple variables through recombination of the original data. It is generally believed that the data with a big variance is closely related to the PCs

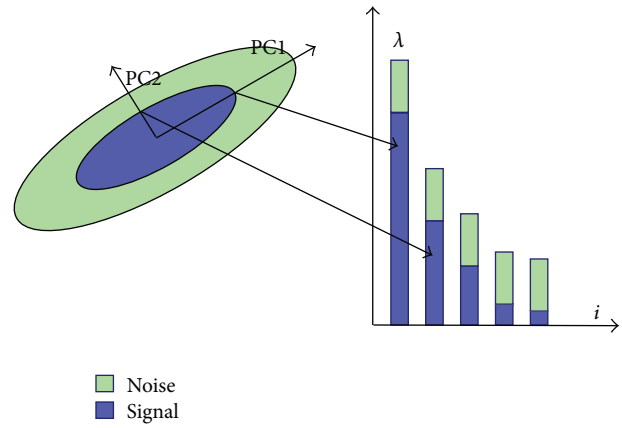

Figure 5: Two views of the "directional" information versus the "unidirectional" noise.

with a big eigenvalue, while other data with a small variance has a strong connection to the PCs with a small eigenvalue. Therefore, different PCs have different effects and impacts on location estimation, and the location accuracy is not in direct proportion to the number of PCs, so it will help increase the stability and accuracy of model by choosing the PCs which can better explain the estimated value to estimate and analyze the data. PCA could transform the original data with a high correlation into mutually independent or irrelevant data, and the data with the biggest signal to noise ratio occurs in the first PCs, and as the eigenvalue becomes smaller, the signal to noise ratio of the data contained in its corresponding eigenvector also becomes smaller. Figure 5 shows the result after such transformation [41].

Through PCA computation of data, only the first several dimensions of PCs are kept, in which not only the scale of original data matrix is compressed, but each obtained new variable which is the linear combination and comprehensive result of the original variables, and it has certain realistic significance. Among the vectors with relatively concentrated noise and small eigenvalue, by eliminating these data with a small signal to noise ratio, the redundancy and noise can be eliminated, and in the meantime, the multicollinearity between variables can also be eliminated. Massy proposed PCR in 1965 [33] based on the idea of PCA, which uses the PCA to retain low-order PCs, ignore high-order PCs, and then run least squares to regression analysis.

4.3. Localization Algorithm Based on Multivariate Analysis. Due to the multicollinearity problem between the coordinate matrices of beacon nodes, it causes matrix $\mathbf{A}^T\mathbf{A}$ irreversible or the fact that $\mathbf{A}^T\mathbf{A}$ cannot used for node estimation. Therefore, we can use the multicollinearity detection method to determine whether the positioning data has multicollinearity phenomenon; then, the PCA method from PCR method can be used to reconstruct matrix detection. The part with eigenvalue of zero, close to zero, or with a very small eigenvalue will be eliminated (only the part with a cumulative variance contribution rate bigger than 90% is kept), and at last, the location is estimated. Because during the computation

Input: **D**: distance matrix between nodes. $\{x_1, x_2, \ldots, x_m\}$ ($m \geq 3$): coordinate of beacon nodes.
Output: $\{\widehat{x}_{m+1}, \widehat{x}_{m+2}, \ldots, \widehat{x}_n\}$: estimated location of the non-beacons.
(1) Conduct standardization treatment to matrix **A**.
(2) To matrix **A** after standardization treatment, use PCA to extract PCs and the score vector. (see Formula (15)).
(3) Use conditional index to determine whether there is multicollinearity problem. If there is, eliminate corresponding PCs with a small characteristic root in accordance with the cumulative variance contribution rate.
(4) Use the left PCs and PCR, and obtain the final location estimation through Formula (18).

Algorithm 3: LE-PCR.

process, the impact of correlation has been considered when choosing data, it has ensured the model's estimability. In the meantime, based on assurance of accuracy, certain data with insignificant impact on the system (noise data) will be abandoned to reduce the model's order and significantly reduce the calculated amount.

This paper uses PCA to conduct feature extraction to matrix **A**, and the obtained first d components form a matrix to replace the original matrix **A** to conduct multivariate analysis. Although part of the data is lost, the accuracy and stability of estimation are increased.

After standardization of matrix **A**, break it down to the sum of d exterior products of vectors; that is,

$$\mathbf{A} = t_1 p_1^T + t_2 p_2^T + \cdots + t_d p_d^T, \tag{15}$$

where t refers to the score vector; p is PCs. Formula (15) can also be expressed as

$$\mathbf{A} = \mathbf{T}\mathbf{P}^T. \tag{16}$$

It is easy to know that, in matrix **T**, each vector has a mutually orthogonal relation with each other; in matrix **P**, each sector is also orthogonal with each other, and each vector length is one. In accordance with above description, it is not difficult to obtain that

$$t_i = \mathbf{A} p_i. \tag{17}$$

Therefore, we can obtain the following conclusion: each score vector is actually the projection of matrix **A** in the direction of its corresponding PCs vector.

In this way, we can obtain the final location estimation as

$$\widehat{\mathbf{x}} = \mathbf{P}\left(\mathbf{T}^T\mathbf{T}\right)^{-1}\mathbf{T}^T\mathbf{b}. \tag{18}$$

The complete steps of PCR-based location estimation (location estimation-PCR, LE-PCR) are described in Algorithm 3.

5. Simulation and Experiments

The wireless sensor network has the characteristic of a big scale. It might require deployment of hundreds or even thousands of nodes in order to verify a localization algorithm, and it is impossible to realize a real network of such a big scale under current experimental conditions. In addition, in order to determine the quality of a localization algorithm, it also requires verifying its adaptability under different scenarios; sometimes it might even require adjusting the parameter of algorithm under the same scenario, and these are difficult to realize under current experimental conditions. Therefore, during research of the localization algorithm for large-scale nodes, the method of software simulation is usually used to evaluate the quality of localization algorithm.

The algorithm referred to in this paper is mainly in accordance with the impact of the relation between beacon nodes on the localization accuracy, and the impact of the distance measurement between nodes on the location estimation accuracy is not a main issue considered in this section. Based on that, this section adopts DV-Hop based on the range-free localization algorithm between beacon nodes as the carrier to verify the concept proposed in this section. In addition, there are many technical standards to measure a localization algorithm, while this paper mainly studies the impact of LU on the positioning performance, so the performance parameter of ALE (average localization error) is used to examine the algorithm performance.

ALE is mainly verified to evaluate localization accuracy, and it is described as follows:

$$\text{ALE} = \frac{\sum_{i=1}^{n}\sqrt{(\widehat{x}_i - x_i)^2 + (\widehat{y}_i - y_i)^2}}{n \times R} \times 100\%. \tag{19}$$

In the formula, $(\widehat{x}_i, \widehat{y}_i)$ represents the estimated coordinate location of the ith node, (x_i, y_i) represents the actual coordinate location of the ith node, (x_i, y_i) represents the number of the unknown nodes, and R represents the communication radius. It can be seen from the above formula that ALE refers to the ratio of the average error of the Euclidean distance from the estimation location of all nodes to the real location in the area to the communication radius. ALE can reflect the stability of the localization algorithm and the positioning accuracy; when the communication radius of the node is given, if the average localization error of the node is smaller, then the positioning accuracy of the algorithm is higher, and vice versa.

First of all, this section briefly introduces the DV-Hop localization algorithm; then, two-dimensional and three-dimensional DV-Hop algorithms are used to verify the algorithms based on geometrical analysis of two-dimensional and three-dimensional LU, respectively; because the localization processes of multivariate analysis in the two-dimensional and three-dimensional spaces are too similar, in the final part of this section, only two-dimensional DV-Hop algorithm is used to verify the idea of PCR algorithm.

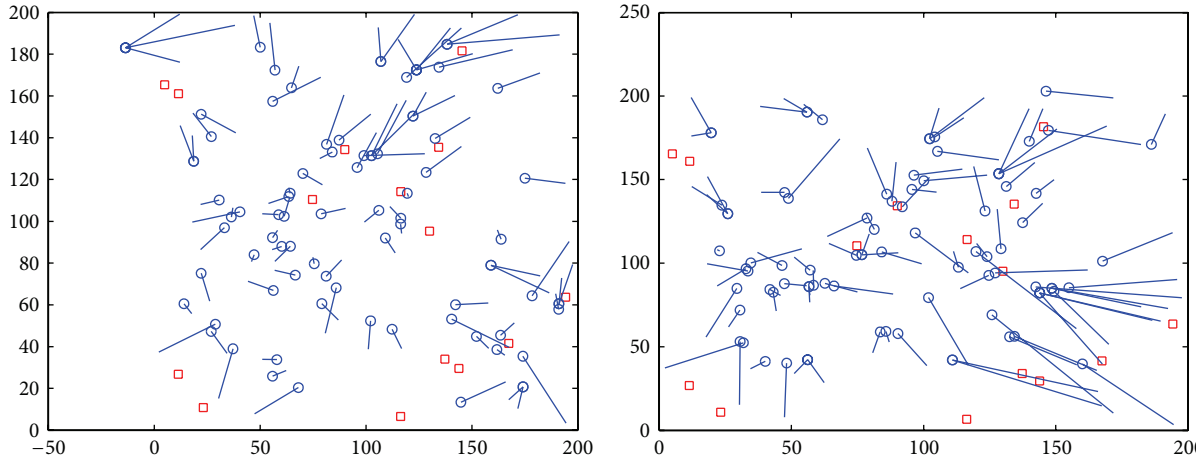

(a) 2D LE-SA (DM = 0.3 beacons = 15)

(b) Ordinary 2D DV-Hop (beacons = 15)

Figure 6: Localization results in 2D environment.

5.1. Introduction of DV-Hop Localization Algorithm. The DV-Hop localization algorithm proposed by Niculescu et al. from Rutgers University [41–43] is one of a series of distributed localization algorithms; it is a localization algorithm not related to the distance, and it smartly uses the distance vector routing and the idea of GPS localization, and this algorithm has great distributivity and expandability. Its localization principle is as follows: firstly, the minimum hop from the unknown node to the beacon node is calculated, then the average distance of each hop is estimated, then the minimum hop is multiplied with the average distance of each hop to obtain the estimated distance between the unknown node and beacon node, and at last trilateration is used to calculate the coordinate of unknown node. DV-Hop method has great distributivity and expandability, and the positioning process consists of the following three steps.

Step 1. The DV-Hop localization algorithm uses the classic distance vector exchange protocol to make all nodes in the deployment area obtain the hop of beacon nodes.

Step 2. The beacon node calculates the average distance of each hop in the network, and after obtaining the locations of other beacon nodes and distance of hop, the beacon node calculates the average distance of each hop in the network, uses it as an adjusted value, and broadcasts it to the network. The average distance of each hop can be expressed by the following formula:

$$\text{HopSize}_i = \frac{\sum_{i \neq j} \sqrt{\left(x_i - x_j\right)^2 + \left(y_i - y_j\right)^2}}{\sum_{i \neq j} h_i}, \tag{20}$$

where (x_i, y_i) and (x_j, y_j) refer to the coordinates of beacon nodes i and j, respectively; h_i refer to the hops of beacon node i and all other beacon nodes. When the unknown node obtains its distance to three or more beacon nodes, it can enter Step 3, that is, calculation of node location.

Step 3. Suppose an unknown node receives the flood messages from three beacons. It uses trilateration or maximum likelihood method to determine its location.

Similar to the common DV-Hop algorithm, the 3D DV-Hop algorithm also consists of three steps.

In accordance with the above description, the DV-Hop is also considered as localization algorithm based on beacon nodes, and its estimation result is related to multicollinearity between nodes in a certain degree. During the solving process, $\mathbf{A}^T\mathbf{A}$ must be reversible; if $|\mathbf{A}^T\mathbf{A}| = 0$ or $|\mathbf{A}^T\mathbf{A}| \approx 0$, the matrix has multicollinearity problem; that is, exact or approximate linear relation occurs in the columns of matrix $\mathbf{A}$, and its existence will cause bad consequence to the final localization accuracy, and when there is complete multicollinearity, the multilateral measurement might even fail. When only incomplete multicollinearity occurs, though the estimated value of location can be obtained, it is unstable. In the meantime, the variance of estimated parameter value will increase, and the increase depends on the severity of multicollinearity.

5.2. 2D LE-SA DV-Hop. In this group of simulation experiments, we suppose 100 nodes were randomly and evenly distributed in a 200 m × 200 m area, and the node communication radius is 50 m. It was assumed the number of beacon nodes increased from 10 to 20. In the meantime, the DM value increased from 0.1 to 0.7, and the step size is 0.1. To reduce the statistical variability, under the same number of beacon nodes and DM value, the reported results here are averaged over 20 repetitions.

Figure 6 shows the location result of 2D LE-SA DV-Hop and ordinary 2D DV-Hop. The squares are beacons and the circles denote the non-beacons. Each line connects a true node location and its estimation. The length of each line denotes the estimation error. We set the number of beacon nodes as 15, DM = 0.3, and plot the location result of each sensor node in Figure 6(a). The ALE is about 29.1%. The final

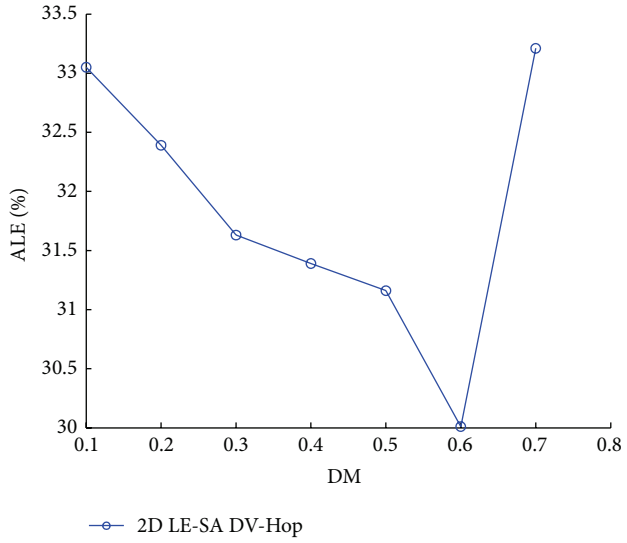

Figure 7: ALE on locations based upon DM in 2D environment.

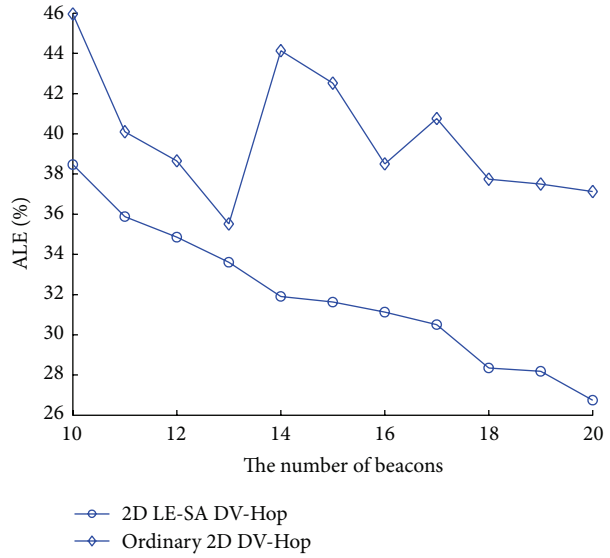

Figure 8: ALE on locations based upon the number of beacons in 2D environment.

estimation of each sensor node of ordinary 2D DV-Hop is shown in Figure 6(b). The ALE is about 40.7%. Obviously, the length of the straight line in Figure 6(a) is shorter than that in Figure 6(b).

We present a quantitative analysis (beacons are fixed 15) of the effect of ALE and DM in Figure 7. We can see that when DM is between 0.1 and 0.6, the ALE value has monotonic decrease; when DM > 0.6, the ALE curve presents a rising trend. The reason is that the DV-Hop algorithm is a localization algorithm based on distance vector routing; it uses the hop distance between nodes to replace the linear distance between nodes, and as the hop distance increases, the error between nodes also increases.

The location estimation method based on shape analysis in this paper actually refers to that during the localization process; only the LU with a high shape quality are chosen during the localization process, and the LU with a poor shape quality are eliminated. When the LU determines that the DM value of multicollinearity is big, the beacon node near the location node (with a small hop) does not satisfy the estimation requirement; it can only choose the beacon nodes far away (with a big hop) as the reference nodes, which causes the idea that the hop distance used in localization is far longer than the actual distance, and the final estimation result will increase instead of decreasing. For this kind of situation, the researchers usually add the threshold value of hops to restrict the hop distance with big hops, but the threshold value of hops will also generate nodes that cannot be estimated in the monitoring area, which further reduces the coverage of monitoring area. Therefore, a compromise should be made to ensure the localization accuracy on the one hand, and the localization coverage on the other hand.

Figure 8 shows the change of ALE curve with the increase of beacon nodes (10–20) in the 2D LE-SA and ordinary 2D DV-Hop when DM = 0.3. In accordance with Figure 8, we can see that because shape analysis is added to the 2D LE-SA algorithm, it has inhibited multicollinearity, and the ALE

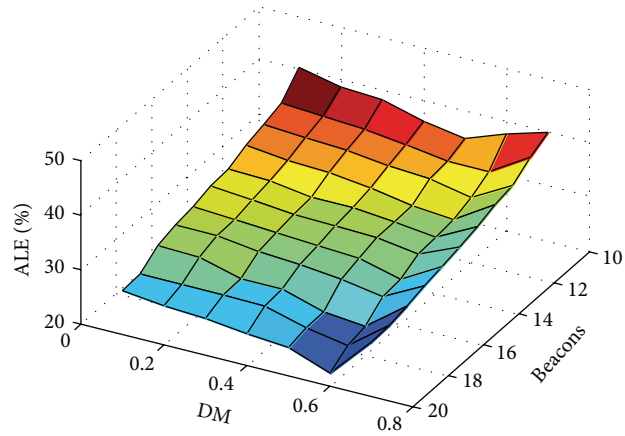

Figure 9: ALE on locations based upon the number of beacons and DM in 2D environment.

curve of 2D LE-SA falls with the increase of beacon nodes; while the ALE curve of ordinary 2D DV-Hop algorithm is not improved with the increase of beacon nodes, it presents up and down motion.

Figure 9 shows the resulting ALE as a function of DM and the number of beacon nodes in the 2D LE-SA. Obviously, after DM > 0.6, the monotonic decrease trend of ALE changes into increase; however, when the DM value is fixed, ALE presents decrease with the increase of beacon nodes. Therefore, it shows that by setting DM threshold value in the localization algorithm, this can help eliminate the impact of multicollinearity and increase the stability of algorithm and accuracy of estimation. However, if the set threshold of DM is too high, it will reduce the reference nodes used for localization, which will further reduce the algorithm performance and coverage. Therefore, pretest should be conducted before setting DM value in a specific area.

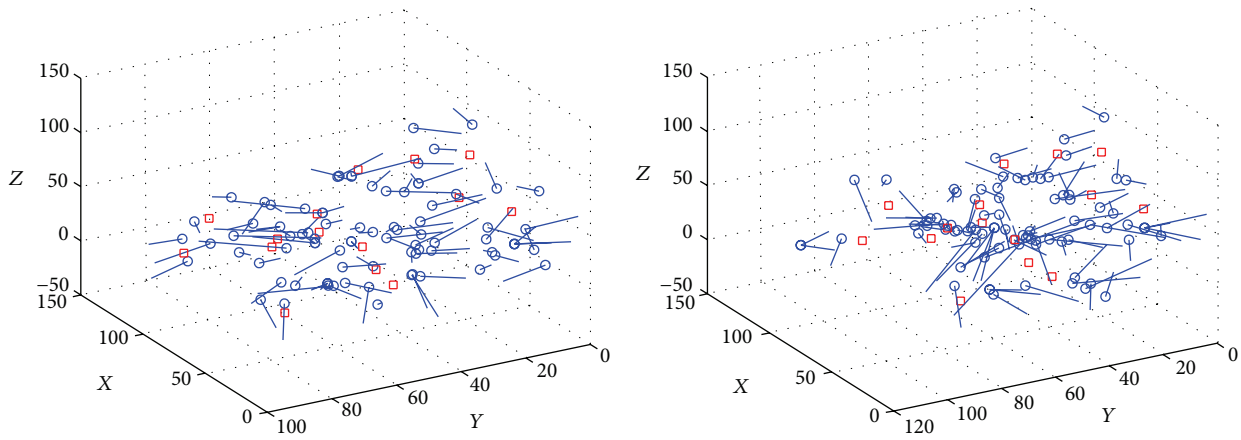

(a) 3D LE-SA (DM = 0.3 beacons = 15)

(b) Ordinary 3D DV-Hop (beacons = 15)

FIGURE 10: Localization results in 3D environment.

5.3. 3D LE-SA DV-Hop. During actual application, it is impossible to place the nodes in a purely two-dimensional plane, and they are generally in a three-dimensional scenario, such as under the water, on the slope, and in a space. Therefore, for the shape analysis and localization method mentioned in this paper, the criterion to determine a three-dimensional shape is different from that to determine a two-dimensional shape, and it needs experiment to verify.

In the simulation experiments, it was assumed that 100 nodes were randomly and evenly distributed in a three-dimensional environment of 100 m × 100 m × 100 m. We set the communication radius of nodes 50 m and the number of beacon nodes increased from 10 to 20; in the meantime, the DM value increased from 0 to 0.6. All of the reported simulation results are the average over 50 trials.

Figure 10 shows the localization result when the number of beacon nodes is 15, where the DM value of 3D LE-SA DV-Hop is 0.3. Figure 10(a) shows the location results of 3D LE-SA DV-Hop where ALE is 31.9% while the ALE of ordinary 3D DV-Hop ALE is 42.6% in Figure 10(b).

We also present a quantitative analysis of the effects of DM in the 3D LE-SA DV-Hop algorithm when there are 15 beacon nodes in Figure 11. We can see that when DM ≤ 0.3, the ALE value has monotonic decrease; when DM > 0.3, the ALE curve presents a rising trend. The reason is that similar to the two-dimensional scenario, a big DM value has restricted selection of surrounding reference beacon nodes, and due to a big error between the beacon nodes far away and the unknown node, it increases the error of the final estimation result instead of reducing it. The difference is that the three-dimensional space causes the nodes to become more "sparse"; when DM is bigger than 0.3, it will cause change to ALE, and the change is more significant; when DM = 0.5, ALE is close to 90%; when DM = 0.6, ALE is even bigger than 120%. The threshold value of hops is added in order to maintain the localization accuracy, and after the beacon nodes with big hops have been limited, it will also cause the decrease of coverage.

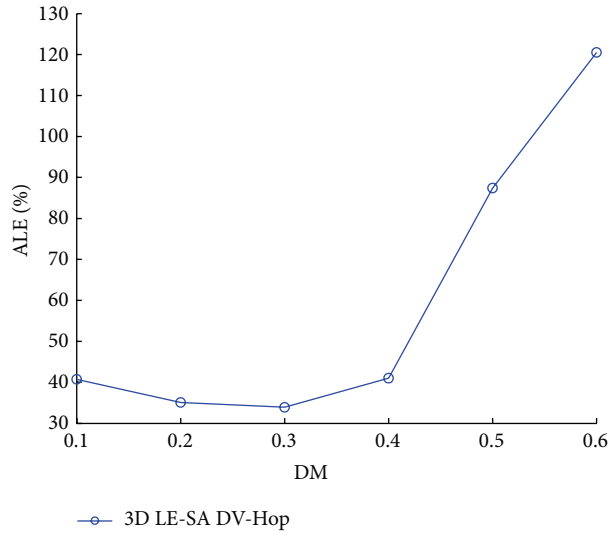

FIGURE 11: ALE on locations based upon DM in 3D environment.

Figure 12 shows the change of ALE curve with the number of beacon nodes varying from 10 to 20. Similarly, the common ordinary 3D DV-Hop algorithm also fails to address the impact of multicollinearity, which makes the ALE curve present up and down motion. Through the 3D LE-SADV-Hop with DM, the impact of multicollinearity problem is avoided, its ALE curve falls with increase of beacon nodes, and its accuracy is better than the ordinary algorithm.

5.4. LE-PCR DV-Hop. Because the localization method based on multivariate analysis only conducts computation processing to the coordinate matrix of beacon nodes, the two-dimensional and three-dimensional methods are very similar; therefore, the third group of experiments in this section only compares the situations in the two-dimensional environment. In this set of experiments, 100 sensors are randomly placed in a 200 m by 200 m square region, and the communication radius is 50 m. Due to the fact that the

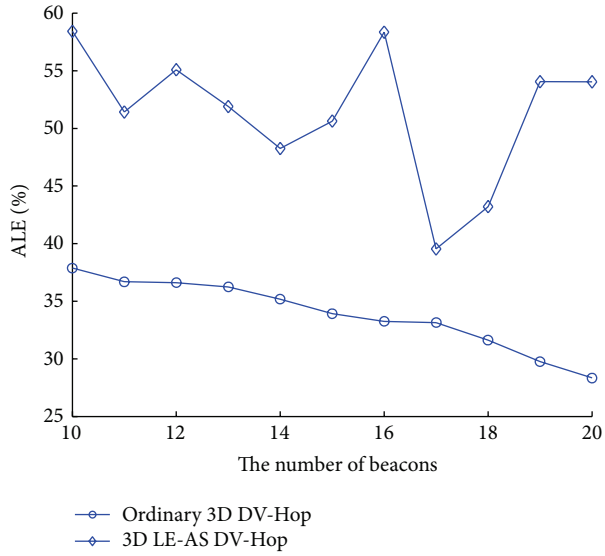

Figure 12: ALE on locations based upon the number of beacons in 3D environment.

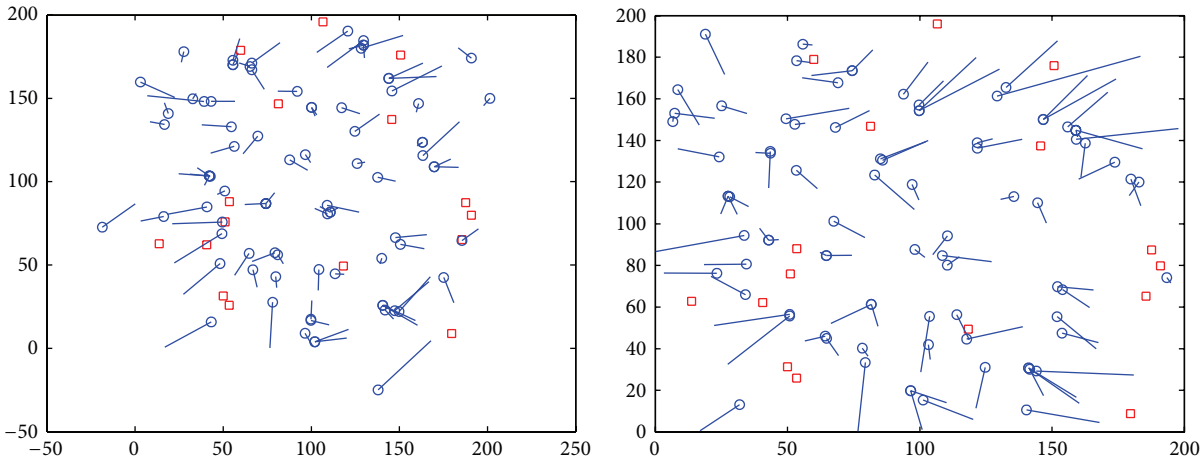

(a) LE-PCR DV-Hop (b) Ordinary DV-Hop

Figure 13: Localization results in 2D environment.

beacon nodes are collinear or approximately collinear, this causes the idea that matrix $\mathbf{A}^T\mathbf{A}$ is irreversible or that matrix $\mathbf{A}^T\mathbf{A}$ cannot be used in node estimation. We can use the PCA method to reconstruct matrix $\mathbf{A}$ and use CI to determine whether there is multicollinearity problem; the part with an eigenvalue of zero, close to zero, or with a very small eigenvalue will be eliminated (only the part with a cumulative variance contribution rate bigger than 90% is kept), and in this way, in the reobtained data, there is no collinear part, and some of noise is eliminated as well.

Similar to the first group of experiments, we show location results of each sensor node in Figure 13. We set 16 beacon nodes were randomly distributed in a monitoring area, cumulative variance contribution rate bigger than 90%, and the final solution of LE-PCR DV-Hop in Figure 13(a). The ALE is about 27.5%. The squares are the beacons, and the circles denote the non-beacons. Each line connects a true sensor location and its estimation. The final estimated location of ordinary DV-Hop is shown in Figure 13(b). The ALE is about 35.8%.

Because the PCR-based method conducts recombination and screening to the coordinate information of beacon nodes, in other words, during the location estimation process, as much coordinate information of beacon nodes as possible will be maintained, and the information not important to location estimation will be eliminated. In addition, the impact of correlation has been considered when choosing data, so it has ensured the estimability of location estimation process. In the meantime, based on assurance of estimation accuracy, it can reduce the estimation model's order and significantly reduce the computational complexity.

Figure 14 shows the change of ALE curve as the number of beacon nodes is gradually increased from 10 to 20 under multiple deployments of the algorithm under the same

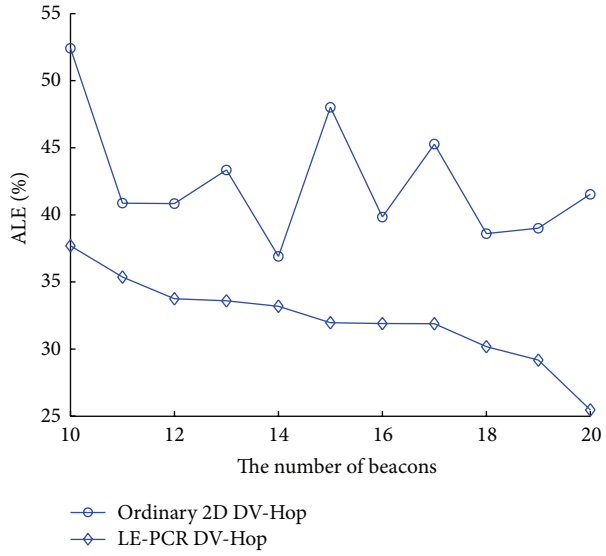

Figure 14: ALE on locations based upon the number of beacons in 2D environment.

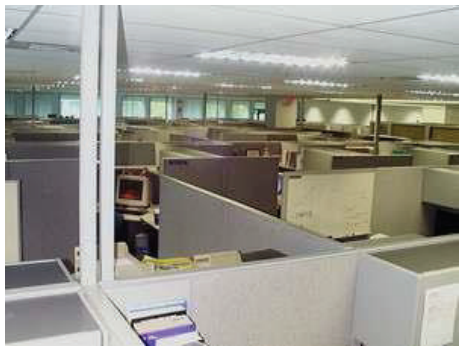

Figure 15: Actual collection area.

scenario (50 times, use average value of ALE). In the actual environment, because the impact of multicollinearity and noise is inevitable, in accordance with Figure 14, we can see that, for the ordinary DV-Hop algorithm (due to the fact that the nodes are randomly redeployed in each experiment, the ALE in Figures 8 and 14 are not the same), ALE does not decrease with the increase of beacon nodes, and the ALE curve presents up and down motion; while in the PCR-based localization algorithm, through reconstruction of the beacon location data, the useful information, the multicollinearity problem, and noise are rearranged, and by setting a certain threshold value (cumulative variance contribution rate), part of the multicollinearity data and noise can be eliminated so that the ALE curve will fall with the increase of beacon nodes. In addition, the ALE of improved method, which is all lower than 40%, is significantly lower than that of common algorithm.

5.5. Performance Evaluation Based on Actually Measured Data. In this group of experiments, we use actually measured data set provided by the SPAN lab. As shown in Figure 15, the network consists of 44 sensor nodes that are deployed in a rectangular office area of $12 \times 14\,m^2$. We randomly choose 4 to 13 nodes as the beacon nodes and make the node communication radius 5 m. In the experiment, the DM value is set to 0.3, and cumulative variance contribution rate is 90%.

Figure 16 shows the localization results of three algorithms under the circumstance that the number of beacons is 9, in which Figure 16(a) shows nodes deployment; Figure 16(b) is localization result of ordinary DV-Hop method, ALE = 36.32%; Figure 16(c) is localization result of 2D LE-SA method, ALE = 31.1%; Figure 16(d) shows localization result of 2D LE-PCR method, ALE = 30.6%. From Figure 9, it can be seen that localization results of 2D LE-SA and 2D LE-PCR method are close, and their localization performance is better than ordinary DV-Hop method.

Figure 17 plots curves of ALE of repeated experiments by three localization algorithms varying with the quantity of beacon nodes in SPAN lab. It is easy to find ALE of ordinary DV-Hop fluctuating as the strongest, and accuracy is the lowest; however, SA-based and PCR-based methods can obtain more stable and higher precision results. Comparing with the ordinary DV-hop algorithm, SA-based and PCR-based algorithms considered the multicollinearity factor of beacons, which makes them obtain better accurate localization results.

6. Conclusion

In this paper, we analyze the problem caused by multicollinearity during the localization computation process. Firstly, we give two kinds of poor-quality of 2-dimensional LU and nine kinds of poor-quality of 3-dimensional LU, respectively. Secondly, we give the corresponding six triangle and four tetrahedron judgment formula. Finally, we employ PCR algorithm, which is dimensionality reduction method, to conduct recombination and extraction to the coordinate matrix of beacon nodes and make use of beacons data to estimate the location of unknown node.

The method based on geometrical analysis of LU is direct. By setting the threshold value, the LU smaller than this threshold value will be excluded. Because the location estimation process only uses the LU with high quality, so it can promote localization accuracy, and the algorithm is stable. However, because some of the LU are excluded from the location estimation process, the number of nonestimated nodes is increased in certain area. In addition, the biggest threshold value of DM should be selected in accordance with the distribution area. The PCR-based localization method extracts PCs in the coordinate matrix, and because there is no correlation between PCs, the impact of multicollinearity problem is avoided. In addition, after abandoning certain PCs that contain noise, the overall localization accuracy is increased, the calculated amount is reduced, it does not need to select threshold value such as DM, and it only requires setting the cumulative variance contribution rate. However, the PCR-based method is a biased estimation method, and certain estimation accuracy will inevitably be lost.

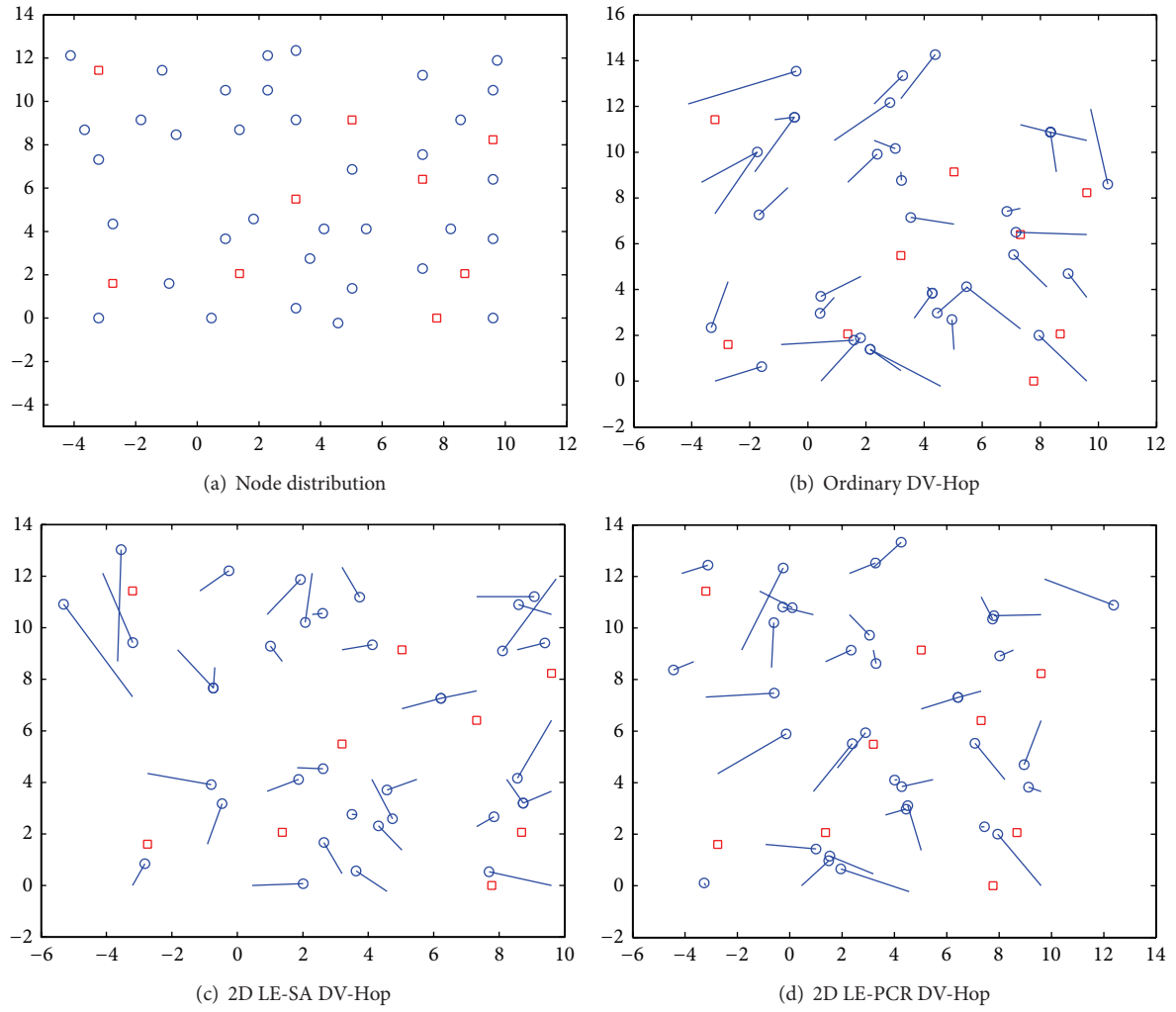

Figure 16: Location estimates with actual measured data.

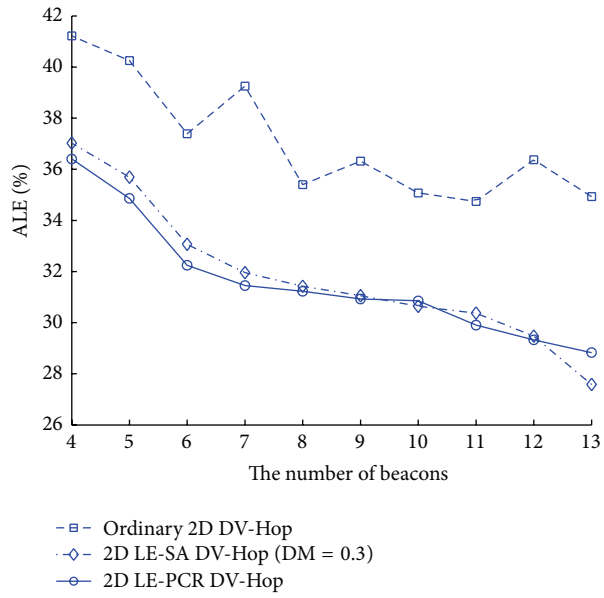

Figure 17: ALE on locations based upon the number of beacons in office area.

Our method can be used for range-free localization, and it can also be used for range localization; furthermore, it can be used for tracking and locating moving targets.

Conflict of Interests

The authors declare that there is no conflict of interests regarding the publication of this paper.

Acknowledgments

The paper is sponsored by the Natural Science Foundation of China (61272379), Prospective and Innovative Project of Jiangsu Province (BY2012201); Provincial University Natural Science Research Foundation of Jiangsu Education Department (12KJD510006, 13KJD520004); the Jiangsu Planned Projects for Postdoctoral Research Funds (1401016B); Doctoral Scientific Research Startup Foundation of Jinling Institute of Technology (JIT-B-201411).

References

[1] S. Khan, A.-S. K. Pathan, and N. A. Alrajeh, *Wireless Sensor Networks Current Status and Future Trends*, CRC Press, London, UK, 2013.

[2] I. M. M. E. Emary and S. Ramakrishnan, *Wireless Sensor Networks: From Theory to Applications*, CRC Press, London, UK, 2013.

[3] I. F. Akyildiz and M. C. Vuran, *Wireless Sensor Networks*, John Wiley & Sons, 2010.

[4] A. A. Hady, S. M. Abd El-Kader, and H. S. Eissa, "Intelligent sleeping mechanism for wireless sensor networks," *Egyptian Informatics Journal*, vol. 14, no. 2, pp. 109–115, 2013.

[5] Y. Zhang, W. Yang, D. Han et al., "An integrated environment monitoring system for underground coal mines—wireless Sensor Network subsystem with multi-parameter monitoring," *Sensors*, vol. 14, no. 2, pp. 13149–13170, 2014.

[6] A. Pascale, M. Nicoli, F. Deflorio, B. Dalla Chiara, and U. Spagnolini, "Wireless sensor networks for traffic management and road safety," *IET Intelligent Transport Systems*, vol. 6, no. 1, pp. 67–77, 2012.

[7] J. Heidemann, M. Stojanovic, and M. Zorzi, "Underwater sensor networks: applications, advances and challenges," *Philosophical Transactions of the Royal Society A: Mathematical, Physical and Engineering Sciences*, vol. 370, no. 1958, pp. 158–175, 2012.

[8] G. Cabri, L. Leonardi, M. Mamei, and F. Zambonelli, "Location dependent services for mobile users," *IEEE Transactions on Systems, Man, and Cybernetics, Part A: Systems and Humans*, vol. 33, no. 6, pp. 667–681, 2003.

[9] Y. Liu and Z. Yang, *Localization, and Localizability Location-Awareness Technology for Wireless Networks*, Springer, 2011.

[10] C. Wu, Z. Yang, Y. Liu, and W. Xi, "WILL: wireless indoor localization without site survey," *IEEE Transactions on Parallel and Distributed Systems*, vol. 24, no. 4, pp. 839–848, 2013.

[11] G. Blumrosen, B. Hod, T. Anker, D. Dolev, and B. Rubinsky, "Enhancing RSSI-based tracking accuracy in wireless sensor networks," *ACM Transactions on Sensor Networks*, vol. 9, no. 3, article 29, 2013.

[12] J. Zhao, W. Xi, Y. He et al., "Localization of wireless sensor networks in the wild: pursuit of ranging quality," *IEEE/ACM Transactions on Networking*, vol. 21, no. 1, pp. 311–323, 2013.

[13] J. Gribben and A. Boukerche, "Location error estimation in wireless ad hoc networks," *Ad Hoc Networks*, vol. 13, pp. 504–515, 2014.

[14] K. Bu, Q. Xiao, Z. Sun, and B. Xiao, "Toward collinearity-aware and conflict-friendly localization for wireless sensor networks," *Computer Communications*, vol. 35, no. 13, pp. 1549–1560, 2012.

[15] D. Kotzor and W. Utschick, "Kernel methods for ill-posed range-based localization problems," *IEEE Transactions on Signal Processing*, vol. 60, no. 8, pp. 4151–4162, 2012.

[16] G. Han, H. Xu, T. Q. Duong, J. Jiang, and T. Hara, "Localization algorithms of Wireless Sensor Networks: a survey," *Telecommunication Systems*, vol. 52, no. 4, pp. 2419–2436, 2013.

[17] H. A. de Oliveira, A. Boukerche, E. F. Nakamura, and A. A. F. Loureiro, "An efficient directed localization recursion protocol for wireless sensor networks," *IEEE Transactions on Computers*, vol. 58, no. 5, pp. 677–691, 2009.

[18] S. Tian, X. Zhang, X. Wang, P. Sun, and H. Zhang, "A selective anchor node localization algorithm for wireless sensor networks," in *Proceedings of the 2nd International Conference on Convergent Information Technology (ICCIT '07)*, pp. 358–362, Gyeongju-si, Republic of Korea, November 2007.

[19] S.-W. Cheng, T. K. Dey, H. Edelsbrunner, M. A. Facello, and S.-H. Teng, "Sliver exudation," *Journal of the ACM*, vol. 47, no. 5, pp. 883–904, 2000.

[20] J. Sarrate, J. Palau, and A. Huerta, "Numerical representation of the quality measures of triangles and triangular meshes," *Communications in Numerical Methods in Engineering with Biomedical Applications*, vol. 19, no. 7, pp. 551–561, 2003.

[21] N. Chunge, L. Jianfei, and S. Shuli, "Study on quality measures for tetrahedral mesh," *Chinese Journal of Computational Mechanics*, vol. 20, no. 5, pp. 579–582, 2003.

[22] J. R. Shewchuk, *Lecture Notes on Delaunay Mesh Generation*, University of California, Berkeley, Calif, USA, 2012.

[23] C. Poggi and G. Mazzini, "Collinearity for sensor network localization," in *Proceedings of the 58th IEEE Vehicular Technology Conference (VTC '03)*, pp. 3040–3044, 2003.

[24] L. F. Wu, M. Q. H. Meng, and H. W. Liang, "A Collinearity-Based Localization Algorithm for wireless sensor networks," *Chinese Journal of Sensors and Actuators*, vol. 22, no. 5, pp. 723–727, 2009.

[25] L. Ke-Zhong, W. Shu, H. Fu-Ping, and X. Chang-Chun, "An Improved DV-hop localization algorithm for wireless sensor networks," *Information and Control*, vol. 35, no. 6, pp. 787–792, 2006.

[26] S.-W. Cheng, T. K. Dey, and J. Shewchuk, *Delaunay Mesh Generation*, Chapman & Hall, CRC, 2012.

[27] Zhouyan, *The Optimizing Selection and Error Analysis of Position Reference Nodes in Smart Space*, Northeastern University, Shenyang, China, 2008.

[28] Y. Zhou, H. Zhao, J. Zhang, and H.-C. Li, "Location error analysis of pervasive computing," *Acta Electronica Sinica*, vol. 37, no. 2, pp. 382–386, 2009.

[29] H. S. AbdelSalam and S. Olariu, "A 3d-localization and terrain modeling technique for wireless sensor networks," in *Proceedings of the 2nd ACM International Workshop on Foundations of Wireless Ad Hoc and Sensor Networking and Computing (FOWANC '09)*, pp. 37–45, May 2009.

[30] S. Sun and J. Liu, "An efficient optimization procedure for tetrahedral meshes by chaos search algorithm," *Journal of Computer Science and Technology*, vol. 18, no. 6, pp. 796–803, 2003.

[31] J. Zheng, Y. E. Sun, Y. Huang, Y. Wang, and Y. Xiao, "Error analysis of range-based localisation algorithms in wireless sensor networks," *International Journal of Sensor Networks*, vol. 12, no. 2, pp. 78–88, 2012.

[32] Q. Qingji, S. Xuanjing, and C. Haipeng, "An improved node localization algorithm based on DV-Hop for wireless sensor networks," *Computer Science and Information Systems*, vol. 8, no. 4, pp. 953–972, 2011.

[33] K. Månsson, G. Shukur, and P. Sjölander, "A new ridge regression causality test in the presence of multicollinearity," *Communications in Statistics: Theory and Methods*, vol. 43, no. 2, pp. 235–248, 2014.

[34] C. F. Dormann, J. Elith, S. Bacher et al., "Collinearity: a review of methods to deal with it and a simulation study evaluating their performance," *Ecography*, vol. 36, no. 1, pp. 27–46, 2013.

[35] A. Wibowo and M. I. Desa, "Kernel based regression and genetic algorithms for estimating cutting conditions of surface roughness in end milling machining process," *Expert Systems with Applications*, vol. 39, no. 14, pp. 11634–11641, 2012.

[36] R. A. P. Dias, J. Petrini, J. B. S. Ferraz et al., "Multicollinearity in genetic effects for weaning weight in a beef cattle composite population," *Livestock Science*, vol. 142, no. 1–3, pp. 188–194, 2011.

[37] S.-M. Huang and J.-F. Yang, "Improved principal component regression for face recognition under illumination variations," *IEEE Signal Processing Letters*, vol. 19, no. 4, pp. 179–182, 2012.

[38] H. Ae, "Application of ridge analysis to regression problems," *Chemical Engineering Progress*, vol. 58, pp. 54–59, 1962.

[39] I. K. Fodor, *A Survey of Dimension Reduction Techniques*, 2002.

[40] S.-H. Fang and T.-N. Lin, "Principal component localization in indoor WLAN environments," *IEEE Transactions on Mobile Computing*, vol. 11, no. 1, pp. 100–110, 2012.

[41] H. Hyötyniemi, *Multivariate Regression—Techniques and Tools*, Helsinki University of Technology, Control Engineering Laboratory, Helsinki, Finland, 2001.

[42] D. Niculescu and B. Nath, "DV based positioning in Ad Hoc networks," *Telecommunication Systems*, vol. 22, no. 1–4, pp. 267–280, 2003.

[43] D. Ma, M. J. Er, B. Wang, and H. B. Lim, "Range-free wireless sensor networks localization based on hop-count quantization," *Telecommunication Systems*, vol. 50, no. 3, pp. 199–213, 2012.

Hindawi Publishing Corporation
Journal of Sensors
Volume 2015, Article ID 964730, 11 pages
http://dx.doi.org/10.1155/2015/964730

Research Article

Failure Mechanism of Rock Bridge Based on Acoustic Emission Technique

Guoqing Chen, Yan Zhang, Runqiu Huang, Fan Guo, and Guofeng Zhang

State Key Laboratory of Geohazard Prevention and Geoenvironment Protection, Chengdu University of Technology, Chengdu, Sichuan 610059, China

Correspondence should be addressed to Guoqing Chen; chgq1982@126.com

Received 17 October 2014; Revised 23 December 2014; Accepted 7 January 2015

Academic Editor: Fei Dai

Acoustic emission (AE) technique is widely used in various fields as a reliable nondestructive examination technology. Two experimental tests were carried out in a rock mechanics laboratory, which include (1) small scale direct shear tests of rock bridge with different lengths and (2) large scale landslide model with locked section. The relationship of AE event count and record time was analyzed during the tests. The AE source location technology and comparative analysis with its actual failure model were done. It can be found that whether it is small scale test or large scale landslide model test, AE technique accurately located the AE source point, which reflected the failure generation and expansion of internal cracks in rock samples. Large scale landslide model with locked section test showed that rock bridge in rocky slope has typical brittle failure behavior. The two tests based on AE technique well revealed the rock failure mechanism in rocky slope and clarified the cause of high speed and long distance sliding of rocky slope.

1. Introduction

Acoustic emission (AE) is a phenomenon about the development of transient elastic waves caused by rapid energy release due to crack growth [1]. Early AE technique has been applied in security problems of metal mines, coal mines, and tunnel engineering. With advanced computerized technique, small sized digital AE analysis equipment can be used to detect the defects and its location and failure propagation. Compared with microseism [2] and other in situ detection methods [3, 4], AE technique can forecast brittle failure before the structural failure.

Rocky landslides contain a lot of rock bridges, and researches on rock bridge were carried out by experimental methods and simulated by analytical and numerical simulation techniques. The laboratory study of AE characteristics during rock stress-strain process was reviewed [5]; real-time failure process [6, 7] and stability evaluation and harm degree of landslides [8] were marked out. Behavior of rock bridge was observed firstly by shear test in 1990 [9]; then cyclic loading test of rock bridge and mechanical behavior was carried out [10]. The failure mechanisms and pattern of coalescence of rock bridges were investigated [11]. Strength, deformability, failure behavior, and AE locations of red sandstone were tested by using triaxial compression [12]. The abovementioned tests showed the basic mechanical behavior, but the brittle failure of rock bridge was rarely tested. Analytical methods such as neural network [13], slice element method [14], and time-dependent degradation failure [15, 16] are used to study the progressive failure of rock bridge. Rock fragmentation processes subjected to static and dynamic loading were examined by the numerical code RFPA [17]. The progressive rock fracture mechanism of cracked chevron notched Brazilian disc rock specimens was numerically simulated [18]. Surface crack initiation and propagation were numerically investigated via parallel finite element analysis [19]. These numerical studies really revealed the progressive failure of rock bridge.

However, the brittle failure of the rock bridge, especially in the rocky slope, is rarely studied. Small scale rock bridge direct shear test and large scale landslide model test with locked section were designed in this paper. The relation curve of AE event count with time and AE source location are obtained through the AE source location technology. The

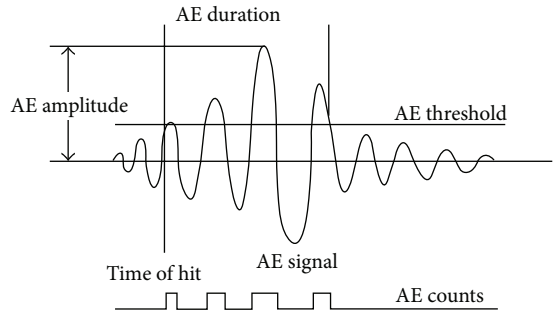

Figure 1: Wave hit feature of AE.

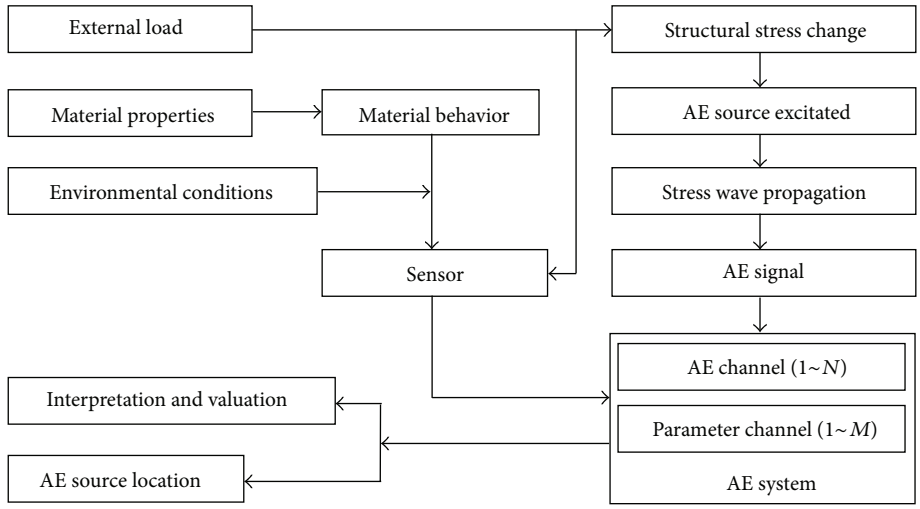

Figure 2: Flow chart of AE source location.

mechanical characteristics and failure mechanism of rock mass with rock bridge and the space evolution process of cracks are discussed.

2. AE Technique

2.1. AE Instrument and Its Principle. AE instrument is Micro-II Digital AE System, which is equipped with the third generation of digital system developed by USA Physical Acoustics Company. Its core is an AE function card with 8 channels on a plate. Compared to other AE devices, Micro-II Digital AE System is one of the latest and highest integration AE systems currently which has the advantages of small volume, convenient carrying, high precision, high speed of data transmission, strong processing ability, and so on. The data obtained from Micro-II Digital AE System is more reliable and AE source location is more precise than other AE devices. Its maximum signal amplitude reached 100 dB and its bandwidth is 1~400 kHz.

Peripheral equipment mainly includes 2/4/6 type preamplifier with its signal gain ranging from 20 dB, 40 dB, or 60 dB (adjustable), which has a high pass filtering function of 20 Hz. Nano-30 type sensors, whose frequency response range is 100~400 kHz and test set monitoring threshold value is 40 dB, use six sensors array data acquisition to ensure the location precision.

AE principle is that elastic wave from AE source which finally transmits to the material surface causing surface displacement, which can be detected by AE sensors. These sensors convert mechanical vibration into electrical signals. Finally, according to the analysis of the obtained data, the following goals can be achieved: (1) determining the AE source location; (2) determining time or load of the AE occurrence; and (3) assessing the degrees of damage to the AE source.

Figure 1 shows AE signal waveform and partial of AE parameters, including AE count, AE amplitude, rise time, AE duration, and AE threshold. In addition, the commonly used AE characterization parameters also include energy, impact, events, energy, time difference, and frequency [20].

2.2. AE Location Technology. AE source location process is shown in Figure 2; different methods of AE source location are adapted for burst and continuous AE signals [21]. Source location of burst AE signal includes time of arrive (TOA) location and region location. Continuous AE signal location includes amplitude measurement type regional location, attenuation measurement type location, cross correlation TOA location, and interference TOA location.

TOA location is widely used for detecting the samples and components, but it would easily lose a large number of low amplitude signals and its location accuracy may be affected by wave speed, attenuation, wave shape, and the shape of component. When the ratio of the length to the radius of the tested object becomes very large, it is appropriate by using linear location for AE detection, such as pipes, bars, and steel beam. Linear location requires at least two AE sensors. Plane location of plate structure needs at least three sensors. Three-dimensional location requires at least four sensors.

The position of sound source can be calculated by the above equation. The basic principle of plane location and three-dimensional location is similar to the linear location, which are all positioned by the velocity and time difference. In this paper, the main AE source location is Geiger method [22] which uses the difference arrive time of P wave [23].

The Geiger method is an application of the Gauss-Newton minimum fitting function; the principle is using iteration method to get the final result from a given initial point (test point). A correction vector $\Delta\theta(\Delta x, \Delta y, \Delta z, \Delta t)$ is calculated through every iteration based on the least square method; the vector $\Delta\theta$ is added to the previous iteration results (test point) to get a new test point. Then it is determined whether the new test point meets the requirements. If it does, the point is the sought source point, if not, the iteration continues until the requirement is met. The result of each iteration is produced by the following time distance equation:

$$\left[(x_i - x)^2 + (y_i - y)^2 + (z_i - z)^2\right]^{1/2} = v_p\,(t_i - t)\,, \quad (1)$$

where x, y, z is the test point coordinate (initial value is artificially settled), t is the time of occurrence of events (initial value is artificially settled), x_i, y_i, z_i is the sensor i location, t_i is the arrival time of P wave which is detected by the sensor i, and v_p is the P wave velocity.

t_{oi} is the time of P wave arrival of each sensor, which can be calculated by the First Order Taylor Series Expansion of arrival time through the test point coordinate:

$$t_{oi} = t_{ci} + \frac{\partial t_i}{\partial x}\Delta x + \frac{\partial t_i}{\partial y}\Delta y + \frac{\partial t_i}{\partial z}\Delta z + \frac{\partial t_i}{\partial t}\Delta t, \quad (2)$$

where t_{oi} is the arrival time of P wave detected by the sensor i and t_{ci} is the arrival time of sensor i of P wave calculated by test point coordinates.

In (2),

$$\frac{\partial t_i}{\partial x} = \frac{(x_i - x)}{vR}, \quad \frac{\partial t_i}{\partial y} = \frac{(y_i - y)}{vR}, \quad \frac{\partial t_i}{\partial z} = \frac{(z_i - z)}{vR},$$
$$\frac{\partial t_i}{\partial t} = 1, \quad R = \left[(x_i - x)^2 + (y_i - y)^2 + (z_i - z)^2\right]^{1/2}. \quad (3)$$

For N positive sensors, you can get N equations written in matrix form:

$$A\Delta\theta = B, \quad (4)$$

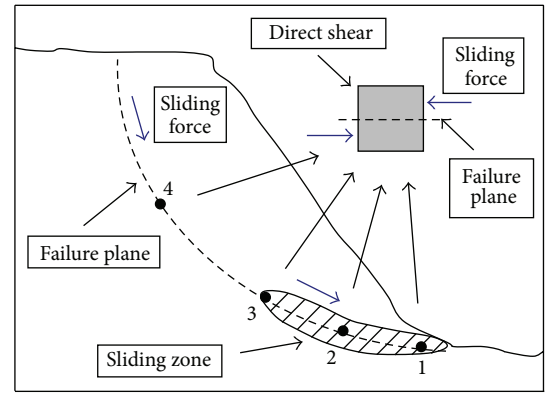

Figure 3: Sketch map of rock slope failure.

where

$$A = \begin{bmatrix} \frac{\partial t_1}{\partial x} & \frac{\partial t_1}{\partial y} & \frac{\partial t_1}{\partial z} & 1 \\ \frac{\partial t_2}{\partial x} & \frac{\partial t_2}{\partial y} & \frac{\partial t_2}{\partial z} & 1 \\ \vdots & \vdots & \vdots & \vdots \\ \frac{\partial t_n}{\partial x} & \frac{\partial t_n}{\partial y} & \frac{\partial t_n}{\partial y} & 1 \end{bmatrix}, \quad B = \begin{bmatrix} t_{o1} - t_{c1} \\ t_{o2} - t_{c2} \\ \vdots \\ t_{on} - t_{cn} \end{bmatrix}. \quad (5)$$

Modification vector is got by Gaussian Elimination (4):

$$A^T A\Delta\theta = A^T B, \quad (6)$$

$$\Delta\theta = \left(A^T A\right)^{-1} A^T B. \quad (7)$$

After correction vector is obtained by (7), use $(\theta + \Delta\theta)$ as the new test point to keep iteration continuous until the error satisfies the requirements.

3. Small Scale Direct Shear Tests with Different Rock Bridge Length

Many scholars have studied macrofailure and micropropagation of cracks evolution under shear loading, such as simulating microdevelopment of crack using cellular automata [24, 25], time distribution features of rock crack [26], brittle failure mechanism of rock [27], the influence of size effect on rock failure [28], and differential resistance sensing technology [29]. But small scale direct shear tests of different rock bridge length using AE are few.

As shown in Figure 3, the points on the failure plane are directly sheared to failure in sliding process. From a microscopic view point, the failure process of rock bridge of landslide is the direct shear failure. So rock bridge direct shear tests are carried out in order to study the failure mechanism with different rock bridge length in this paper.

3.1. Sample Preparation and Test Instrument. The mass ratio of test sample is 1 : 3 : 1 : 1 (cement : sand : water : gypsum).

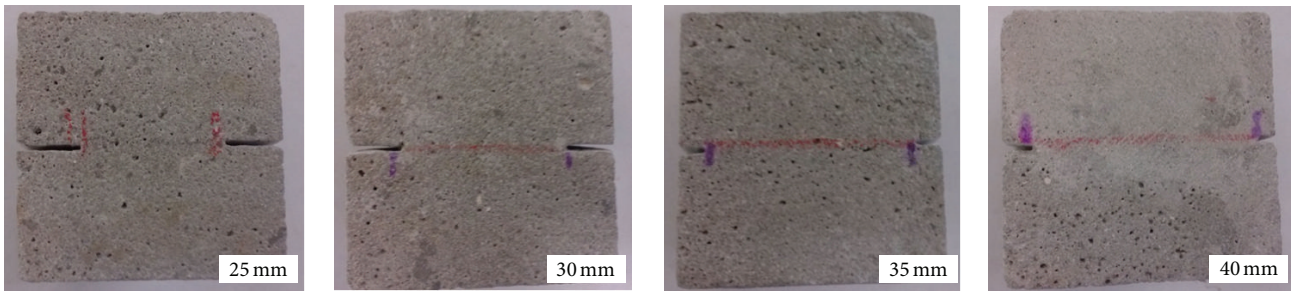

Figure 4: Different reserved rock bridge length.

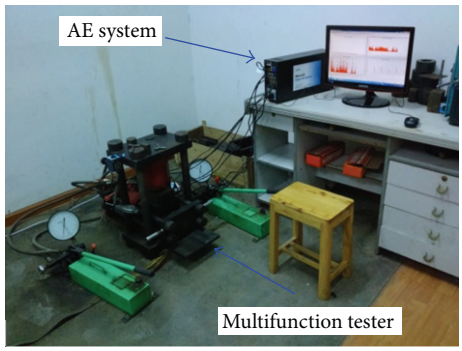

Figure 5: Direct shear test system associate with AE system.

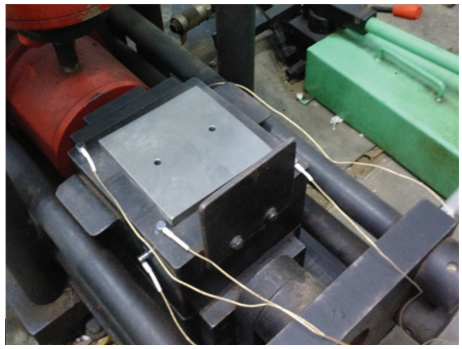

Figure 6: AE sensor arrangement.

According to the requirements of test instrument, the samples were processed into $50 * 50 * 50\,mm^3$. The samples were divided into 4 groups and each sample is 25 mm, 30 mm, 35 mm, and 40 mm, respectively (Figure 4).

The tests make use of two sets of devices that would load control system and AE monitoring system (Figure 5). The test instrument can be used to reasonably simulate rock stress condition, obtain the accurate parameters of shear strength, and complete stress-strain curve of sample. AE monitoring system is Micro-II Digital AE System which can be used to conduct real-time monitoring and record the whole process of the test. AE sensor arrangement is shown in Figure 6.

3.2. Test Method. The tests were divided in four groups of 16 samples. The sample was loaded in sample box, while AE sensor was attached to the surface of sample box by means of coupling agent. Ready after all, the sample was applied positive pressure by means of normal jack and pressure values of each set of 4 samples under the vertical pressure were 0.4 MPa, 0.6 MPa, 0.8 MPa, and 1.0 MPa, respectively. Positive pressure was applied after completion and then shear stress was applied by using the horizontal jack. AE monitoring system came to work at the same time. Horizontal pressure was applied until the sample failure and pressure gauge data were recorded in order to obtain horizontal shearing forces during the test. AE monitoring system records the AE activity of rock automatically.

3.3. Test Results and Analysis

3.3.1. The Characteristics of AE Event Counts. To explore the AE change pattern under different rock bridge length and different vertical pressure, the AE event count with time graph is obtained under different rock bridge lengths of sample including 25 mm, 30 mm, 35 mm, and 40 mm under 0.6 MPa vertical pressures (Figure 7), and the AE event count is obtained when vertical pressure of sample is 0.4 MPa, 0.6 MPa, 0.8 MPa, and 1.0 MPa with 30 mm rock bridge length (Figure 8). The AE event peak count with the rock bridge length and the vertical pressure graph are also mapped (Figures 9 and 10).

It can be seen that the sample failure mechanism has the following characteristics.

(1) In Figures 7 and 9, AE activity is more frequent and the appearance time of the AE event count peak value also increases with the increase of rock bridge length. This is because the arrival time of peak value increases with shear area under the same conditions, while shear area gains with rock bridge length.

(2) In Figures 8 and 10, AE event counts with the time have the same change trend; AE activity is more frequent. With the increasing of vertical pressure, AE event count peak value occurs much later. Shear stress increases with normal stress based on Mohr-Coulomb yield criterion, so the appearance time of peak value delays with the increase in vertical pressure.

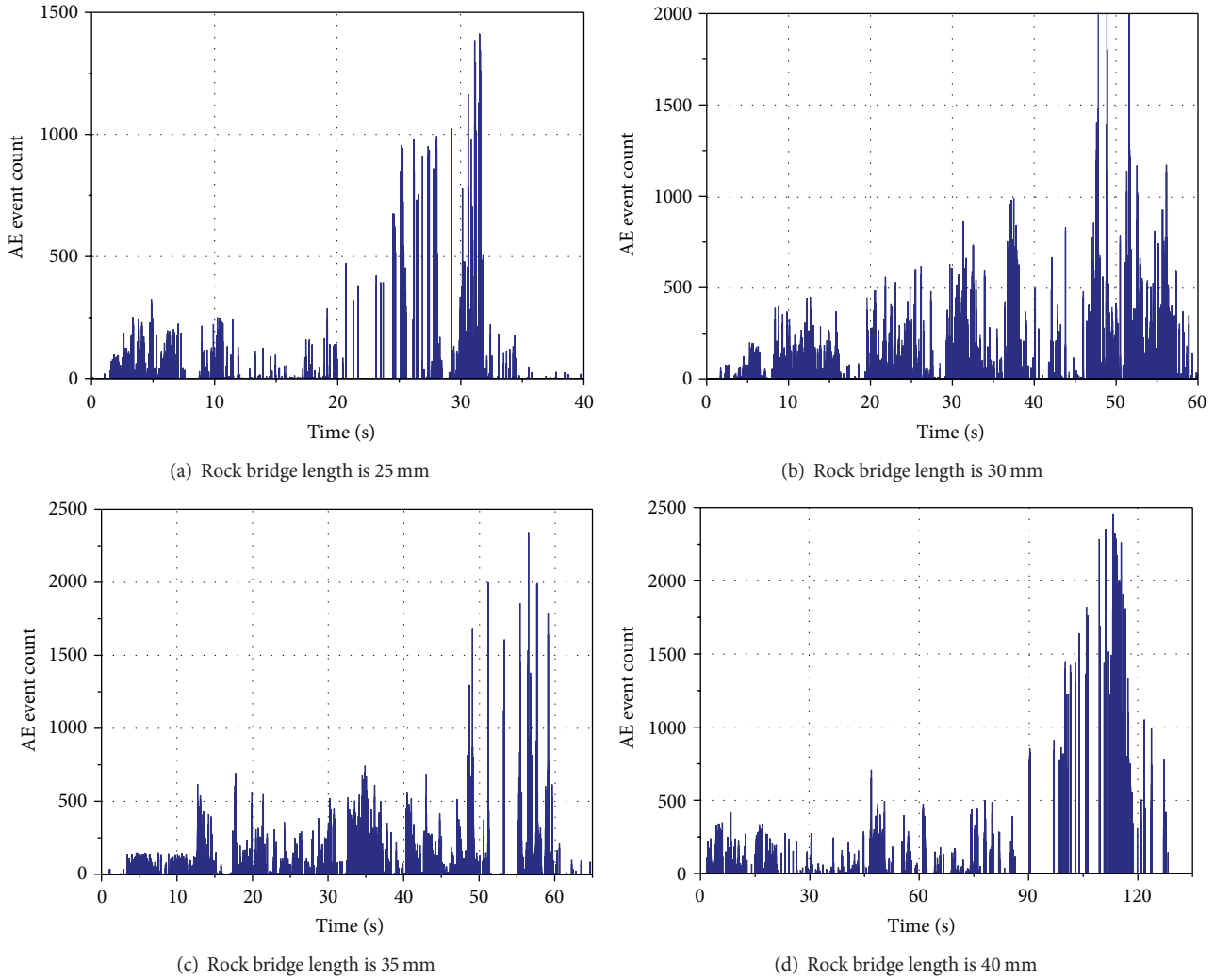

Figure 7: Relationship of AE event count and time at 0.6 MPa normal pressure under different rock bridge lengths.

3.3.2. Characteristics of AE Three-Dimensional Location. Figure 11 is the AE source location and the actual failure under different rock bridge lengths of 25 mm, 30 mm, 35 mm, and 40 mm under 0.6 MPa vertical pressure. Figure 12 is the AE source location of samples and the actual failure under different vertical pressure, consisting of 0.4 MPa, 0.6 MPa, 0.8 MPa, and 1.0 MPa under 30 mm length. Three-dimensional location result is shown by a side of sample in a picture to make AE three-dimensional location patterns more clear, and also it leads to some location points which overlap with each other. It can be found that the AE source location and the macroscopic failure mode of rock are in good match in Figures 11 and 12. The AE source location also has the following characteristics.

(1) In Figure 11, the number of AE location points was obtained with the increase of the rock bridge length. The crack shear angle increases from the horizontal direction to a certain angle, and the number of microcracks increases in the same vertical pressure under the different rock bridge length. It seems that location points with rock bridge of 30 mm break less than those with 25 mm in Figure 11.

(2) In Figure 12, the number of AE location points increases and its distribution is comparatively dispersive with the increase of vertical pressure; the crack shear angle was obtained from the horizontal direction to a certain angle in different vertical pressure under the same rock bridge length. The sample is easier to break with the increase of vertical pressure.

3.3.3. Failure Mechanism and Characteristics of Samples. As shown in Figure 13, it can be found that failure process can be divided into three stages by strain value.

(1) Stage 1 is the stage where strain value is 1~2% in which the shear stress is less than the shear strength of rock. The shear stress is much higher at the tip of rock bridge and the distribution of stress on the shear surface is uniform. At this stage, the AE activity is less, and it remains at a lower level and increases slowly.

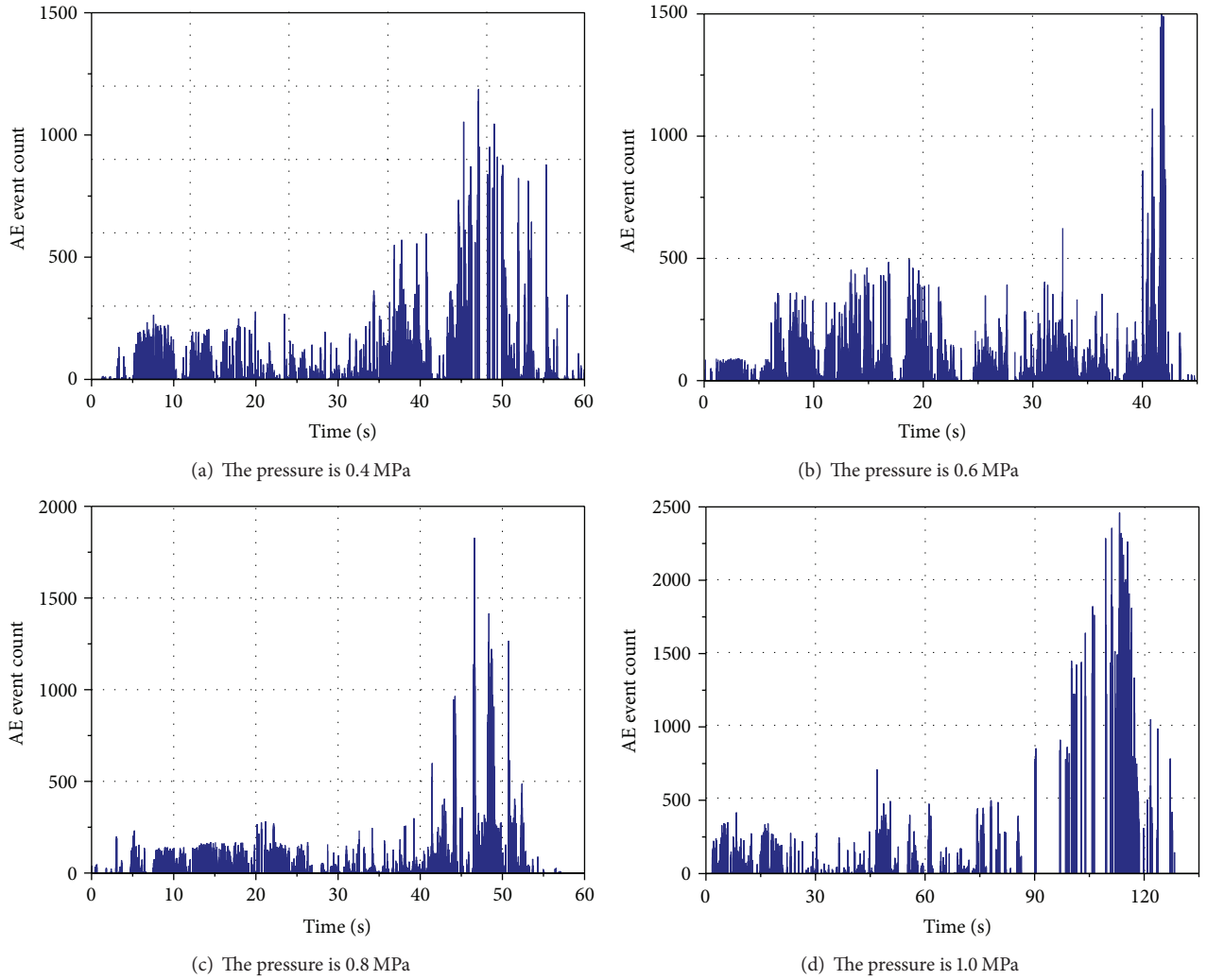

Figure 8: Relationship of AE event count and time at 30 mm rock bridge length under different vertical pressure.

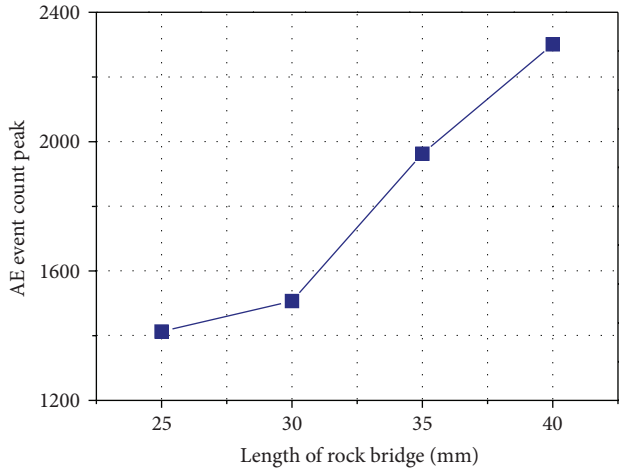

Figure 9: Relationship curves between AE event count peak and rock bridge length.

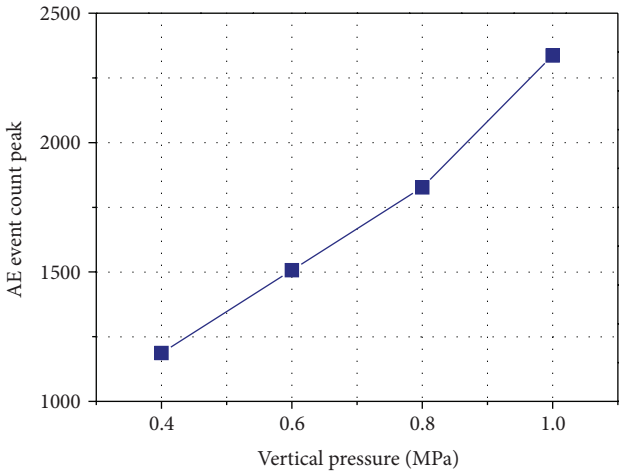

Figure 10: Relationship curves between AE event count peak and vertical pressure.

(2) Stage 2 is the stage where strain value is 2~3%; the sample enters the stage of plastic deformation and begins to develop cracks with the increase of shear stress. Because of the stress concentration at the tip

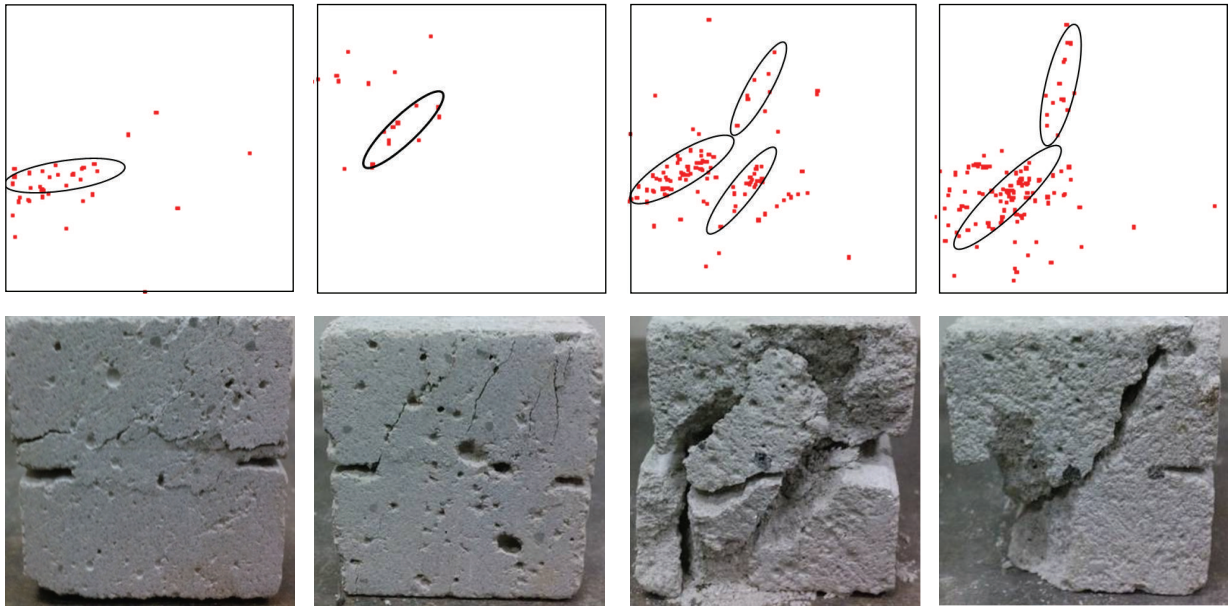

Figure 11: AE source locations of sample and the actual failure under different rock bridge length (25 mm, 30 mm, 35 mm, and 40 mm).

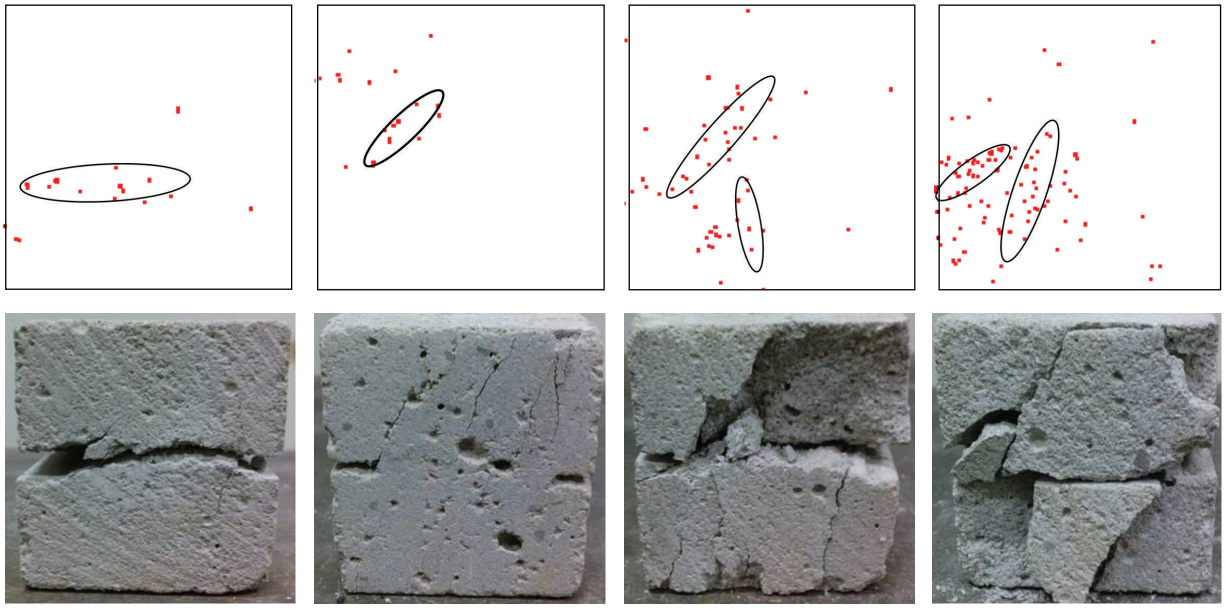

Figure 12: AE source locations of sample and the actual failure under different vertical pressure (0.4 MPa, 0.6 MPa, 0.8 MPa, and 1.0 MPa).

of rock bridge, the cracks often generate firstly from the tip of the rock bridge and finally grow into the main crack, and there form several groups of larger cracks parallel to the main crack near the rock bridge. A sudden integral brittle fracture occurs along the main rupture surface of the sample when the shear stress reaches the shear strength of rock. At this stage, AE activity frequency increases rapidly and AE count peak appears when the sample shear stress reaches the maximum value.

(3) Stage 3 is the stage with strain value after reaching 3%. As the sample is further damaged, the shear stress decreases rapidly and cracks extend further. At the end, the sample is completely cut out. At this stage, AE activity decays rapidly after maximum shear stress value and this stage is often shorter than others.

4. Large Scale Landslide Model with Locked Section Test

The locked section of rock slope refers to rock bridge near middle of sliding zone which has a relatively highly strength. The occurrence of large-scale rock landslides is generally accompanied by sudden brittle failure of the "locked

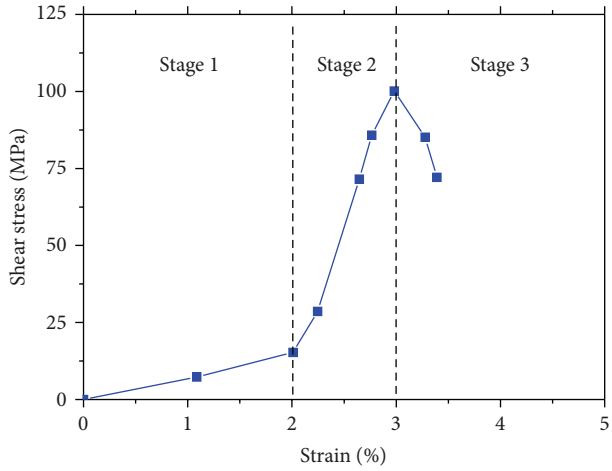

FIGURE 13: Sample stress-strain curve of direct shear test.

section." It means that "locked section" plays an important role in deformation control and stability mechanism of rock slope, hence a key in assessment and control on slope disaster.

Some authors had investigated the micro- and macrocharacteristics of shear or tensile failure under the action of gravity creep by the view of creep mechanics of rock mass [30]. Some authors had researched the creep fracture degree of bedrock and distribution of serious landslide hazard areas by using seismic wave velocity test [31] and other methods [32]. The researches were carried out to study locked section in various aspects, but the AE technique is rarely used. In this paper, the dynamic test characteristics of AE are used to carry out the large scale landslide model test with locked section to have a further study on its failure mechanism.

4.1. Samples Preparation and Test Instruments. The mass ratio of test sample is set at 1 : 3 : 1 : 1 (cement : sand : water : gypsum), with the sample size shown in Figure 14(a). The locked section is circular arc and reserved length of 65 mm. The test system uses a multisystem integrated test method in order to achieve a better physical simulation condition. Loading platform is two-dimension geological system framework and it is 4 m long, upper beam 2.5 m high, and foot beam 0.3 m high. Hydraulic jack which contacts the model is fixed on the framework and controlled by hydraulic system. The jack provides different pressure to simulate the sliding of gravity according to the test requirement. The arrangement of AE sensors is shown in Figure 14(b). The bedrock boundary is fixed with the sliding mass boundary being set free. Vertical load is imposed on upper part of sliding mass.

4.2. Test Method. After the installing of AE system and sensors, then starting the hydraulic control system, controlling oil pump to create pressure, and taking gradual loading increase by 2 MPa every level, the gradual loading changes to 1 MPa every level when the crack propagation is obvious in locked section until the model failure during the end loading phase. The AE keep monitoring and recording during the whole test process.

4.3. Test Results and Analysis

4.3.1. The Characteristics of AE Event Count and AE Energy. According to test data, the AE event count and AE energy change with time during test progress of landslide model with the locked section are shown in Figure 15. The following can be concluded from Figure 15.

It can be seen from Figure 15 that the test is not like the direct shear test. The energy of locked section accumulates continuously because of the increase of stress. The energy suddenly releases and then rock mass of locked section is cut out. This process has the characteristic of sudden and brittle failure; it reflects the development process of rock slope that from the progressive damage evolutes to brittle failure. AE event count with time and AE energy with time of slope model with locked section are almost the same as each other where both have the same change trend and characteristics. It can be corroborated to well respond to the deformation and failure characteristics of the slope model.

4.3.2. Characteristics of AE Plane Location. The failure process and characteristics of locked section test model are examined through the comparison of Figure 16; the conclusion is as follows.

(1) In Figure 16, the failure surface is basically in the predetermined locked section; along with locked section, an inclined plane is formed with the right being high and the left being low. The length of shear failure section is about 40 mm, and the shear failure surface has obvious scratches. The tensile failure section is 20 mm, and tension cracks can be observed obviously (Figure 16(a)).

(2) It can be found in Figure 16(b) that the AE source location is in accordance with the actual failure. Analysis of AE source location process shows that the location point first appears in the outside of sensor array, and its position finally locates within the two-sensor array as AE source points appear continuously with the time. The location point is more intensive at the edge of locked section because of the stress concentration.

(3) From the perspective of overall effect of AE source and its location technology, AE source located accurately and the space-time evolution of cracks in locked section is reflected; the failure process and characteristics of slope during the localization process can also be demonstrated. Rock landslide with locked section has the characteristics such as higher energy accumulation, the sudden release of energy, and brittle failure, which cause long sliding distance and serious failure.

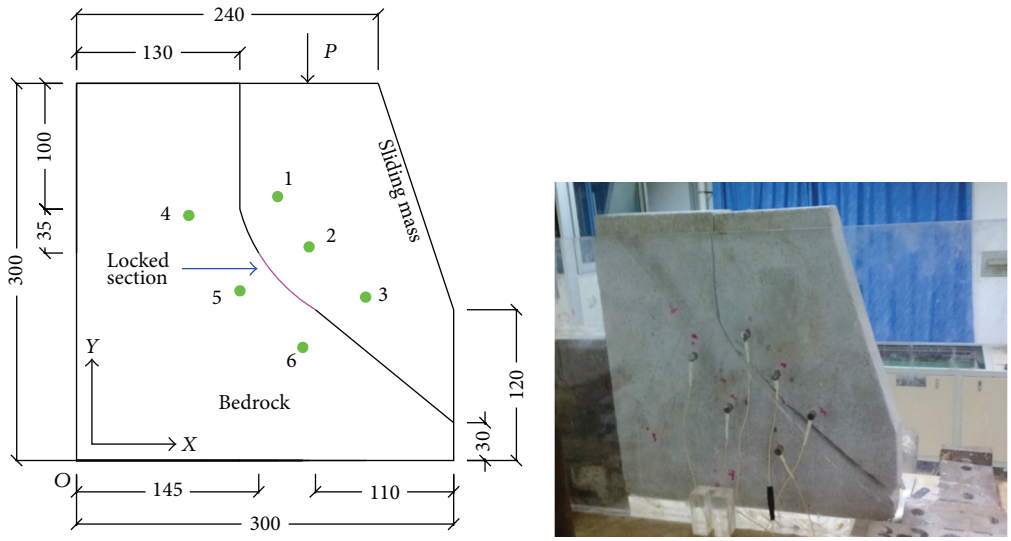

(a) Schematic diagram (mm)

(b) Actual sample

FIGURE 14: Sample size and sensor position.

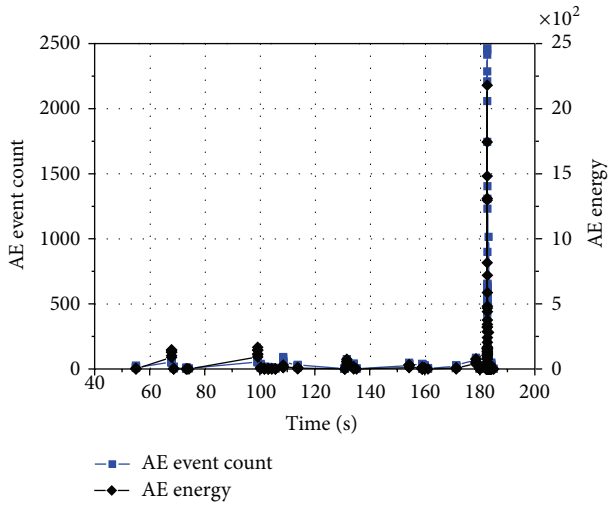

FIGURE 15: Relationship curves of AE event count with time and AE energy with time.

5. Conclusion

In this paper, small scale direct shear tests with different lengths and large scale rock landslide model with locked section test are carried out; both of them aim to study the failure mechanism and mechanics characteristics of rock bridge of landslide. The AE event count and AE source location under different circumstances are analyzed. The conclusions can be summarized as follows.

(1) AE source location can be accurately located during small scale tests in small scale direct shear tests. the AE event count peak value increases with the increasing of rock bridge length and vertical stress. In addition, the time of AE event count peak value appearing goes back with the increase of the length and the vertical stress.

(2) AE resource location was accurately and reliably located during large scale landslide model test with locked section. Based on the locating process, rock sample failure features and cracks time-space evolution process were revealed. AE showed that the brittle failure feature of landslide with locked section was reflected well.

(3) AE technology plays an important role in rock mechanics and related research fields. The two tests based on AE technique well revealed the rock failure mechanism in rocky slope and clarified the reason of high speed and long distance sliding of rocky slope that cause serious disasters and catastrophe.

Conflict of Interests

The authors declare that there is no conflict of interests regarding the publication of this paper.

Acknowledgments

This work is supported by the National Basic Research Program of China (973 Program, no. 2013CB733202) and the National Natural Science Foundation of China (Grant nos. 41272330 and 41130745). This work is also supported by the funding of Science and Technology Office of Sichuan Province (Grant no. 2015JQO020).

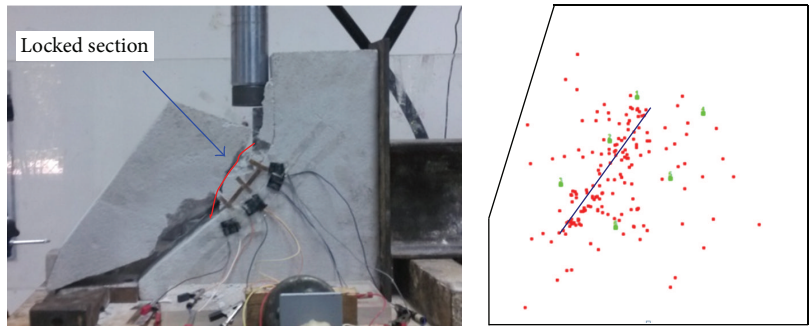

(a) Failure of locked section (b) AE source location of failure

Figure 16: Failure of locked section under continuous loading.

References

[1] D. Lockner, "The role of acoustic emission in the study of rock fracture," *International Journal of Rock Mechanics and Mining Sciences and*, vol. 30, no. 7, pp. 883–899, 1993.

[2] N. W. Xu, C. A. Tang, L. C. Li et al., "Microseismic monitoring and stability analysis of the left bank slope in Jinping first stage hydropower station in Southwestern China," *International Journal of Rock Mechanics and Mining Sciences*, vol. 48, no. 6, pp. 950–963, 2011.

[3] S. Li, X.-T. Feng, Z. Li, B. Chen, C. Zhang, and H. Zhou, "*In situ* monitoring of rockburst nucleation and evolution in the deeply buried tunnels of Jinping II hydropower station," *Engineering Geology*, vol. 137-138, pp. 85–96, 2012.

[4] Q. Jiang, J. Cui, and J. Chen, "Time-dependent damage investigation of rock mass in an in situ experimental tunnel," *Materials*, vol. 5, no. 8, pp. 1389–1403, 2012.

[5] V. Rudajev, J. Vilhelm, and T. Lokajíček, "Laboratory studies of acoustic emission prior to uniaxial compressive rock failure," *International Journal of Rock Mechanics and Mining Sciences*, vol. 37, no. 4, pp. 699–704, 2000.

[6] D. P. Jansen, S. R. Carlson, R. P. Young, and D. A. Hutchins, "Ultrasonic imaging and acoustic emission monitoring of thermally induced microcracks in Lac du Bonnet granite," *Journal of Geophysical Research*, vol. 98, no. 12, pp. 22231–22243, 1993.

[7] S. Wang, R. Huang, P. Ni, R. P. Gamage, and M. Zhang, "Fracture behavior of intact rock using acoustic emission: experimental observation and realistic modeling," *Geotechnical Testing Journal*, vol. 36, no. 6, 2013.

[8] D.-S. Cheon, Y.-B. Jung, E.-S. Park, W.-K. Song, and H.-I. Jang, "Evaluation of damage level for rock slopes using acoustic emission technique with waveguides," *Engineering Geology*, vol. 121, no. 1-2, pp. 75–88, 2011.

[9] C. Li, O. Stephansson, and T. Savilahti, "Behavior of rock joints and rock bridges in shear testing," in *Proceedings of the International Symposium on Rock Joints*, pp. 259–266, 1990.

[10] B. Shen and O. Stephansson, "Cyclic loading characteristics of joints and rock bridges in a jointed rock specimen," in *Proceedings of the International Symposium on Rock Joints*, pp. 725–729, 1990.

[11] R. H. C. Wong, K. T. Chau, P. M. Tsoi, and C. A. Tang, "Pattern of coalescence of rock bridge between two joints under shear testing," in *Proceedings of the 9th International Congress on Rock Mechanics*, pp. 735–738, 1999.

[12] S.-Q. Yang, H.-W. Jing, and S.-Y. Wang, "Experimental investigation on the strength, deformability, failure behavior and acoustic emission locations of red sandstone under triaxial compression," *Rock Mechanics and Rock Engineering*, vol. 45, no. 4, pp. 583–606, 2012.

[13] A. Ghazvinian, V. Sarfarazi, S. A. Moosavi et al., "Analysis of crack coalescence in rock bridges using neural network," in *Proceedings of the European Rock Mechanics Symposium*, pp. 255–258, 2010.

[14] F.-M. Zhang, B.-H. Wang, Z.-Y. Chen, X.-G. Wang, and Z.-X. Jia, "Rock bridge slice element method in slope stability analysis based on multi-scale geological structure mapping," *Journal of Central South University of Technology*, vol. 15, no. 2, pp. 131–137, 2008.

[15] J. Kemeny, "Time-dependent drift degradation due to the progressive failure of rock bridges along discontinuities," *International Journal of Rock Mechanics and Mining Sciences*, vol. 42, no. 1, pp. 35–46, 2005.

[16] W. Zhu, S. Li, R. H. C. Wong, K. T. Chau, and J. Xu, "A study of fracture mechanism and shear strength of rock bridges through analytical and model-testing methods," *Key Engineering Materials*, vol. 261–263, pp. 225–230, 2004.

[17] S. Y. Wang, W. Sloan, H. Y. Liu, and C. A. Tang, "Numerical simulation of the rock fragmentation process induced by two drill bits subjected to static and dynamic (impact) loading," *Rock Mechanics and Rock Engineering*, vol. 44, no. 3, pp. 317–332, 2011.

[18] F. Dai, M. D. Wei, N. W. Xu, Y. Ma, and D. S. Yang, "Numerical assessment of the progressive rock fracture mechanism of cracked chevron notched Brazilian disc specimens," *Rock Mechanics and Rock Engineering*, 2014.

[19] Z. Z. Liang, H. Xing, S. Y. Wang, D. J. Williams, and C. A. Tang, "A three-dimensional numerical investigation of the fracture of rock specimens containing a pre-existing surface flaw," *Computers and Geotechnics*, vol. 45, pp. 19–33, 2012.

[20] H. G. Li, R. Zhang, M. Z. Gao, G. Wu, and Y. F. Zhang, "Advances in technology of acoustic emission of rock," *Chinese Journal of Underground Space and Engineering*, vol. 9, pp. 1794–1804, 2013.

[21] Y.-L. Ding, Y. Deng, and A.-Q. Li, "Advances in researches on application of acoustic emission technique to health monitoring for bridge structures," *Journal of Disaster Prevention and Mitigation Engineering*, vol. 30, no. 3, pp. 341–351, 2010.

[22] L. Geiger, "Probability method for the determination of earthquake epicenters from the arrival time only," *Bulletin of St. Louis University*, vol. 8, pp. 60–71, 1912.

[23] W. Spence, "Relative epicenter determination using P-wave arrival-time differences," *Bulletin of the Seismological Society of America*, vol. 70, no. 1, pp. 171–183, 1980.

[24] P.-Z. Pan, F. Yan, and X.-T. Feng, "Modeling the cracking process of rocks from continuity to discontinuity using a cellular automaton," *Computers & Geosciences*, vol. 42, pp. 87–99, 2012.

[25] X. T. Feng, P. Z. Pan, and H. Zhou, "Simulation of the rock microfracturing process under uniaxial compression using an elasto-plastic cellular automaton," *International Journal of Rock Mechanics and Mining Sciences*, vol. 43, no. 7, pp. 1091–1108, 2006.

[26] X.-T. Feng and M. Seto, "Fractal structure of the time distribution of microfracturing in rocks," *Geophysical Journal International*, vol. 136, no. 1, pp. 275–285, 1999.

[27] G. Chen, T. Li, G. Zhang, H. Yin, and H. Zhang, "Temperature effect of rock burst for hard rock in deep-buried tunnel," *Natural Hazards*, vol. 72, no. 2, pp. 915–926, 2014.

[28] D. Y. Li, C. C. Li, and X. B. Li, "Influence of sample height-to-width ratios on failure mode for rectangular prism samples of hard rock loaded in uniaxial compression," *Rock Mechanics and Rock Engineering*, vol. 44, no. 3, pp. 253–267, 2011.

[29] G. Zhao, H. Pei, and H. Liang, "Measurement of additional strains in shaft lining using differential resistance sensing technology," *International Journal of Distributed Sensor Networks*, vol. 2013, Article ID 153834, 6 pages, 2013.

[30] M. Chigira, "Long-term gravitational deformation of rocks by mass rock creep," *Engineering Geology*, vol. 32, no. 3, pp. 157–184, 1992.

[31] N. W. Xu, F. Dai, Z. Z. Liang, Z. Zhou, C. Sha, and C. A. Tang, "The dynamic evaluation of rock slope stability considering the effects of microseismic damage," *Rock Mechanics and Rock Engineering*, vol. 47, no. 2, pp. 621–642, 2014.

[32] G. S. Zhao, G. Q. Zhou, X. D. Zhao, Y. Z. Wei, and L. J. Li, "R/S analysis for stress evolution in shaft lining and fracture prediction method," *Advanced Materials Research*, vol. 374–377, pp. 2271–2274, 2012.

Hindawi Publishing Corporation
Journal of Sensors
Volume 2015, Article ID 531428, 7 pages
http://dx.doi.org/10.1155/2015/531428

Research Article

A Study on Distribution Measurement and Mechanism of Deformation due to Water Loss of Overburden Layer in Vertical Shaft

Chunde Piao, Jun Yuan, Dangliang Wang, and Pengtao Li

School of Resources and Geosciences, China University of Mining and Technology, Xuzhou, Jiangsu 221116, China

Correspondence should be addressed to Chunde Piao; piaocd@126.com

Received 17 October 2014; Accepted 30 November 2014

Academic Editor: Fei Dai

Based on FBG fiber Bragg grating technology and BOTDA distributed optical fiber sensing technology, this study uses fine sand to simulate overburden layer in vertical shaft model equipment. It studies the placing technique and test method for optical fiber sensors in the overburden layer, combined with MODFLOW software to simulate the change of the water head value when the overburden layer is losing water, and obtains the deformation features of overburden layer. The results show, at the beginning of water loss, the vertical deformation increases due to larger hydraulic pressure drop, while the deformation decreases gradually and tends to be stable with the hydraulic pressure drop reducing. The circumferential deformation is closely related to such factors as the distance between each drainage outlet, the variations of water head value, and the method of drainage. The monitoring result based on optical fiber sensing technology is consistent with the characteristics of water loss in overburden layer simulated by MODFLOW software, which shows that the optical fiber sensing technology applied to monitor shaft overburden layer is feasible.

1. Introduction

A series of problems have cropped up in coal mining; the shaft lining rupture and local buckling deformation are always major problems [1]. Since the mine disaster is caused by rupture of shaft lining, through a large number of theoretical studies and testing data, it is proved that the vertical additional force which results from consolidation settlement due to drainage in thick overburden is the major factor which could lead to rupture of shaft lining [2]. At present, to monitor the shaft deformation, most researches analyze stability of the shaft lining structure by geometric metrology or the sensors installed in the outer part of shaft lining, but monitoring methods of overburden settlement are studied less before [3]. If overburden could be effectively monitored and the hydrophobic settlement deformation characteristics could be immediately recognized during operation of shaft lining, the fatal accidents will be avoided through effective measures.

As one of the most promising technologies in fiber optic sensor, distributed optical fiber sensing technology has many advantages, such as distributed monitor, long distance, antielectromagnetic interference, corrosion resistance, great durability, small size, and light weight. This technology has been widely used in engineering field including slope [4–7], pile foundation [8], and tunnel [9]. Facing the current situation of serious rupture of shaft lining, this paper, based on FBG fiber grating technology and BOTDA optical fiber sensing technology, uses the test device of shaft model, studies the placing technique for optical fiber sensors in the overburden layer, establishes the monitoring method based on optical fiber sensing technology, and analyzes hydrophobic settlement deformation characteristics, thus providing a firm theoretical and technical support for the exploitation of coal resources.

2. Optical Fiber Sensor Monitoring Technique

2.1. Fiber Bragg Grating Technology. In 1978, Hill et al. at Communications Research Centre in Ottawa, Canada, first found photosensitivity in a Germanium-doped silica fiber and made the first optical fiber grating sensor by using standing wave method [10]. With increasing researches all

over the world, fiber Bragg grating (FBG) sensor has become the most widely used optical fiber sensor in structural health monitoring. The basic principle of fiber Bragg grating sensor is that when the broadband incident light enters the fiber, the light which meets wave length conditions of Bragg grating will be reflected to become reflection light, and the rest of the light will become transmitted light. External temperature and strain changes will cause wavelength shift of reflection light, so by detecting the change of center wavelength, the change of measured signal can be obtained. The relationship between the strain and the center wavelength of fiber grating plus temperature is shown as follows [11, 12]:

$$\frac{\Delta\lambda_B}{\lambda_B} = c_\varepsilon \Delta\varepsilon + c_T \Delta T. \quad (1)$$

In the formula above, λ_B is the initial central wavelength of reflection light, and $\Delta\lambda_B$ is the drift amount of central wavelength. $\Delta\varepsilon$ and ΔT are the variable quantity of strain and temperature, respectively. c_ε and c_T refer to strain coefficient and temperature coefficient of fiber Bragg grating, respectively. At present, temperature accuracy of fiber Bragg grating is 0.1°C and strain accuracy is 1 $\mu\varepsilon$.

2.2. Brillouin Optical Time-Domain Analysis. Brillouin optical time-domain analysis (BOTDA) was first proposed by Horiguchi et al. in 1989. It was then applied to fiber nondestructive measurement in fiber communication field, and its spatial resolution was 100 m and strain accuracy was 100 $\mu\varepsilon$ [13].

Kishida et al. introduced the prepumped pulse method based on the theory model of leakage light pumped pulse. The Neubrex Company developed type NBX-6000 Pulse-PrePump-Brillouin Optical Time-Domain Analyzer (PPP-BOTDA) [14]. In terms of the measuring principle of PPP-BOTDA, it works by changing the structure of pumping laser pulse, during which both ends of fiber are, respectively, injected with step index pump pulse light and continuous light, and prepump pulse stimulates acoustic wave before pump pulse arrives at detection zone; thus, prepump pulse, pump pulse, probe laser, and stimulated acoustic wave interact with each other in the fiber, creating stimulated Brillouin scattering. Through the continuous frequency adjustment of the exploring laser light source, the continuous light power output is detected from the other end of fiber, which determines the frequency difference when fiber's Brillouin gains maximum in every small area, and this frequency difference is equal to fiber's Brillouin frequency shift in each part of area. Thus, according to the linear relation of Brillouin frequency shift and strain temperature, the change of strain and temperature can be determined on the various points along the fiber and it is shown in the following formula [15]:

$$v_B(\varepsilon, T) = v_B(0) + \frac{dv_B(\varepsilon)}{d\varepsilon} \cdot \varepsilon + \frac{dv_B(T)}{dT} \cdot (T - T_0). \quad (2)$$

In the formula above, $v_B(\varepsilon, T)$ is the drift amount of fiber Brillouin frequency with the change of strain and temperature, while $v_B(0)$ is the drift amount of fiber Brillouin frequency without the change of strain and temperature. ε is the axial dependent variable of sensing optical fiber. $(T - T_0)$ is the variable quantity of external temperature. $dv_B(\varepsilon)/d\varepsilon$ and $dv_B(T)/dT$ refer to influence coefficient of strain and temperature, respectively.

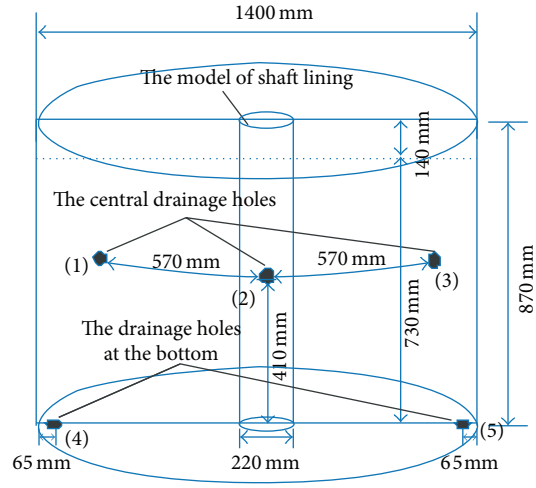

FIGURE 1: The size of shaft lining model equipment.

At present, the minimum spatial resolution of 10 cm can be reached and strain accuracy is 25 $\mu\varepsilon$ in measurement range of 1 km when this measurement technique is applied.

3. Model Test on Deformation in Overburden Layer

3.1. Test Scheme. Through simulating overburden layer with fine sand, this experiment uses the self-made vertical shaft model equipment to study the settlement and deformation, which results from the drainage in overburden layer. The diameter of the model equipment is 1400 mm, the height is 870 mm, and the diameter of the shaft lining is 220 mm. There are two drainage outlets at the bottom of the model equipment and three central drainage outlets are 410 mm above from the bottom, with the diameter of all drainage outlets being 20 mm. The height of fine sand is 730 mm. During the test medium, the nonuniform coefficient (Cu) of fine sand is 2.56, and the curvature coefficient (Cc) is 1.03. The permeability coefficient is 9 m/d; the water storage capacity is 0.1; the effective porosity is 0.1. The specific size of the model equipment is shown in Figure 1.

To measure the vertical settlement and circumferential deformation caused by the overburden losing water, we lay FBG optical fiber grating sensors and tight buffered optical fibers on the vertical and circumferential directions. Based on the layout scheme, 200 mm above from the bottom of the model equipment, we put every 100 mm distance, 5 circumferential tight buffered fibers, whose circumferential radius is 400 mm away from shaft lining. The iron plate with width of about 20 mm and length of about 750 mm is installed about 200 mm away from the shaft lining between the shaft lining and the central drainage hole 2. Five sensors FBG are pasted onto the iron plate whose length is 10 mm. The layout

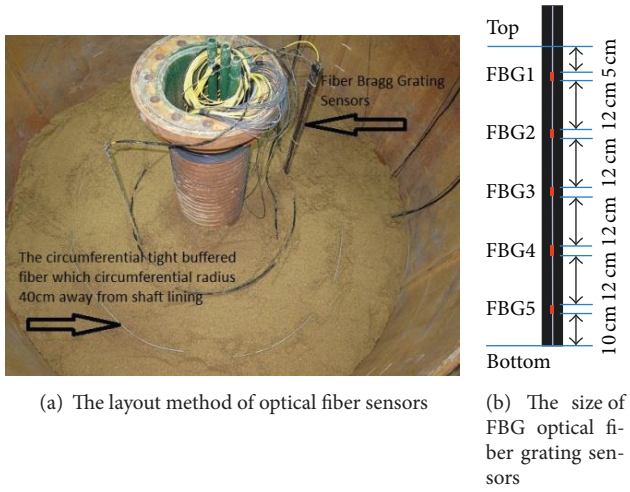

(a) The layout method of optical fiber sensors

(b) The size of FBG optical fiber grating sensors

FIGURE 2: The layout method of optical fiber sensors and the size of FBG optical fiber grating sensors.

method of optical fiber sensors and the size of FBG optical fiber grating sensors are shown in Figure 2. The sensors FBG2 and FBG3 fail during the test.

The bearing plate with thickness of 10 mm and diameter of 1360 mm is set on the top of fine sand layer in the experiment, whose weight is about 745 N. The jack and the weight are installed on the bearing plate to simulate soil pressure. The test is carried out in two steps. The first step is putting the weights of 1000 N, 3000 N, and 5000 N on the bearing plate to study the vertical and circumferential deformation of fine sand layer in the function of the upper pressure before water injection test. The second step is injecting water into the top of fine sand layer and then opening both central drainage outlets and bottom drainage outlets simultaneously, in order to study consolidation settlement and circumferential deformation of fine sand layer caused by the drainage.

3.2. Analysis on Water Loss of Fine Sand Layer by MODFLOW Software. Based on the model of shaft lining, this study uses the finite difference software Visual MODFLOW to construct the two-dimensional seepage model and obtain the change of head value when the fine sand layer loses water. The central drainage outlets and the drainage outlets at the bottom are opened at the same time. Figure 3 is the variation distribution map of water head value when the fine sand layer begins to lose water, and Figure 4 is the variation distribution map of water head value when the water level reaches the central drainage outlets.

From Figures 3(a) and 3(c), at drainage time, the water head value on both top and bottom of overburden layer has relatively minor change. However, Figure 3(b) shows that, under the influence of central drainage outlets, the water head value of plane 0.41 m away from the bottom changes significantly, yet its influence scope is only near the drainage outlets. As shown in Figure 4(a), when the water level reaches 0.41 m, the water head value near the drainage outlets decreases considerably, and the range of influence is between the central drainage outlets and the headline whose value is 0.46, but the value at other positions remains unaffected. Figure 4(b) shows that, near the drainage outlets at the bottom, the water head value of plane 0 m will drop, but its influence range is relatively small.

4. Result Analysis on Deformation Monitoring of Overburden Layer

4.1. Settlement and Compression Deformation of Overburden Layer Caused by Loading. As is shown in Figure 5, the deformation of fine sand layer, monitored by the sensors FBG1, FBG4, and FBG5, changes with time, when the bearing plate is bearing the weights of 1000 N, 3000 N, and 5000 N.

From Figure 5, it can be found that the deformation of fine sand layer gradually increases with the load increasing under changeable load, while the deformation gradually decreases with the depth increasing. For the sensors FBG4 and FBG5 at the bottom of fine sand layer, the deformation curve takes on an obvious form of stepladder because the fine sand layer completes settlement and tends to be stable within a short period of time. For the sensor FBG1 installed on the top of fine sand layer, the deformation is small and temporary with lower loads. When loads increasing, the soil pore is gradually filled with solid particles and the linear deformation intensifies.

Based upon BOTDA distributed fiber sensing technology, we detect the annulus sensing fiber, which is 40 cm far away from the shaft lining, and get the value of the circumferential deformation of fine sand layer under changeable loads, as is shown in Figure 6.

Figure 6 shows that the circumferential deformation of fine sand layer increases with the load rising, and its value gradually drops from the top to bottom; only soil is compressed under load, and the change of hoop strain at the same level stays the same.

4.2. Settlement and Compression Deformation Caused by Water Loss of the Aquifer. In the experiment, we apply 5000 kN load to the laminate on the top of overburden layer and inject water into the model equipment of shaft by the central drainage outlets. Then till the fine sand layer is submerged, we subsequently open both central and bottom drainage outlets and analyze the settlement character of the mineshaft during the process. During the experiment, the water level reaches the central drainage outlets after injecting water to the shaft for about 80 minutes. The fine sand layer continues to lose water through the drainage outlets at the bottom with time going on. The settlement character of the fine sand layer when losing water can be seen in Figure 7.

As shown in Figure 7, during the fine sand layer losing water, the effective stress increases and the pore water pressure decreases [16]. The fine sand is in transition from loose state to dense state and gradually stabilizes from top to bottom. The deformation of the sensors depends on buried depth and water losing conditions. For the sensor FBG1 at the top of sand layer, the deformation increases when the initial hydraulic pressure drop is great. With the decrease of hydraulic pressure drop, the deformation gradually decreases and tends to be stable. For the sensor FBG4, the fine sand

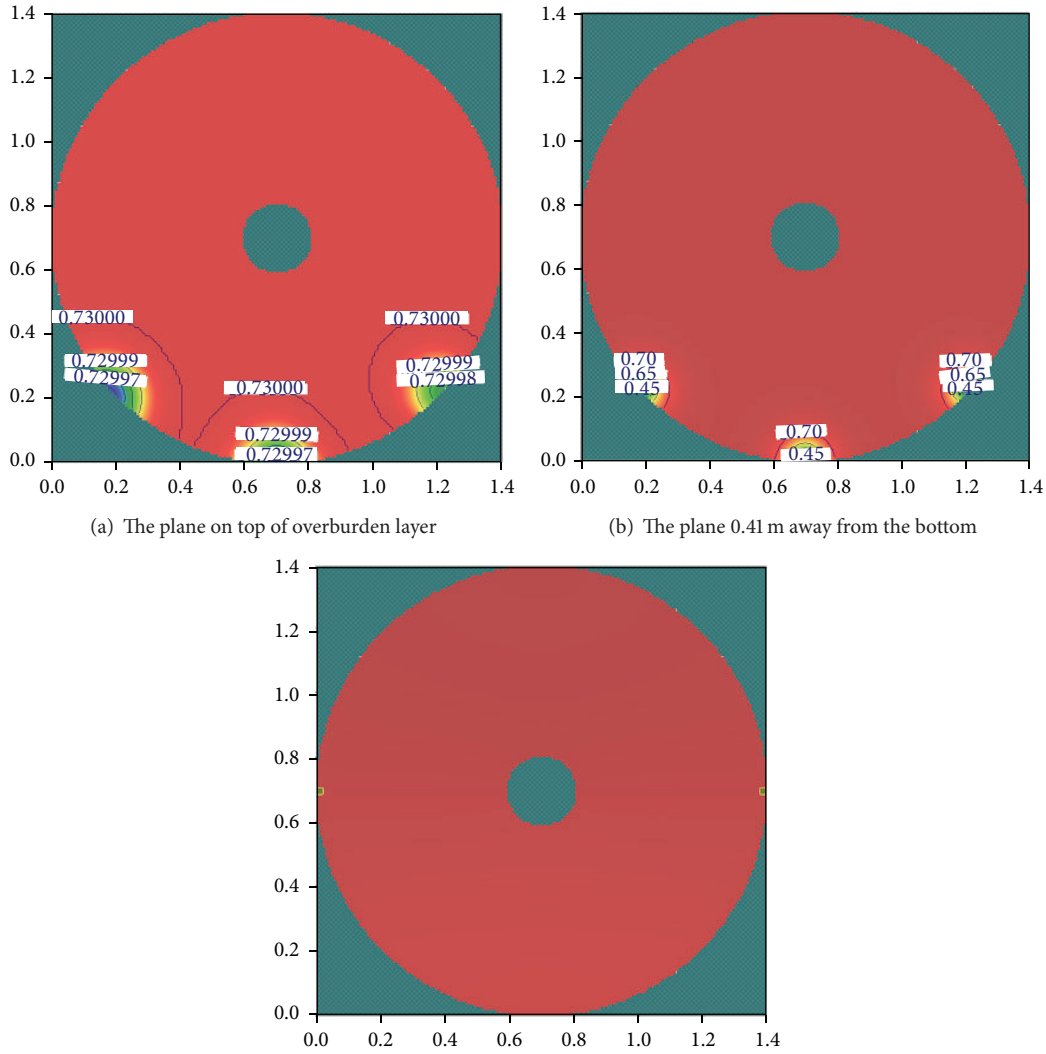

(a) The plane on top of overburden layer

(b) The plane 0.41 m away from the bottom

(c) The plane on bottom of overburden layer

Figure 3: The distribution map showing the variation of water head value of overburden layer at drainage time.

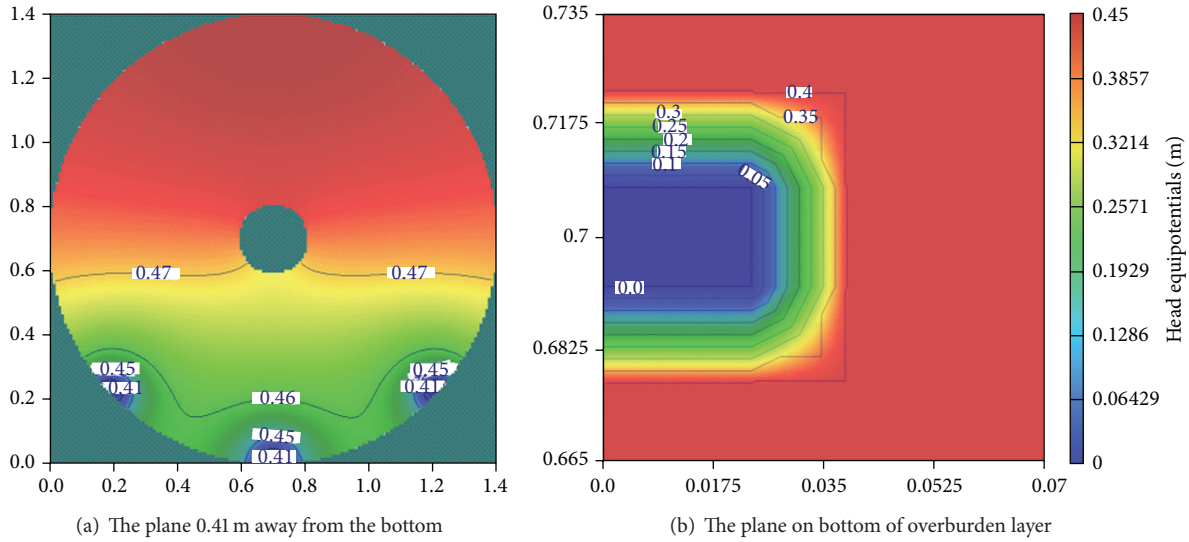

(a) The plane 0.41 m away from the bottom

(b) The plane on bottom of overburden layer

Figure 4: The distribution map of the variation of water head value of overburden layer when the water level reached 0.41 m.

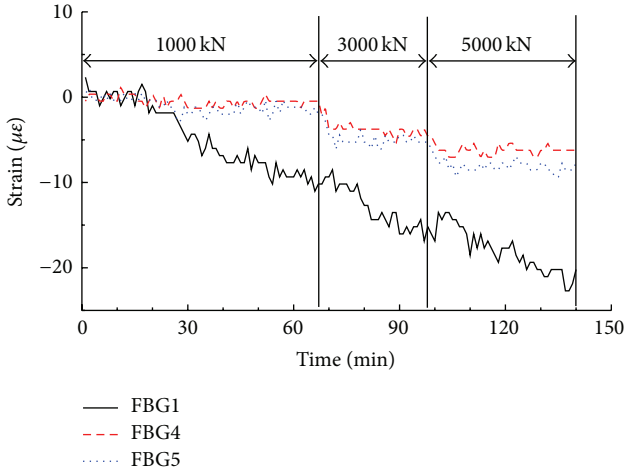

Figure 5: Dependent variable of fine sand layer along with variation of time under load.

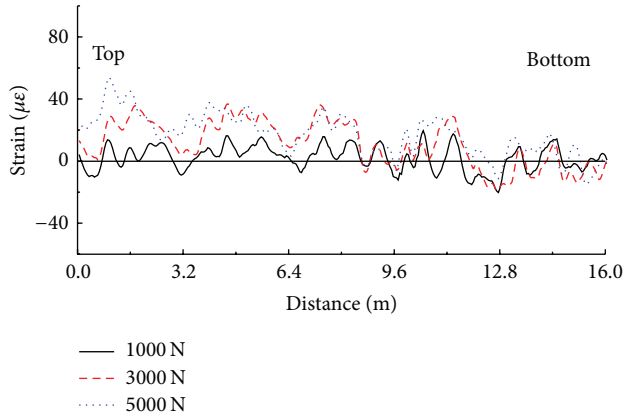

Figure 6: Circumferential deformation of fine sand layer 40 cm away from the shaft lining under load.

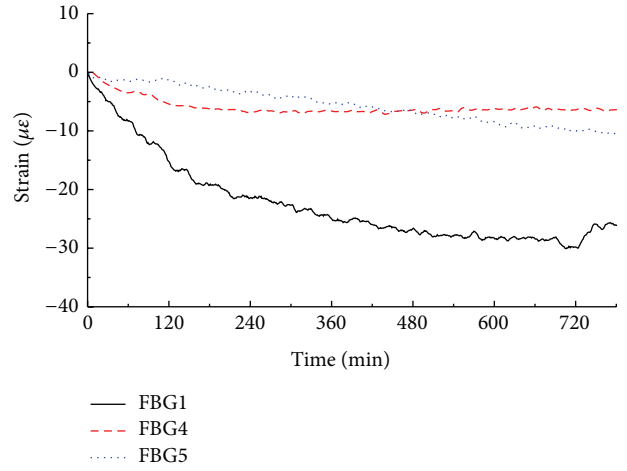

Figure 7: Dependent variable of fine sand layer along with variation of time under water loss.

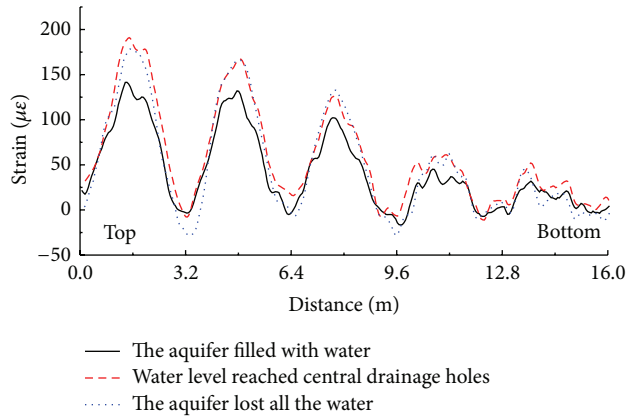

Figure 8: Circumferential deformation of fine sand layer 40 cm away from the shaft lining under water loss.

deformation increases gradually with its water loss. As the sensor has been located below the drainage outlets of the central shaft, the deformation caused by water loss is smaller. FBG5 has been laid at the bottom of the sand layer, and the deformation of the sand layer is relatively small at the beginning. Yet when aquifer loses water only via the bottom drainage outlets, the porosity rises and the deformation of aquifer increases linearly under the monitoring of sensor FBG5.

According to the change of water head value illustrated in Figure 4, along with the curve of circumferential strain shown in Figure 8, it can be found that affected by the loss of water in central drainage outlets, with the reducing distance from the drainage outlets, the porosity of the sand layer increases while the density decreases, so the circumferential deformation value of the fine sand layer increases, and the deformation value becomes stable while the change of water head is relatively smaller.

Figure 8 is the curve of circumferential strain of fine sand layer during losing water, which has been detected by BOTDA.

According to the curves of circumferential strain in Figures 6 and 8, without considering overburden pressure, the circumferential strain distribution can be obtained when the sand layer loses water. At the same plane of sand layer, the circumferential deformation is related to the distance between each drainage outlet, the variations of the water head value, and the method of drainage. When the drainage outlets are set in the middle, because of water loss of the aquifer, the water head value changes obviously and the deformation increases, as the distance between water level and the drainage outlets reduces. When the drainage outlets are set at the bottom, affected by water quantity, only the water head value near the drainage outlets changes and the circumferential deformation tends to undergo a uniform change. In vertical direction, when water level of saturated fine sand layer decreases to the central drainage outlets, the deformation near the drainage outlets gradually decreases from top to bottom while the dependent variable far away from the drainage outlets keeps invariant without

any variation in the water head value. When the pore water is excreted out of the aquifer only through the drainage outlets at the bottom, the settlement of soil is homogeneous and there is nearly no circumferential deformation.

5. Conclusions

Based on the above analysis, the main conclusions can be drawn as follows.

(1) According to the monitoring results of settlement by FBG fiber Bragg grating technology, the vertical deformation of fine sand layer depends on water losing conditions and buried depth of the sensors. Under the same load, the force on the soil at the bottom of shaft is smaller, and the soil tends to be stable in a short period of time, during which the deformation curve takes on an obvious form of stepladder, yet meanwhile the force on the soil on the top of shaft is larger, and the soil tends to be stable for a long period of time. The hydraulic pressure drop of the soil on the top of shaft is larger and the deformation increases at the initial stage of water loss, while the deformation decreases gradually and tends to be stable with the hydraulic pressure drop reducing.

(2) The monitoring result of overburden layer based on BOTDA distributed optical fiber sensing technology shows that the circumferential deformation is connected with such factors as the distance between each drainage outlet, the change in the water head value, and the method of drainage. When the drainage outlets are set in the middle, with water level of saturated fine sand layer decreasing to the central drainage outlets, the water head value, caused by the aquifer losing water, changes significantly as the distance between water level and the drainage outlets reduces. Near the drainage outlets, the deformation gradually decreases from top to bottom, yet when it is far away from the drainage outlets, the dependent variable remains the same. When the drainage outlets are set at both ends of the bottom, the pore water is running out only through the drainage outlets at the bottom. Then it is only near the drainage outlets that the water head value changes. And the circumferential deformation is almost in uniform change.

(3) Based on FBG fiber Bragg grating technology and BOTDA distributed fiber sensing technology, the study obtains deformation features of overburden layer under the water losing conditions. The research result is consistent with the characteristics of overburden layer losing water simulated by MODFLOW software. It shows that, in monitoring shaft overburden layer, the placing technique and test method for optical fiber sensors are plausible.

Conflict of Interests

The authors declare that there is no conflict of interests regarding the publication of this paper.

Acknowledgments

The work is funded by National Science Foundation for Youth (no. 51004103), China Postdoctoral Science Foundation (no. 20100481175), and the Project Funded by the Priority Academic Program Development of Jiangsu Higher Education Institutions.

References

[1] W. Sui, G. Zhang, Z. Jiang et al., "The state-of-the-art of chemical grouting treatment for quicksand hazards in coal mines and the prospect of several key problems," *Journal of Engineering Geology*, vol. 1, supplement 1, pp. 73–77, 2008.

[2] H. Lv, W. Yang, X. Cheng et al., "The research on mechanism and control techniques of the shaft lining rupture under special strata (the second)," *Journal of China University of Mining & Technology*, vol. 26, no. 2, pp. 1–4, 1997.

[3] Z.-Q. Liu, G.-Q. Zhou, G.-S. Zhao, H.-C. Liang, and J.-S. Zhou, "The control method and its application about the soil grouting reinforcement process in vertical shaft," *Journal of the China Coal Society*, vol. 30, no. 4, pp. 472–475, 2005.

[4] H. Zhu, B. Shi, and J. Zhang, "Distributed fiber optic monitoring and stability analysis of a model slope under surcharge loading," *Journal of Mountain Science*, vol. 11, no. 4, pp. 979–989, 2014.

[5] H.-H. Zhu, A. N. L. Ho, J.-H. Yin, H. W. Sun, H.-F. Pei, and C.-Y. Hong, "An optical fibre monitoring system for evaluating the performance of a soil nailed slope," *Smart Structures and Systems*, vol. 9, no. 5, pp. 393–410, 2012.

[6] H.-H. Zhu, B. Shi, J.-F. Yan, J. Zhang, C.-C. Zhang, and B.-J. Wang, "Fiber Bragg grating-based performance monitoring of a slope model subjected to seepage," *Smart Materials and Structures*, vol. 23, no. 9, Article ID 095027, 2014.

[7] Y. Ding, B. Shi, H.-L. Cui, W.-B. Suo, and L. Liu, "A fiber optic sensing net applied in slope monitoring based on Brillouin scattering," *Chinese Journal of Geotechnical Engineering*, vol. 27, no. 3, pp. 338–342, 2005.

[8] C.-D. Piao, B. Shi, G.-Q. Wei, Y.-Q. Zhu, and D. Zhang, "Application of distributed fiber optic sensing techniques in bored pile detection," *Chinese Journal of Geotechnical Engineering*, vol. 30, no. 7, pp. 976–981, 2008.

[9] B. Shi, X.-J. Xu, D. Wang et al., "Study on BOTDR-based distributed optical fiber strain measurement for tunnel health diagnosis," *Chinese Journal of Rock Mechanics and Engineering*, vol. 24, no. 15, pp. 2622–2628, 2005.

[10] K. O. Hill, Y. Fujii, D. C. Johnson et al., "Potosensitivity in optical fiber waveguides: application to reflection filter fabrication," *Applied Physics Letters*, vol. 32, no. 10, pp. 647–649, 1978.

[11] A. Othonos and K. Kalli, *Fiber Bragg Gratings: Fundamentals and Applications in Telecammunications and Sensing*, Artech House, London, UK, 1999.

[12] H. Zhu, J. Yin, C. Hong et al., "Fiber optic based monitoring technologies of slope engineering," *Geotechnical Investigation & Surveying*, no. 3, pp. 6–9, 2010.

[13] T. Horiguchi, T. Kurashima, and M. Tateda, "Tensile strain dependence of Brillouin frequency shift in silica optical fibers," *IEEE Photonics Technology Letters*, vol. 1, no. 5, pp. 107–108, 1989.

[14] K. Kishida, C. S. Li, and S. Lin, "Pulse pre-pump method to achieve cm-order spatial resolution in Brillouin distributed measuring technique," *Technical Report of IEICE, OFT*, vol. 47, pp. 15–20, 2004.

[15] T. Guo, A. Li, Y. Song, B. Zhang, Y. Liu, and N. Yu, "Experimental study on strain and deformation monitoring of reinforced concrete structures using PPP-BOTDA," *Science in China Series E: Technological Sciences*, vol. 52, no. 10, pp. 2859–2868, 2009.

[16] G. Chen, T. Li, and Y. He, "Formation mechanism of groundwater for the land subsidence," *Research Journal of Chemistry and Environment*, vol. 16, no. s2, pp. 56–62, 2012.

Hindawi Publishing Corporation
Journal of Sensors
Volume 2015, Article ID 470905, 12 pages
http://dx.doi.org/10.1155/2015/470905

Research Article

Deformation Monitoring of Geomechanical Model Test and Its Application in Overall Stability Analysis of a High Arch Dam

Baoquan Yang,[1] Lin Zhang,[1] Enlong Liu,[1] Jianhua Dong,[1] Honghu Zhu,[1,2] and Yuan Chen[1]

[1] *State Key Laboratory of Hydraulics and Mountain River Engineering, College of Water Resource & Hydropower, Sichuan University, Chengdu 610065, China*
[2] *School of Earth Sciences and Engineering, Nanjing University, Nanjing 210023, China*

Correspondence should be addressed to Yuan Chen; chenyuan8899@163.com

Received 16 November 2014; Revised 6 January 2015; Accepted 20 January 2015

Academic Editor: Fei Dai

Geomechanical model testing is an important method for studying the overall stability of high arch dams. The main task of a geomechanical model test is deformation monitoring. Currently, many types of deformation instruments are used for deformation monitoring of dam models, which provide valuable information on the deformation characteristics of the prototype dams. However, further investigation is required for assessing the overall stability of high arch dams through analyzing deformation monitoring data. First, a relationship for assessing the stability of dams is established based on the comprehensive model test method. Second, a stability evaluation system is presented based on the deformation monitoring data, together with the relationships between the deformation and overloading coefficient. Finally, the comprehensive model test method is applied to study the overall stability of the Jinping-I high arch dam. A three-dimensional destructive test of the geomechanical model dam is conducted under reinforced foundation conditions. The deformation characteristics and failure mechanisms of the dam abutments and foundation were investigated. The test results indicate that the stability safety factors of the dam abutments and foundation range from 5.2 to 6.0. These research results provide an important scientific insight into the design, construction, and operation stages of this project.

1. Introduction

Currently, the construction of high arch dams in China is undergoing vigorous development. Several high arch dams about 300 m high, which represent an advanced class of arch dams, are planned or under construction. For example, the Xiaowan arch dam (294.5 m high) was built on the Lancang River. The Jinping-I arch dam (305 m high) on the Yalong River is under construction. The Baihetan (289 m high) and Wudongde arch dams (265 m high) on the Jinsha River and the Songta arch dam (313 m high) on the Nujiang River are currently in the design phase. Most of them involve great dam heights and huge reservoir capacities. These large-scale arch dam projects are accompanied with large flood discharges, high earthquake intensities, and complicated geological conditions [1]. To guarantee the safety of these projects, it is important to study the stability of both arch dams and dam foundations, to select optimum foundation reinforcement schemes, and to evaluate the strengthening effects of the corresponding reinforcement measures. A lot of efforts have been made to monitor the field performance of dams [2], but the instrumentation costs are expensive and the interpretation of field monitoring results is complicated. Geomechanical model testing is an important approach that can solve these problems.

Geomechanical model testing is a method that can reasonably simulate the dam under investigation, by taking into account the geological structure of the dam abutment and its reinforcement measures using certain similarity principles [3, 4]. The primary purpose of this test is to obtain deformation characteristics and failure pattern of the prototype through overloading or strength reduction [5]. Using this method, the influences of the geological structure on the dam safety can be evaluated, which can provide a reference for designing foundation reinforcement schemes. In addition, by studying the deformation monitoring data and the failure mechanisms of dam abutments and foundations, the safety factor of the dam and foundation can be determined. Such monitoring

results are very intuitive for dam designers and decision makers.

Deformation monitoring is very important for geomechanical model tests. However, as the deformation of small-scale models is much smaller than the prototype, the deformation instruments should have very high precision. They should also have small sizes and light weights, so that they can be easily installed in the model dams. Currently, different types of deformation instruments, including mechanical sensors, inductive sensors, resistance strain gage, and differential transformers, are available. All of these instruments have been frequently used for deformation monitoring of geomechanical models and can meet the high-accuracy requirements. Due to the development of measurement technologies, especially the rapid development of computers and automation technologies, the measurement methods and techniques in model tests developed rapidly. These sensors are more accurate and reliable than conventional ones. For example, the internal displacement transducer developed by Zhang et al. [6] can be used to monitor the relative deformation of the structural planes in the rock mass. The small two-way resistance displacement sensor developed by Huang and Chen [7] can replace resistance strain gauges in the model instrumentation system. The fiber optic sensing method is another important advance for geomechanical model tests [8–10]. The fiber optic sensors have many advantages over conventional sensors, such as small size, high accuracy, and inherent resistance to corrosion and electrical noise [11–14].

Although the development of deformation testing techniques can meet the requirements of geomechanical model tests, more works should be conducted to relate the deformation measurements gained to the overall stability of high arch dams. Zhou et al. [15, 16], Liu et al. [17], and Zhang et al. [18] of Tsinghua University established an analysis and evaluation system for the model tests of several high arch dams in China, such as the Xianghongdian, Qingshiling, and Jinshuitan dams. They summarized the test results of these dams and grouped a set of safety evaluation methods based on λ_1 (initial cracking load), λ_2 (nonlinear start load), and λ_3 (limit fracture load) values. They also introduced the evaluation index into the engineering design specifications of China. Peng et al. [19] of Tongji University presented a systematic method for slope safety evaluation utilizing multisource monitoring information. However, a complete set of stability evaluation systems was not formed for the comprehensive test method of geomechanical models.

In this paper, a relationship for assessing the stability of dam safety is established based on the comprehensive model test method. A stability evaluation system is presented based on the deformation monitoring results. Two inflection points are proposed to indicate the stability condition of high arch dams. Finally, the comprehensive model test method was applied to study the overall stability of the Jinping-I high arch dam. A three-dimensional (3D) destructive test of a geomechanical model dam was conducted under reinforced foundation conditions. The deformation characteristics and failure mechanisms of the dam abutments and foundation were investigated in detail.

2. Comprehensive Test Method for Geomechanical Models

2.1. Principles of the Comprehensive Test Method. For geomechanical models, three test methods are widely used, including the overloading method, the strength reduction method, and the comprehensive method. The overloading method mainly considers the upstream overloading effect on the stability of the dam abutments. The strength reduction method focuses on the effects of the decreasing mechanical strengths of the rocks and weak structural planes in the abutments and foundation on the dam stability. The comprehensive method is a combination of the overloading and strength reduction methods, through which a variety of factors can be investigated within one model [20]. For the overloading method, multistage loadings are generally accomplished by using jacks installed on the upstream surface of the model dam, through which the water overloading is applied. The overloading method is extensively applied in geomechanical model tests because of its convenience. The comprehensive method can consider more factors simultaneously, but overloading and strength reduction must be conducted in one model, which results in a certain degree of difficulty. Here, we proposed a comprehensive test method for geomechanical models, which takes advantages of special temperature analogous materials [21–23].

The safety factor of the comprehensive test method was assessed by using the basic concepts of degree of safety (or the point safety factor) and the principles of the overloading method and the strength reduction method. The point safety factor can be expressed as follows:

$$K = \frac{(f \cdot N + c \cdot A)}{P} = \frac{\int (f \cdot \sigma + c)\, dA}{P} = \frac{\int \tau dA}{P}, \quad (1)$$

where K is the point safety factor, P is the design water pressure on the upstream dam surface (sliding force), f is the shear friction coefficient, c is the cohesion, N is the normal force of the sliding surface, A is the sliding surface area, σ is the normal stress on the surface of the integral infinitesimal, dA is the integral infinitesimal area, and τ is the shear strength at the surface of the integral infinitesimal.

Equation (1) can be rewritten as

$$1 = \frac{(f \cdot N + c \cdot A)}{K \cdot P} = \frac{\int (f \cdot \sigma + c)\, dA}{K \cdot P} = \frac{\int \tau dA}{K \cdot P}. \quad (2)$$

Equation (2) shows that in the overloading method the material mechanical parameters of f and c and the shear strength τ will remain constant. Thus, we can increase the design water pressure P until the model dam fails. The coefficient of the overload that corresponds to the failure of the model dam is called the overloading safety factor K.

Equation (2) can be rewritten as in the following format:

$$1 = \frac{(f \cdot N + c \cdot A)/K}{P} = \frac{\int [(f \cdot \sigma + c)/K]\, dA}{P} = \frac{\int (\tau/K)\, dA}{P}. \quad (3)$$

Equation (3) represents the concept of the strength reduction method. This method is under constant load conditions, but the mechanical parameters f and c of the rock mass and structural plane of the model gradually decrease in the test, until the model dam fails. The lowest coefficient of the mechanical parameters of the model materials in the model tests is called the strength reduction safety factor K.

If the K in (3) is decomposed into two parts, that is, the strength reduction coefficient K_1 and the overloading coefficient K_2, the following relationship can be obtained:

$$1 = \frac{(f \cdot N + c \cdot A)/K_1}{K_2 \cdot P} = \frac{\int [(f \cdot \sigma + c)/K_1]\, dA}{K_2 \cdot P} = \frac{\int (\tau/K_1)\, dA}{K_2 \cdot P}. \quad (4)$$

Equation (4) shows the concept of the comprehensive test method, from which the comprehensive safety factor K_c can be represented as follows:

$$K_c = K_1 \cdot K_2. \quad (5)$$

According to (1) to (5), the comprehensive method is advantageous because it considers not only the overloading effect of the dam but also the influence of decreasing strength of rock mass and structural planes. Thus, this method integrates the merits of the overloading method and the strength reduction method.

2.2. Safety Factors of the Comprehensive Test Method. As shown in (5), the safety factor in the comprehensive test method is a product of the strength reduction coefficient K_1 and the overloading coefficient K_2. The strength reduction coefficient K_1 is the reduction factor of the mechanical parameters f and c, which mainly consider the softening effect of rock masses and structural planes under the actions of reservoir water. This situation occurs under the normal operation conditions of a dam. In the dam stability analysis, the degree of strength reduction for the structural planes is often assigned a value of 15%~30% according to engineering experiences [24]. Thus, the strength reduction coefficient K_1 is between 1.15 and 1.3 in the comprehensive model tests.

The overloading coefficient K_2 represents multiples of the design water pressure P, which can be withstood by the dam structure. The situation when the dam is subjected to an unusually large load is considered [25]. Obtaining the overloading coefficient K_2 in the comprehensive test method is very important. The deformation of the dam body and dam foundation directly reflects the dam stability and potential damage. Therefore, in a geomechanical model test, the monitoring results of the deformation of the dam and dam abutments should be analyzed in detail. In this study, the deformation catastrophe theory [26] is used to propose characteristic points of the deformation curves obtained from model tests, which provides a basis for evaluating the overloading coefficient. A typical curve between the dam deformation and the overloading coefficient of a dam model is shown in Figure 1.

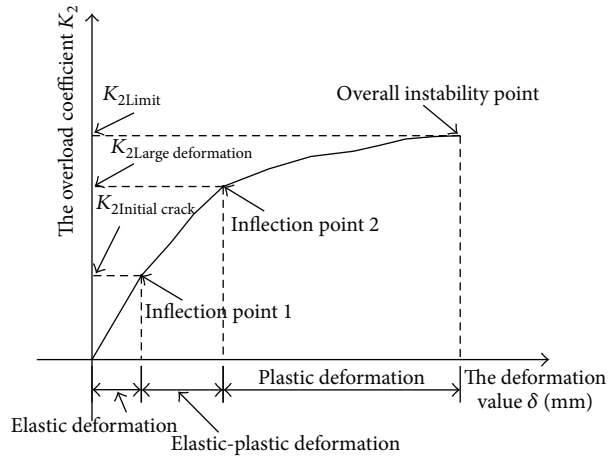

FIGURE 1: Typical curve between the deformation value δ and the overloading coefficient K_2 of a dam model.

Figure 1 shows that the failure process of a model dam can be divided into three stages, that is, the elastic deformation stage, the elastic-plastic deformation stage, and the overall instability stage. The curve has two inflection points. Before the first inflection point, the model is in the elastic deformation stage and the dam is in the normal operation phase. When the first inflection point approaches, the dam is assumed to have a small crack. At this point, the overloading coefficient K_2 is also called the initial cracking coefficient $K_{2\text{Initial crack}}$. As the overload continues to increase, the model dam enters the elastic-plastic deformation stage. In this stage, more and more cracks appear on the surface of the model dam but the dam structure remains stable. After the second inflection point is reached, the dam deformation increases suddenly and the model dam enters the plastic deformation stage. Finally, the entire model dam shows overall instability tendencies. In the model test, the second inflection point is called the large deformation inflection point, and the corresponding overloading coefficient is called $K_{2\text{Large deformation}}$. In addition, the overloading coefficient corresponds to the overall instability and is called $K_{2\text{Limit}}$. Based on the catastrophe theory and engineering practices [27], the second inflection point is critical for evaluating the stability of the model dam. In this study, the second inflection point of the deformation curve is considered as the indicator of the overloading coefficient $K_{2\text{Large deformation}}$.

2.3. Deformation Monitoring in the Comprehensive Method Test. In the comprehensive test method of geomechanical models, the measurement system of the model consists of three parts. The first part is to monitor the surface deformation of the dam and dam shoulders and the second part is to measure the strains of the dam. The third part is for monitoring the relative deformation of the internal structural planes in the abutment rock masses. Currently, linear variable differential transformers (LVDTs) are commonly used in modal tests to monitor the surface deformation. These instruments are based on Faraday's law of electromagnetic

induction and the sensing unit can convert the change of the measured signal to the change of mutual inductance. The transformer consists of a primary coil, a secondary coil, and an iron core. When an electric current passes through the primary coil, an initial voltage output is generated. This output causes the iron core to become mobile when the measured object moves, changing the mutual inductance coil. At this time, the output voltage varies with the change in the mutual inductance coil, which is proportional to the applied displacement. Consequently, the displacement measurement can be obtained. The SP-10A digital displacement measuring instrument is commonly used in geomechanical model tests. The instrument is characterized by its simple structure, high sensitivity, and easy installation. The measurement range of displacement is ±1 to ±50 mm, with an accuracy of 0.001 mm.

The monitoring instruments of strain and relative deformation are all based on the electrical resistance measurement technique. Resistance strain gauges are used as sensing elements, and the Wheatstone bridge principle is used for data collection. Commonly used equipment for data collection is the UCAM-70A and UCAM-8BL universal digital testing device. The surface and internal displacements of a model dam are directly related to the stability of the dam and foundation. Once the deformation of the model dam is captured, the evaluation of the health condition of the prototype structure can be carried out. In the following sections, the monitoring results of a comprehensive model test of the Jinping-I high arch dam are presented and the deformation and failure characteristics of this dam are discussed.

3. Jinping-I High Arch Dam

3.1. Project Background. The Jinping-I hydropower station is a large-scale cascade hydropower station in China, which is located on the main branch of the Yalong River in Sichuan Province. This hydropower project has a total capacity of 3600 MW. The maximum height of the concrete hyperbolic arch dam is 305 m, which is the tallest arch dam under construction in the world.

The watercourse of the site area is straight, and the river flows towards N25°E. The valley consists of deep V-shaped canyons with a relative elevation difference of 1500 m to 1700 m. The rock stratum of the left river bank is a reverse slope. The upper and lower rock strata are mainly composed of sandy slate and marble, respectively. The rock stratum of the right river bank forms a consequent slope, and the rock stratum consists of marble. The slope of the lower part is steep and the higher part is gentle. The typical geological profile of this site is shown in Figure 2.

The rock masses in the arch dam abutment are strongly affected by geological tectonics. Within the rock masses, faults, alteration veins, inner layer compressed zones, joint fissures, deep cracks, and other types of weak structural planes exist, which greatly influence the overall stability of the dam and foundation. The most critical geological structures include the following: (a) the faults f5, f2, f8, f42-9, f9, and F1; (b) the compressed zone g; (c) the lamprophyre dike X and deep cracks on the left bank; (d) the faults f13, f14, and f18; (e) the greenschist lens; and (f) the steep dip joints in the South-North (SN) direction on the right bank.

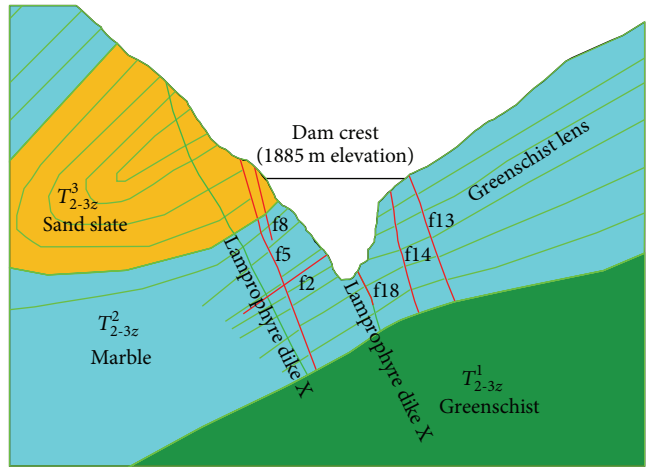

Figure 2: Typical geological condition at the Jinping-I arch dam site.

3.2. Reinforcement Measures of the Dam Abutment and Foundation. Because the geological conditions of the Jinping-I high arch dam are very complex, large amounts of reinforcements are needed to assure the stability of the dam and foundation. Considering the main geological structures and technical feasibility, the main reinforcement measures in this project include the following: (a) the concrete seating replacement in the left abutment; (b) the concrete replacement grids and hole-plugs for the weak structural planes; (c) the shearing resistant holes, the grooving replacement, and the consolidation grouting. For example, according to the development situation of the fault f2 and the compressive belt (g), grooving replacement was used in the foundation surface near an elevation of 1670 m, where f2 and g were intensively exposed and some of the fault f5 was replaced by two layers of flat holes and four inclined shafts of concrete. The lamprophyre dike X was replaced by three layers of concrete replacement holes and seven concrete replacement holes. Some of the left bank abutment was replaced by concrete cushion blocks at elevations of 1730 m to 1885 m, and three shearing resistant holes were set along the fault f42-9 at elevations of 1883 m, 1860 m, and 1834 m. Furthermore, five dowel holes were set up at elevations of 1829 m, 1785, m and 1730 m. In the right abutment, the concrete grooving replacement, the concrete grids, and the hole-plug replacement for the weak structural planes and the consolidation grouting were adopted as the main reinforcement measures. For example, five concrete inclined adits were adopted along the fault f13 at an elevation of 1601 m to the exposed place, and three layer flat concrete replacement holes and five concrete replacement deviated holes were used to reinforce the fault f14. According to the development of the fault f18 and the accompanying lamprophyre dike X, grooving replacement was used in the foundation surface near an elevation of 1580 m where f18 and X were intensively exposed. A diagram of the reinforcement measures is shown in Figure 3.

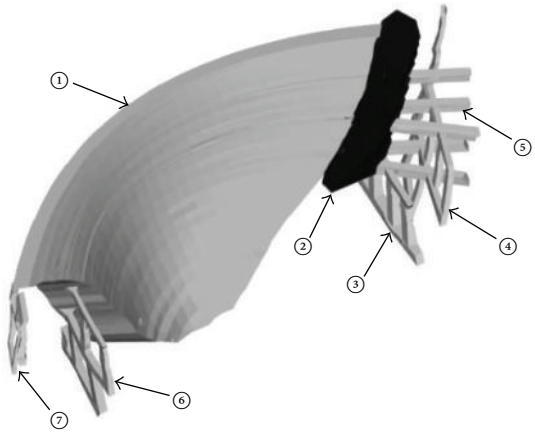

Figure 3: Schematic of the typical reinforcement measures used at the Jinping-I arch dam. ① The hyperbolic arch dam; ② the concrete seating replacement; ③ the concrete grids and hole-plug replacement for the fault f5; ④ the concrete grids and hole-plug replacement for the lamprophyre dike X; ⑤ the concrete shearing resistant holes; ⑥ the concrete grids and hole-plug replacement for the fault f14; ⑦ the concrete grids and hole-plug replacement for the fault f13.

4. Design of the 3D Geomechanical Model Test

4.1. Model Similarities and Mechanical Parameters of the Rock Masses and Structure Planes. A geomechanical model test is a type of destructive testing. According to the model similarity theory [28], the geomechanical model test must satisfy the following similar relationships: $C_\gamma = 1$, $C_\varepsilon = 1$, $C_f = 1$, $C_\mu = 1$, $C_\sigma = C_\varepsilon C_E$, $C_\sigma = C_E = C_L$, and $C_F = C_\sigma C_L^2 = C_\gamma C_L^3$. Here, C_E, C_γ, C_L, C_σ, and C_F are the deformation modulus ratio, the bulk density, the geometric ratio, the stress ratio, and the concentration force ratio, respectively. In addition, C_μ, C_ε, and C_f are Poisson's ratio, the strain, and the friction factor ratio, respectively. Combined with the practical engineering of the Jinping-I high arch dam, we selected a geometric ratio of $C_L = 300$, a bulk density of $C_\gamma = 1$, and model simulation dimensions of 4 m × 4 m × 2.83 m (river length × river width × height), which was equivalent to a region of 1200 m × 1200 m × 850 m in the prototype project. The load combination simulated in the test was performed based on the sum of the water pressure, the earth pressure, and the self-weight loads.

According to the physical and mechanical parameters of the arch dam concrete (the replacement concrete material), all types of rock masses, and the main structure plane materials provided by the designers, all types of physical and mechanical parameters can be obtained for the model materials by using a similarity relationship conversion. The main physical and mechanical parameters of the prototype and model materials are shown in Table 1.

4.2. Simulation of Rock Masses and Reinforcement Measures in the Dam Abutments and Foundation. In the geomechanical model test, the rock masses in the dam abutments and foundation were generally composed of small blocks of model materials that accurately simulated the nonlinear and multi-slit characteristics of the rock masses. Before the model test was performed, a large number of material tests were carried out based on the conversion of the mechanical parameters. The barite powder was the main material, and the high-grade engine oil was used as the cementing agent. They were mixed together at different proportions with additives to form the model material mixtures. Afterward, the model material mixtures were compressed using a BY −100 semiautomatic molding machine and became small blocks with dimensions of 10 cm × 10 cm × (5~7) cm (length × width × height).

In the geomechanical model, the arch dam, the left abutment concrete seating replacement, the concrete replacement, and other concrete materials were made from the mixtures of barite powder, gypsum, water, and small amounts of additives. The mixing proportions of the additives were selected according to the mechanical parameters of the model material. The model materials for the prototype concrete were molded according to the similarity relations.

4.3. Development of Temperature Analogous Materials for the Main Structural Planes. In this experiment, the main structural planes that affect the stability of the dam abutment were simulated, such as the faults f2, f5, f42-9, and F1, the lamprophyre dike X, the interlayer extrusion fault zone at the left-bank abutment, the faults f13, f14, and f18, and the greenschist lens at the right-bank abutment. To adopt the comprehensive test method and determine the influence of the main weak structural planes, a type of temperature-analogue material was developed to realize a gradually decreasing process of shear strength of the model material. Using this material, shear strength decreasing of the main faults f2, f5, f13, f14, and f18 and the lamprophyre dike X can be accurately controlled. The other structural planes were simulated using traditional model materials without adding polymer materials and additives and were produced by filling compaction with different thicknesses and mixing proportions. The mechanical parameters of the temperature-dependent analogous material are provided in Table 1. The relationships between shear strength and temperature were obtained using a series of shear tests, as shown in Figure 4. Prior to the test, the temperatures of the materials were calculated using the following equations: $\tau = 0.0001T^2 - 0.0177T + 1.131$ and $\tau = 0.0001T^2 - 0.1167T + 4.2714$. During the test, the shear strength of the temperature-analogue material was accurately reduced through a temperature control system.

When testing the shear strength indexes of the rock mass and the structural plane (f and c), we generally considered the combined effects of the shear strength as $\tau = f + c\tau = \sigma f + c$ because the friction factor ratio is $C_f = 1$ with a cohesion ratio of $C_c = C_\gamma \cdot C_L$ (where C_L is the geometric ratio and C_γ is the bulk density ratio). Thus, the modeled material cohesion c_m of conversion is very small, and the influences of cohesion c_m have often been neglected in previous experiments. Generally, the friction coefficient f_m of the geomechanical model material is smaller and the cohesion c_m is larger. Thus, the value of cohesion c_m is virtually increased, which greatly affects the test results.

Table 1: Main physical and mechanical parameters of the prototype and model materials.

Types of material	μ_p	E_p (10^3 MPa)	f_p	c_p (MPa)	μ_m	E_m (MPa)	f_m	c_m (MPa)
Arch dam concrete (natural foundation)	0.17	24	1.4	2.0	0.17	80.00	1.4	0.0067
Arch dam concrete (reinforcement foundation)	0.17	34	1.7	5.0	0.17	113.33	1.7	0.0167
Replacement concrete	0.17	31	1.5	3.5	0.17	103.33	1.5	0.0117
II class of rock mass	0.2	26.5	1.35	2	0.2	88.33	1.35	0.0067
III_1 class of rock mass	0.25	12	1.07	1.5	0.25	40.00	1.07	0.0050
III_2 class of rock mass	0.27	8	1.02	0.9	0.27	26.67	1.02	0.0030
IV_1 class of rock mass	0.3	3.5	0.7	0.6	0.3	11.67	0.7	0.0020
IV_2 class of rock mass	0.3	2.5	0.6	0.4	0.3	8.33	0.6	0.0013
V_1 class of rock mass	0.3	0.45	0.3	0.02	0.3	1.50	0.3	0.0001
Fault f2 (compressive zone g)	0.38	0.4	0.3	0.02	0.38	0.0013	0.3	0.0001
Fault f5	0.38	0.4	0.3	0.02	0.38	0.0013	0.3	0.0001
Fault f42-9	0.38	0.4	0.3	0.02	0.38	0.0013	0.3	0.0001
Lamprophyre dike X (fresh)	0.28	6.5	0.9	0.64	0.28	0.0217	0.9	0.0021
Lamprophyre dike X (weathering)	0.30	3.0	0.4	0.065	0.30	0.0100	0.4	0.0002
Fault f13	0.38	0.8	0.3	0.02	0.38	0.0027	0.3	0.0001
Fault f14	0.38	0.5	0.3	0.02	0.38	0.0017	0.3	0.0001
Fault f18	0.38	0.5	0.3	0.02	0.38	0.0017	0.3	0.0001
Greenschist lens	0.30	3.0	0.6	0.15	0.30	0.0100	0.6	0.0005

Note: ① μ, E, f, and c are Poisson's ratio, deformation modulus, friction coefficient, and cohesion, respectively; ② the subscript m represents a similarity model and the subscript p represents a prototype.

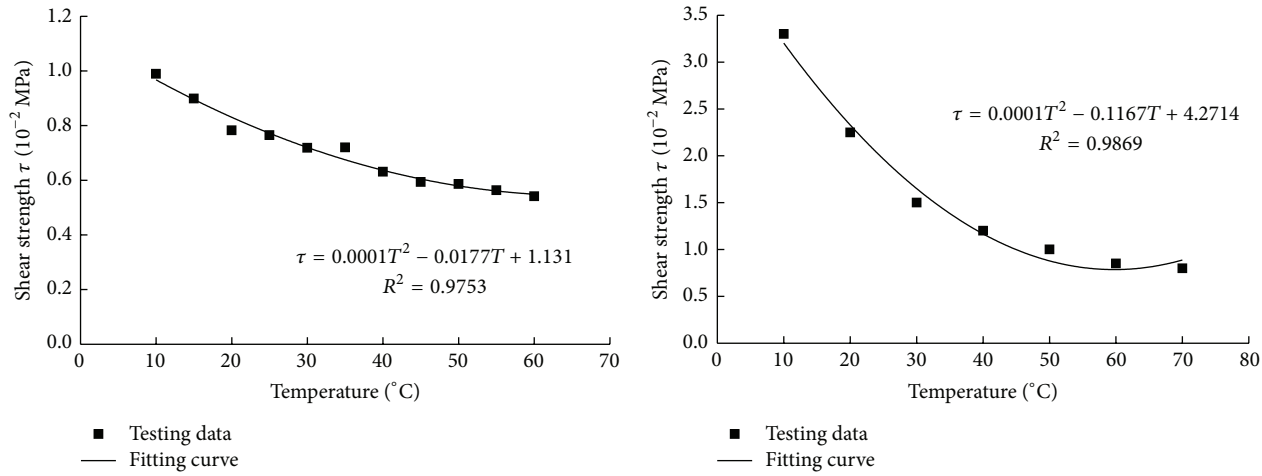

(a) Faults f2, f5, f13, f14, and f18 (faults fi)

(b) Lamprophyre dike X

Figure 4: Shear strength ~ temperature curve of the temperature analogous material.

If the combined effects of the two factors are considered by making the shear strength τ_m of the model material meet similar requirements, we will make the model results correspond more with practical engineering. Thus, in this 3D geomechanical model test of the Jinping-I high arch dam, the strength reduction stage test was conducted by considering the lower shear strength τ_m.

4.4. Model Construction. The geomechanical model was made of small masonry blocks. The position of the geological structures in the dam abutment and foundation was mainly dependent on the geological sliced figures, and the vertical and horizontal geological profiles determined the dip directions and dip angles. The model dam body and its reinforcement were placed and bonded to each other in

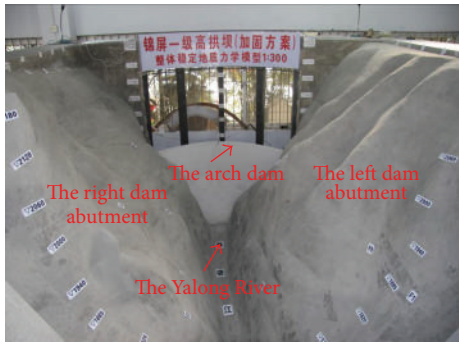

Figure 5: Photograph of the 3D geomechanical model of the Jinping-I arch dam.

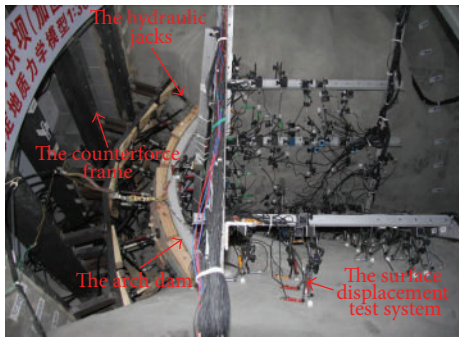

Figure 6: Arrangement of the loading system on the upstream surface of the model dam and the measurement system for the two dam shoulders.

steps. The internal relative displacement transducers and the temperature control system were installed during the model construction process. After the model was built, the model was refined according to the similarity scales. An overall view of the geomechanical model after completing the model refinement is shown in Figure 5.

4.5. Model Loading System. The load combination simulated in the test consisted of the water pressure, the earth pressure, and the self-weight load. Because the bulk density ratio $C_\gamma = 1$, the weights of the model and prototype materials are the same. In addition, the loading system applied the water pressure and earth pressure on the model dam through several layers of hydraulic jacks that were arranged on the upstream surface. By comprehensively considering the distributions of the water and earth pressures, the dimensions of the prototype dam, and the loading capacities of the loading system, the total load was divided into five layers. Meanwhile, the load of each layer was divided into several blocks. The calculated load on each block was applied at the block center using a servocontrolled hydraulic jack. The total load on the upstream surface of the model dam was divided into 24 blocks, and the loads were applied using 24 jacks. Several load-spreading boards were used to eliminate concentrated stress. A photograph of the loading system on the upstream surface of the model dam is shown in Figure 6.

4.6. Model Measurement System. In this model test, the requirements of the measurement data are mainly for the surface displacement and strain of the dam, surface displacement of the dam shoulders, and relative displacement of the internal structural planes in the abutment rock masses. Overall, 13 two-way or three-way deflection surface displacement measuring points for the downstream face of the dam were arranged at the elevations of 1880 m, 1830 m, 1750 m, 1670 m, and 1620 m to monitor the radial, tangential, and vertical displacements of the dam surface. 28 displacement transformers were installed to monitor the surface displacement and their data were collected by a SP-10A digital displacement measuring instrument. The arrangement of the surface deformation monitoring points on the downstream face is shown in Figure 7.

Overall, 15 strain measuring points were arranged on the downstream face of the model dam at the elevations of 1880 m, 1830 m, 1750 m, 1670 m, and 1620 m on the arch crown and arch abutment. Three resistance strain gauges were installed at every point to form a strain rosette. The strains at 0° direction (horizontal), 45° direction and 90° direction (vertical) were measured continuously using a UCAM-8BLuniversal digital testing device.

The surface displacements of 56 displacement monitoring points at the left and right dam abutments and the reinforcements were measured. To be specific, 33 measuring points were arranged on the left bank and 23 were arranged on the right bank. For every measurement point, the displacements of two opposite directions were automatically recorded by a SP-10A digital displacement measuring instrument. Therefore, there were a total of 112 displacement transformers. The arrangement of the surface displacement monitoring points of the left and right abutments and the reinforcements is shown in Figure 8.

Meanwhile, 88 relative displacement transducers were installed at the faults f13, f14, f18, f2, f5, f9, and F1, the lamprophyre dike X, the greenschist lens, and the SL15 deep cracks and at other weak structural planes to monitor the internal movement along the structures. Their readings were collected by a UCAM-8BL universal digital testing device.

5. Analysis of the Test Results

The 3D geomechanical model test was conducted for the Jinping-I high arch dam under reinforcement foundation conditions. First, a very small preloading was applied on the model dam. The normal load was applied afterward and remained constant. In the next stage, the shear strengths of the main structural planes were decreased gradually by heating the temperature analogous materials of the faults f2 and f5, the lamprophyre dike X in the left bank, and the faults f13, f14, and f18 in the right bank. The heating process was divided into six steps (from T1 to T6). The highest temperature was 50°C, which made the shear strength of the main structures reduce by approximately 30%. Then, the temperature level was maintained, and the loading was increased in stages using loading steps of 0.2~0.3 P (P is the design water pressure) until the model dam and foundation failed. During the test,

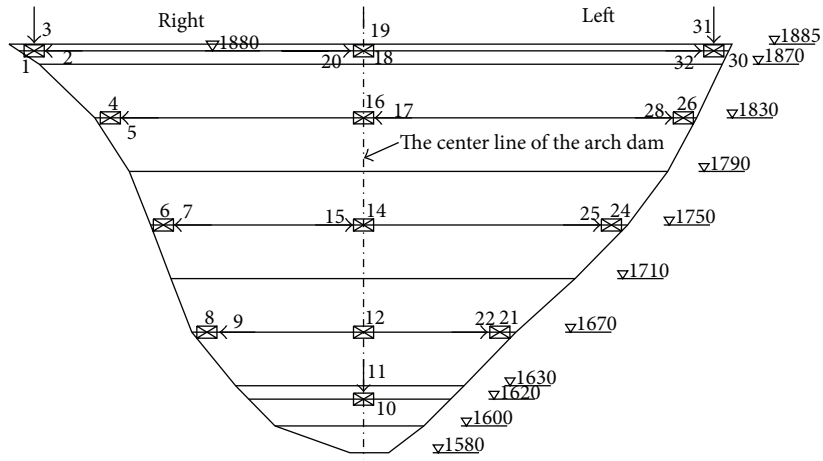

↓ represents the vertical displacement measuring point; the vertical upward deformation has a positive value.
⊠ represents the radial displacement measuring point; the downstream deformation has a positive value.
⟶ represents the tangential displacement measuring point; the deformation point to the left has a positive value.
10 represents the serial number of the deformation measuring point; total 28 displacement meters were installed.

Figure 7: Arrangement diagram for the surface deformation monitoring points of the downstream face of the arch dam.

the surface displacements, the internal displacements, and the strains of the geomechanical model were collected continuously. The monitoring data obtained in the test include the following: (a) the distributions of surface displacements of the dam structure and their development curves; (b) the distributions of surface displacements of the two abutments and the reinforcements and their development curves; (c) the distributions of relative displacements of the main faults, the lamprophyre dike and the weak structural zones in the dam foundation, abutment and reinforcements, and their development curves; and (d) the strain development curves of the model dam at typical heights. The failure processes and failure patterns of the abutment and the reinforcements were observed. The main results are presented and discussed as follows.

5.1. Analysis of the Displacements. The distribution characteristics of the dam displacement can be summarized as follows. (a) Under the normal or work load conditions, the dam displacements were almost symmetric. The maximum radial displacement was 80 mm (prototype value), which occurred at an elevation of 1880 m on the arch crown. (b) During the strength reduction phase and at the beginning of overloading, the dam displacements were small and the displacements of the left arch and right arch were still symmetric. (c) As the overloading increased, certain asymmetric displacements appeared, especially after K_2 = 4.0~4.6. The deformations at the left end of the arch obviously increased, and the displacements at the left end of the arch were slightly larger than the right arch. The left and right sides of the tangential displacement of the arch were roughly equal to each other throughout the loading process. The typical displacement curves are shown in Figure 9.

Many of the displacement curves indicate the following. (a) Under the normal load conditions with an overloading coefficient of K_2 = 1.0, the dam displacement was small. (b) During the strength reduction phase, the dam displacement curves slightly fluctuated, but the change was minor. (c) During the overloading phase, the deformation of the dam body gradually increased as the overload coefficient increased. (d) After the overload coefficient increased to 4.0~4.6, the slope of the displacement curves sharply changed, and the development of the displacements was accelerated. (e) When the overloading coefficient K_2 = 7.0~7.6, the dam deformation was very large, and the model arch dam and foundation had the tendencies of overall instability.

The distribution characteristics of surface displacements on the dam abutment and reinforcements can be summarized as follows. (a) The deformations near the end of the arch and near the exposed place of the lamprophyre dike X were generally larger than other areas. The deformation gradually decreased with the distance to the arch end. The typical displacement curve of the abutment is shown in Figure 10. Under normal load conditions and in the strength reduction phase, the surface displacements of the abutment and reinforcements were small, and the displacements of the left and right abutments were symmetrical. (b) During the overloading phase and before K_2 reached 4.0~4.6, the displacement gradually increased in a small magnitude. (c) After the overloading coefficient K_2 reached 4.6, the deformation of the abutment significantly increased as the overloading increases. This phenomenon indicates that large plastic deformation gradually occurred in the abutments and reinforcements. The displacements of the right bank were slightly larger than the left bank. Most of the displacement curves show an obvious turning point or a reduced slope between the overloading coefficients of K_2 = 4.0~4.6. When K_2 = 5.0~6.0, the slopes of the deformation curves further increased. (d) When K_2 = 7.0~7.6, the deformation of the abutment rock mass was very large. The surface cracks of

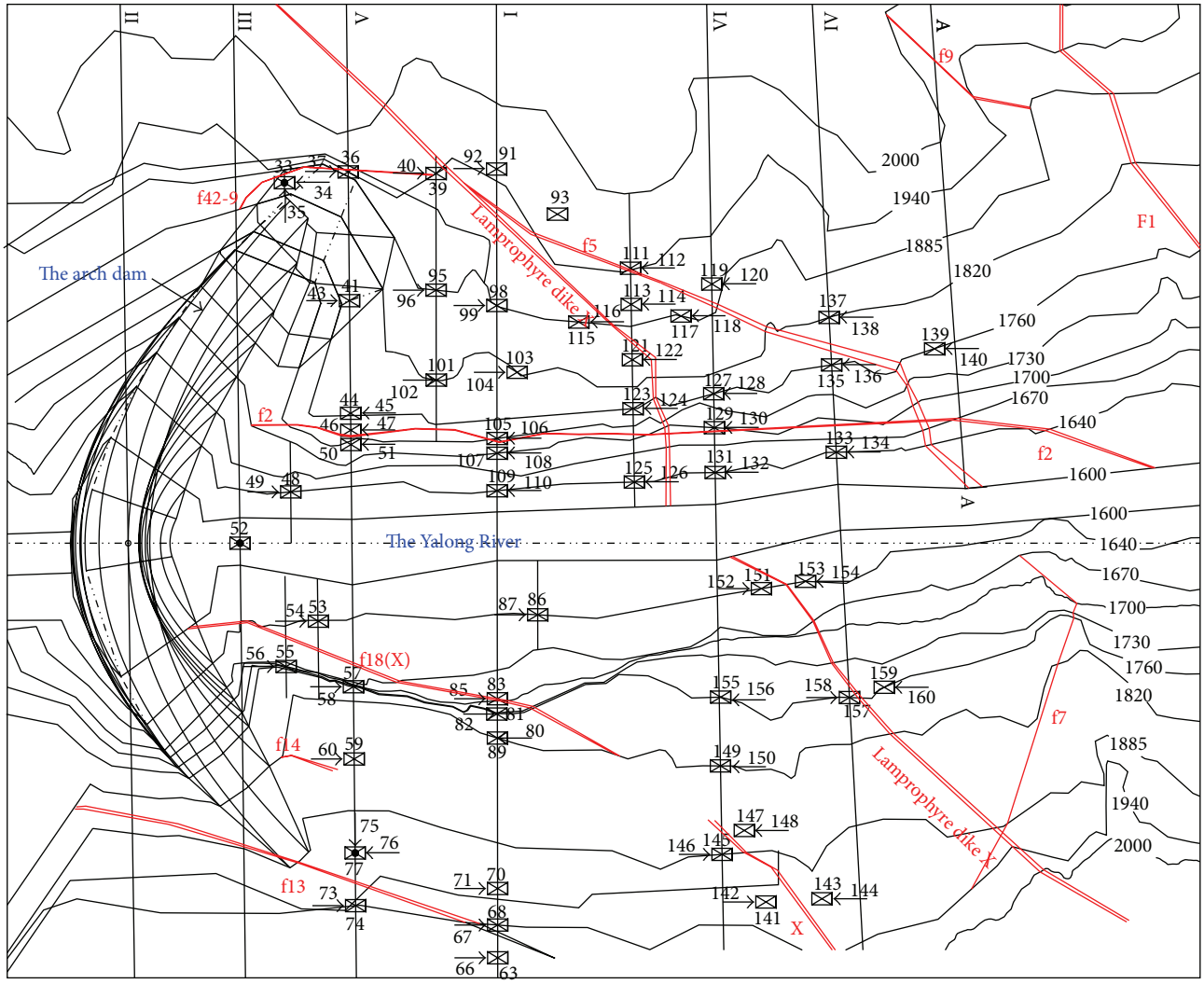

⟷ represents the displacement measuring point along river; the downstream deformation has a positive value.
⊠ represents the lateral displacement measuring point; to the river center deformation has a positive value.
40 represents the serial number of the deformation measuring point; total 112 displacement meters were installed.

Figure 8: Arrangement diagram for the surface deformation monitoring points of the left and right dam abutments.

the rock mass gradually propagated and connected with each other, and the abutment exhibited overall instability tendencies.

5.2. Analysis of Failure Processes and Failure Patterns. According to the observations, cracking of the model dam initiated at the dam heel when the overloading coefficient was K_2 = 1.4~1.6. When K_2 = 2.6~2.8, the abutment rock mass began to crack near the arch end of the dam crest at the faults f42-9 and f13. In addition, the fault f18 was exposed at its middle-lower portion. When K_2 = 4.0~4.6, the large deformation stage of the model dam was reached. The cracks of the two abutments increased and the dam heel crack significantly propagated and connected from the left to right. More and more cracks appeared and extended at the faults f42-9, f5, f2, f13, f14, and f18 and the lamprophyre dike X. The surface cracks increased in the middle portions of the two abutments and in the rock mass on the right bank near the dam crest. When K_2 = 7.0~7.6, the surface cracks in the left and right abutment rock masses were mutual intersections and were connected with each other. In addition, the model dam, the dam shoulder reinforcements, and weak structural planes demonstrated plastic instability. The final failure patterns of the model under the reinforcement foundation conditions are shown in Figures 11 and 12.

From the observations of the failure patterns, the following conditions are known. (a) After reinforcement, the final failure zones in the right abutment were mainly located in the triangle area from the fault f18 to the dam crest. This pattern mainly resulted from the interactions of cutting faults and steep dip cracks in the SN direction. Greenschist lenses were deposited in the middle portions of the right abutment,

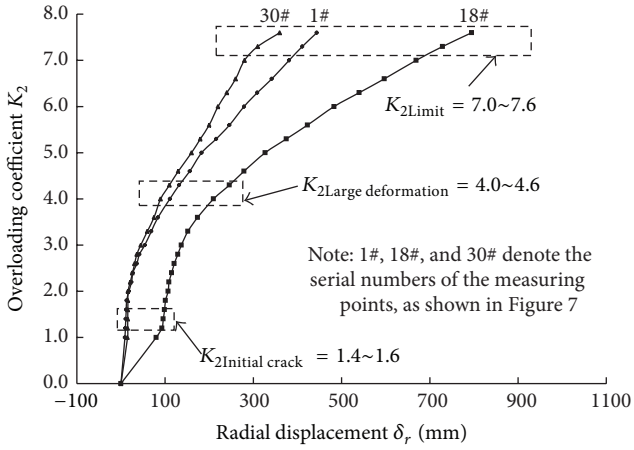

Figure 9: δ_r~K_2 relation curves regarding the radial displacement downstream at an elevation of 1880 m on the arch ring and the overloading coefficient.

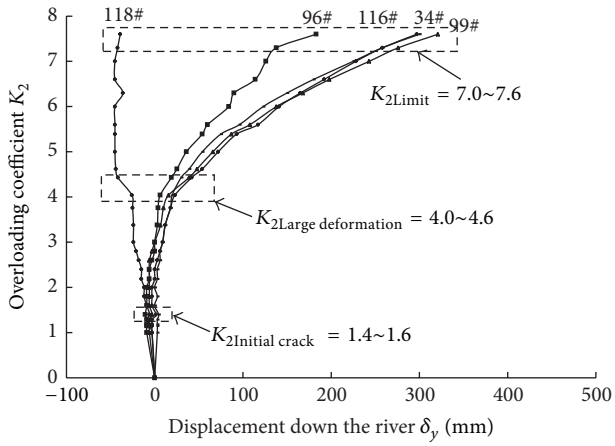

Figure 10: δ_y ~ K_2 relation curves regarding the deformation down the river at an elevation of 1885 m in the left bank and the overloading coefficient. Note: 34#, 96#, 99#, 116#, and 118# denote the serial numbers of the measuring points, as shown in Figure 8.

resulting in successive cracking at the faults f13, f14, and f18. The cracks in the rock masses expanded continuously in the steep dip direction of the fracture with mutual intersection and connectivity of the faults. (b) The final failure pattern of the left abutment is that the abutment significantly cracked along the structural planes of the faults f42-9, f5, and f2 and the lamprophyre dike X. These cracks were mainly due to the complex geological conditions of the left bank.

5.3. Analysis of the Overall Stability Safety Factor. Based on the geomechanical model tests, comprehensive evaluation of the overall stability and determination of the safety of the dam and foundation can be conducted based on the following five results: the surface displacement curves and strain curves of the dam body, the surface displacement curves of the reinforcements of the two dam shoulders, the internal relative displacement curves of the weak structural

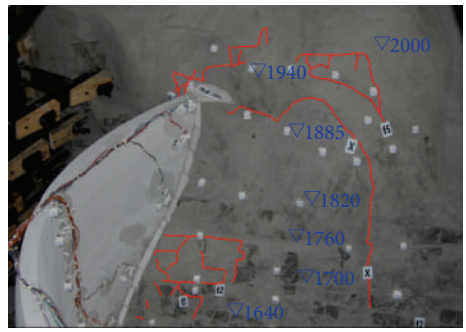

Figure 11: Failure patterns of the left abutment (K_2 = 7.6). Note: the red lines show the cracks in the model.

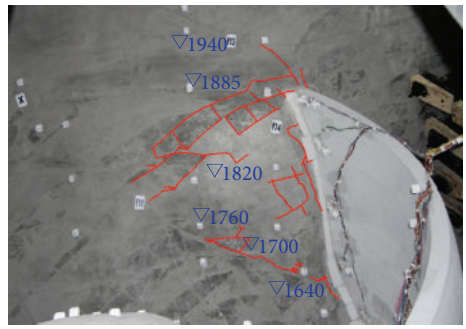

Figure 12: Failure patterns of the right abutment (K_2 = 7.6). Note: the red lines show the cracks in the model.

planes in the abutment rock masses, the observations of the deformation process and failure patterns of the abutments and the reinforcements, and the strength reduction magnitudes. According to the characteristics of the displacement curves, we can determine the strength reduction coefficient K_1 and the overloading coefficient K_2 of the arch dam and foundation. From the theory of the comprehensive test method, the comprehensive safety degree K_c can be represented as $K_c = K_1 \times K_2$.

The comprehensive analysis based on the information and results obtained from this experiment indicate that the Jinping-I high arch dam has a strength reduction coefficient of K_1 = 1.3 and an overloading coefficient of K_2 = 4.0~4.6. Thus, the comprehensive degree of safety of the Jinping-I high arch dam under reinforced foundation conditions should be $K_c = K_1 \times K_2$ = 5.2~6.0.

6. Conclusions

In this paper, a stability evaluation system for high arch dams based on deformation monitoring data obtained in comprehensive tests of geomechanical models was proposed. This method was used to investigate the overall stability of the Jinping-I high arch dam. Based on theoretical analysis and experimental investigations, the following conclusions were drawn.

(1) According to the basic principles of the three destructive test methods of geomechanical models and the basic concepts of point safety factors, an approach to assess the

stability and safety of dams was established based on the comprehensive geomechanical model test method.

(2) The stability evaluation system is presented based on the deformation monitoring data and the deformation-overloading coefficient curves. Based on the catastrophe theory and engineering practices, the second inflection point of the deformation curve is used to evaluate the stability of the model dam. An overloading coefficient $K_{2\text{Large deformation}}$ that corresponds to this inflection point is proposed. These results provide a theoretical basis for the comprehensive test method of geomechanical models.

(3) Using the comprehensive test method, a 3D geomechanical model test of the Jinping-I high arch dam under reinforced foundation conditions was conducted. During this test, the deformation characteristics, failure patterns, and mechanisms of the dam abutment and foundation were captured. The safety evaluation based on the experimental results indicates that the stability safety factors of the dam abutment and foundation range from 5.2 to 6.0. These research results have been applied in engineering. The proposed stability evaluation system in the context can be helpful for similar complex high arch dam projects.

Conflict of Interests

The authors declare that there is no conflict of interests regarding the publication of this paper.

Acknowledgments

This work was financially supported by the National Natural Science Foundation of China (nos. 51109152, 51379139, and 51409179) and Open Fund of State Key Laboratory of Hydraulics and Mountain River Engineering (Grant no. SKLGP2012 K011).

References

[1] J. Z. Pan and J. He, *Fifty Years of Chinese Dam*, China Water Power Press, Beijing, China, 2000, (Chinese).

[2] P. Bukenya, P. Moyo, H. Beushausen, and C. Oosthuizen, "Health monitoring of concrete dams: a literature review," *Journal of Civil Structural Health Monitoring*, vol. 4, no. 4, pp. 235–244, 2014.

[3] E. Fumagalli, *Statical and Geomechanical Models*, Springer, New York, NY, USA, 1973.

[4] X. H. Chen, *Structure Model Test for Brittle Material*, Water Resources and Electric Power Press, Beijing, China, 1984 (Chinese).

[5] X.-L. Yang, Z.-B. Wang, J.-F. Zou, and L. Li, "Bearing capacity of foundation on slope determined by energy dissipation method and model experiments," *Journal of Central South University of Technology*, vol. 14, no. 1, pp. 125–128, 2007.

[6] L. Zhang, B. Q. Yang, Y. Chen, C. Q. Hu, and J. H. Dong, "Measurement technology of structural plane displacement in deep sliding stability test of gravity dam," *China Science Paper*, vol. 9, no. 5, pp. 543–547, 2014 (Chinese).

[7] W. Huang and J. Chen, "Development of the internal displacement meter and the displacement observation automation used in structure model test," *Yangtze River*, vol. 6, pp. 19–20, 1997 (Chinese).

[8] H. H. Zhu, J. H. Yin, J. H. Dong, and L. Zhang, "Physical modelling of sliding failure of concrete gravity dam under overloading condition," *Geomechanics and Engineering*, vol. 2, no. 2, pp. 89–106, 2010.

[9] H.-H. Zhu, J.-H. Yin, L. Zhang, W. Jin, and J.-H. Dong, "Monitoring internal displacements of a model dam using FBG sensing bars," *Advances in Structural Engineering*, vol. 13, no. 2, pp. 249–261, 2010.

[10] W. S. Zhu, Q. B. Zhang, H. H. Zhu et al., "Large-scale geomechanical model testing of an underground cavern group in a true three-dimensional (3-D) stress state," *Canadian Geotechnical Journal*, vol. 47, no. 9, pp. 935–946, 2010.

[11] H. H. Zhu, A. N. L. Ho, J. H. Yin, H. W. Sun, H. F. Pei, and C. Y. Hong, "An optical fibre monitoring system for evaluating the performance of a soil nailed slope," *Smart Structures and Systems*, vol. 9, no. 5, pp. 393–410, 2012.

[12] S. C. M. Ho, L. Ren, H.-N. Li, and G. Song, "A fiber Bragg grating sensor for detection of liquid water in concrete structures," *Smart Materials and Structures*, vol. 22, no. 5, Article ID 055012, 2013.

[13] T. Guo, F. Liu, B.-O. Guan, and J. Albert, "Polarimetric multimode tilted fiber grating sensors," *Optics Express*, vol. 22, no. 6, pp. 7330–7336, 2014.

[14] C. Piao, J. Yuan, D. Wang, and P. Li, "A study on distribution measurement and mechanism of deformation due to water loss of overburden layer in vertical shaft," *Journal of Sensors*. In press.

[15] W. Y. Zhou, R. Q. Yang, and G. R. Yan, "Stability analysis system for large dams," *Chinese Journal of Rock Mechanics and Engineering*, vol. 16, no. 5, pp. 424–430, 1997 (Chinese).

[16] W. Zhou, R. Yang, Y. Liu, and P. Lin, "Research on geomechanical model of rupture tests of arch dams for their stability," *Journal of Hydroelectric Engineering*, vol. 24, no. 1, pp. 53–64, 2005 (Chinese).

[17] Y. R. Liu, F. H. Guan, Q. Yang, R. Q. Yang, and W. Y. Zhou, "Geomechanical model test for stability analysis of high arch dam based on small blocks masonry technique," *International Journal of Rock Mechanics and Mining Sciences*, vol. 61, pp. 231–243, 2013.

[18] L. Zhang, Y. R. Liu, and Q. Yang, "Evaluation of reinforcement and analysis of stability of a high-arch dam based on geomechanical model testing," *Rock Mechanics and Rock Engineering*, 2014.

[19] M. Peng, X. Y. Li, D. Q. Li, S. H. Jiang, and L. M. Zhang, "Slope safety evaluation by integrating multi-source monitoring information," *Structural Safety*, vol. 49, pp. 65–74, 2014.

[20] L. Zhang, Y. Chen, B. Q. Yang, J. Y. Chen, and C. Q. Hu, "A comprehensive testing method for global stability analysis of high arch dams," *Joumal of Rock Mechanics and Geotechnical Engineering*, vol. 4, no. 1, pp. 73–81, 2012.

[21] C. G. Li and L. Zhang, "Application of poikilothermic-similar material in structural model test," *Design of Hydroelectric Power Station*, vol. 11, no. 2, pp. 1–6, 1995 (Chinese).

[22] W.-P. Fei, L. Zhang, and R. Zhang, "Experimental study on a geo-mechanical model of a high arch dam," *International Journal of Rock Mechanics and Mining Sciences*, vol. 47, no. 2, pp. 299–306, 2010.

[23] Y. Chen, L. Zhang, G. X. Yang, J. H. Dong, and J. Y. Chen, "Anti-sliding stability of a gravity dam on complicated foundation with multiple structural planes," *International Journal of Rock Mechanics & Mining Sciences*, vol. 55, pp. 151–156, 2012.

[24] L. Zhang and J. Y. Chen, *The Engineering Application of Model Test about Hydraulic Dams and Foundation*, Sichuan University Press, Chengdu, China, 2009.

[25] N. H. Ru and Z. S. Jiang, *Arch Dams—Accident and Safety of Large Dams*, China Waterpower Press, Beijing, China, 1995 (Chinese).

[26] T. F. Bao, M. Xu, and L. Chen, "Stability analysis of concrete gravity dam foundation based on catastrophe model of plastic strain energy," *Procedia Engineering*, vol. 28, pp. 825–830, 2012.

[27] X. T. Ding, C. S. Gu, and Y. Jiang, "Analysis of stability of high arch dams based on FEM and catastrophe theory," *Journal of Hohai University (Natural Sciences)*, vol. 36, no. 2, pp. 175–178, 2008.

[28] X. S. He, H. Q. Ma, L. Zhang, and J. Chen, "Study of test method of geomechanical model and temperature analogous model material," *Chinese Journal of Rock Mechanics and Engineering*, vol. 28, no. 5, pp. 980–986, 2009 (Chinese).

Hindawi Publishing Corporation
Journal of Sensors
Volume 2015, Article ID 139695, 11 pages
http://dx.doi.org/10.1155/2015/139695

Research Article

Structural Health Monitoring of Wind Turbine Blades: Acoustic Source Localization Using Wireless Sensor Networks

Omar Mabrok Bouzid,[1] Gui Yun Tian,[2] Kanapathippillai Cumanan,[3] and David Moore[4]

[1] *Faculty of Engineering, Al-Jabel Al-Garbi University, Gharian, Libya*
[2] *School of Electrical and Electronic Engineering, Newcastle University, Newcastle upon Tyne NE1 7RU, UK*
[3] *Department of Electronics, University of York, York YO10 5DD, UK*
[4] *School of Engineering and the Built Environment, Glasgow Caledonian University, Cowcaddens Road, Glasgow G4 0BA, UK*

Correspondence should be addressed to Omar Mabrok Bouzid; drombouzid@gmail.com

Received 4 August 2014; Revised 14 December 2014; Accepted 15 December 2014

Academic Editor: Xiaowei Ye

Structural health monitoring (SHM) is important for reducing the maintenance and operation cost of safety-critical components and systems in offshore wind turbines. This paper proposes an *in situ* wireless SHM system based on an acoustic emission (AE) technique. By using this technique a number of challenges are introduced due to high sampling rate requirements, limitations in the communication bandwidth, memory space, and power resources. To overcome these challenges, this paper focused on two elements: (1) the use of an *in situ* wireless SHM technique in conjunction with the utilization of low sampling rates; (2) localization of acoustic sources which could emulate impact damage or audible cracks caused by different objects, such as tools, bird strikes, or strong hail, all of which represent abrupt AE events and could affect the structural health of a monitored wind turbine blade. The localization process is performed using features extracted from aliased AE signals based on a developed constraint localization model. To validate the performance of these elements, the proposed system was tested by testing the localization of the emulated AE sources acquired in the field.

1. Introduction

Offshore wind turbines are often situated in remote areas which are difficult to reach. Faults can cause significant downtime and are often costly to address. In order to meet these challenges turbines are being combined with structural health monitoring (SHM) systems for continuous online health monitoring. This form of monitoring helps in detecting abnormal changes in structural health so that prompt maintenance can be carried out. It also enables engineering inspectors to easily monitor turbines from off-site locations without any safety risks [1, 2]. Incorporating SHM techniques in many applications ranging from civil to engineering applications such as bridges [3, 4] and wind turbines provides significant advantages. These include minimizing operation and maintenance costs as well as the ability to collect information and data for future design and optimisation of blades. However, for wind turbine blades, using these techniques has some associated challenges due to the remote location of the turbines and the accessibility to them during extreme weather conditions. *In situ* monitoring approaches for wind turbines play a key role in addressing those challenges as they can help in detecting faults while the turbines are in operation, allowing appropriate action to be taken in time to avoid further damage or failure.

Recently, there have been some attempts to extend laboratory methods as *in situ* monitoring systems while the blades are static and in service [5–10]. These *in situ* techniques show potential for wind turbine blade inspection. Nevertheless, such techniques may be costly, time-consuming, relying on regular inspection intervals, and needing to be supervised by an operator which makes them impractical for offshore wind turbines. In contrast, wireless passive inspection techniques could be a more appropriate solution for providing an *in situ* monitoring. The main reasons for this are that a large number of wind farms are being placed in remote areas, and the size of the turbines has become physically larger. These factors make their transportation and reaching them for inspection very

difficult. Thus, the selection of suitable passive techniques and the integration of several different technologies are important to develop a robust continuous online SHM system [11].

This has motivated the proposal of an *in situ* SHM system for wind turbine blades based on the integration of wireless sensor networks (WSNs) and acoustic emission (AE) technology. AE is a passive technique that can be applied to locate and assess complex composite structures [12]. For wind turbine blade, the AE allows the investigation of defects in their structure under wind load while the wind turbine is in service. In addition, most types of blade failure cause detectable AE waves, including crack initiation and growth and crack opening as well as closure [13].

WSNs also provide an ideal means for sending AE sensing data to a remote control unit. The integration of these two technologies in this application, however, faces several challenges. The large size of the wind turbine blades requires the deployment of a considerable number of AE sensors to achieve full blade coverage. It is also necessary that the proposed system should be able to sense the condition of the blades' structure all of the time. Such conditions lead to the generation of enormous amounts of sensing data which would overload the resources of WSNs in terms of data transmission and memory space.

Thus, the monitoring system proposed in this paper is employed in conjunction with the novel concept of utilizing low sampling rates in acquiring acoustic signals, discussed in [14], so that a significant reduction of data can be achieved during the monitoring process of wind turbine blades. In [15], the novelty of using such system in monitoring environmental conditions using different AE features extracted from the aliased versions on-board has been validated. This paper aims to use AE features such as arrival time and peak amplitude also extracted from the aliased versions on-board for locating AE sources. To the authors' knowledge, no *in situ* wireless SHM system for wind turbine blades has yet been developed with use of low sampling rates below the Nyquist criterion to locate AE sources. The proposed system is validated using the *in situ* wireless system deployed on wind turbine blades. The main contributions of this paper are as follows:

(i) Through the implementation of an *in situ* SHM system on a 300 W wind turbine installed at Newcastle University, the concept of utilizing low sampling rates in the acquisition operation of AE signals has been evaluated in a real world scenario.

(ii) The use of features extracted from aliased AE signals to localize emulated AE sources in conjunction with a localization model developed for the complex structure of wind turbine based on a constraint geometrical point localization technique. To validate the performance, the proposed system has been tested and precise source localization results have been achieved.

The paper is structured as follows. In Section 2, source localization methods using low sampled data are discussed for locating artificial AE sources on wind turbine blades. The *in situ* wireless SHM system for monitoring wind turbine blades is discussed in Section 3. Section 4 presents the strategies of acquiring AE events and AE feature extraction when performing field studies. In Section 5, the results of AE source localization at low sampling rates are presented. Finally, conclusion is laid out in Section 6.

2. Source Localization on Wind Turbine Blades

Acoustic source localization using WSNs has a number of possible applications, including intruder detection, sniper localization [16]. Wang et al. [17] and Saric et al. [18] present an overview of such wireless localization systems with detailed analyses and characterisations of typical source localization algorithms in WSNs. In [19], a PZT-based wireless system for composite impact monitoring is proposed to give a localized search area for further inspection. The wireless AE source localization technique, proposed in the course of this paper, is intended to be used for SHM of wind turbine blades. It differs from work in the aforementioned studies in the sense that it utilises aliased versions of AE signals instead of the original signals in the localization process. Therefore, the results presented in [17–19] would not be appropriate for a fair comparison.

In contrast to the work presented in [20], the calculations of localization features such as arrival time and peak amplitude are locally extracted by the individual acoustic wireless units. These features are then transferred to the control unit where they are assembled and fused to estimate the location of AE events.

A line-of-sight localization is conducted in order to measure the velocity with which AE signals propagate in the wind turbine blades. In addition, it is used to verify the possibility of locating AE events based on their arrival times extracted by the individual wireless units from the aliased versions. The wind turbine blade is made of carbon fibre and artificial AE events are generated by hitting the blade with a metallic ball at known positions between the sensors. The ball has a diameter of 9 mm and a mass of 3 g.

It is important for the experiments conducted that the AE events are traced in order to specify the active zone or blade (i.e., the damaged blade). This is useful so that more attention can be given to that particular zone or blade. This can be done by a zonal localization, where each blade is assigned to an AE wireless unit and via a comparison between the maximum amplitudes of AE signals received at the wireless units, the active blade can be specified. To trace the active region within a large structure of wind turbine blade (i.e., in two-dimensional position), AE wireless units can be spaced apart on the blade and AE sources can be assumed to be within a region and less than halfway between the wireless units. In this case, methods explained in [21] can be applied to trace the AE source. In this paper, the zonal localization is used to specify the active blade, and the results of this localization are presented in Section 5. Constraint geometrical point location technique is used to pinpoint precisely the AE source based on the arrival time and the predetermined sound velocity (v).

Due to the small size of the 300 W wind turbine used in this study, a combination of zonal and constraint geometrical

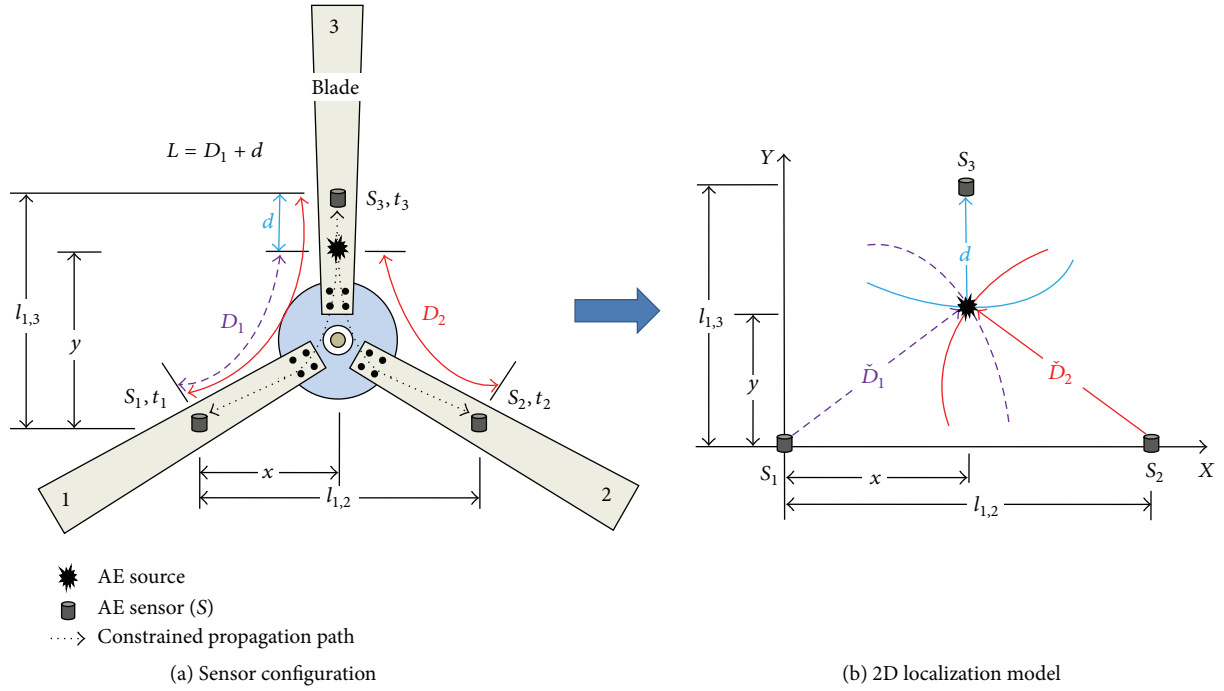

FIGURE 1: Proposed configuration of acoustic wireless units and 2D model: x and y are the unknown coordinates of AE source, t_i is the arrival time of AE signal at AE sensor S_i, d is the distance between S_3 and the AE source, and $l_{1,3}$ and $l_{1,2}$ are the approximated distances between S_1 and S_3 as well as S_1 and S_2, respectively.

point localization is implemented as shown in Figure 1(a). To apply this localization technique to the wind turbine blades, a model of 2D localization needs first to be developed. To achieve this, AE sensors are assumed to be configured as shown in Figure 1(a). In this configuration, it is also assumed that the AE sensors are located in a 2D plane and the AE signals generated propagate in constrained paths along the blades as denoted by dashed lines. In Figure 1(a), D_1 and D_2 represent the shortest paths which will be taken by the AE signals in order to reach the AE sensors S_1 and S_2, respectively.

Based on the configuration shown in Figure 1(a) and abovementioned assumptions, a 2D model is derived as shown in Figure 1(b) where the shortest paths D_1 and D_2 are approximated by $\check{D}_1$ and $\check{D}_2$, respectively. In this case, the basic principle of constraint geometrical point localization, explained in [22], is used to estimate the unknown coordinates of the AE source, x and y, which are indicated by the intersection of hyperbolas which are not shown in this figure. The arrival time features of aliased AE signals are calculated using the first threshold crossing. This method is applied in conjunction with the extracted envelope to overcome the ambiguity caused by utilizing low sampling rates. It also leads to enhancing the detection accuracy of the arrival times of the captured aliased AE versions.

A simple time synchronization procedure is applied to overcome the drift in the clocks of the wireless units in which the wireless units time-stamp the arrival of a start sample command based on local times of the individual wireless units, which is denoted by t_{bi}. These times are affected by the drift in the individual clocks. Thus, to overcome such a drift these timestamps are converted to a global time according to the relation: $global\ arrival\ time = (t_i - t_{bi})$, where t_i is the local arrival time of the detected AE signal at each wireless unit and $i \in (1, 2, 3)$. A sequence of line-of-sight measurements has been conducted, as discussed above, in order to test the robustness of this method, in which the arrival times were calculated with and without using the global arrival time relation.

By comparing the results obtained from both cases, it has been found that using the above mentioned relation of global arrival time reduces the time synchronization errors from 46.33 μs to 1.55 μs which represents an average improvement of 96.65% according to the setting of the experiments conducted. The reason behind this enhancement is that the use of the global time instead of the local time minimises the effect of the drift in the clocks of the individual wireless units.

Such an improvement will have a positive impact on both velocity and localization measurements. Based on detected arrival times t_1 and t_2 of the detected AE signals, a calibration method is used to measure the velocity of wave propagation (v) using the relation: $v = L/(t_2 - t_1)$, where L is the known distance between the two AE sensors (i.e., wireless units). Due to the short length of the blade used, only a small number of measurements are conducted. However, to show the robustness and repeatability of these measurements, each one is repeated a number of times and the results are discussed in Section 5.

The proposed approach is examined by conducting several experiments to locate AE sources produced at a known

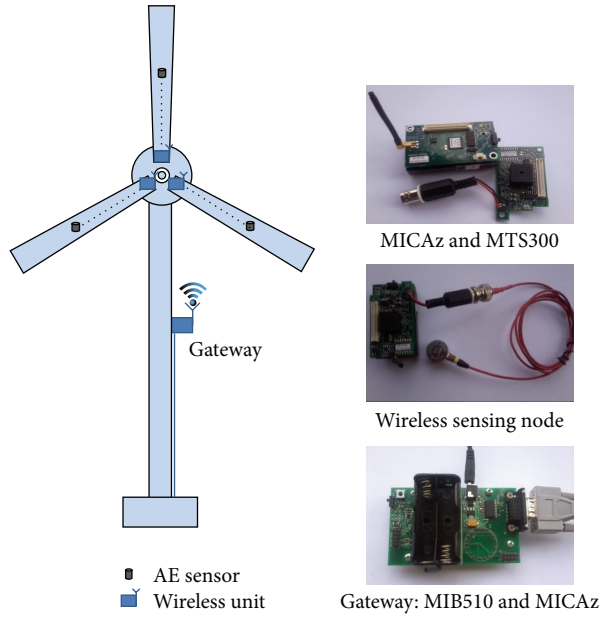

(a) System deployment

(b) Hardware components used

Figure 2: Wireless monitoring network installed on the top of a 300 W wind turbine.

location on blades by artificial AE events produced via hitting the blades with a plastic stick which has a diameter and length of 15 mm and 500 mm, respectively. The intention of using such sound sources, instead of using pencil break test with graphite lead, is to emulate impact damage or audible cracks caused by different objects such as tools, bird strikes, or strong hail. The results of these experiments are discussed in Section 5. Next, the wireless SHM setup is discussed.

3. *In Situ* Wireless SHM System for Wind Turbine Blades

3.1. Components of Wireless Sensing Node. The development of the *in situ* SHM system takes advantage of wireless technology to form a monitoring network. This system is comprised of MICAz motes equipped with the sensor board (MTS310) which are used in developing the wireless system, as shown in Figure 2. MICAz motes represent one of the low-cost current state-of-the-art sensor technologies that provide capabilities to build wireless networks [23]. The MICAz is 2.4 GHz, IEEE/ZigBee 802.15.4 boards equipped with 4 KB of RAM. At the centre of the mote is the processing core which contains function modules for data collection, processing, and communication control. The MPR2400 is based on the Atmel ATmega128L and capable of running at speeds up to 7.3 MHz. This mote also supports a 10-bit analogue to digital converter with 8 channels and 0–3 V input range.

The omnidirectional microphone sensor of the MTS310 board is replaced by a BNC connector for AE sensors, as shown in Figure 2(b). The AE sensor is the BII-7070 from "Benthowave Instrument Inc." (http://www.bentho-wave.com/) and operates at a usable frequency range of 0.1 Hz to 400 kHz with a size of $\Phi \times L = 18.6 \times 20$ mm. It is characterised by a relatively small mass and low cost.

All of the sensing units communicate with a PC base station via a radio-frequency interface and are programmed in a TinyOS environment [24]. The PC base station includes an MIB510 gateway board incorporating MICAz mote which is used to forward the extracted features or the raw data to the PC for monitoring and processing.

3.2. In Situ Wireless SHM System Deployment. The wireless prototype system is applied to a 300 W wind turbine which is installed on the roof of the School of Electrical and Electronic Engineering (EEE). This wind turbine has three blades made of carbon with a diameter of 1.5 m. Each AE sensor takes charge of one blade of the wind turbine structure and records the AE events independently. Each unit is programed with a unique identification to prevent data chaos in data transmission.

Bringing together the entire component subsystems into one system, which is integrated into the wind turbine unit for *in situ* monitoring requires, ensures that the attachment of sensing units to the wind turbine blades will last for a long time. This is achieved by placing the wireless units in waterproofed plastic secured by cable tidy-ties in the wind turbine nose. This has the advantage that it makes the radius of rotation of the wireless units very small, so that the rotation of the wind turbine blades has no effect on the data transmitted. This is because the path loss is inversely proportional to the rotating radius of wireless units [25].

A diagram showing the attachment configuration is given in Figure 3, where a portion of a protection tube of 18.7 mm diameter and 24 mm in length is fixed by an Araldite adhesive

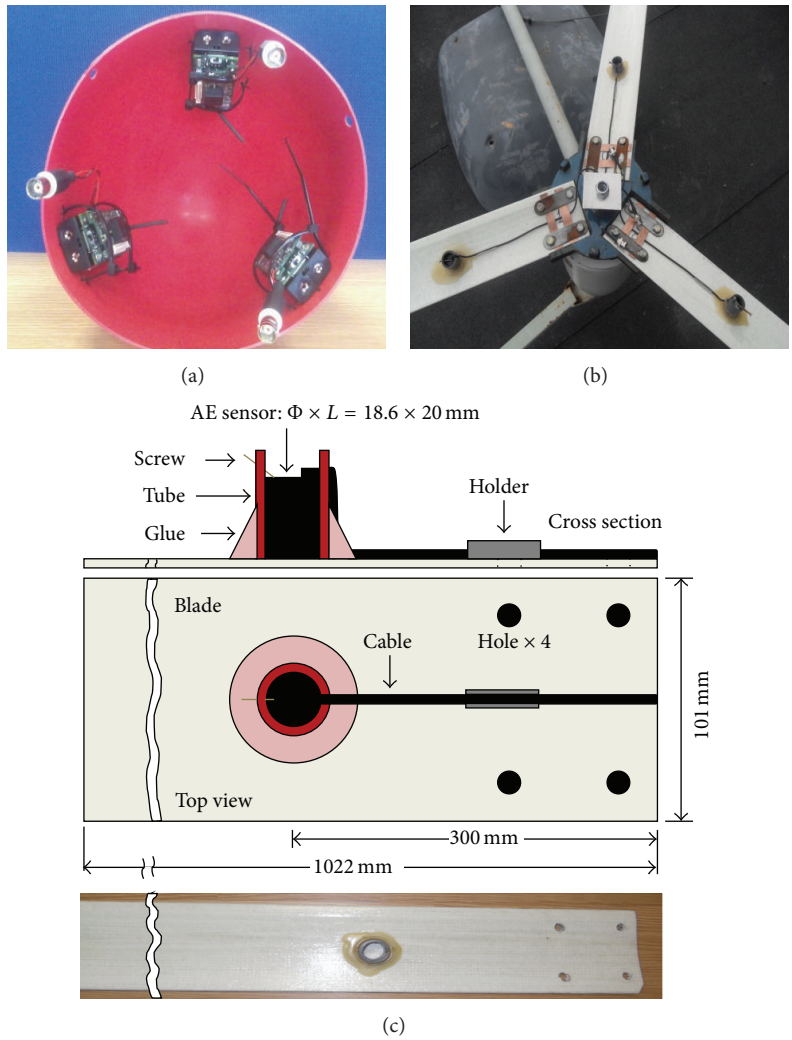

FIGURE 3: Wireless unit installation: (a) photograph of WSN node inside the nose, (b) photograph of acoustic emission sensors fixed on the blades, and (c) diagram of acoustic emission sensors fixed on the blades.

to the blade. The AE sensor is positioned in the tube and secured by a screw, and its cable is held by a cable holder which is fastened to the blade using the Araldite adhesive. The reason for this attachment is that it gives the system the flexibility to allow changes to be made to the AE sensor at any time and also minimises the noise generated compared to the use of tabs [26]. The AE sensor is attached at an equal distance of 300 mm, which is almost 30% along the length of the blade from the root section. It has been found by both simulation and experimental methods for the fact that this area is more prone to damage [5].

The AE data captured from the rotating blades is sent through wireless medium to the MIB510 serial gateway which is attached to the wind turbine tower. This data can then be transferred to the remote control unit via wired or wireless communication, such as using Wi-Fi or any other wireless techniques. The study of limitation of wireless signal transmission which can be presented in real situations is out of the scope of this paper, having been considered in future work. In this application, the gateway forwards the collected data to the PC base station in the lab through a serial cable which is also used to provide power to the serial gateway.

The entire wind turbine unit was installed with the wireless SHM system on the School's roof. The gateway is placed in a waterproof case and attached next to the wind turbine tower, as discussed above. This gateway is basically used for sending a start sensing command and setting the threshold value of the sensing process as well as switching between the transmission modes discussed in the next section. These commands are initiated by a control unit which is located in the School's lab as discussed below.

To make communication between the control unit and the wireless sensing units easier and to control the wireless monitoring system, a software package for this system was designed. This package is run by a PC and it consists of an operating package, a Java application, and MATLAB scripts to provide a user-friendly graphical user interface (GUI). The former package is executed by the TinyOS operating system installed on the MICAz hardware platform, and its main function is to perform the operations of sensing and

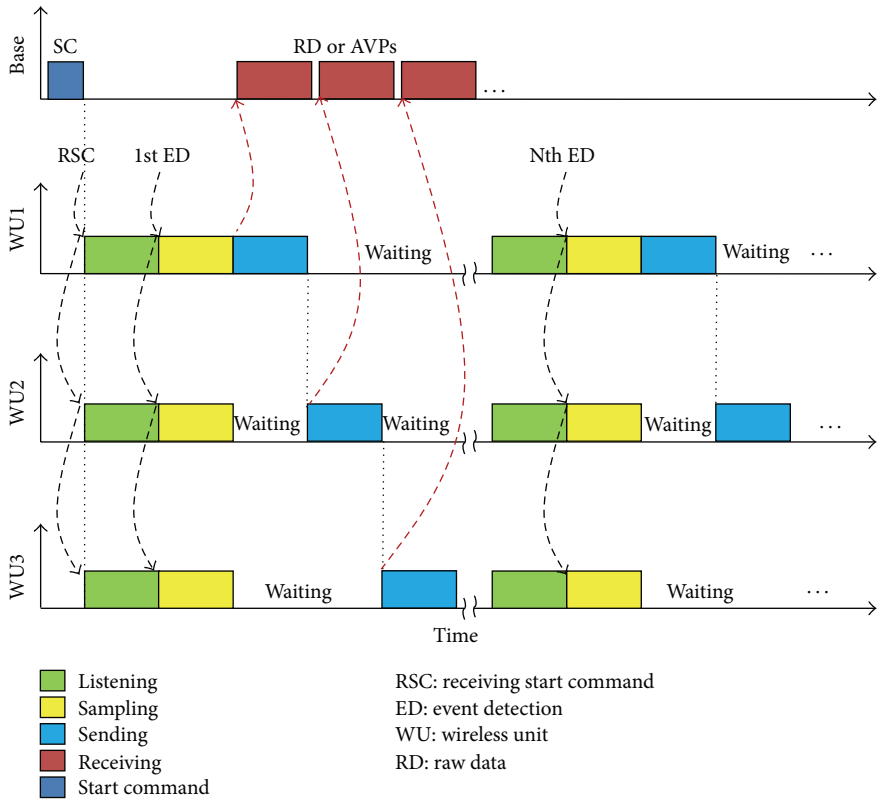

Figure 4: Schematic diagram of synchronised sensing and transmission operations.

the transmission of AE data. The GUI is used to control and interact with the developed wireless monitoring system.

4. Field Study

For field studies where continuous online monitoring obviously is required, the use of wireless sensing systems requires approaches for decentralised data processing (i.e., on-board the wireless units). In this case, important AE features can be locally extracted from the raw data and only those features to be sent to the collection point. Next, the strategies of acquiring AE events and feature extraction algorithm for the field study of this work are presented.

4.1. Synchronized Sensing and Transmission Operations. The sensing of the AE events, in this application, differs slightly from that explained in [20]. This process commences in all wireless sensing units with the receipt of a start command, indicated by "SC" in Figure 4. This command is broadcast by the base station and forces the wireless units to enter into a listening mode which makes them wait for AE events to occur which are above a preset threshold value, indicated by "ED." Once the wireless units detect such events they start acquiring AE signals at a sampling rate of almost 4.8 KHz for a sampling period of 0.11 s.

After finishing the sensing operation, the sensing units start to execute the sending operation based on the transmission mode as discussed below. As soon as they complete the sending operations, they enter again into the listening mode and a similar procedure is repeated in the same sequence.

In the proposed wireless system, the transmission operation is an event-based process, in which wireless units will not send any data unless an AE event is detected. Once the AE event is detected, these units will transfer their data after completing the sampling process according to the strategy explained in [20]. Note that the waiting period for each wireless unit is very small, due to the short time required for the transmission process. This is in particular for the transmission of acoustic vector properties (AVPs) which incorporate features extracted from the aliased AE versions, since this is the default transmission option as explained below. Thus, data loss will be rare and there will be no need to compensate for the data that is not captured during the waiting period of each sensor unit.

Moreover, depending on the transmission mode, the wireless units will send either raw data or the AVPs to the control unit. The default setting of this mode is set to AVP mode. In this case, the wireless units process the raw data in order to extract AE features from the aliased versions; and only those in the form of AVPs, instead of the aliased versions, will be sent to the remote control unit. For cases where the transmission mode is set to raw data, the wireless units will follow the same sending strategy explained in [20]. Irrespective of transmission mode, data are collected from

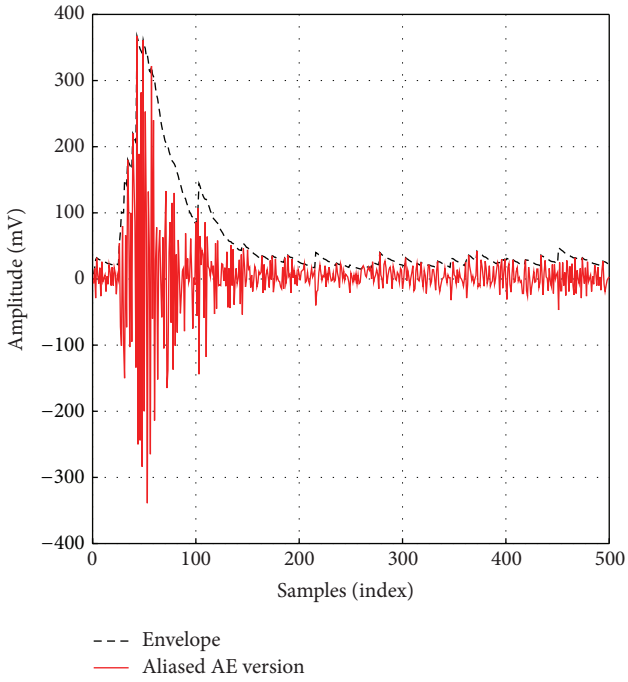

Figure 5: Aliased AE signal with its envelope.

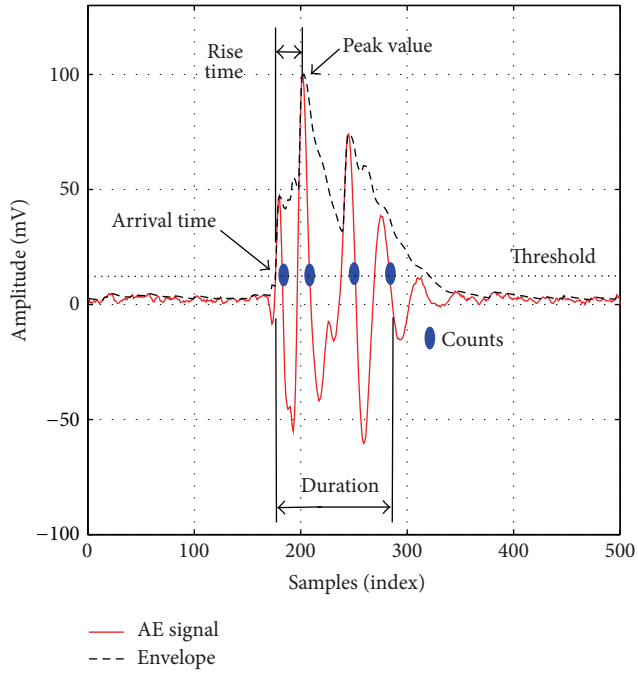

Figure 6: Key features of an aliased AE signal.

various wireless units and aggregated into the control unit for further analysis.

4.2. Signal Processing and AE Feature Extraction Algorithms. The wireless system developed here is based on the use of MICAz platforms, which have limited power resources and low processing capabilities. Therefore, relatively simple signal processing algorithms need to be considered for on-board AE feature extraction. In addition, for better analysis and localization results, content-based features should be extracted from the envelope of the received AE aliased versions rather than from the amplitude values of the time domain signal. This is because envelopes optimise the signal shape and minimise the ambiguity in the signal caused by lowering the sampling rate [14]. The envelope of the aliased AE signal is extracted on-board as explained in [15], where relatively simple and not computationally complex algorithm is used.

Figure 5 shows an example of an aliased AE version with the envelope extracted using a one-pole filter. The aliased version was captured using the developed *in situ* SHM system.

As it is known AE waves are abnormal and transient activities, which are affected by the characteristics of the induced stress field. These waves can be converted into a number of useful AE parameters or features, as shown in Figure 6, which can then be used to identify these events. Some of these parameters are as follows [27]:

(i) Amplitude, A, is the maximum amplitude which is usually measured in decibels (dB).

(ii) Rise time, R, is the time interval between the first threshold crossing and the time when the AE signal reaches its amplitude.

(iii) Duration, D, represents the time difference between the first and the last crossings of the threshold value.

(iv) Counts, N, refer to the number of times the signal crosses the threshold value.

(v) Power, P, is the area under the curve or the summation of the squared sample values.

(vi) Arrival time, T, is the time of the first threshold crossing.

(vii) Root mean square, RMS, is a statistical average parameter used for comparatively long transients.

One of the advantages of the utilization of low sampling rates is that the original shape can be conserved, which helps in maintaining the most salient information or features of the original AE signals without requiring to reconstruct them. This means that the most relevant AE event parameters, discussed above, will be retained if the aliased versions of acoustic signals are used. Fortunately, most of them are time-domain features. However, not all of the common AE features can be extracted from these versions. For example, counts are one of the exceptional AE features due to the reason that this feature represents the number of threshold crossings along the timespan between the initial and the last crossings of the threshold value. These in-between crossings are in most cases unavailable when envelopes are utilised in the extraction process. On the other hand, the duration feature which represents the timespan between these two points is still valid in this domain, since the threshold crossings occur at these points.

Other AE features, including peak value, arrival time, mean value, and power value, are extracted from the envelopes of the aliased AE signals. These features have the

Table 1: Line-of-sight results of AE events localization based on AVPs.

Exp. #	L (cm)	d (cm)	Average of estimated d (cm) from 6 readings	STD of d	Error (%)
1	82	35	35.52	0.69	1.49
2		20	19.65	1.23	1.75
3		15	13.47	0.36	10.20
4	88	40	40.03	0.57	0.08
5		30	31.52	1.03	5.07
6		21	22.30	1.55	6.19

advantage that they can be computed while the sensing process is in progress without the need to have acquired the whole signal first. The extracted features transferred to the control unit where they are characterised and used to localize the AE events, as discussed in the next section.

5. Results and Discussion

To evaluate the new concept for the sensing technique proposed in [14] for field test studies, wireless localization measurements were conducted using the *in situ* wireless SHM system discussed in Section 3. In these measurements, locations of AE sources were estimated based on the use of features locally extracted from aliased AE signals. The following subsections discuss the functionality of this system in terms of the localization of AE events on the wind turbine blades caused by artificial AE sources via hitting the blades with the same plastic stick discussed in Section 2. Such an AE source could emulate impact damage or audible cracks caused by different objects, such as tools, bird strikes, or strong hail, all of which represent abrupt AE events.

5.1. Line-of-Sight Localization of Events. Different artificial AE events were generated at known positions and localized using line-of-sight localization on a single wind turbine blade. The results show the potential of the AE source localization at low sampling rates based on the arrival time feature. The relation $d = 0.5 \cdot (L - v \cdot \Delta t_{21})$ is used to localize the AE source, where d is the distance from first hit AE sensor, v is the velocity measured, and Δt_{21} is the difference in arrival times between AE sensors. The results gained from six experiments are summarised in Table 1.

From the results shown in Table 1, the actual and estimated results are closely matched giving an overall error of 4.13% based on the measurement setting. This percentage error was calculated according to

$$\text{Error } \% = \frac{|\text{measured value} - \text{actual value}|}{\text{actual value}} \cdot 100\%. \quad (1)$$

As seen in Table 1, the rate of estimated error decreases as the distance d increases. This is because the use of low sampling rates led to decreasing spatial resolution, which in contrast increases the error in the detection of arrival times of the signals as d becomes smaller. In addition and based on these measurements, there is no effect of sampling speed of data acquisition on the precision of the AE localization.

5.2. Active Blade Identification. Active (damaged) blade identification has a significant importance in the application in SHM of offshore wind turbine blades. This is because it can restrict the inspection process to that particular blade, which saves cost and time. Figure 7 shows the AE aliased signals received as a consequence of hitting the three blades individually while they were static. Each reading consists of 500 samples and all of them are initiated by a simple threshold crossing condition (100 mv), which was chosen experimentally to be above noise level. Figure 7(a) illustrates the results of hitting blade number one. It is clear that a strong AE event was occurring at this blade, which needs to be taken into account in event detection and localization as discussed next. The other two plots show the results of the propagation of this event to blades two and three.

In contrast Figures 7(b) and 7(c) depict the consequence of hitting blades two and three, respectively. In both cases, the strongest aliased AE signal can be used to specify which blade was subject to the hit, whereas weak signals were obtained in each case as a result of the propagation of both strongest aliased AE signals to the other blades. In addition, it can be observed in Figure 7(a) that there is a slight difference between the waveforms shown in this figure and those in Figures 7(b) and 7(c) in which the first shows that there is a minor hit result following the main hit result.

These aliased signals shown in Figure 7 also demonstrate that applying uniform sampling rates lower than Nyquist requirements in the acquisition process can still preserve the shape or contents of the AE signals. The shape and common AE features of these aliased versions are correlated with the AE signals captured at high sampling rates [27]. This is a very important criterion in the extraction of AE features in SHM applications, which is not satisfied in techniques previously applied where a set of random projected samples was used [28].

The determination of the active blade can also be achieved based on the AVPs received, as depicted in Figure 8 which summarises the results illustrated in Figure 7. For each test, the maximum peak values indicate the active blade which was hit. This means that, from Figure 8, and based on the peak values, the first test shows that the AE event occurred on blade number one, whereas they occurred on blades two and

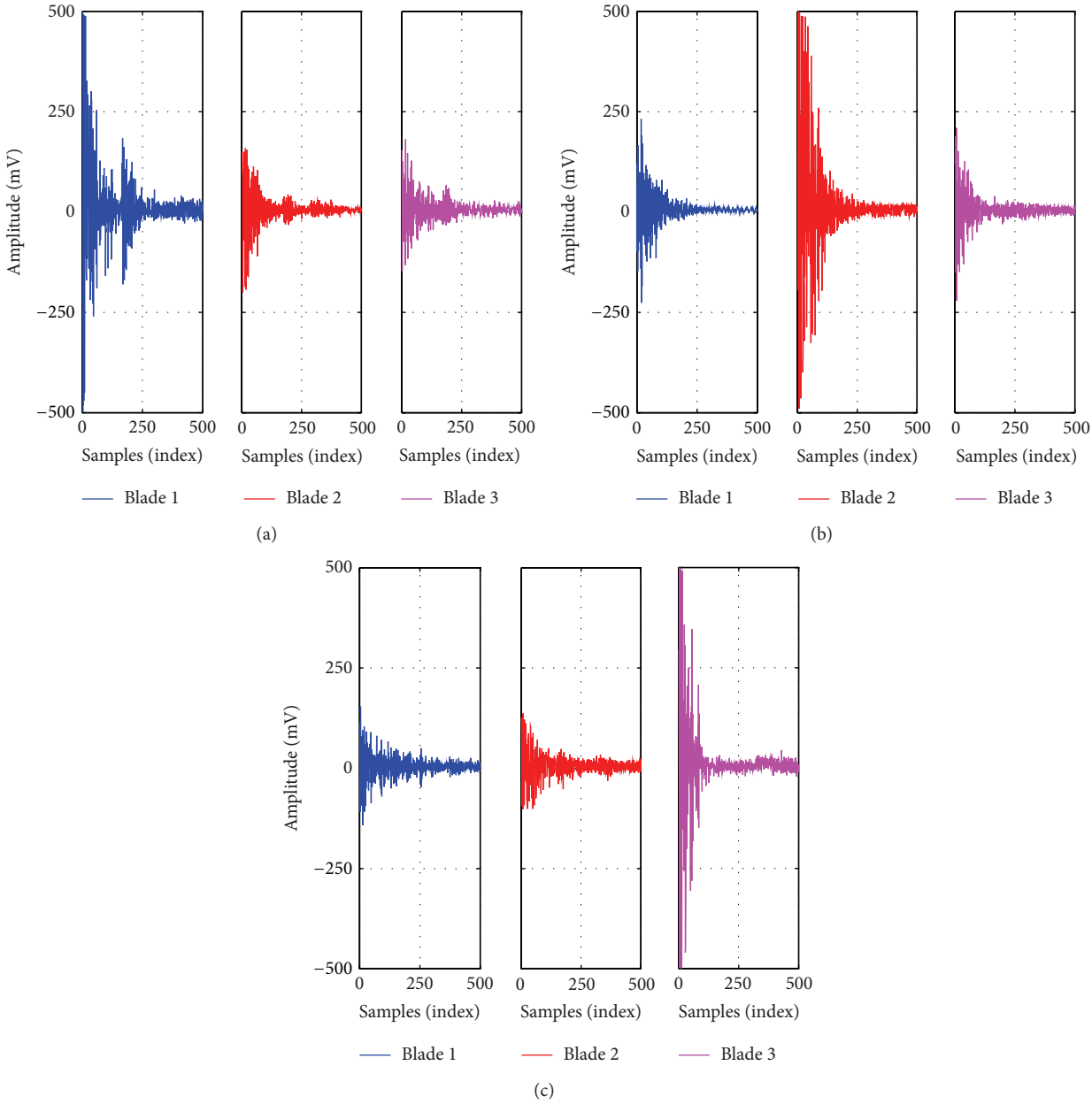

Figure 7: Aliased AE signals received from the wireless units as a consequence of hitting the three blades individually: (a) one, (b) two, and (c) three.

three in the second and third tests, respectively. The results gained here can be combined with those of the constraint geometrical point location technique to provide more precise source localization results for large scale wind turbine blades, as discussed next.

5.3. Constraint Geometrical Point Localization of AE Events. Due to the symmetry of the sensor configuration in Figure 1(a), the distance x is known and equals $l_{1,2}/2$ and the arrival times at S_1 and S_2 are equal, which means that $\Delta t_{21} = 0$. Thus, any two sensors located on the propagation path are sufficient to estimate the distance d and consequently the coordinate y. In addition, once the active blade is specified based on zonal location, as explained in Section 2, then the proposed model in Figure 1(b) can be adjusted accordingly.

The proposed approach is examined by conducting wireless experiments to locate AE sources produced at known locations on blades by artificial AE events. For this purpose, the locations of AE sensors were changed to 50 cm instead of 30 cm on each blade, in order to provide more scope for changing the value of d. In these measurements, a calibration method as discussed in Section 2 is used to measure the velocity of wave propagation from the measured time difference between the different AE sensors on the blades, and it is found to be around 2×10^4 m/s on average. It is worth mentioning that as the distance between the two AE sensors decreases the

Table 2: Estimation results of constraint geometrical point localization.

Exp. #	$l_{1,2}$, $l_{1,3}$ (cm)	L (cm)	d (cm)	Average of estimated d (cm) from 6 readings	STD of d	Error (%)
1	92	103	15	17.58	0.55	17.20
2			20	21.70	1.68	8.50
3			25	23.19	0.39	7.24
4			30	31.90	1.50	6.33
5			35	36.60	0.91	4.57
6			40	41.61	0.74	4.02

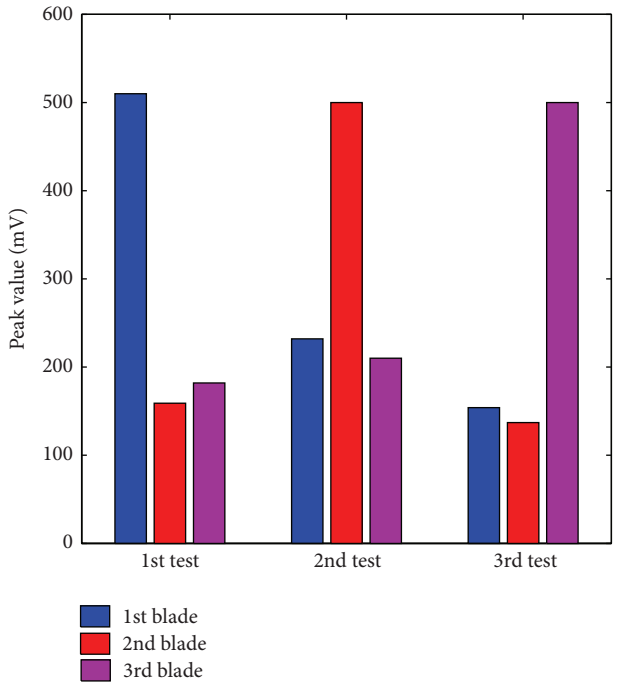

Figure 8: Active blade identification based on peak value features of AE events shown in Figure 7.

measured velocity becomes inaccurate. The reason behind this is that the velocity measurement will be dominated by the small distance between the two sensors which is dominated by the complex structure of the wind turbine at hub, whereas as this distance increases, it will be dominated by the simple one-dimensional structures of the blades.

The localization results obtained are summarised in Table 2. From these results, the actual and the estimated results are closely matched. They give an overall error of 7.98%, which shows the feasibility of the proposed model for AE source localization at sampling rates much lower than the Nyquist rate for the specific wind turbine structure. The percentage error was calculated according to (1). It is noticeable that the percentage error also increases with a decrease in d. This is because as the d decreases the difference in arrival times of signals at AE sensors decreases as well; therefore, estimation errors increase. In addition, the results obtained here show a systematic error within 2 cm which is most likely due to the gap between the AE sensors and wind turbine blades. These results show also that the sampling speed of data acquisition does not harm the precision of the AE localization. Such results, though for a small wind turbine system, show significant potential to be extended to large-scale offshore wind turbine blades.

6. Conclusions

In this paper, the implementation of an *in situ* SHM system for wind turbine blades was introduced and described based on the integration of the AE technique and wireless technology. The developed system was integrated onto a 300 W wind turbine installed on the roof of Newcastle University. This system was used to evaluate a promising low sampling sound localization technique proposed in previous work. This was achieved by utilizing the content-based features extracted from the aliased AE signals on-board the wireless units to locate AE sources which emulated impact damage.

In addition, a localization model for constraint geometrical point localization technique was developed and applied to the three wind turbine blades. Wireless localization measurements were carried out to assess the localization capabilities of the proposed model on the wind turbine blades. The results show the feasibility of this model for AE source localization at sampling rates much lower than the Nyquist rate in this specific wind turbine structure.

Such conclusions are important for the further design and development of wireless SHM systems and their application in developing continuous *in situ* offshore large scale wind turbine blades condition monitoring systems. Further studies of this work will consider AE features with low sampling rate that can be used for the damage identification.

Conflict of Interests

The authors declare that there is no conflict of interests regarding the publication of this paper.

Acknowledgments

The authors would like to thank the FP7 HEMOW Project, "Health Monitoring of Offshore Wind Farms" (FP7-PEOPLE-2010-IRSES, 269202, http://www.hemow.eu/), for funding the work. The authors would also like to express their gratitude to all the people from both mechanical and electronic workshops (School of Electrical and Electronic Engineering,

Newcastle University) who have given their full support in making this implementation a success.

References

[1] P. J. Schubel, R. J. Crossley, E. K. G. Boateng, and J. R. Hutchinson, "Review of structural health and cure monitoring techniques for large wind turbine blades," *Renewable Energy*, vol. 51, pp. 113–123, 2013.

[2] Z. Hameed, Y. S. Hong, Y. M. Cho, S. H. Ahn, and C. K. Song, "Condition monitoring and fault detection of wind turbines and related algorithms: a review," *Renewable and Sustainable Energy Reviews*, vol. 13, no. 1, pp. 1–39, 2009.

[3] Y. Q. Ni, X. W. Ye, and J. M. Ko, "Monitoring-based fatigue reliability assessment of steel bridges: analytical model and application," *Journal of Structural Engineering*, vol. 136, no. 12, pp. 1563–1573, 2010.

[4] X. W. Ye, Y. Q. Ni, K. Y. Wong, and J. M. Ko, "Statistical analysis of stress spectra for fatigue life assessment of steel bridges with structural health monitoring data," *Engineering Structures*, vol. 45, pp. 166–176, 2012.

[5] C. C. Ciang, J.-R. Lee, and H.-J. Bang, "Structural health monitoring for a wind turbine system: a review of damage detection methods," *Measurement Science and Technology*, vol. 19, no. 12, Article ID 122001, 20 pages, 2008.

[6] J.-R. Lee, H.-J. Shin, C. C. Chia, D. Dhital, D.-J. Yoon, and Y.-H. Huh, "Long distance laser ultrasonic propagation imaging system for damage visualization," *Optics and Lasers in Engineering*, vol. 49, no. 12, pp. 1361–1371, 2011.

[7] C. S. Shin, B. L. Chen, and S. K. Liaw, "An FBG-based impact event detection system for structural health monitoring," *Advances in Civil Engineering*, vol. 2010, Article ID 253274, 8 pages, 2010.

[8] N. Elkmann, T. Felsch, and T. Förster, "Robot for rotor blade inspection," in *Proceedings of the 1st International Conference on Applied Robotics for the Power Industry (CARPI '10)*, pp. 1–5, Montreal, Canada, October 2010.

[9] P. Meinlschmidt and J. Aderhold, "Thermographic inspection of rotor blades," in *Proceedings of the 9th European Conference on NDT*, Berlin, Germany, 2006.

[10] N. Tralshawala and W. I. Faidi, "System and method for inspecting a wind turbine blade," United States Patent 8120522, 2011.

[11] I. Amenabar, A. Mendikute, A. López-Arraiza, M. Lizaranzu, and J. Aurrekoetxea, "Comparison and analysis of non-destructive testing techniques suitable for delamination inspection in wind turbine blades," *Composites Part B: Engineering*, vol. 42, no. 5, pp. 1298–1305, 2011.

[12] F. Ciampa and M. Meo, "A new algorithm for acoustic emission localization and flexural group velocity determination in anisotropic structures," *Composites Part A: Applied Science and Manufacturing*, vol. 41, no. 12, pp. 1777–1786, 2010.

[13] M. Huang, L. Jiang, P. K. Liaw, C. R. Brooks, R. Seeley, and D. L. Klarstrom, "Using acoustic emission in fatigue and fracture materials research," *JOM*, vol. 50, pp. 1–14, 1998.

[14] O. M. Bouzid, G. Y. Tian, J. Neasham, and B. Sharif, "Investigation of sampling frequency requirements for acoustic source localisation using wireless sensor networks," *Applied Acoustics*, vol. 74, no. 2, pp. 269–274, 2013.

[15] O. M. Bouzid, G. Y. Tian, K. Cumanan, and J. Neasham, "Wireless AE event and environmental monitoring for wind turbine blades at low sampling rates," in *Proceedings of the World Conference on Acoustic Emission—2013: Advances in Acoustic Emission Technology*, G. Shen, Z. Wu, and J. Zhang, Eds., vol. 158 of *Springer Proceedings in Physics*, p. 400, 2015.

[16] Á. Lédeczi, A. Nádas, P. Völgyesi et al., "Countersniper system for urban warfare," *ACM Transactions on Sensor Networks*, vol. 1, pp. 153–177, 2005.

[17] M. Wang, L. Ci, P. Zhan, and Y. Xu, "Acoustic source localization in wireless sensor networks," in *Proceedings of the Workshop on Intelligent Information Technology Application (IITA '07)*, pp. 196–199, December 2007.

[18] Z. M. Saric, D. D. Kukolj, and N. D. Teslic, "Acoustic source localization in wireless sensor network," *Circuits, Systems, and Signal Processing*, vol. 29, no. 5, pp. 837–856, 2010.

[19] P. Liu, S. Yuan, and L. Qiu, "Development of a PZT-based wireless digital monitor for composite impact monitoring," *Smart Materials and Structures*, vol. 21, no. 3, Article ID 035018, 2012.

[20] O. M. Bouzid, G. Y. Tian, J. Neasham, and B. Sharif, "Envelope and wavelet transform for sound localisation at low sampling rates in wireless sensor networks," *Journal of Sensors*, vol. 2012, Article ID 680383, 9 pages, 2012.

[21] R. Gangadharan, G. Prasanna, M. R. Bhat, C. R. L. Murthy, and S. Gopalakrishnan, "Acoustic emission source location in composite structure by Voronoi construction using geodesic curve evolution," *Journal of the Acoustical Society of America*, vol. 126, no. 5, pp. 2324–2330, 2009.

[22] W. Wevers and K. Lambrighs, "Applications of acoustic emission for structral health monitoring: a review," in *Encyclopedia of Structural Health Monitoring*, John Wiley & Sons, Chichester, UK, 2009.

[23] J. Yick, B. Mukherjee, and D. Ghosal, "Wireless sensor network survey," *Computer Networks*, vol. 52, no. 12, pp. 2292–2330, 2008.

[24] P. Levis and D. Gay, *TinyOS Programming*, Cambridge University Press, Cambridge, UK, 2009.

[25] Y. Leng, D. Wenfeng, S. Peng, X. Ge, G. J. Nga, and S. Liu, "Study on electromagnetic wave propagation characteristics in rotating environments and its application in tire pressure monitoring," *IEEE Transactions on Instrumentation and Measurement*, vol. 61, no. 6, pp. 1765–1777, 2012.

[26] M. J. Blanch and A. G. Dutton, "Acoustic emission monitoring of field tests of an operating wind turbine," *Key Engineering Materials*, vol. 245-246, pp. 475–480, 2003.

[27] Á. Lédeczi, T. Hay, P. Völgyesi, D. R. Hay, A. Nádas, and S. Jayaraman, "Wireless acoustic emission sensor network for structural monitoring," *IEEE Sensors Journal*, vol. 9, no. 11, pp. 1370–1377, 2009.

[28] Y. Bao, J. L. Beck, and H. Li, "Compressive sampling for accelerometer signals in structural health monitoring," *Structural Health Monitoring*, vol. 10, no. 3, pp. 235–246, 2011.

Hindawi Publishing Corporation
Journal of Sensors
Volume 2015, Article ID 678634, 8 pages
http://dx.doi.org/10.1155/2015/678634

Research Article

Application of Distributed Optical Fiber Sensing Technology in the Anomaly Detection of Shaft Lining in Grouting

Chunde Piao,[1] Jun Yuan,[1] Bin Shi,[2] Haijun Lu,[3] Guangqing Wei,[4] and Chunsheng Gu[1]

[1]*Resources and Geosciences College, China University of Mining and Technology, Xuzhou, Jiangsu 221116, China*
[2]*Department of Geo-Engineering & Geo-Informatics, Nanjing University, Nanjing, Jiangsu 210023, China*
[3]*Pingdingshan Coal Co., Ltd., Pingdingshan, Henan 467000, China*
[4]*Suzhou Nanzee Sensing Technology Co., Ltd., Suzhou, Jiangsu 215123, China*

Correspondence should be addressed to Chunde Piao; piaocd@126.com

Received 17 October 2014; Revised 1 February 2015; Accepted 2 February 2015

Academic Editor: Zhenhua Zhu

The rupture of the shaft lining caused by grouting has seriously undermined the safety in coal mining. Based on BOTDR distributed optical fiber sensing technology, this paper studied the layout method of optical fiber sensors and the anomaly detection method of the deformation and obtained the evolution law of shaft deformation triggered by grouting. The research results showed that the bonding problem of optical fiber sensors in damp environment could be effectively solved, by applying the binder consisting of sodium silicate and cement. Through BOTDR-based deformation detection, the real-time deformation of the shaft lining caused by grouting was immediately spotted. By comparing the respective strain of shaft lining deformation and concrete deformation, the risk range of shaft lining grouting was identified. With the additional strain increment of the shaft lining triggered by each process of grouting, the saturated condition of grouting volume in strata was analyzed, providing an important technical insight into the field construction and the safety of the shaft lining.

1. Introduction

The shaft is like the throat of coal mine. The safety of the shaft itself is the basic foundation to ensure the normal operation of the whole mining activities [1]. The existing shafts deform due to many factors, such as the water loss of thick overburden and the high grouting pressure during the repair of shaft lining [2]. If an effective monitoring system is used in the shaft lining to timely identify the deformation during mining, the potential danger in the shaft lining will be noticed in advance, and effective measures can be taken to avoid serious accidents. At present, as to the monitoring methods of shaft deformation, the changes of strain at different horizons in the processes of shaft rupture have been analyzed, and the evolution mechanism of shaft lining fractures has been explored by installing conventional sensors (such as concrete strain meters [3]) and fiber Bragg grating strain sensors [4, 5] in the circumferential, vertical, and radial directions on the surface of shaft lining. Using a three-dimensional laser scanner and convergence measurements [6], the applicability of support patterns installed to control massive spalling during shaft sinking has been investigated and the selection flowchart of the concrete lining span has been proposed to control its severe damage prior to shaft excavation. But these sensors have many limitations, such as the poor anti-interference performance, the low integration degree, and the limited monitoring range. Therefore it is difficult for them to meet the requirement of shaft safety monitoring. In the aspect of recognition methods of grouting, ground penetrating radar [7], seismic reflection wave method [8], and some other methods have been applied. They can detect the changes of waveform, amplitude, and frequency before and after grouting and obtain the abnormal range behind shaft. The grouting effect inner rock body and reinforcement range have been identified by using microseismic monitoring technology [9] to detect the rock microcracks. These methods have some advantages, such as low cost and the macroscopical ability to grasp the structure of geological body. But they also

entail many disadvantages, such as poor antielectromagnetic interference ability and the uncertainty as well as multiplicity in their detection results. As the frontier in the development of optical fiber sensing technology, distributed optical fiber sensing technology utilizes the one-dimensional characteristic of fiber geometry. Taking the measured parameters as a function of the fiber position, it can perform continuous measurement of the external physical parameters along the fiber geometric path in the entire length of optical fiber and can obtain the spatial distribution along with the time-sensitive information of the measured physical quantity at the same time [10–13]. In distributed optical fiber sensing technology, the fiber is both the sensing medium and the transmission channel, which boasts many merits such as small size, light weight, adaptable geometry, antielectromagnetic interference, excellent insulating characteristic, high sensitivity, and applicability in far distance observation. Thus, it can be expected that distributed optical fiber sensing technology is the future of the new generation monitoring techniques [14–18].

With the progress of science and technology, the fundamental way to solve the problems in the shaft lining safety is to establish a modern, high-quality, completely reliable, and immensely sensitive monitoring method of deformation. By using BOTDR distributed optical fiber sensing technology, this paper studied the techniques in laying fiber sensors and the method of monitoring the grouting process. Through analyzing the vertical and circumferential deformation of the shaft lining caused by grouting, the research constructed an anomaly detection method of shaft lining in grouting based on distributed optical fiber sensing technology. Thus, the results of this study would provide the theoretical and technical support in identifying the features of deformation during the grouting process, which promoted the safe and effective exploitation of coal resources.

2. BOTDR Distributed Detection and Anomaly Detection Method

2.1. The Layout of Optical Fiber Sensors in Shaft Lining. The layout of optical fiber sensors has a direct impact on the detection performance. Therefore, on the basis of previous engineering applications of distributed optical fiber sensing technology in reinforced concrete beams [19], pile foundations [20], and tunnels [21, 22], the following layout method of shaft lining has been taken. On the concrete surface, the U-shaped groove with 3 mm width and 5 mm depth was made along the shaft lining. After dusts were removed in the U-shaped groove, the single mode fiber of a diameter of 0.9 mm was laid. The binder combined with sodium silicate [$Na_2O \cdot n(SiO_2)$] and cement was filled into the groove to ensure the uniform deformation of the shaft lining and the fiber. The 5 m long sensing fiber was reserved under special protection during installation and was connected to the transmission cable later.

When monitoring the deformation in the certain range of depth, the four-core cable with sheath was placed in the fiber laying position along the shaft lining surface from the ground and got fused with the sensing fiber reserved previously, and the other end of the cable on the ground was connected with BOTDR. In order to prevent the damage of the optical fiber sensors during shaft lining construction and operation, the metal bellows were used to enwrap the connection part. And the related schematic diagram of the sensing fiber layout is shown in Figure 1.

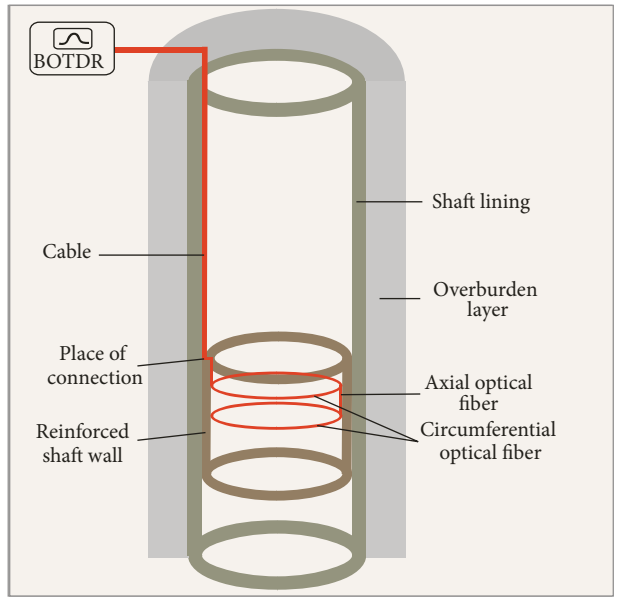

Figure 1: Schematic diagram of the sensing fiber layout.

2.2. Distributed Detection Method of Shaft Lining in Grouting. Before grouting, such parameters as the testing scope, frequency and precision, which BOTDR would test, were set according to the shaft depth and detection requirements. At the same time, the deformation was measured as the initial value. With the number of times or the amount of grouting as the unit, we monitored the shaft lining deformation caused by grouting and subtracted the deformation in a certain frequency from the initial value as the shaft lining additional strain. The spatial location of the shaft lining deformation was calculated, according to the distance between BOTDR and Brillouin scattering light which returned through the fiber from a point, as is shown as follows:

$$Z = \frac{c \cdot T}{2n}, \tag{1}$$

where Z is the distance between force bearing point along the sensing fiber line and the input end of BOTDR; c is the speed of light in vacuum; T is the time interval between the emitted pulsed light and the receiving Brillouin scattered light which returns from the force bearing point; and n is the refraction coefficient of the optical fiber.

2.3. The Anomaly Detection Method of the Shaft Lining Deformation in Grouting. Through the buried fiber sensors, the grouting-triggered additional strain was detected in the vertical and circumferential directions and was compared

Table 1: Main aquifers that the shaft crosses.

Layer	Thickness (m)	Aquifer thickness (m)	Aquifer type	Static water level (m)	Estimated water inflow (m^3/h)
The Quaternary	99	50	Confined pore water	+120.52	63.89
Liujiagou group of Triassic sandstone	283	159	Porous-fractured water	+150.28	762.78
The Permian Shiqianfeng formation + first division sandstone	262.5	168.7	Porous-fractured water	+149.38	176.93
The Permian coal stratum	521	122	Porous-fractured water	+90.292	13.47

with the circumferential yield strain ε_s and the circumferential failure strain ε_k, based on which the risk zones of shaft lining deformation were found [23]. The evaluation index τ of shaft lining deformation is illustrated as

$$\tau = \begin{cases} \varepsilon \le \varepsilon_s & \text{Shaft lining safety} \\ \varepsilon_s < \varepsilon \le \varepsilon_k & \text{Shaft lining damage} \\ \varepsilon > \varepsilon_k & \text{Shaft lining fracture.} \end{cases} \quad (2)$$

The additional strain increment upon the shaft lining resulting from each process of grouting can be calculated by

$$\Delta\varepsilon = \varepsilon_{i+1} - \varepsilon_i, \quad (3)$$

where ε_i and ε_{i+1} are the respective deformation volume of the shaft lining after the i and the $i + 1$ time of grouting.

With the additional strain increment obtained from (3), the filling condition of slurry on shaft was analyzed. In order to ensure the shaft lining safety, the uniform deformation of the stress region was adjusted to reinforce the overburden layer around shaft lining and to seal off the aquifer, through taking such control measures as stopping grouting, slowing grouting, changing grouting hole or grouting horizon, and so on.

3. Project Example and Data Analysis

3.1. Project Background. The project discussed in this paper locates at a coal mine of Pingdingshan Coal Co. Ltd. in Henan province. With the freezing method adopted in construction, its lining was double reinforced concrete shaft lining with the design diameter of 6.5 m. The shaft wall thickness in the 0–393.6 m section was 1050 mm; in the 393.6–520 m section, 700 mm; in the 520–676 m section, 800 mm; and in the 676–1075 m section, 500 mm. The concrete strength of the shaft lining within the depth of 420 m was C50 and below the depth of 420 m was C70. According to the data of the existing exploration hole and the real strata conditions, it can be found that the strata mainly consist of clastic rock, and the aquifers mainly consist of multilayer sandstone. The main aquifers crossed by the shaft lining are shown in Table 1.

Under the normal construction of the shaft lining, there are close hydraulic connections between Liujiagou formation and the Pingdingshan formation. Influenced by the "surrounding rock loose circle," the backwall sand layer bears the high water pressure [24]. Based on the Pingdingshan coal mining districts' geological conditions and the features of water disasters in the aquifer, backwall grouting for blocking water was conducted in line with the construction design. But during the repair of shaft lining grouting, a 0.6 m diameter hole appeared at the depth of 589 m plane in the direction of 23° north by west, because of the high grouting pressure. With the high water pressure upon the backwall, a large amount of sand body rushed into the shaft wall, resulting in the shaft lining fracture and damage from 587 m to 605 m. In order to strengthen it, the shaft lining from 580 m to 610 m was reinforced with another wall, making the net diameter of the new shaft lining increase to 6.2 m.

Water infiltrated the new shaft lining because of the high dynamic water pressure upon the shaft backwall, which undermined the safety of the shaft lining. To solve the problem, we put two circumferential sensing optical fibers at the depth of 582.5 m plane and 590 m plane and put the vertical sensing optical fiber which crossed the two circumferential sensing optical fibers in the direction of 35° north by west, at the depth between 582.5 m and 590 m. After that, the meeting points of sensing optical fibers were fused with each other and the series sensing optical fibers were then fused with the transmission cable which was put at the detection position. And the other end of the cable was connected with BOTDR strain analyzer, testing the shaft lining deformation caused by grouting. The laying method of sensing fibers and the monitoring of shaft are shown in Figure 2.

3.2. Repair of Shaft Lining Grouting. The grouting process can be divided into two parts, according to the shaft lining's additional strain and the seepage condition. First, cement was grouted behind the concrete shaft lining between the depths of 280 m to 290 m. Secondly, chemical grouting was conducted into the spaces between the concrete of the shaft lining. The grouting location and grouting volume of shaft lining are given in Table 2.

3.3. Analysis on Detection Results of Grouting. The circumferential strain distribution of shaft lining caused by each

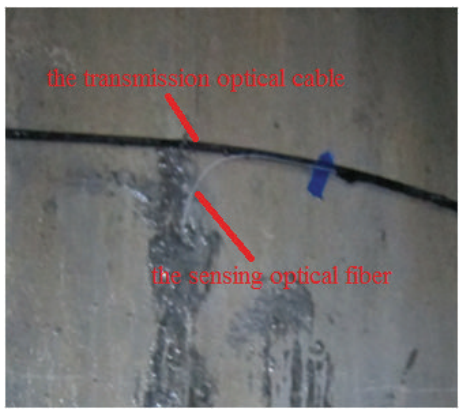

(a) Connection of the sensing optical fibers

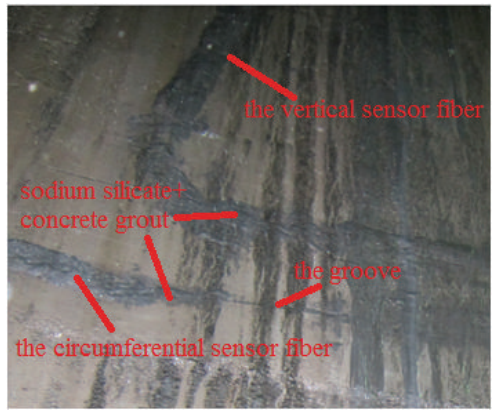

(b) Layout of the sensing optical fibers

(c) Shaft detecting site

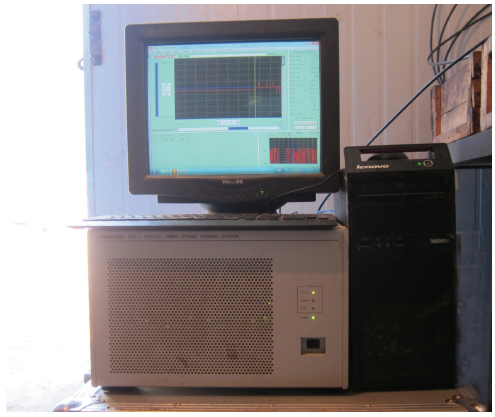

(d) BOTDR interrogator

Figure 2: Installation of the monitoring systems in the field.

Table 2: Grouting process of shaft lining.

Grouting step number	Grouting location (m)	Grouting amount (m^3)
1	280–285 288.5–292.5	2 (cement grouting)
2	282.5–285 288.5–292.5	1.5 (cement grouting)
3	282.5–285 287.5–288	1.5 (cement grouting)
4	282.5–285	1 (cement grouting)
5	282.5–285 287.5–290	1 (cement grouting)
6	282.5–285 287.5–290	1 (cement grouting)
7	280–290	0.77 (chemical grouting)
8	280–290	0.83 (chemical grouting)

process of grouting was obtained by the two circumferential sensing optical fibers at the depth of 582.5 m and 590 m, as shown in Figures 3 and 4. The strain distributions were the strains that expanded in anticlockwise order from the starting point of the north direction. After expansion, the circumference of shaft lining was 19.468 m.

As shown in Figures 3 and 4, the deformation of shaft lining had a larger fluctuation caused by grouting. The additional strain distribution at position of 0 m and 3.7 m in Figure 3 and the positions of 0 m, 3.7 m, and 16.2 m in Figure 4 showed that the compression strain value in circumferential directions was larger and the stress state presented the obvious feature of regionality. The main reason was that, affected by the early stage of shaft lining fracture, many cavities appeared in the shaft lining behind the shaft rock wall at position of 589 m plane in the direction of 23° north by west. These cavities were firstly filled by the slurry when injecting the cement slurry. The shaft lining gradually produced the inward deformation caused by grouting and the compression strain value in circumferential directions gradually increased. The main influence range of cement slurry concentrated upon the grouting region of grouting holes because of high viscosity, large granules, and short diffusion distance. The additional strain of the slurry which flowed through the void and fracture behind the shaft sandstone gradually increased due to the influence of surrounding

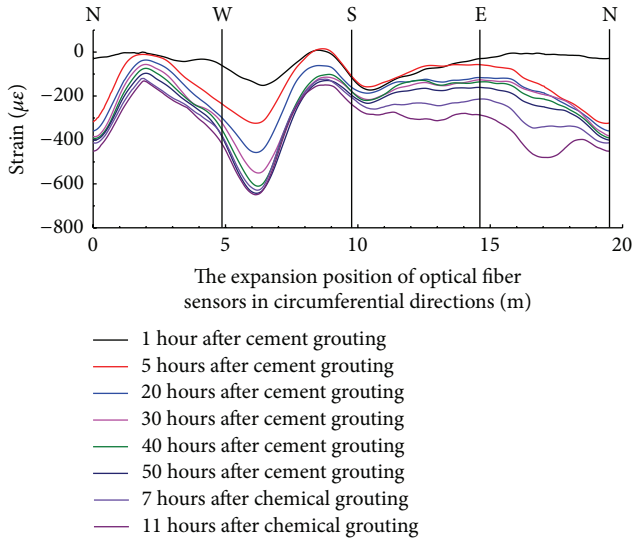

Figure 3: The circumferential strain distribution of shaft lining at the depth of 582.5 m plane.

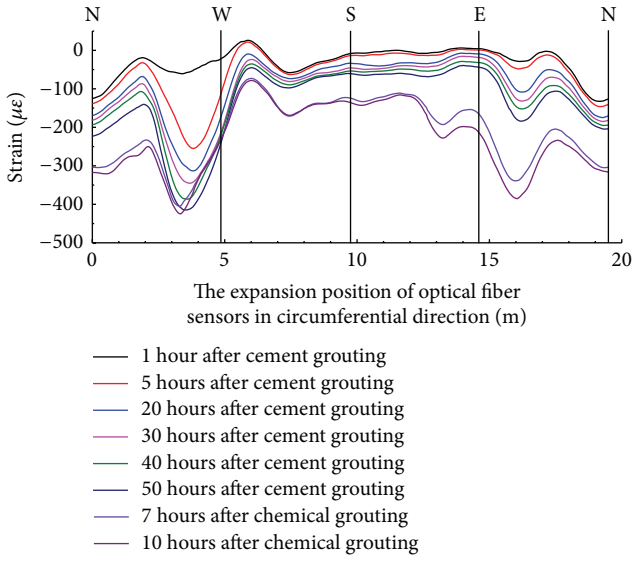

Figure 4: The circumferential strain distribution of shaft lining at the depth of 590 m plane.

rock loose circle when injecting the cement slurry into the shaft lining behind the shaft rock wall. That is to say, the circumferential deformation was relevant to the range of rock loose circle behind the shaft rock wall and the grout amount.

The strain value in circumferential directions increased evenly and the slurry spread to the surrounding far distance as the center of grouting holes when injecting chemical grout between the shaft rock wall based on the advantages of high-quality grouting, low viscosity, and excellent impermeability. The additional strain distribution on the range of 0–5.2 m in Figure 3 and the range of 2.5–5.5 m in Figure 4 shows that the void of double-layer shaft wall was compressed gradually caused by grouting using the cement slurry while

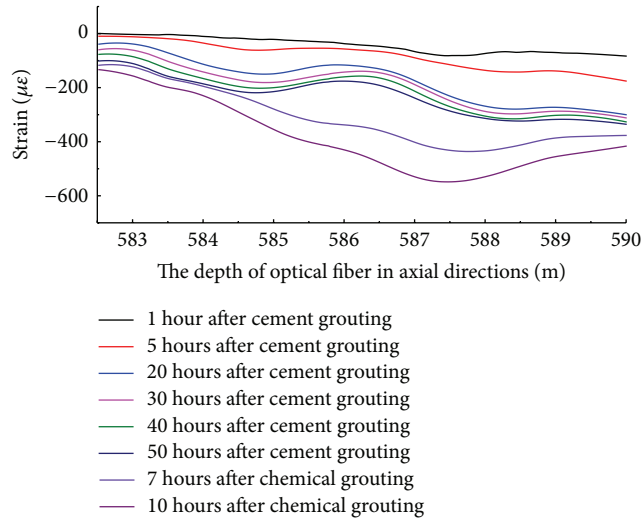

Figure 5: The additional strain distribution of the shaft lining in axial directions.

less deformation of the shaft lining was caused by chemical grouting. The additional strain distribution on the range of 10–19.5 m in Figure 3 and the range of 5.5–19.5 m and 0–2.5 m in Figure 4 shows that the deformation of the shaft lining caused by grouting using cement slurry was comparatively smaller. At this time, the grouting of chemical grout increased and the deformation of the shaft lining became larger with the grouting capacity of chemical grout increasing.

The additional strain value of the shaft lining in axial directions caused by grouting is as shown in Figure 5.

As shown in Figure 5, the additional strain on the range of 582.5–587 m was essentially consistent when injecting cement slurry into the shaft lining. The reason was that the strengthening area of surrounding soil caused by grouting in axial directions was uniform. The grouting capacity near the depth of 589 m plane increased due to the influence of the previous shaft lining fracture and caused the compressive strain in which the surrounding soils acted on the shaft lining increasing. So the additional strain on the depth between 587.5 m and 590 m increased. The compression strain on the depth between 585 m and 587.5 m in axial directions increased rapidly when injecting chemical grout between the shaft rock wall. There were mainly two reasons behind this phenomenon. On the one hand, deformation of the shaft lining at the depth between 585 m and 587.5 m was small caused by cement slurry and the void was filled by chemical grout. On the other hand, the shaft lining at the depth between 575.5 m and 590 m was damaged seriously because of pregrouting pressure. The strengthening area of cement slurry mainly concentrated near the grouting holes, and away from the grouting holes, the fracture existed in the shaft lining. With chemical grout injecting into the shaft lining behind the shaft rock wall along the fracture plane, the section of shaft lining was reinforced effectively.

According to the actually measured data, the yield strain of high strength concrete in circumferential directions was −1400 $\mu\varepsilon$ and the fracture strain in circumferential directions

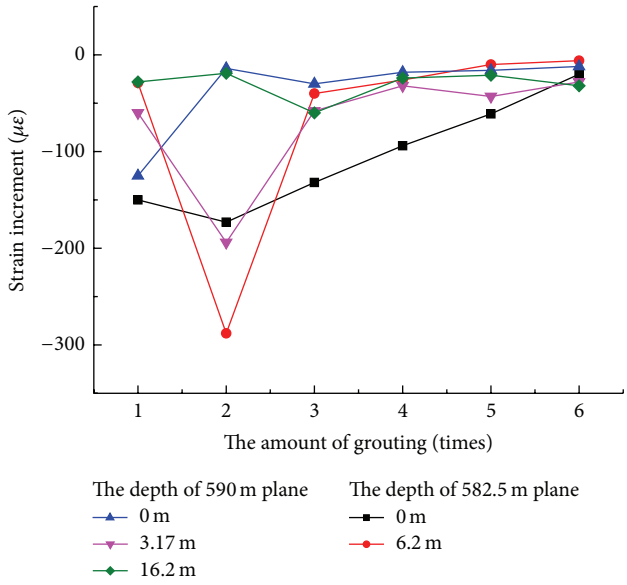

FIGURE 6: The relationship between the amount of grouting using cement slurry and the strain increment in circumferential directions.

was −3400 $\mu\varepsilon$ [25, 26]. The maximum strain of shaft lining caused by grouting in circumferential directions was −648 $\mu\varepsilon$ caused by grouting. As shown in (2), the maximum strain was smaller than the yield strain in circumferential directions. The results showed that the concrete shaft lining was in safe conditions.

In order to understand the evolution characters of shaft lining caused by grouting behind the shaft rock wall using cement slurry, several strain values with larger deformation were chosen in the distribution curve of the upper and lower optical fiber sensors in circumferential directions. The strain increment in circumferential directions caused by grouting was calculated by (3), as shown in Figure 6.

As shown in Figure 6, the additional strain increment was volatile due to the influence of sand layers structure at the beginning of grouting. The slurry volume injected into the grouting holes gradually reduced and the strain increment of the shaft lining gradually turned to be consistent and stable with the amount of grouting increasing. It showed that the voids in sandstone were replaced by slurry and slurry volume had reached the saturation point. The above analysis shows that the change of slurry volume and the deformation of shaft lining can be detected effectively in grouting based on the distributed optical fiber sensing technology.

4. Discussions

(1) The binder, made of epoxy and curing agent, was used to glue the optical fiber sensors on structures, such as tunnels and pile foundations [27, 28], but this binder was more suitable for structures with dry surfaces, because the adhesive strength would be too small when used on damp surfaces. As for the shaft lining which needs grouting, the surface of some part of the shaft lining was seeping or flowing with water due to the deep burial depth and a close connection between the sidewall and the surrounding aquifer. The binder, made of the sodium silicate and concrete, is characterized by faster consolidation speed and higher adhesive strength, so it can make the fiber sensor and the shaft lining bond together, which will effectively solve the problems caused by the seeping water.

(2) The repair of shaft lining is faced with such hidden dangers as the problem of shaft lining crack caused by the high-pressure grouting, and the problem of water-gushing and sand-gushing resulted from overflowing serosity along the shaft lining crack [29]. So far, the traditional detection methods of grouting effects include rock coring, sonic testing, and electromagnetic method [2]. Nevertheless, grouting response of the shaft lining is a dynamic process; the static methods mentioned above fail to measure the real-time deformation during the process of grouting. Traditional detection methods, which install stress meter or stress gauge in several monitoring places on the shaft lining, cannot comprehensively record the entire deformation, leading to some damages undetected [29]. By comparison, the BOTDR-based detection method, through the circumferentially and axially laid sensing optical fiber, can establish the shaft deformation monitoring network and detect the additional strain caused by grouting, validate the abnormal area and value of the additional strain, obtain the impact of the ground disturbance upon the shaft lining deformation, and reveal the distribution of serosity along cracks and fracture of the ground. Therefore, this method can effectively guide the informative construction during the grouting process, which guarantees the safety of the shaft lining.

5. Conclusions

(1) In view of the seepage in the grouting segment of shaft lining, the binder, made of sodium silicate and cement, can effectively solve the bonding problem of the sensing fiber in the damp environment. Considering the structure and deformation characteristic of shaft lining, this study puts forward the layout methods of the sensing fiber, including grooving, *Actinobacillus*, and filling binder.

(2) This research constructed the methods of data detection and data processing during grouting and established the distributed detection method of the deformation of shaft lining in grouting, through the axial and circumferential sensing fiber laid in the shaft lining. Based on the experimental example of grouting, it has been found that the distributed optical fiber detection method can effectively identify the grouting condition in the serosity and can offer a new method for the anomaly detection of grouting quantity, thus reinforcing the safety of the shaft lining.

(3) The cement grouting and the chemical grouting act as an interactive system in fixing the shaft lining. Through the distributed detection of the grouting process, the study analyzed the additional strain on the shaft lining caused by each process of grouting and obtained the "saturated" condition of the grouting capacity in the strata. With the advantages of high intensity and high durability in cement slurry and the merits of low viscosity in chemical grout,

the combination of these two methods promoted a uniform deformation in the grouting segment of the shaft lining, which not only could effectively block the leakage problem of the shaft lining but also would prevent the shaft lining from rupturing triggered by concentrated stresses.

Conflict of Interests

The authors declare that there is no conflict of interests regarding the publication of this paper.

Acknowledgments

The work is funded by National Science Foundation for Youth (no. 51004103), China Postdoctoral Science Foundation (no. 20100481175), and the Priority Academic Program Development of Jiangsu Higher Education Institutions.

References

[1] H. Q. Liang, G. S. Zhao, and H. C. Liang, "Theory and practice in the control of shaft-lining rupture through soil grouting," *China Safety Science Journal*, vol. 19, no. 1, pp. 5–9, 2009.

[2] H.-C. Xia and M.-A. Tang, "Mechanism and application of grouting into topsoil to prevent shaft lining from fracturing," *Journal of Mining and Safety Engineering*, vol. 26, no. 4, pp. 407–412, 2009.

[3] X. D. Zhang, Y. R. Han, S. J. Liu, and C. S. Su, "Deformation prediction analysis model for the mine shaft-wall," *Journal of Liaoning Technical University (Natural Science)*, vol. 33, no. 8, pp. 1070–1073, 2014.

[4] C. Zhang, W. H. Yang, J. G. Qi, H. P. Li, and T. Zhang, "Construction technology and monitoring analysis of a new single-layer shaft lining in deep aqueous bedrock during freezing sinking," *Chinese Journal of Rock Mechanics and Engineering*, vol. 31, no. 2, pp. 337–346, 2012.

[5] H.-C. Liang, G.-Q. Zhou, G.-S. Zhao, and B. Liao, "Strain characters of shaft lining crack," *Journal of the China Coal Society*, vol. 35, no. 2, pp. 198–202, 2010.

[6] K. Tsusaka, D. Inagaki, M. Nago, K. Kamemura, M. Matsubara, and M. Shigehiro, "Relationship between rock mass properties and damage of a concrete lining during shaft sinking in the horonobe underground research laboratory project," in *Proceedings of the World Tunnel Congress: Underground—The Way to the Future (WTC '13)*, G. Anagnostou and H. Ehrbar, Eds., pp. 2014–2021, June 2013.

[7] D. M. Pan, H. Zhang, and X. J. Zhao, "Application of ground radar tom ine shaft liner grouting and result inspection," *Coal Science and Technology*, vol. 35, no. 2, pp. 24–26, 2007.

[8] P.-S. Zhang and L.-Q. Guo, "Detection technology by reflection wave for backwall grouting quality of a vertical shaft," *Journal of Mining & Safety Engineering*, vol. 28, no. 1, pp. 115–121, 2011.

[9] N. W. Xu, C. A. Tang, L. C. Li et al., "Microseismic monitoring and stability analysis of the left bank slope in Jinping first stage hydropower station in southwestern China," *International Journal of Rock Mechanics and Mining Sciences*, vol. 48, no. 6, pp. 950–963, 2011.

[10] M. Kihara, K. Hiramatsu, M. Shima, and S. Ikeda, "Distributed optical fiber strain sensor for detecting river embankment collapse," *IEICE Transactions on Electronics*, no. 4, pp. 952–960, 2002.

[11] K. Komatsu, K. Fujihashi, and M. Okutsu, "Application of optical sensing technology to the civil engineering field with optical fiber strain measurement device (BOTDR)," in *Advanced Sensor Systems and Applications*, vol. 4920 of *Proceedings of SPIE*, pp. 352–361, 2002.

[12] H. Ohno, H. Naruse, T. Kurashima, A. Nobiki, Y. Uchiyama, and Y. Kusakabe, "Application of Brillouin scattering-based distributed optical fiber strain sensor to actual concrete piles," *IEICE Transactions on Electronics*, no. 4, pp. 945–951, 2002.

[13] H. Ohno, H. Naruse, M. Kihara, and A. Shimada, "Industrial applications of the BOTDR optical fiber strain sensor," *Optical Fiber Technology*, vol. 7, no. 1, pp. 45–64, 2001.

[14] N. Yasue, H. Naruse, J.-I. Masuda, H. Kinq, T. Nakamura, and T. Yamaura, "Concrete pipe strain measurement using optical fiber sensor," *IEICE Transactions on Electronics*, no. 3, pp. 468–474, 2000.

[15] H. Naruse, Y. Uchiyama, T. Kurashima, and S. Unno, "River levee change detection using distributed fiber optic strain sensor," *IEICE Transactions on Electronics*, no. 3, pp. 462–467, 2000.

[16] H.-H. Zhu, J.-H. Yin, L. Zhang, W. Jin, and J.-H. Dong, "Monitoring internal displacements of a model dam using FBG sensing bars," *Advances in Structural Engineering*, vol. 13, no. 2, pp. 249–261, 2010.

[17] H.-H. Zhu, A. N. L. Ho, J.-H. Yin, H. W. Sun, H.-F. Pei, and C.-Y. Hong, "An optical fibre monitoring system for evaluating the performance of a soil nailed slope," *Smart Structures and Systems*, vol. 9, no. 5, pp. 393–410, 2012.

[18] H.-H. Zhu, B. Shi, J.-F. Yan, J. Zhang, C.-C. Zhang, and B.-J. Wang, "Fiber Bragg grating-based performance monitoring of a slope model subjected to seepage," *Smart Materials and Structures*, vol. 23, no. 9, Article ID 095027, 2014.

[19] J. Q. Gao, B. Shi, W. Zhang, D. Zhang, and H. Zhu, "An experimental study for measuring the distributed strain of reinforced concrete beam using BOTDR," *China Civil Engineering Journal*, vol. 38, no. 9, pp. 74–79, 2005.

[20] C.-D. Piao, B. Shi, G.-Q. Wei, Y.-Q. Zhu, and D. Zhang, "Application of distributed fiber optic sensing techniques in bored pile detection," *Chinese Journal of Geotechnical Engineering*, vol. 30, no. 7, pp. 976–981, 2008.

[21] B. Shi, H. Xu, B. Chen et al., "A feasibility study on the application of fiber-optic distributed sensors for strain measurement in the Taiwan strait tunnel project," *Marine Georesources and Geotechnology*, vol. 21, no. 3-4, pp. 333–343, 2003.

[22] Y.-S. Wang, W.-H. Yang, J.-H. Huang, L. Song, and Y.-L. Ren, "Study of freeze sinking period concrete strain of outer shaft wall of Longgu Coal Mine auxiliary shaft," *Journal of the China Coal Society*, vol. 31, no. 3, pp. 296–300, 2006.

[23] Z.-W. Qian, Z.-Q. Jiang, L.-W. Cao, and Q. Sun, "Research on backfill grouting based on surrounding rock loose circle theory," *Journal of the China Coal Society*, vol. 38, no. 2, pp. 189–193, 2013.

[24] J. Wu and W. W. Qian, "Horizontal ultimate bearing capacity test of high strength reinforced concrete shaft lining," *Journal of Anhui University of Science and Technology (Natural Science)*, vol. 32, no. 4, pp. 56–59, 2012.

[25] T. Han, W.-H. Yang, Y.-L. Ren, and Z.-J. Yang, "Horizontal ultimate bearing capacity of encased steel concrete shaft lining," *Journal of Mining and Safety Engineering*, vol. 28, no. 2, pp. 181–186, 2011.

[26] D. Zhang, B. Shi, and H. Z. Xu, "The BOTDR-based strain monitoring for tunnel," *Journal of Engineering Geology*, vol. 12, no. 4, pp. 422–426, 2004.

[27] G.-Q. Wei, B. Shi, J.-X. Jia, S. Hu, K. Li, and D. Zhang, "Application of distributed optical fiber sensing to testing inner force of prefabricated piles," *Chinese Journal of Geotechnical Engineering*, vol. 31, no. 6, pp. 911–916, 2009.

[28] H.-L. Fu, "Strain variation regularity of shaft lining during grouting reinforcement process for deep topsoil ground," *Rock and Soil Mechanics*, vol. 24, pp. 21–23, 2003.

[29] G.-Q. Zhou, Y.-Z. Liu, X.-W. Feng, and G.-S. Zhao, "Application and effect of grouting in surrounding soil on releasing and restraining additional stress of shaft lining," *Chinese Journal of Geotechnical Engineering*, vol. 27, no. 7, pp. 742–745, 2005.

Hindawi Publishing Corporation
Journal of Sensors
Volume 2015, Article ID 108209, 10 pages
http://dx.doi.org/10.1155/2015/108209

Research Article

Development and Application of Smart Geogrid Embedded with Fiber Bragg Grating Sensors

Zheng-fang Wang,[1] Jing Wang,[1] Qing-mei Sui,[1,2] Xun-mei Liang,[3] Lei Jia,[1] Shu-cai Li,[4] and Shi-de Lu[3]

[1]*College of Control Science and Engineering, Shandong University, Jingshi Road 17923, Jinan 250061, China*
[2]*Shandong University Suzhou Graduate School, Lingquan Street 377, Suzhou 215123, China*
[3]*TAIAN Road Engineering Materials Co. Ltd., Taiwen Road, Taian 271000, China*
[4]*Geotechnical Engineering Center, Shandong University, Jingshi Road 17923, Jinan 250061, China*

Correspondence should be addressed to Jing Wang; wangjingkz@sdu.edu.cn

Received 8 October 2014; Revised 18 December 2014; Accepted 28 December 2014

Academic Editor: Fei Dai

Smart geogrids embedded with fiber Bragg grating (FBG) for reinforcement as well as measurement of geotechnical structures have been developed. After the fabricating process of the geogrids is detailed, finite element (FE) simulations are conducted to analyze the strain distribution of geogrids and the strain transfer characteristics from geogrids to fiber optic. Results indicate that FBG should be deployed in the middle of the geogrids rib to make sure that uniform strain distribution along the FBG. Also, PVC protective sleeves, which are used to protect fiber optic when integrated with geogrids, have smaller strain transfer loss than nylon sleeves. Tensile experiments are conducted to test strain measurement performance of proposed geogrids, and the results demonstrate that proposed smart geogrids have good linearity and consistency. Temperature experiments show that FBG embedded in geogrids has higher temperature sensitivity, and the temperature induced error can be compensated by an extra FBG strain-independent sensor. Furthermore, designed smart geogrids are used in a geotechnical model test to monitor strain during tunnel excavation. The strain tendency measured by smart geogrids and traditional strain sensor agree very well. The results indicate that smart geogrids embedded with FBGs can be an effective method to measure strains for geological engineering related applications.

1. Introduction

Geosynthetics in form of geogrids have been extensively utilized to fulfill reinforcement of geotechnical structures such as dikes, dams, railways, embankments, landfills, and slopes [1–4]. By integrating with a series of sensors, the geosynthetics are capable of sensing strains, temperature or other parameters when used for reinforcement [5]. These multifunctional or even "smart" geosynthetics can sense and react to critical mechanical deformation/load or other external stimuli in geotechnical structure, which make them promising materials in geological engineering to prevent potential disasters and ensure safe construction and operation of civil engineering.

Over the past two decades, adhered electrical resistance strain gauges had been widely used as sensing components when integrated with geogrids, and diverse methods for installing strain gauges on geogrids were investigated [6–9]. However, the strain gauges adhered on geogrids were susceptible to fall off, and the gauges might be affected by moisture or electromagnetic interference (EMI) when being used in harsh environments, which provided unreliable strain measurement results.

Fiber optic sensors, both distributed fiber optic sensor and quasidistributed optic fiber Bragg grating (FBG) sensor, have a series of advantages over traditional electrical sensors when integrated with Geogrids, soil nails and other geotechnical reinforcements [10–16]. Due to their fibrous nature, fiber optic sensors can be ideally processed like standard warps threads to embed within geogrids. Moreover, fiber optic sensors exhibit better long-term reliability, since they are noncorrosive, immune to EMI, waterproof, and

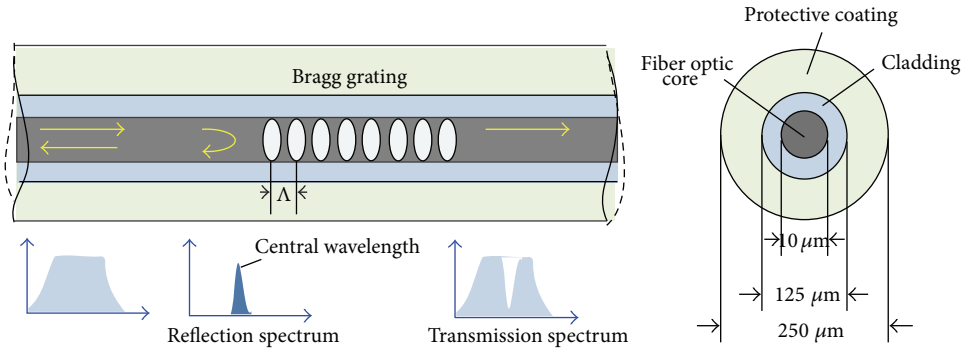

Figure 1: Schematic principle of fiber Bragg grating.

intrinsically safe. Additionally, fiber optic sensors based sensing system can be used for distributed/quasidistributed real-time monitoring and then delivering all sensing information through one single fiber optic cable [17–21]. Therefore, the smart geogrids integrated with fiber optic sensor have attracted considerable attention. Krebber et al. developed smart geotextiles integrated with distributed silica optic fiber (for strain of less than 1%) and polymer optic fiber (POF) (for strain of more than 40%), respectively, and applied them for dike and slope monitoring [22–24]. These smart geotextiles which are on the basis of distributed fiber optic sensor are ideal for geotechnical structures with large dimensions. Nevertheless, due to the limitation of its strain measurement accuracy and spatial resolution, the distributed fiber optic sensor is not applicable for some applications where accurate measurement of local strain is required (such as geotechnical model test). As a widely used fiber optic component, FBG is able to measure local strain with better accuracy and reliability compared to the distributed fiber optic sensor, it is thus necessary to investigate smart geogrids embedded with FBG for the demands of more extensive applications.

In this research, an in-depth study regarding development and application of smart geogrids embedded with fiber Bragg grating sensors is conducted. Two finite element models are built to analyze the strain distribution of FBG embedded in the geogrids and the strain transfer behavior from geogrids to FBG. Then, details of the calibration experiments, including tensile experiments and temperature experiments are reported, and the experimental results are analyzed. Finally, the designed smart geogrids are utilized in a geotechnical model test to monitor strain variation during the excavation of tunnel. The results demonstrate that proposed smart geogrids are a promising solution for reinforcement and measurement of geotechnical structure with small dimension and could be utilized in civil engineering related applications.

2. Development of Smart Geogrids Embedded with FBG

2.1. FBG Sensing Principle. The principle of FBG technology is shown in Figure 1. It is formed by inscribing permanent and periodic modulation of the refractive index along a short section (<10 mm) inside the fiber optic core [25]. This periodic refractive index demodulation, called as grating, enables FBG to reflect light with special wavelength on the basis of the Bragg law:

$$\lambda_B = 2 \cdot n_{\text{eff}} \cdot \Lambda, \tag{1}$$

where λ_B is the Bragg wavelength representing the wavelength at which reflection occurs, Λ is the grating period, and n_{eff} is the effective refractive index of fiber core.

The reflected Bragg wavelength λ_B will shift as a function of ambient temperature T and/or axial strain of fiber optic ε, as expressed in

$$\Delta\lambda_B = \lambda_B \cdot \left[(\alpha + \xi) \cdot \Delta T + \left(1 - P_e\right) \Delta\varepsilon\right], \tag{2}$$

where $\Delta\lambda_B$ is the wavelength shift, α and ξ are coefficient of thermal expansion and thermal-optic coefficient, respectively, and P_e, whose value is 0.22, is valid photoelastic coefficient. Thus, $\Delta\lambda_B$ is proportional to axial strain ε and/or temperature T.

2.2. Fabrication of Smart Geogrids. It is a pivotal and challenging task to integrate fiber optic into geogrids during the weaving process. The warps knitted PET geogrids are selected as the carrier of fiber optic cable due to their yarns are not easy to bend in the entire weaving process. A bunch of PET warps thread is replaced by the fiber optic cable which consist of protective sleeves and fiber optic with FBG arrays (10 mm gauge length). The cable is then guided to machine with other warps thread and wove with weft threads. Double-axis warps-knitting machine utilized for fabrication of smart geogrids, needs to be operated very carefully so as to precisely control the movement of the warps threads, weft threads, and binder yarns. The junctions of warps (both with and without fiber optic cable) and weft threads are bound automatically by binder yarns with high strength.

Geogrids being knitted only are unavailable for application since their low stiffness. Also, their junctions are susceptible to slip, which may cause the embedded fiber optic to be stripped from geogrids. Thus it is essential to coat the geogrids by special polymer. Geogrids being coated have high stiffness, resistance to corrosion, and better integration with embedded fiber optic. It is thereby applicable to geotechnical

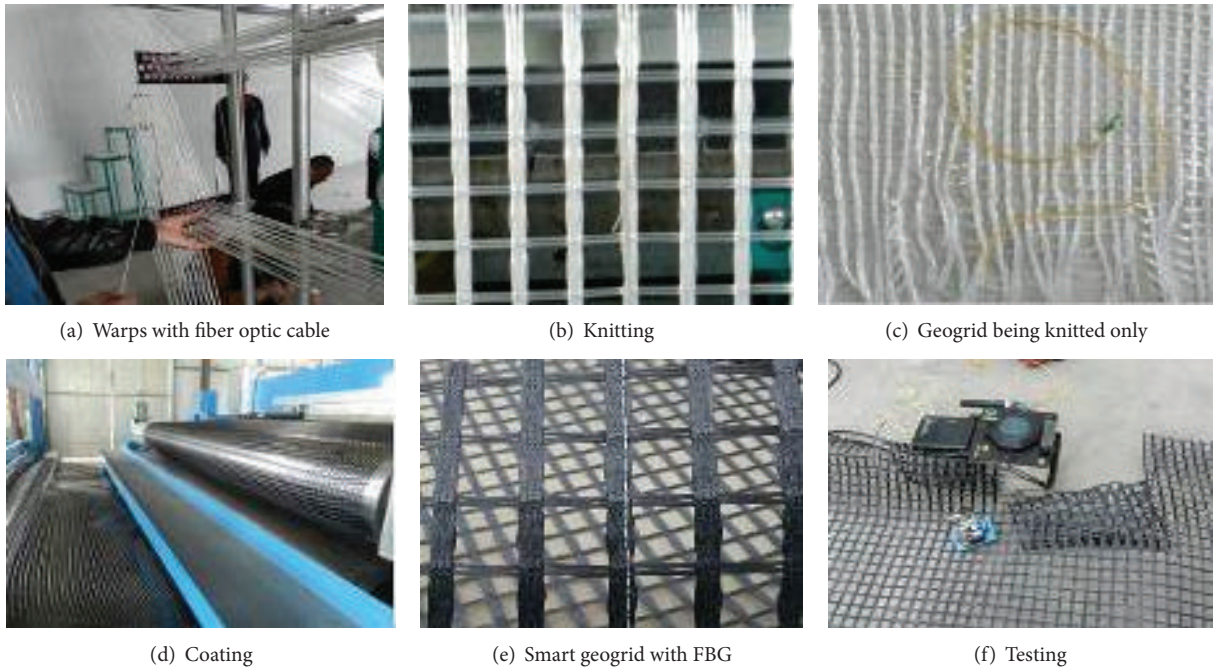

(a) Warps with fiber optic cable (b) Knitting (c) Geogrid being knitted only

(d) Coating (e) Smart geogrid with FBG (f) Testing

Figure 2: Fabrication of smart geogrids.

engineering for reinforcement and measurement. Figure 2 shows the fabricating steps of warps-knitted geogrids embedded with FBG.

Three important issues need to be highlighted during the fabrication: (1) To minimize the influence of bending which is inevitable in geotechnical engineering related application, each bunch of warps threads is marked and the threads-guiding equipment is refitted to adjust the fiber optic into the centerline of geogrids' thickness direction. (2) Since the fiber optic with FBG is more fragile compared with POF and normal silica fiber optic without FBG, the tightly bonded polymer protective sleeves are designed to protect fiber optic with FBG and ensure strain transfer from geogrids to FBG. The protective sleeves can also work as a buffer to protect fiber optic when strain on the geogrids exceeds the maximum strain of the fiber optic. (3) When suffering from nonuniform strain, the spectrums of FBG will distort and cause unreliable measurement results. To solve this issue, finite element simulation is used to analyze strain distribution profile of geogrids and determine optimal location for FBG where strain profile is uniform.

3. Simulations and Analysis

To get reliable strain results, one important task when considering integration of fiber optics into geogrids is to ensure accurate strain transfer from ribs of geogrids to FBG. Another factor need to be noted is strain distribution profile along embedded FBG should be uniform to prevent spectrum being distorted. In this section, finite element simulations are utilized to simulate the strain distribution of geogrids with different specifications and to analyze the strain transfer characteristics from geogrids to fiber optic cable with FBG.

3.1. Strain Distribution of Geogrids under Tensile Displacement. Two finite element models of warps knitted PET geogrids with different specifications were established, as shown in Table 1. Six 3D cylinders with a diameter of 3 mm were set up and bonded together to simulate the six bunches of warps threads. For the weft threads, 3D cuboid models were built, and the junctions of warps and wefts threads were bonded. One end of the geogrids was fixed, and uniform tensile displacement of 3.6 mm, which is 1% elongation (10000 $\mu\varepsilon$), was applied on the other end of the geogrids model. The visco-elastic model was selected for calculation.

Figure 3 shows the simulated results of two geogrids (mesh size 40 $*$ 40 mm and 25.4 $*$ 25.4 mm) when elongation is 1%. The strain along the axis where fiber optic cable is embedded is shown in Figure 4. The strain distribution profiles of both geogrids are not uniform under tensile stress. As can be seen in Figure 4(a), strains along the two geogrids' ribs are approximately equal whereas the strain at the junction area shows a significantly decreases due to the stress concentration. The strain profiles within one rib are shown in Figure 4(b) which depicts approximate 32 mm in the middle section of the rib distributed evenly for geogrids (40 $*$ 40 mm), while for geogrids (25.4 $*$ 25.4 mm) the length is about 18 mm. Due to the difficulty for precisely controlling the position of FBGs, geogrids (40 $*$ 40 mm) are better for the integration of FBG (10 mm grating gauge) in contrast to geogrids (25.4 $*$ 25.4 mm).

3.2. Analysis of Strain Transfer. To understand strain transfer behavior of smart Geogrids embedded within FBG and determine appropriate polymer materials to protect fiber optic, finite element model of geogrids (40 $*$ 40 mm) was built to analyze strain transfer from geogrids' ribs to fiber

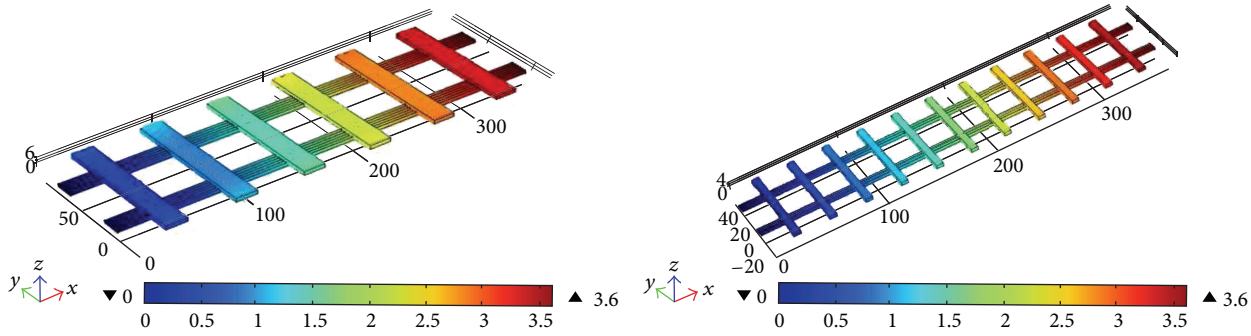

(a) Geogrids with mesh size of 40 ∗ 40 mm (b) Geogrids with mesh size of 25.4 ∗ 25.4 mm

FIGURE 3: Simulation model and displacement display.

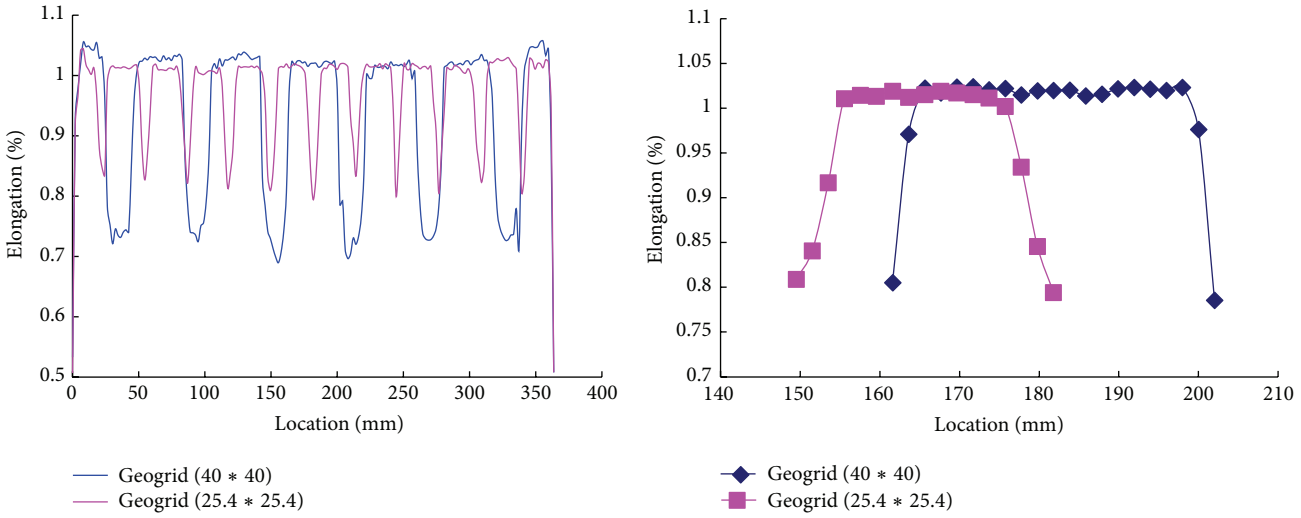

(a) Strain distribution of geogrids (b) Strain distribution of one rib

FIGURE 4: Strain distribution of two geogrids.

TABLE 1: Specifications of the two geogrids models.

	G1	G2
Mesh Size (mm ∗ mm)	40 ∗ 40	25.4 ∗ 25.4
Number of Warps	6	3
Number of Wefts	6	2
Length (mm)	360	360
Width (mm)	116	64
Thickness (mm)	3	2

TABLE 2: Parameters used in the FE simulation.

	PVC	Nylon	Fiber optic
Elastic modulus (GPa)	3.92	8.3	73.1
Poisson's ratio	0.38	0.28	0.17
Diameter (mm)	1	1	0.25

optic. Since the protective sleeves are tightly adhered with fiber optic to minimize strain transfer loss, and the fiber optic cable is knitted and coated with PET warps threads together, it is assumed in the simulation that interface between geogrids and protective sleeve is no-slipping and so is the interface between protective sleeve and fiber optic.

Both PVC and nylon were selected as protective sleeve in the simulation. Parameters of the two materials are shown in Table 2, the other parameters used in the simulation are provided by industrial collaborator (TAIAN Road Engineering Materials co. Ltd). Six parallel 3D cylinders each with a diameter of 3 mm were built as the model of six bunches of warps threads, and fiber optic was modeled by one 3D cylinder with a diameter of 0.25 mm. Between the fiber optic and warps threads, one 3D annular model with a thickness of 0.375 mm was built as the protective sleeve. All the interfaces were bonded together. The fiber optic cable was placed in the middle of the six warps threads as can be shown in Figure 5.

The visco-elastic material model was applied on warps threads and its coating, while the elastic material model was selected for fiber optic and protective sleeve. The fiber optic, protective sleeve and coating were defined as free constraint,

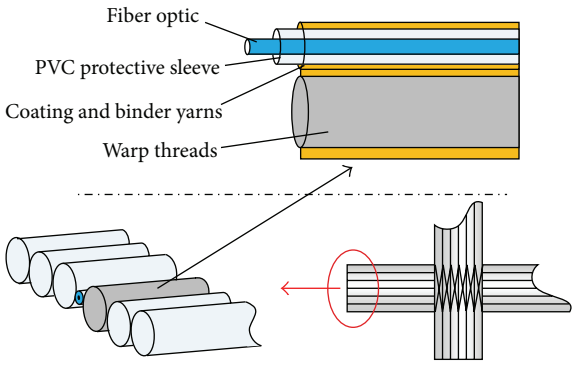

Figure 5: Schematic of strain transfer model.

and 0.4 mm displacement (1% elongation) was prescribed on the warps threads only. Simulation results are shown in Figure 6. The displacement results of fiber optic and one warp thread next to the fiber optic were displayed while other warp threads and the coating were hidden.

Comparison of the axial elongation of the two FBGs protected by PVC sleeve and nylon sleeve, respectively is shown in Figure 7. It is evident that with a tensile strain of 10000 $\mu\varepsilon$ in the warps thread of geogrids, the fiber optic inside the PVC sleeve gets a strain of 9859 $\mu\varepsilon$, which is about 98% of the actual strain, while fiber optic inside the nylon sleeve gets a strain of 9572 $\mu\varepsilon$, which is about 95% of the applied strain. In contrast to nylon sleeve, the fiber optic with PVC sleeve is more suitable for smart geogrids as its higher strain transfer rate.

The strain transfer rates from geogrids to fiber optic with PVC sleeves in different elongations (i.e., 0.05%, 0.1%, 0.3%, 0.5%, 1%, 1.5%, 2%, and 3%) are calculated, respectively (Figure 8). It indicates that the strain transfer rate will change with the applied elongation. Moreover, the minimum strain transfer rate (maximum strain loss) is approximately 0.983 when elongation is equal to 0.5%. Although there is a slightly strain transfer loss in the smart geogrids, it is still acceptable for the strain measurement of geotechnical engineering application.

4. Experiments and Discussions

The sensing performance of proposed smart geogrids embedded with FBG is crucial to the application of smart geogrids for reinforcement as well as measurement. Thus, tensile experiments as well as temperature experiments were conducted to test the sensing characteristics. Warps knitted geogrids with mesh size of 40 ∗ 40 mm were utilized as testing geogrids and FBGs with PVC sleeves were embedded in the warp threads.

4.1. Tensile Experiments. Two series of tensile experiments were carried out. The tensile displacement was applied by displacement calibrating bench, and the applied displacements were recorded by a digital displacement sensor with an accuracy of 0.01 mm. The wavelengths of FBGs inside the geogrids were monitored by interrogator SM125, which has wavelength measurement accuracy of 1 pm from 1510 nm to 1590 nm. The experimental setup is shown in Figure 9.

In the first stage, two ends of the testing geogrids embedded with one FBG with wavelength of 1540 nm were clamped on the calibrating bench. The length of testing geogrids was 400 mm, and FBG was deployed in the middle of the testing geogrids. The geogrids were prestretched at the beginning of the each loading cycle to make sure the FBG inside geogrids was strained. The displacement was applied from 0 mm to 1 mm, corresponding to 0~2500 $\mu\varepsilon$, in an increment of approximately 0.1 mm (250 $\mu\varepsilon$) per step. After the loading cycle finished, the calibration bench was reset manually and the prestress was applied on the geogrids again. The same process was conducted three times, and the wavelength variation of embedded FBG with strain was obtained, as shown in Figure 10.

It can be seen in Figure 10 that the wavelength of FBG increases linearly with the elongation at the range of 0~2500 $\mu\varepsilon$. The relationship between Bragg wavelength and strain ε of each time was fitted by Least-square algorithm, and the functions, respectively, are

$$\begin{aligned} \lambda_{B1\text{st}} &= 9.10 \times 10^{-4} \cdot \varepsilon + 1540.610; \qquad R^2 = 0.9906; \\ \lambda_{B2\text{nd}} &= 8.93 \times 10^{-4} \cdot \varepsilon + 1540.722; \qquad R^2 = 0.9994; \\ \lambda_{B3\text{rd}} &= 8.84 \times 10^{-4} \cdot \varepsilon + 1540.822; \qquad R^2 = 0.9986. \end{aligned} \tag{3}$$

The strain sensitivity each time is 0.910 pm/$\mu\varepsilon$, 0.893 pm/$\mu\varepsilon$, and 0.884 pm/$\mu\varepsilon$, respectively, and R^2 of each loading cycle is 0.9906, 0.0094, and 0.9986, respectively, which indicate FBG inside the geogrids has good linearity. As expected, strain transfer losses exist although the value slightly larger than the simulated result. The strain sensitivity gradually decreases with testing time, which is partly due to the creep characteristics of PVC sleeve and geogrids which are fabricated by PET threads and polymer coating. In the first loading cycle, when Geogrids was stretched, the stress was transferred to the FBG and then led to wavelength shift. In the second loading cycle, due to the creep characteristics, the geogrids could not be recovered to its original length, and FBG was still stretched. If now same displacement was applied on the geogrids, FBG might suffer from less displacement which led to a smaller wavelength shift. As a result, the sensitivity decreased compared with that at the first time. The same situation might happen in the third loading cycle. Another reason for this phenomenon is that due to the precision limitation of the experiment setup, the calibrating bench need to be manually adjusted every time in order to prestretch the geogrids, which might induce errors. By averaging the sensitivity obtained by multiple tests, the deviation of can be minished. It should be noted that the deviation of original wavelength was attributed to the prestretching of the testing geogrids as the applied prestress was uneasy to be precisely controlled.

In the second series of experiments, geogrids embedded with four FBGs were tested to validate the response of FBGs in the same geogrids. The fiber optic cable was embedded in the centerline of warps threads and the positions of the four FBGs are as Figure 11.

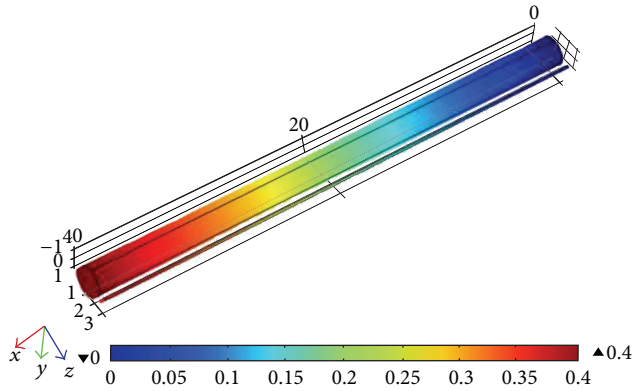

Figure 6: Displacement display of warps thread and fiber optic.

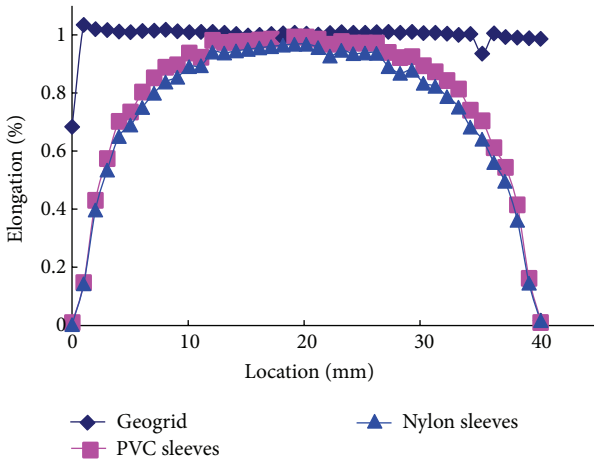

Figure 7: Simulation results of strain transfer.

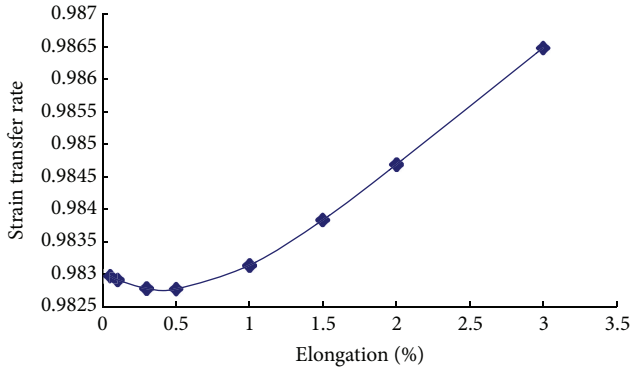

Figure 8: Variation of strain transfer rate with elongation.

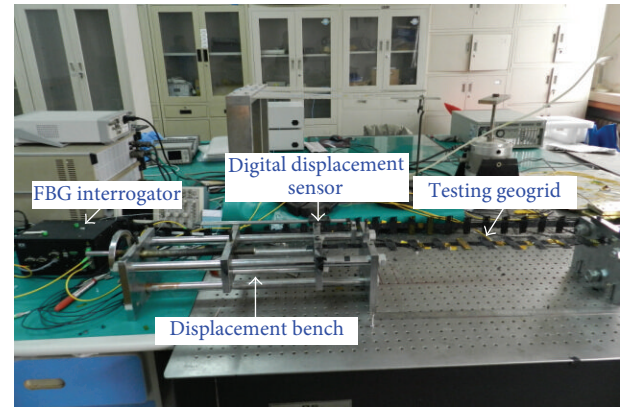

Figure 9: Tensile experiments setup.

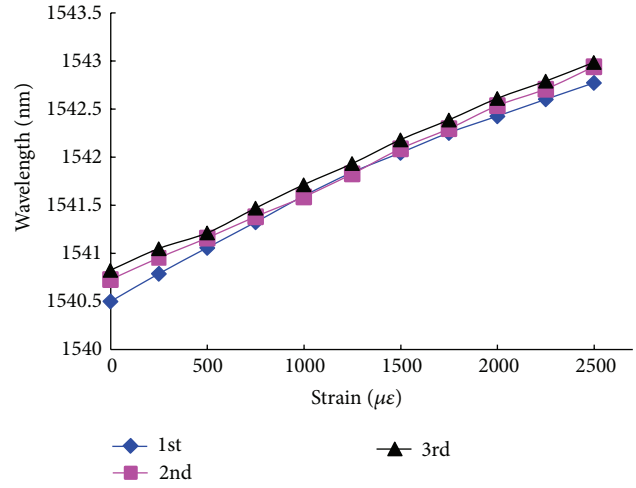

Figure 10: Results of tensile experiment.

The wavelengths of the four FBGs were 1536.187 nm, 1542.732 nm, 1548.475 nm, and 1552.721 nm, respectively. The length of testing geogrids was 800 mm, and displacement was applied from 0 mm to 1.6 mm, corresponding to 0~2000 $\mu\varepsilon$, in an increment of approximately 0.2 mm (250 $\mu\varepsilon$) per step. Experimental procedure was same as the first stage.

To compare consistency of the four FBGs, the Bragg wavelength shifts $\Delta\lambda$ for each FBG are calculated by subtracting the original wavelength. Variation of $\Delta\lambda$ with strain ε is shown in Figure 12. It can be seen that despite the slight fluctuations, the wavelengths of all FBGs shift linearly

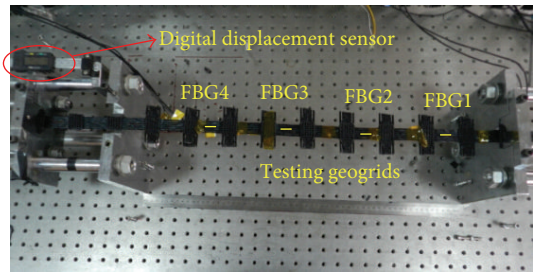

Figure 11: Position of four FBGs in the geogrids.

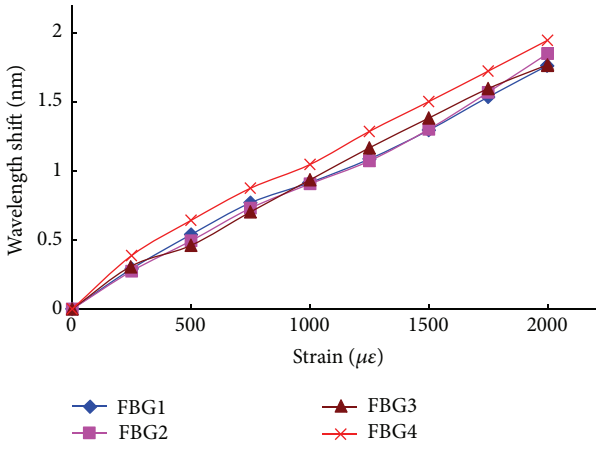

Figure 12: Results of tensile experiment.

with the applied strain. The relationship between Bragg wavelengths λ and strain ε of each FBG are

$$\begin{aligned}
\lambda_1 &= 8.42 \times 10^{-4} \cdot \varepsilon + 1536.257; \quad R^2 = 0.994;\\
\lambda_2 &= 8.84 \times 10^{-4} \cdot \varepsilon + 1542.761; \quad R^2 = 0.996;\\
\lambda_3 &= 8.83 \times 10^{-4} \cdot \varepsilon + 1548.518; \quad R^2 = 0.998;\\
\lambda_4 &= 9.29 \times 10^{-4} \cdot \varepsilon + 1552.838; \quad R^2 = 0.993.
\end{aligned} \tag{4}$$

The results demonstrate that four FBGs inside the geogrids exhibit good linearity and consistency in the tensile test, and mean strain sensitivity of each FBG is 0.842 pm/$\mu\varepsilon$, 0.884 pm/$\mu\varepsilon$, 0.883 pm/$\mu\varepsilon$, and 0.929 pm/$\mu\varepsilon$, respectively.

4.2. Temperature Experiments. As FBG is not only sensitive to axial strain but also to ambient temperature, it is necessary to perform experiments to evaluate the temperature performance of embedded FBG. A bared FBG and smart geogrids embedded with FBG were put into the temperature calibrating oven which provided constant temperature. The wavelength of FBG inside Geogrids was 1540 nm, and so was the bared FBG. Temperature was varied from 25°C to 65°C with an increment of 10°C per step. Each step last for 1 hour for stabilization before recording the wavelength of the two FBGs.

Figure 13 shows the wavelength variation of the two FBGs with temperature. Within a temperature range 25°C–65°C, the wavelength of the FBG inside the geogrids increase with temperature, and its sensitivity is approximately 0.014 nm/°C. Compared with the bared FBG, whose sensitivity is 0.011 nm/°C, the embedded FBG exhibit larger sensitivity due to the influence of geogrids. Even though the result of embedded FBG did not exactly match with linear profile, the measurements were evenly distributed around it. Thus the temperature induced wavelength shifts of FBGs inside the geogrids could be compensated by extra FBG temperature sensors when using in practical application.

5. Model Test

During the construction of tunnel and other underground engineering, water inrushes occur frequently with disastrous consequences. For most of tunnels, the filling-type fissure widely exists in the rock as one kind of typical geological structure. To investigate the failure mechanism when water inrush happens in tunnel with the filling-type fissure, a geological model test was carried out to investigate water inrush process caused by filling body seepage failure in the practical engineering.

5.1. Model Test and Testing Procedure. A 3D visual water inrush model test system at a size of 3.0 × 1.2 × 2.7 m ($L \times W \times H$) was set up to investigate tunnel's instability process during excavation (Figure 14). The model test system consisted of frame system, pressure loading system, and real-time data acquisition system. The frame system was made of steel combining with tempered glasses which were glued and sealed to realize 3D visualization. Excavation section was left in the front of tempered glasses, and one hole on each side of the frame system was left for sensor's wires. Similar materials for both surrounding rock as well as the filling body were developed and filled inside the frame system to simulate the properties of geological structure. The under width of fissure was 5 cm while the upper width was 10 cm, and the length of fissure was 17 cm. Angle of fissure with tunnel axis is 30°, and so the vertical direction, as shown in Figure 15. On the top of the similar materials a water storage section consisted of a permeable plate and pipes with holes was designed to provide water pressure for the system. Water was pumped from water tank to the water storage section. A water-resisting plate was covered and sealed to make the whole system water-tight. Jacks controlled by hydraulic pressure system were used for controllable load.

The real-time monitoring system was utilized to acquire information of key parameters such as: displacement, seepage, pressure, and strain. The sensors and geogrids were imbedded to the designed position when filling the similar materials. Three FBGs with the wavelength of 1536.187 nm, 1542.732 nm, and 1548.475 nm respectively were embedded in the geogrids, while a piece of FBG (1552.721 nm wavelength) embedded smart geogrids, which was protected to be strain-independent, was used for temperature compensation. Smart geogrids were placed at a groove behind the fissure to evaluate

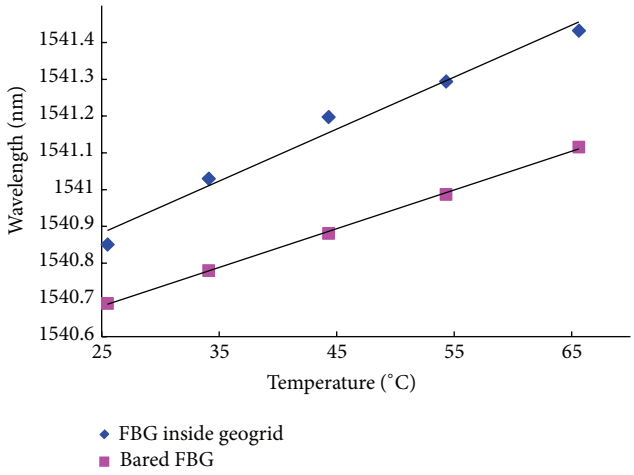

Figure 13: Results of temperature experiment.

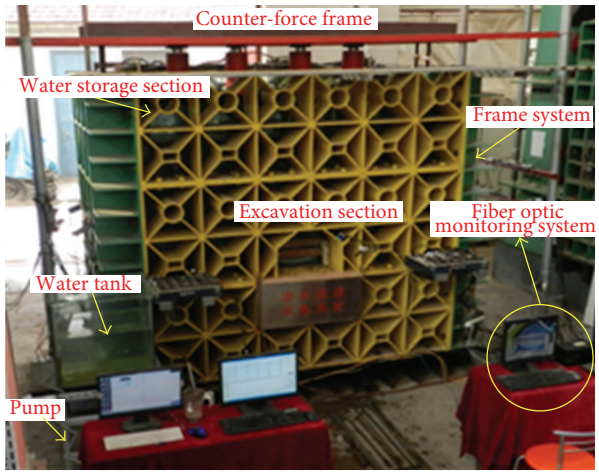

Figure 14: Photograph of the model test system.

strain variation during tunnel excavation. Each end of the geogrids was bound with a section of a PVC pipe which was inserted into the similar materials. Tense steel wires were bound and glued with PVC pipes at one end, and fixed on the steel frame at the other end. During the whole imbedding process, we kept tensing the geogrids to avoid bending. Similar materials were covered on tense geogrids and steel wires and then compacted to make sure no displacement on the boundary of the geogrids. Due to the water issue, the traditional strain gauges without waterproof were not suitable to be used in the model as the moisture might impact the strain reading. So FBG based strain sensor, which was developed by adhering 3 FBGs (vertical, horizontal, and slant 45°) on one surface of similar material block at a size of 3 cm × 3 cm × 3 cm, was utilized as the traditional strain monitoring approach. The strain sensor, which was placed at one side of the fissure, was closed to the position of FBG2. The horizontal strain collected by this sensor was used to compare with strain collected by Geogrids. FBG interrogator was used to acquire wavelength signal and the data were saved in the computer. The model test system and arrangement of Smart geogrids are shown in Figure 15.

The constant water pressure was loaded in the water storage section before excavation. The benching tunneling method was adopted for the excavation at a footage of 3 cm per step, while lower bench was 12 cm behind the upper bench during the excavation. The tunnel had a total length of 60 cm, and the process consisted of 24 steps. Supporting was one step behind the excavation. The next step would begin after the tunnel was stable.

5.2. Results and Discussions. Figure 16 shows the strains measured by the smart geogrids and strain sensor during tunnel excavation. At the beginning of excavation (Step 1–Step 8), the variation of measured strains increased gradually as surrounding rock and filling body in the fissure were relatively steady. Due to the water pressure, filling body which consisted of similar materials with large particles and low strength was compressed. As a result, the measured strains showed a slightly increase from Step 2 to Step 4. At Step 5 and Step 6, the strains decreased probably because water which was originally reserved in the filling body was permeated into tunnel through some cracks. This phenomenon was also captured by the strain sensor. From Step 9 to Step 13, as tunnel face went through the fissure, the stress of surrounding rock and filling body was released, which led to a rapid increase of the strains. At this stage, the strain variation measured by the strain sensor was larger than the one measured by FBG2 of Geogrids, which is possibly because the strain sensor was placed more closed to fissure. After Step 13, the tunnel face had gone through the fissure, but the strains kept increasing until Step 16. Thereafter, the strains were gradually stabilized. Although the strains measured by Geogrids were slightly smaller than that measured by strain sensor, the tendency agreed very well. The strain of FBG2 which was close to arch crown was larger than strains sensed by the other two FBGs during the whole excavation process. This phenomenon indicated that the deformation of arch crown was larger.

During the total process of model test, the smart geogrids exhibited desirable performance. The test results demonstrate that proposed smart geogrids embedded with FBG can be an effective and promising geosynthetics method for the real-time monitoring of strains for geological model test and other geotechnical engineering related applications.

6. Conclusion

This paper develops smart geogrids embedded within FBGs for reinforcement and measurement of geotechnical engineering applications as well as geotechnical model tests. The fabricating process of smart geogrids has been introduced in detail. The strain distribution within the warps threads of geogrids' ribs is investigated by finite element simulation. To protect the fragile fiber optic and minimize strain transfer error, the strain transfer characteristics of geogrids embedded with fiber optic have been analyzed base on the simulation results, which indicate that protective sleeve made by PVC have better strain transfer performance than that made by

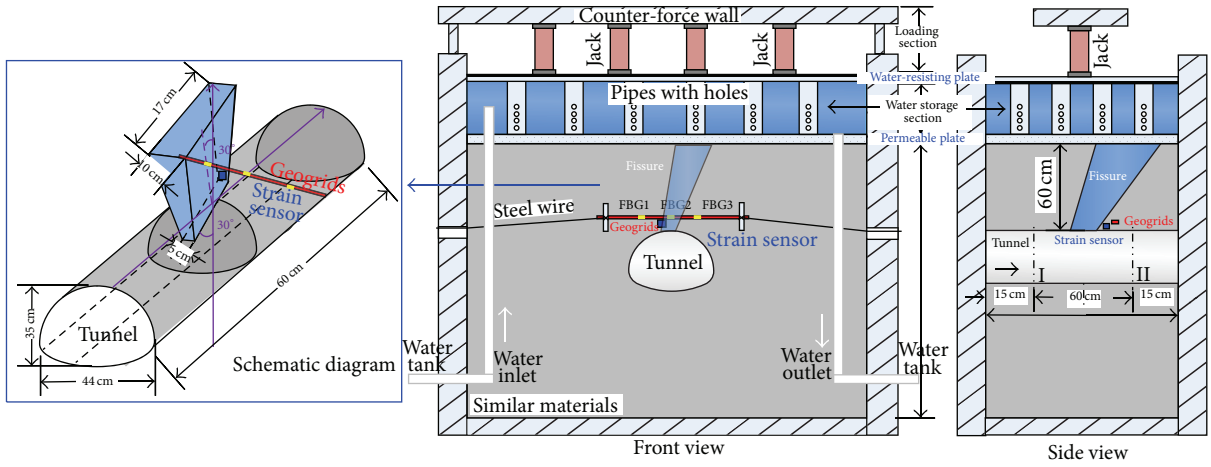

Figure 15: The model test system and arrangement of Smart geogrids.

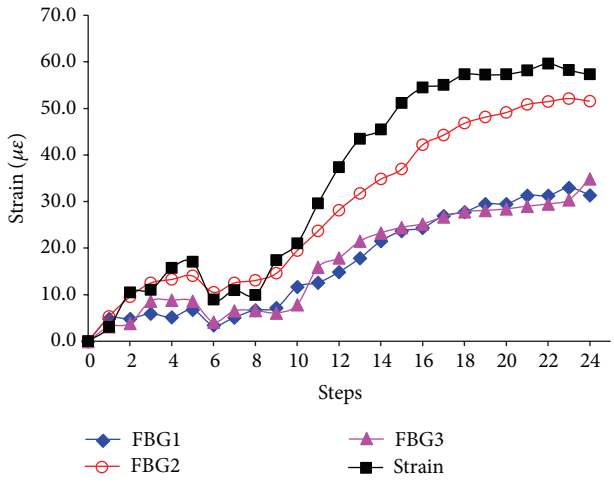

Figure 16: Strain results of Geogrids and strain sensor.

nylon, and the minimum strain transfer rate of PVC sleeves is approximately 0.983 when elongation is 0.5% at a the range of 0%~3%. A series of experiments, including tensile experiments and temperature experiments, have been conducted to verify the performance of proposed smart geogrids. The results of tensile experiment demonstrate that the wavelength of FBGs embedded within geogrids varies linearly with the tensile displacement, and the proposed smart geogrids also exhibit good consistency. Temperature experiment show that the temperature sensitivity of FBG integrated with geogrids is slightly higher than that of the normal FBG, and the temperature induced wavelength shifts can be compensated by an extra FBG temperature sensors. Finally, the designed smart geogrids are used in a geotechnical model test to monitor strains during the tunnel excavation, and results indicate that proposed smart geogrids embedded with FBGs can be usd effectively to measure strains for geological engineering related applications.

Conflict of Interests

The authors declare that there is no conflict of interests regarding the publication of this paper.

Acknowledgments

The research of this paper is supported by the National Science Foundation of China (41472260 and 41202206) and the Science Project of Suzhou City (SYG201306). The authors also express their appreciation to TAIAN Road Engineering Materials co. Ltd.

References

[1] M. A. El Sawwaf, "Behavior of strip footing on geogrid-reinforced sand over a soft clay slope," *Geotextiles and Geomembranes*, vol. 25, no. 1, pp. 50–60, 2007.

[2] K. Kazimierowicz-Frankowska, "Influence of geosynthetic reinforcement on the load-settlement characteristics of two-layer subgrade," *Geotextiles and Geomembranes*, vol. 25, no. 6, pp. 366–376, 2007.

[3] G. M. Latha and V. S. Murthy, "Effects of reinforcement form on the behavior of geosynthetic reinforced sand," *Geotextiles and Geomembranes*, vol. 25, no. 1, pp. 23–32, 2007.

[4] H. Zhou and X. Wen, "Model studies on geogrid- or geocell-reinforced sand cushion on soft soil," *Geotextiles and Geomembranes*, vol. 26, no. 3, pp. 231–238, 2008.

[5] K. S. C. Kuang, C. Y. Tan, S. H. Chew, and S. T. Quek, "Monitoring of large strains in submerged geotextile tubes using plastic optical fibre sensors," *Sensors and Actuators A: Physical*, vol. 167, no. 2, pp. 338–346, 2011.

[6] R. K. Rowe and C. T. Gnanendran, "Geotextile strain in a full scale reinforced test embankment," *Geotextiles and Geomembranes*, vol. 13, no. 12, pp. 781–806, 1994.

[7] R. K. Rowe and B. L. J. Mylleville, "A geogrid reinforced embankment on peat over organic silt: a case history," *Canadian Geotechnical Journal*, vol. 33, no. 1, pp. 106–122, 1996.

[8] C. T. Gnanendran and A. P. S. Selvadurai, "Strain measurement and interpretation of stabilising force in geogrid reinforced," *Geotextiles and Geomembranes*, vol. 19, no. 3, pp. 177–194, 2001.

[9] B. V. S. Viswanadham and D. König, "Studies on scaling and instrumentation of a geogrid," *Geotextiles and Geomembranes*, vol. 22, no. 5, pp. 307–328, 2004.

[10] B.-J. Wang, K. Li, B. Shi, and G.-Q. Wei, "Test on application of distributed fiber optic sensing technique into soil slope monitoring," *Landslides*, vol. 6, no. 1, pp. 61–68, 2009.

[11] H.-H. Zhu, J.-H. Yin, A. T. Yeung, and W. Jin, "Field pullout testing and performance evaluation of GFRP soil nails," *Journal of Geotechnical and Geoenvironmental Engineering*, vol. 137, no. 7, pp. 633–642, 2011.

[12] W. R. Habel and K. Krebber, "Fiber-optic sensor applications in civil and geotechnical engineering," *Photonic Sensors*, vol. 1, no. 3, pp. 268–280, 2011.

[13] H.-H. Zhu, A. N. L. Ho, J.-H. Yin, H. W. Sun, H.-F. Pei, and C.-Y. Hong, "An optical fibre monitoring system for evaluating the performance of a soil nailed slope," *Smart Structures and Systems*, vol. 9, no. 5, pp. 393–410, 2012.

[14] C.-C. Zhang, H.-H. Zhu, Q. Xu, B. Shi, and G. Mei, "Time-dependent pullout behavior of GFRP soil nail in sand," *Canadian Geotechnical Journal*, vol. 51, pp. 1–10, 2014.

[15] X. Weng, H.-H. Zhu, J. Chen, D. Liang, B. Shi, and C.-C. Zhang, "Experimental investigation of pavement behavior after embankment widening using a fiber optic sensor network," *Structural Health Monitoring*, vol. 14, no. 1, pp. 46–56, 2014.

[16] C.-C. Zhang, H.-H. Zhu, B. Shi, F.-D. Wu, and J.-H. Yin, "Experimental investigation of pullout behavior of fiber-reinforced polymer reinforcements in sand," *Journal of Composites for Construction*, Article ID 04014062, 2014.

[17] H.-H. Zhu, J.-H. Yin, L. Zhang, W. Jin, and J.-H. Dong, "Monitoring internal displacements of a model dam using FBG sensing bars," *Advances in Structural Engineering*, vol. 13, no. 2, pp. 249–261, 2010.

[18] H.-H. Zhu, J.-H. Yin, J.-H. Dong, and L. Zhang, "Physical modelling of sliding failure of concrete gravity dam under overloading condition," *Geomechanics and Engineering*, vol. 2, no. 2, pp. 89–106, 2010.

[19] H.-H. Zhu, B. Shi, J.-F. Yan, J. Zhang, C.-C. Zhang, and B.-J. Wang, "Fiber Bragg grating-based performance monitoring of a slope model subjected to seepage," *Smart Materials and Structures*, vol. 23, no. 9, Article ID 095027, 2014.

[20] C.-C. Zhang, H.-H. Zhu, B. Shi, and J.-K. She, "Interfacial characterization of soil-embedded optical fiber for ground deformation measurement," *Smart Materials and Structures*, vol. 23, no. 9, Article ID 095022, 2014.

[21] H.-H. Zhu, B. Shi, J. Zhang, J.-F. Yan, and C.-C. Zhang, "Distributed fiber optic monitoring and stability analysis of a model slope under surcharge loading," *Journal of Mountain Science*, vol. 11, no. 4, pp. 979–989, 2014.

[22] N. Nöther, A. Wosniok, K. Krebber, and E. Thiele, "A distributed fiber optic sensor system for dike monitoring using Brillouin optical frequency domain analysis," in *Optical Sensors*, vol. 7003 of *Proceedings of SPIE*, pp. 69330T-1–69330T-9, April 2008.

[23] E. Thiele, R. Helbig, H. Erth et al., "Dike monitoring," in *Proceedings of the 4th International Symposium on Flood Defense*, pp. 19-1–19-7, 2008.

[24] K. Krebber, S. Liehr, and J. Witt, "Smart technical textiles based on fiber optic sensors," in *22nd International Conference on Optical Fiber Sensors (OFS '12)*, vol. 8421 of *Proceedings of SPIE*, pp. 84212A-1–84212A-10, October 2012.

[25] C. Crunelle, M. Wuilpart, C. Caucheteur, and P. Mégret, "Original interrogation system for quasi-distributed FBG-based temperature sensor with fast demodulation technique," *Sensors and Actuators A: Physical*, vol. 150, no. 2, pp. 192–198, 2009.

Hindawi Publishing Corporation
Journal of Sensors
Volume 2015, Article ID 915837, 13 pages
http://dx.doi.org/10.1155/2015/915837

Research Article

Axis-Exchanged Compensation and Gait Parameters Analysis for High Accuracy Indoor Pedestrian Dead Reckoning

Honghui Zhang,[1] Jinyi Zhang,[1,2,3] Duo Zhou,[2] Wei Wang,[1] Jianyu Li,[2] Feng Ran,[2,3] and Yuan Ji[2,3]

[1]*Key Laboratory of Special Fiber Optics and Optical Access Networks, Ministry of Education, Shanghai University, Shanghai 200072, China*
[2]*Microelectronic Research and Development Center, Shanghai University, Shanghai 200072, China*
[3]*Key Laboratory of Advanced Displays and System Application, Ministry of Education, Shanghai University, Shanghai 200072, China*

Correspondence should be addressed to Jinyi Zhang; zhangjinyi@staff.shu.edu.cn

Received 22 September 2014; Revised 12 January 2015; Accepted 27 January 2015

Academic Editor: Zhenhua Zhu

Pedestrian dead reckoning (PDR) is an effective way for navigation coupled with GNSS (Global Navigation Satellite System) or weak GNSS signal environment like indoor scenario. However, indoor location with an accuracy of 1 to 2 meters determined by PDR based on MEMS-IMU is still very challenging. For one thing, heading estimation is an important problem in PDR because of the singularities. For another thing, walking distance estimation is also a critical problem for pedestrian walking with randomness. Based on the above two problems, this paper proposed axis-exchanged compensation and gait parameters analysis algorithm to improve the navigation accuracy. In detail, an axis-exchanged compensation factored quaternion algorithm is put forward first to overcome the singularities in heading estimation without increasing the amount of computation. Besides, real-time heading is updated by R-adaptive Kalman filter. Moreover, gait parameters analysis algorithm can be divided into two steps: cadence detection and step length estimation. Thus, a method of cadence classification and interval symmetry is proposed to detect the cadence accurately. Furthermore, a step length model adjusted by cadence is established for step length estimation. Compared to the traditional PDR navigation, experimental results showed that the error of navigation reduces 32.6%.

1. Introduction

With the increasing popularity of location based service (LBS), as a key factor in LBS, the importance of positioning is widely acknowledged. In practice, outdoor location technology is much more mature than indoor location technology. This imbalance leads to the fact that LBS can hardly be achieved in weak GNSS signal environment such as indoor location. Therefore, numerous scholars and groups are devoted to the research of indoor location, for example, indoor location technologies based on WIFI [1], RFID [2], Bluetooth [3–5], and wireless sensor networks [6]. However, the abovementioned technologies are susceptible to external environment.

Differentiated from other technologies, MEMS-IMU is a technique that applied to positioning with advantages of autonomous measurement. And pedestrian dead reckoning (PDR), one of the most important methods to achieve navigation with MEMS-IMU, was first proposed by Judd and Levi in 1996 [7]. According to the view of Judd and Levi, PDR is simplified by heading detection, filtering, cadence detection, and step length estimation. For convenient analysis, we further simplify four steps to heading detection and walking distance estimation. Cadence and step length are the two gait parameters contained in walking distance estimation.

As for heading estimation, the direction represented by three-parameter method leads to singularities, which have always confused us. To solve this problem, many methods have been put forward. In [8], improved predicted singularity robustness (PSR) is introduced to mitigate the influence of singularities. However, this improvement does not eliminate singularities completely. Thus, according to Lie group, Park

and Chung presented the Lie group geometric method which is singularity-free [9]. While the two aforementioned methods focus on avoiding singularities, Yun et al. have chosen to overcome singularities by using "borrow angle" and "return angle" [10]. This method provides a high accuracy overall, but at the cost of an increased calculation workload. Although singularities have been eliminated to a certain extent in the above methods, they are all in static state and are either too deficient or too complex.

As for walking distance estimation, starting with the gait parameters of cadence and step length, [11] calibrates the step length model for each person with two hybridization filters, while it has the inconvenience of offline calibration. To solve this problem, the authors proposed a real-time walking parameters estimation model in [12], where zero-approximation step detection algorithm and walking speed are integrated into the above model to improve the accuracy. Nevertheless, it is a complex calculation process. In application domain, Honeywell first proposed the relationship between cadence and step length in [13], which achieved navigation by accumulating step length obtained from IMU. Most of the step length models are the complex offline training required, and the cadence detection is not sufficiently accurate.

With the problems of deficiency and complexity in heading estimation, offline training, and inaccuracy in walking distance, to deal with the above problems, this paper proposed axis-exchanged compensation and gait parameters analysis algorithm of PDR to achieve a relatively high accuracy indoor navigation by MEMS-IMU. At the beginning, heading singularities are fixed by axis-exchanged compensation factored quaternion algorithm in static state. Then we updated the quaternion by R-adaptive Kalman filter to obtain a real-time heading. Subsequently, walking distance, especially cadence and step length, is estimated according to the characteristic of walking pedestrian. To address cadence, method of cadence classification and interval symmetry is applied to detection; meanwhile, a step length model adjusted by cadence is built to estimate the step length. In addition, since the step length of pedestrian is influenced by walking speed, cadence, individual differences, and other reasons, we customized the step length model for every pedestrian to improve the accuracy of indoor PDR navigation. As the above algorithms and methods are applied to PDR navigation, experiments showed that the navigation error reduces 32.6% by axis-exchanged compensation and gait parameters analysis algorithm.

The rest of this paper is organized as follows. Section 2 describes the heading estimation with axis-exchanged compensation factored quaternion algorithm. To achieve real-time heading output, R-adaptive Kalman filter is proposed as well. Section 3 proposes the estimation method of walking distance in cadence by classification and interval symmetry and in step length by model which is adjusted by cadence. Then, Section 4 describes the entire PDR when it applies axis-exchanged compensation and gait parameters analysis algorithm, while experiments and performance are listed in Section 5. Finally Section 6 concludes this paper.

2. Heading Estimation

Heading direction is an important factor for PDR navigation. In order to obtain the direction, factored quaternion algorithm is used with the advantage of only one-step calculation. However, this method inevitably brings in singularities at some situation because it derived from 3D orientation Euler angles. To eliminate the singularities, axis-exchanged compensation algorithm is applied to factored quaternion without increasing the amount of computation. While the above algorithm is based on static state, for obtaining a real-time heading direction, Kalman filter is used to update the direction. In addition, R-adaptive mechanism is proposed to improve the Kalman estimation accuracy.

2.1. Axis-Exchanged Compensation and Factored Quaternion

2.1.1. Factored Quaternion Algorithm. To describe the factored quaternion algorithm and orientation, we first introduce two coordinate systems including body coordinate and North-East-Down coordinate. The body coordinate represents the orientation of MEMS-IMU, and North-East-Down (NED) coordinate represents the orientation of earth. Initially, body coordinate coincides with the NED coordinate, and body coordinate rotates the yaw angle (heading direction) φ degree around z-axis. Then, it rotates pitch angle θ degree around y-axis as well. Subsequently, the coordinate rotates roll angle γ degree around x-axis. In this way, the above three Euler angles can represent any orientation. Moreover, we applied factored quaternion algorithm to Euler angles and computed quaternions along with Euler angles, respectively. And finally three direction quaternions are fused to one unit quaternion.

(1) Quaternion of Pitch and Roll. Due to the rotation independence of horizontal plane and vertical plane, for convenience, pitch and roll are calculated in advance.

The quaternions are derived in [10] and quaternion of pitch is

$$q_\theta = \cos\frac{\theta}{2}\begin{bmatrix}1 & 0 & 0 & 0\end{bmatrix} + \sin\frac{\theta}{2}\begin{bmatrix}0 & 0 & 1 & 0\end{bmatrix}, \tag{1}$$

where

$$\sin\frac{\theta}{2} = \operatorname{sign}(\sin\theta)\sqrt{\frac{(1-\cos\theta)}{2}}, \qquad \cos\frac{\theta}{2} = \sqrt{\frac{(1+\cos\theta)}{2}}. \tag{2}$$

Here, $\operatorname{sign}(a) = 1$ when $a \geq 0$; conversely, $\operatorname{sign}(a) = -1$ when $a < 0$.

Similarly, quaternion of roll is given by

$$q_\gamma = \cos\frac{\gamma}{2}\begin{bmatrix}1 & 0 & 0 & 0\end{bmatrix} + \sin\frac{\gamma}{2}\begin{bmatrix}0 & 1 & 0 & 0\end{bmatrix}, \tag{3}$$

where

$$\sin\gamma = -\frac{\overline{a}_y}{\cos\theta}, \qquad \cos\gamma = -\frac{\overline{a}_z}{\cos\theta}. \tag{4}$$

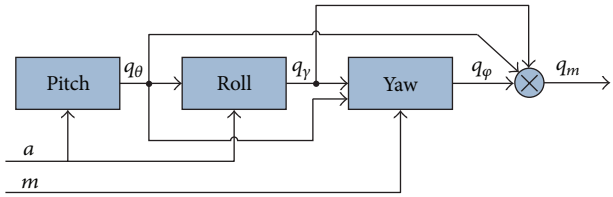

Figure 1: Flow of the factored quaternion algorithm.

Here, $\overline{a}_y$ and $\overline{a}_z$ are the acceleration of y-axis and z-axis, respectively.

(2) Quaternion of Yaw. For obtaining yaw φ, the magnetic flux density is assumed as $m_b = \begin{bmatrix} m_{bx} & m_{by} & m_{bz} \end{bmatrix}^T$ and then converted to horizontal plane. The transformation formula is

$$m_c = \left(q_\theta q_\gamma\right) m_b \left(q_\theta q_\gamma\right)^*. \tag{5}$$

In order to further simplify the problem, the declination exists in magnetic north and due north is ignored, and the geomagnetic field north is represented by symbol B_N. At this point, relationship between magnetic flux density and geomagnetic field intensity in horizontal plane can be described as follows:

$$\begin{aligned} m_{cx} \cdot \cos\varphi - m_{cy} \cdot \sin\varphi &= B_N, \\ m_{cx} \cdot \sin\varphi + m_{cy} \cdot \cos\varphi &= 0. \end{aligned} \tag{6}$$

Calculating the normalized magnetic flux densities $\overline{m}_{cx}$ and $\overline{m}_{cy}$ in horizontal plane, the sine and cosine value for yaw are

$$\cos\varphi = \overline{m}_{cx}, \qquad \sin\varphi = -\overline{m}_{cy}. \tag{7}$$

Finally quaternion of yaw can be represented as

$$q_\varphi = \cos\frac{\varphi}{2}\begin{bmatrix} 1 & 0 & 0 & 0 \end{bmatrix} + \sin\frac{\varphi}{2}\begin{bmatrix} 0 & 0 & 0 & 1 \end{bmatrix}. \tag{8}$$

(3) Quaternion Data Fusion. To improve the accuracy, formulas (1), (3), and (8) are fused together as a unit quaternion q_m, which can be expressed as

$$q_m = q_\varphi q_\theta q_\gamma. \tag{9}$$

The flow of fusion is illustrated in Figure 1.

So far, the factored quaternion algorithm utilizes gravity and geomagnetic field intensity as a reference. In contrast with the traditional static orientation estimation, factored quaternion algorithm eliminates the inexact matching by decomposing and fusing. For the most part, this inexact matching leads to estimation error in vertical direction, which will affect the horizontal direction (yaw) as well. While factored quaternion algorithm not only eliminates the inexact matching but also improves computational efficiency and avoids trigonometry operations by using half-angle formulas, the only imperfection is singularity in calculation. Thus axis-exchanged compensation algorithm is proposed.

2.1.2. Axis-Exchanged Compensation Algorithm. According to (4), when the pitch angle θ turns to 90°/−90°, singularities will appear in roll calculation and finally lead to wrong attitude estimation. To overcome these singularities, [10] proposed a method of borrow angle compensation. The main idea is that the pitch angle rotates an additional α when $\cos\theta < \varepsilon$ (ε is a positive number which closes with 0); in this case, the equivalent pitch is θ-α. Based on the additional rotation, acceleration and magnetic flux density are transformed as well, and so is the factored quaternion algorithm. The above procedures are called borrow angle; on the contrary, the return angle is only one step that multiplies the calculated quaternion by additional rotation angle quaternion q_α. Therefore the final quaternion returns to actual one, and singularities are avoided by the above steps at the same time. However, this method increases the amount of computation due to the complicated borrow angle and return angle.

Through the above analysis and geometry application, axis-exchanged compensation algorithm is proposed. This algorithm estimates singularities without increasing the amount of computation and thereby saves hardware overhead and improves the overall algorithm in real-time performance.

In the view of geometry, singularities are introduced in rotation order z-y-x when pitch angle θ turns to 90°/−90° around the middle level y-axis. In this situation, x-axis coincides with z-axis, which means that it loses the freedom of third level shaft. In other words, this phenomenon is the so-called gimbal lock in classical orientation estimation. Based on the above analysis, it is not difficult to find out that singularities can be avoided by combining quaternion algorithm with solution of gimbal lock. In practice, when the gimbal lock occurs, it can be avoided by changing rotation as follows.

Step 1. Return to the original posture.

Step 2. Rotate the yaw angle 180° around z-axis.

Step 3. Rotate the roll angle 180° around x-axis.

Step 4. Rotate the pitch angle 90° around y-axis.

In the same way, when the pitch angle θ closes with 90°/−90°, axis-exchanged compensation algorithm can be applied to avoid singularities. The steps are similar to the solution of gimbal lock when singularities appeared.

Step 1. Match the measured acceleration data and magnetic flux density to the reverse side.

Step 2. Regard the pitch angle θ as 0 degree and substitute it into formulas (3) and (8).

Step 3. Substitute the original pitch angle θ into formula (9) for obtaining the final unit quaternion.

According to the above steps, axis-exchanged compensation algorithm is able to avoid singularities by data matching

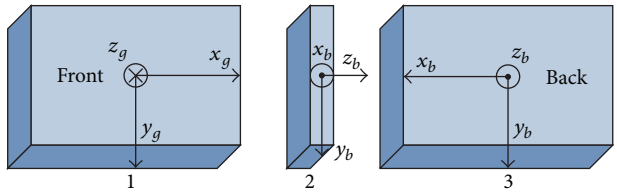

Figure 2: Data matching by axis-exchanged compensation.

without increasing the amount of computation. Figure 2 illustrates an example of data matching in axis-exchanged compensation algorithm. In Figure 2, gimbal lock occurs when the body changes position 1 to position 2 along with the pitch direction (y-axis). In this case, we match the data from position 2 to position 3 according to axis-exchanged compensation steps. Thus the x-axis data in position 3 and the z-axis data in position 2 are a pair of opposite numbers; meanwhile, the z-axis data in position 3 equals the x-axis data in position 2. So far, singularities are avoided by axis-exchanged compensation factored quaternion algorithm.

In general, changing the rotation order means changing the shaft level relationship. As a matter of fact, the axis-exchanged compensation can never eliminate singularities indeed; it merely transfers them. In other words, when singularities occurred, the essence of axis-exchanged compensation algorithm is to change the rotation order from z-y-x to z-x-y. But the calculation order has never been changed, which means that the shaft level relationship has never been changed neither, so there is nothing to worry about introducing other singularities.

2.2. R-Adaptive Kalman Filter. The above axis-exchanged compensation factored quaternion algorithm is based on static state; in order to obtain a real-time direction estimation, R-adaptive Kalman filter is presented in this paper. According to the quaternion differential equation and static unit quaternion provided in Section 2.1, R-adaptive Kalman filter is designed for acquiring real-time orientation quaternion.

2.2.1. Kalman Filter Based on Quaternion. A Kalman filter for quaternion is proposed in [14]; thus we briefly introduce the Kalman filter and put the emphasis on R-adaptive adjustment. In quaternion algorithm, the relationship of angular velocity ω is provided by gyro and quaternion q could be written as

$$\dot{q} = \frac{1}{2} R\left[\omega_b\right] \cdot q, \tag{10}$$

where

$$R\left[\omega_b\right] = \begin{bmatrix} 0 & -\omega_b \\ \omega_b & \omega_* \end{bmatrix},$$

$$\omega_* = \begin{bmatrix} 0 & \omega_{bz} & -\omega_{by} \\ -\omega_{bz} & 0 & \omega_{bx} \\ \omega_{by} & -\omega_{bx} & 0 \end{bmatrix}. \tag{11}$$

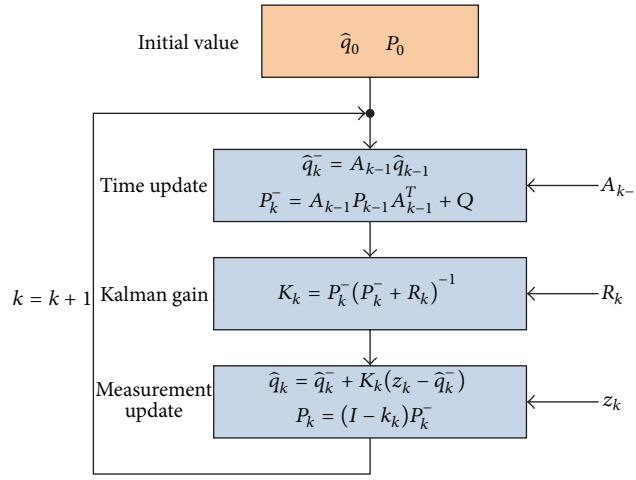

Figure 3: Flow of the quaternion-based Kalman filter.

According to (10), a quaternion-based Kalman filter is constructed and shown in Figure 3.

As shown in Figure 3, the flow of quaternion-based Kalman filter can be described as follows.

Step 1. Calculate the state variable $\widehat{q}_0$ and error covariance P_0 by factored quaternion algorithm as the initial value.

Step 2. The *a priori* state estimate $\widehat{q}_k^-$ and the *a priori* estimate error covariance P_k^- are computed by time update equations.

Step 3. Noise covariance matrices Q and R are used to calculate the Kalman gain K_k based on the Kalman gain equation.

Step 4. Substitute the measurement variable z_k which is a static quaternion that derived from factored quaternion algorithm into the measurement update equation; meanwhile, adjust the weights between the *a prior* state estimate $\widehat{q}_k^-$ and innovation $z_k - \widehat{q}_k^-$ for obtaining a relatively accurate real-time orientation quaternion.

2.2.2. R-Adaptive Adjustment. Axis-exchanged compensation factored quaternion algorithm is used in the condition of static state or quasi-static state, while nonlinear acceleration will be introduced in the measurement when MEMS-IMU moves at high speed, thereby leading to large bias. So the measurement variable z_k in Kalman filter not only loses its ability of calibration but also causes mistakes. To avoid this situation, R-adaptive adjustment mechanism is applied to Kalman filter. As a result, R-adaptive Kalman filter eliminates the influence caused by nonlinear acceleration via controlling the Kalman gain. In detail, for adjusting the noise covariance matrix R in real time, the mechanism sets the dynamic and static thresholds through the relationship between thresholds and 3-axis acceleration.

If we define the 3-axis acceleration as $\delta a = \left|\sqrt{a_x^2 + a_y^2 + a_z^2} - g\right|$ and set the static threshold as $a_{\text{sta}} = \sqrt{\sigma_{ax}^2 + \sigma_{ay}^2 + \sigma_{az}^2}$, where σ_a denotes the noise standard

deviation in static state and a_{dyn} denotes the dynamic threshold, the rules are designed as follows.

Rule 1. When $\delta a \le a_{sta}$, it means that the measured object is in static state and the measured data is reliable and accurate. So R need not be adjusted or need to be adjusted slightly. Thus

$$R_k = s \cdot R, \quad s \in \left[10^{-1}, 1\right]. \tag{12}$$

Rule 2. When $a_{sta} \le \delta a \le a_{dyn}$ and $|\delta a_k - \delta a_{k-1}| \le a_{sta}$, it means that the measured object has the tendency to move; thus $R_k = R$. If the $|\delta a_k - \delta a_{k-1}| > a_{sta}$, it means that the measured object has the tendency to make nonlinear acceleration, while the measured data is still worth reference. Thus

$$R_k = \left[\frac{(\delta a_k - \delta a_{k-1})}{a_{sta}}\right] \cdot R. \tag{13}$$

Rule 3. When $\delta a > a_{dyn}$, it means that the measured object is in high speed; at this time, the measured data loses value completely. Thus

$$R_k = I. \tag{14}$$

The noise covariance matrix R is adjusted by the above rules in real time, and the adjusted R_k is substituted into Kalman gain formula to obtain K_k. In this manner, the weights of dynamic and static quaternion are modified by Kalman gain K_k in real time, thereby achieving a relatively accurate heading estimation. As heading (yaw) is the only required orientation for navigation in PDR, consequently, we just need to take yaw data out of the unit quaternion.

3. Walking Distance Estimation

Walking distance estimation is another important link in PDR navigation, where cadence and step length are two gait parameters on which we focused the most.

3.1. Classification and Interval Symmetry Detection of Cadence. In cadence detection, method of peak detection is usually used with fixed time window and fixed threshold. However, the detection accuracy decreases with the varying cadence of pedestrian. So in order to improve the detection accuracy, in this subsection, peak detection is developed according to the various intervals. In this manner, the sensor data is collected and the characteristics of 3-axis total acceleration are analyzed for designing method of cadence classification and interval symmetry.

The collected 3-axis total acceleration is depicted in Figure 4 when pedestrian walks with a single cadence. In this figure, as mixing with noise, waveforms of raw data are described with periodicity and complexity. Taking into account the indoor environment, walking cadence of normal pedestrian is usually falling in the frequency of 1~3 Hz; therefore a FIR low-pass filter of 3 Hz cut-off [15] is applied to raw data. And the output result is shown in Figure 5. As can be seen from Figure 5, noise has been nearly filtered and the regularity of acceleration is obvious.

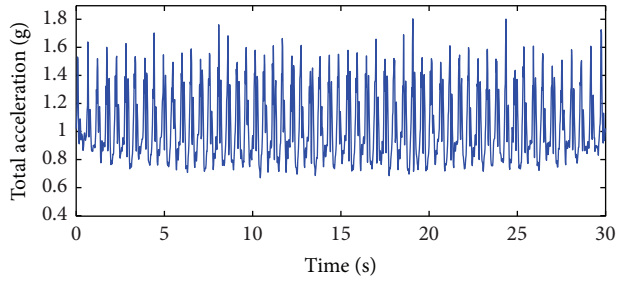

Figure 4: Raw acceleration of single cadence.

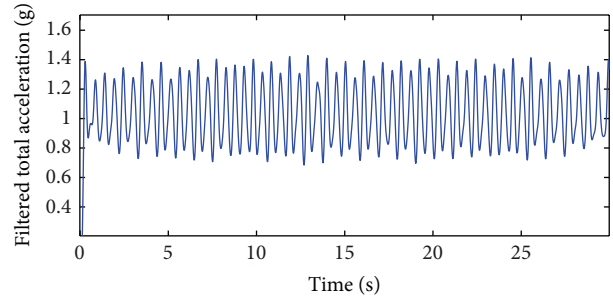

Figure 5: Filtered acceleration of single cadence.

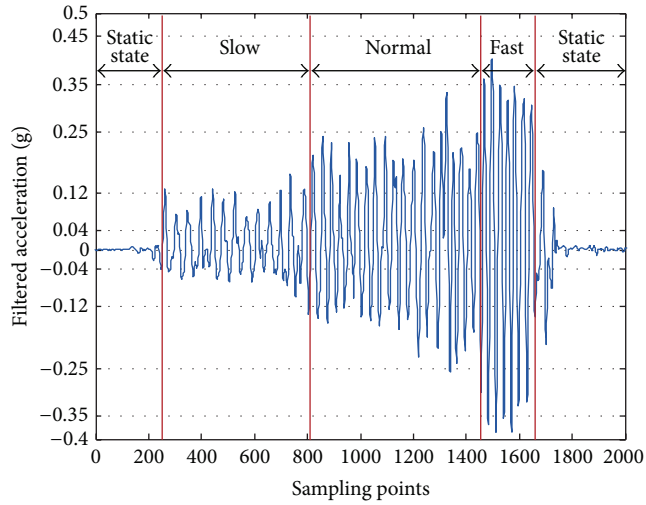

Figure 6: Filtered acceleration of changing cadence.

Based on Figure 5, we can get that the tendency of total acceleration in a stride rose first and dropped later. Moreover, the rising interval and dropping interval are well symmetrical and appear alternatively with the maximum and minimum values.

Back to the question of walking with random cadence, for example, the walking cadence changes from slow to fast. As a result, the filtered 3-axis total acceleration is illustrated in Figure 6.

Figure 6 shows the waveforms changing from being sparse to dense with the increasing acceleration amplitude. Thus the result is that not only the cadence but also acceleration amplitude is changed with varying walking. From

the above analysis, we can get that different detection threshold needs to be used in different walking cadence. In contrast with Figures 5 and 6, characteristics of walking cadence and acceleration amplitude can be described as follows.

Characteristic 1. Divide the normal pedestrian walking cadence range 1~3 Hz into three conditions: slow (1~1.6 Hz), normal (1.6~2 Hz), and fast (2~3 Hz). As a matter of fact, rising interval time is half of the whole stride. Thus the rising interval time corresponds to three conditions: slow (0.3~0.5 s), normal (0.25~0.3 s), and fast (0.16~0.25 s). Likewise, when the sampling frequency is 50 Hz, sampling points of rising interval correspond to three conditions: slow (15~20), normal (12~15), and fast (8~12).

Characteristic 2. The maximum and minimum values of acceleration appeared alternatively. In addition, the amplitude changes with cadence too. Meanwhile, the static state acceleration amplitude changes from −0.04 to 0.04. Hence, we divided the threshold range into three conditions as well: slow [0.04, 0.12], normal (0.12, 0.25], and fast (0.25, 0.5]. In this condition, acceleration changes under different experiments should meet different maximum and minimum values.

Based on the above two characteristics, a method of cadence classification and interval symmetry is designed for detecting cadence; the exact flow is shown in Figure 7. As the acquired acceleration, motion conditions (slow, normal, and fast) are firstly determined by the rising interval. Then the preset thresholds are selected based on the motion conditions; in the meantime, maximum value of rising interval is judged whether it falls in the threshold condition. Due to the symmetry of gait, minimum value of drop interval needs to be judged as well. When the above conditions are satisfied, cadence can be calculated with sampling frequency and sampling points.

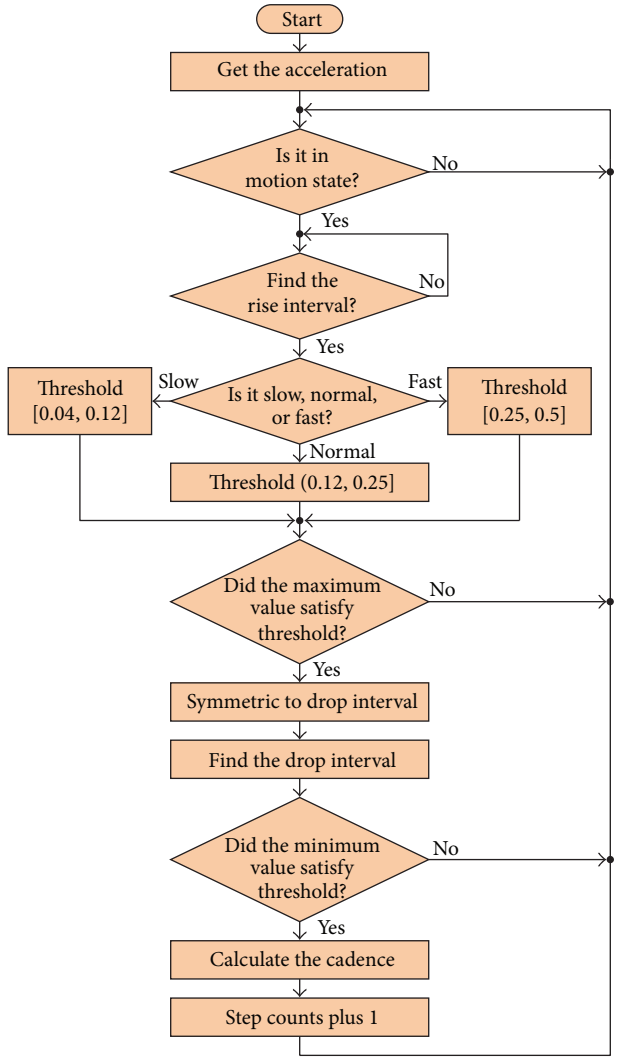

Figure 7: Method of cadence classification and interval symmetry.

3.2. Frequency Adjustment Step Length Estimation Model. Another important gait parameter is step length. As we all know, the pedestrian step length is variable; it changes with walking speed, cadence, individual difference, and so forth. However, traditional nonlinear step length estimation models generally lack adaptability. And neural networks models have good adaptability while usually requiring lots of training to ensure the accuracy [16, 17]. On this basis, this paper designed a step length model adjusted by cadence. The model not only increases the adaptability and improves the accuracy but also reduces the computational complexity for most parts.

Human biology shows the relationship between pedestrian cadence and walking speed. In [18], great deals of experiments are tested for recording the relationship of cadence and speed under different walking environment. The relationship is:

$$v = af^2 + cf + b, \tag{15}$$

where v is walking speed (m/s), f is cadence (Hz), and a, b, and c are constants.

On the basis of (15) and the relationship between step length, cadence, and walking speed, the adjusted step length model is derived out. Assuming l is the step length, f is cadence, v is walking speed, and the relationship is

$$v = l \times f. \tag{16}$$

Combining (15) and (16), we can get

$$l = \frac{v}{f} = af + \frac{b}{f} + c. \tag{17}$$

So far, (17) is the step length model which is adjusted by cadence, where a, b, and c are the model parameters and cadence f is detected by method of cadence classification and interval symmetry. Since the normal pedestrian walking cadence is in range of 1~3 Hz, the cadence f refers to 1~3 Hz in this paper either.

The model parameters a, b, and c are obtained by brief calibration. The calibration experiment is in a 40-meter long corridor in this paper, and experimental subjects walk with slow (1~1.6 Hz), normal (1.6~2 Hz), and fast (2~3 Hz) three speeds, respectively. In order to calibrate the parameters,

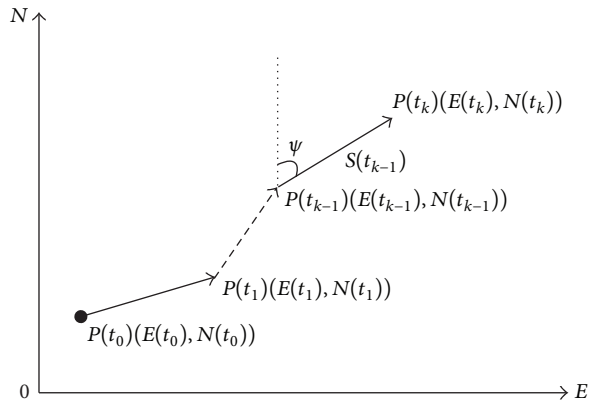

Figure 8: Schematic of pedestrian dead reckoning.

five groups of data are collected to fit the least squares curve. Due to the individual differences, parameters a, b, and c will change a lot with different people even having the same height. Therefore, for guaranteeing the performance of step length estimation, the model parameters a, b, and c are personalized for each user through the brief calibration before navigation.

4. Axis-Exchanged Compensation and Gait Parameters Analysis Algorithm Applied to PDR with MEMS-IMU

Sections 2 and 3 present the axis-exchanged compensation and gait parameters analysis algorithm separately, while the algorithms are applied to PDR for indoor navigation.

The basic schematic of pedestrian dead reckoning is shown in Figure 8, where the horizontal axis represents east and the vertical axis represents north. Assuming the initial position is $p(t_0)$, pedestrian walks from position $p(t_0)$ to position $p(t_k)$ during time $t_0 \sim t_k$. The position $p(t_k)$ is obtained by (18), where $(E(t_{k-1}), N(t_{k-1}))$ and ψ are the position and heading direction in time t_{k-1} and $S(t_{k-1})$ is the step length during time $t_{k-1} \sim t_k$:

$$\begin{aligned} E(t_k) &= E(t_{k-1}) + S(t_{k-1}) \times \sin\psi, \\ N(t_k) &= N(t_{k-1}) + S(t_{k-1}) \times \cos\psi. \end{aligned} \tag{18}$$

From the schematic of PDR, we can see that the factors that influence navigation most are as follows: initial position, heading, and walking distance. In practice, the initial position can be preset or obtained by GPS. The heading direction (yaw) can be taken out from unit quaternion equation (9) and be updated by R-adaptive Kalman filter for real-time estimation. The walking distance is obtained by the following procedures. Firstly, the measured 3-axis total acceleration of MEMS-IMU is used to detect the cadence with method of cadence classification and interval symmetry. Then, the step length is obtained by (17) and the walking distance can be computed by accumulating.

Table 1: Specifications of MEMS-IMU.

Sensor	Range	Sensitivity	Output noise
3-axis accelerometer MMA8453Q	±8 g	3.9 mg/LSB	126 $\mu g/\sqrt{Hz}$
3-axis gyroscope ITG3200	±2000 dps	14.375 LSB/(dps)	0.38 dps
3-axis magnetometer MAG3110	±1000 μT	0.1 μT/bit	0.4 μT rms

Figure 9: Hardware system.

Therefore, indoor PDR navigation is achieved by estimated initial position, heading, and walking distance with (18). And the aforementioned flows are axis-exchanged compensation and gait parameters analysis algorithm of PDR.

5. Experiments and Analysis

5.1. A Verification System Construction. The verification hardware system consists of PC and 9-axis MEMS-IMU; the whole experimental hardware is shown in Figure 9. And 9-axis MEMS-IMU is made up of 3-axis accelerometers, 3-axis gyroscopes, and 3-axis magnetometers; the performance of each sensor is shown in Table 1. In PDR navigation, MEMS-IMU is attached on the rear waist of pedestrian, which is shown in Figure 10. The serial communication baud rate of MEMS-IMU is 115200 bit/s, and the sampling frequency is 50 Hz.

In walking experiment, a 12 m long and 8 m wide indoor room is selected, and the total walking route is 40 meters long, which is depicted in Figure 11. In Figure 11, the horizontal axis represents south and the vertical axis represents east. During the experiment, pedestrian starts from position A, walking along with the direction of arrow, and finally back to position A. In this process, the data collecting device MEMS-IMU is attached on the rear waist of pedestrian, as in Figure 10;

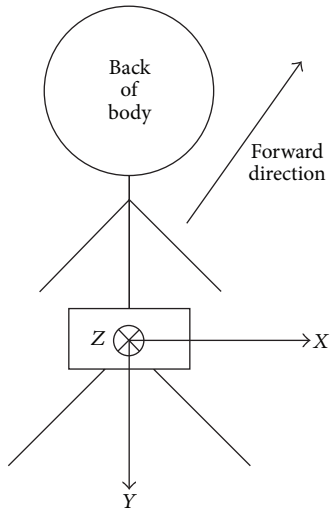

Figure 10: Coordinate of body.

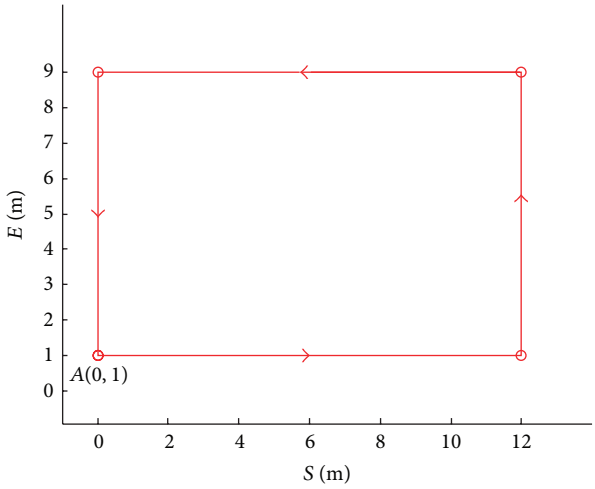

Figure 11: Walking routes.

axes X, Y, and Z point to the right of forward direction, the vertical direction, and forward direction, respectively.

In addition, for better analysis of singularities in heading estimation, 9-axis MEMS-IMU is fixed on the cloud platform, which is shown in Figure 12. In this situation, the rotation of yaw (heading) and roll can be achieved from $-\pi$ to π, and the pitch can rotate from 0 to $\pi/2$. In experiments, this cloud platform basically meets the requirements.

5.2. Experimental Result and Analysis

5.2.1. Singularities Compensation. Equation (3) in Section 2.1.1 shows that singularities occur in factored quaternion algorithm when the pitch angle reaches 90°/−90°. Figure 13 describes a process that MEMS-IMU rotates along with the pitch angle from 0° to 90°, making a brief stop in 90° and then returning to the start. The vertical axis and horizontal axis represent the degree and sampling points, respectively,

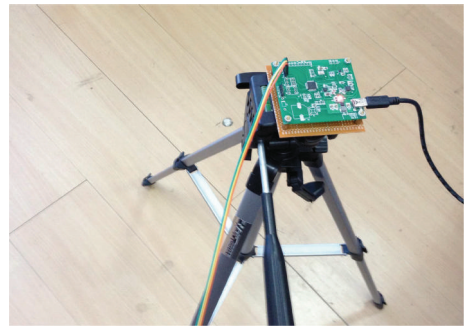

Figure 12: Rotation cloud platform.

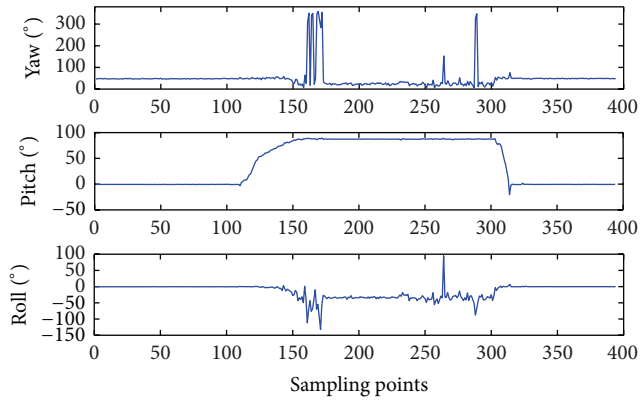

Figure 13: Rotation without compensation.

and pitch angle makes a brief stop in 90° during 150 to 300 sampling points. When the pitch angle reaches 90°, yaw and roll show a large fluctuation that completely deviated from the actual degree. This phenomenon indicates that singularity cannot be estimated by factor quaternion algorithm. Thus, axis-exchanged compensation factored quaternion is proposed for avoiding singularity. As shown in Figure 14, the fluctuation in Figure 13 is basically eliminated. Based on the above result, R-adaptive Kalman filter is used to further obtain a real-time heading direction, as shown in Figure 15. From the experiment, when pitch angle reaches 90°, flag flipped from 0 to 1 that means the opening of axis-exchanged compensation. Conversely, the flag flipped from 1 to 0 when the pitch leaves 90°. The above tests show that real-time heading direction can be estimated accurately by axis-exchanged compensation factored quaternion algorithm and R-adaptive Kalman filter without increasing the amount of computation. In addition, the calculated attitude is equivalent to the reverse side of actual attitude when axis-exchanged compensation algorithm is enabled. Thus, for obtaining the actual attitude, yaw and roll angle should be minus 180° and plus 180°, respectively.

As the singularity is eliminated, axis-exchanged compensation factored quaternion algorithm is taken out for further comparison with standard attitude estimation algorithm like borrow angle compensation factored quaternion algorithm [10]. The above experiments illustrate that singularity happens in 150 to 300 sampling points. Also, based on the above

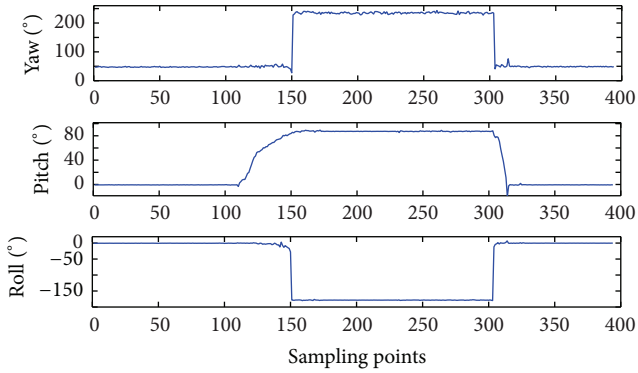

Figure 14: Rotation with compensation.

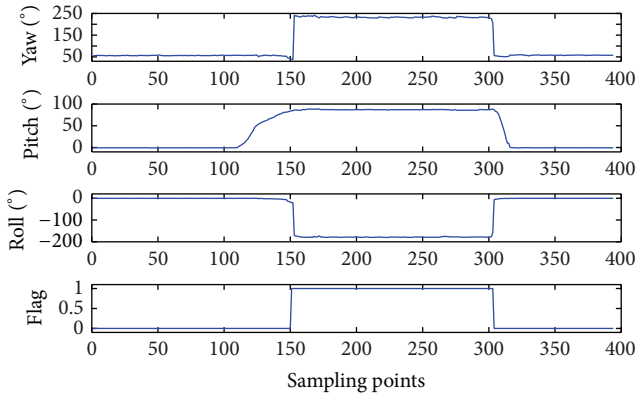

Figure 15: Rotation with compensation after R-adaptive Kalman filter.

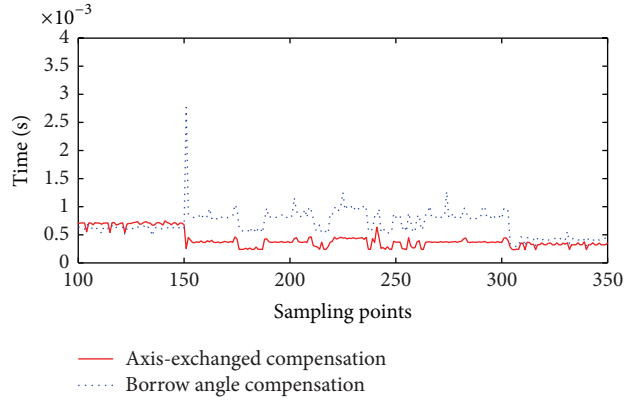

Figure 16: Computing time comparison.

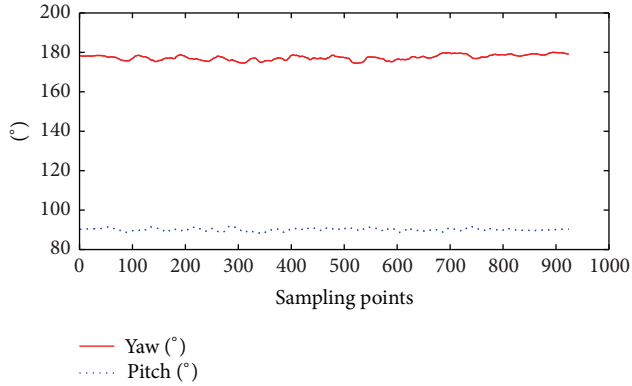

Figure 17: Walking without axis-exchanged compensation factored quaternion algorithm.

experiment data, the computing time of two singularity compensation algorithms is contrasted in Figure 16. In this figure, the vertical axis and horizontal axis represent time and sampling points, respectively; similarly, the dotted line and solid line represent borrow angle compensation factored quaternion algorithm and axis-exchanged compensation factored quaternion algorithm. As the axis-exchanged compensation factored quaternion algorithm is enabled in 150 to 300 sampling points, we can see that the computing time of proposed axis-exchanged compensation factored quaternion algorithm is far below the borrow angle compensation factored quaternion algorithm in this range, only about 50% of the borrow angle compensation. In addition, the computing time of axis-exchanged compensation factored quaternion algorithm is more stable, while borrow angle compensation algorithm has a surge point at the beginning, which will consume large amount of hardware overhead in practice. The reason of low computing time is that axis-exchanged compensation eliminates singularity only by changing the rotation order instead of borrowing and returning angle, which will increase additional calculations. Therefore axis-exchanged compensation factored quaternion algorithm has higher operation efficiency at the point of singularity eliminating.

So far, the attitude experiments are still rotated on cloud platform. For obtaining the heading direction in PDR navigation, we further verified the attitude estimation ability of axis-exchanged compensation factored quaternion algorithm in walking status. The MEMS-IMU is attached on the back. As axis-exchanged compensation factored quaternion algorithm is applied to MEMS-IMU, the yaw and pitch angle are shown in Figure 17 when walking straight. The vertical axis and horizontal axis represent degree and sampling points, respectively; likewise, the dotted line and solid line represent pitch and yaw. We can see that the yaw keeps stability even when the pitch angle sometimes equals 90° during walking. Thus the yaw can be regarded as heading direction in PDR application. And since the stable heading direction is obtained, in the following step, we would like to estimate the walking distance.

5.2.2. Walking Distance Estimation. As for walking distance estimation, the first step is to detect the cadence. In order to observe the effects of cadence classification and interval symmetry, a pedestrian is randomly selected to walk from slow to fast. As a result, the collected 3-axis total acceleration by MEMS-IMU is depicted in Figure 18. During the walking, acceleration waveform changes from sparse to dense; at

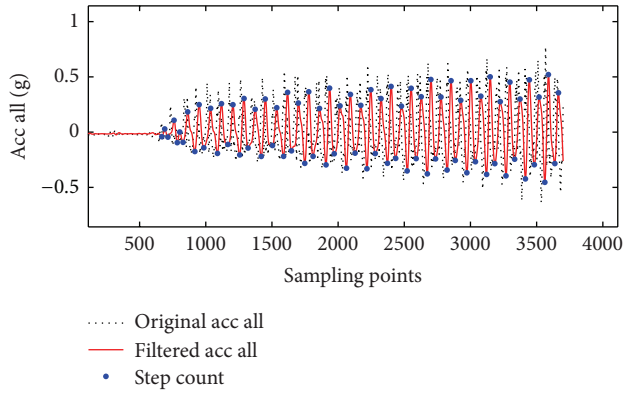

Figure 18: Cadence detection.

Table 2: Result of walking distance.

Number	Sex	Cadence detection/%	Walking distance/m	Estimation error/%
1	Female	100	40	0.34
2	Female	99	40	0.58
3	Female	99	40	0.48
4	Female	100	40	0.37
5	Female	100	40	0.34
6	Male	99	40	0.46
7	Male	100	40	0.29
8	Male	99	40	0.39
9	Male	98	40	0.62
10	Male	100	40	0.35
Mean value	—	**99.4**	**40**	**0.42**

the same time, amplitude grows from low to high. Based on the above analysis, we can see that the waveform in Figure 18 meets the actual walking process, and particularly the cadence detection is without missed detection point or false alarm.

Then the step length needs to be estimated according to the above cadence. Before estimation, parameters a, b, and c of step length model should be calibrated by training. Therefore, 10 pedestrians are selected for training, and each pedestrian walked through a 40-meter long corridor for 5 times. In training, parameters a, b, and c for each pedestrian are personalized by least squares curve fitting. Then, based on the cadence detected above and the calibrated parameters, step length is estimated with step length model equation (17). Table 2 reveals the performance of gait parameters analysis method, the average cadence detection accuracy of 40-meter walking is 99.4%, and the walking distance estimation error is 0.42%, which means an excellent performance in walking distance estimation.

Since the estimation is based on acceleration, so, in considerable acceleration senor measurement accuracy, we

Table 3: Comparison of walking distance estimation error.

	Nonlinear peak detection	Method of gait parameters analysis
Actual walking distance/m	36.6	40
Average walking distance error/m	0.26	0.17
Average walking distance error/%	0.71	0.42
Average walking distance error reduction/%	—	34.6

contrast the proposed method of gait parameters analysis and nonlinear peak detection described in Table 3. Table 3 shows that the average walking distance error reduces 34.6% by method of gait parameters analysis; the result reveals an obvious advantage in walking distance estimation. Two points contribute to the estimation.

Point 1. The method of gait parameters analysis uses cadence classification and interval symmetry for cadence detection. It improves the cadence detection accuracy and robustness.

Point 2. The method of gait parameters analysis uses a step length model adjusted by cadence for step length estimation. The parameters in step length model are calibrated by easy training, which improves the accuracy. In addition, cadence is used in estimating the step length that improves the adaptability compared to the nonlinear peak detection.

5.2.3. Indoor PDR Navigation. The method of gait parameters analysis applied to walking distance estimation performs well, while in this subsection the whole method of axis-exchanged compensation and gait parameters analysis algorithm of PDR is applied to indoor PDR navigation with the acquired heading direction and walking distance. In experiment, pedestrian 1 is selected for walking in a 12 m long and 8 m wide room, which is depicted in Figure 11. Similar to the walking route in Section 5.1, pedestrian 1 starts from position A, walking along with the direction of arrow, and finally back to position A. The walking result is shown in Figure 19. The line with asterisks represents the axis-exchanged compensation and gait parameters analysis algorithm of PDR indoor navigation when using MEMS-IMU. In this figure, we can see that the PDR navigation route basically meets the preset route. Furthermore, in order to obtain a more general navigation, pedestrian 1 is requested for walking with the preset route by 10 times. Calculating the maximum error between the PDR route and the preset route in 10 experiments separately, the errors are shown in Figure 20. According to the measured results in Figure 20, the maximum error is 1.1230 m, which also performs well in indoor PDR navigation.

Similarly, to contrast the proposed algorithm and nonlinear peak navigation in [19], Table 4 shows that the navigation error reduces 32.6% by axis-exchanged compensation and

Table 4: Comparison of navigation error.

	Nonlinear peak navigation	Axis-exchanged compensation and gait parameters analysis PDR
Actual walking distance/m	36.6	40
Navigation error RMS/m	1.44	0.97
Navigation error RMS/%	3.93	2.42
Navigation error reduction/%	—	32.6

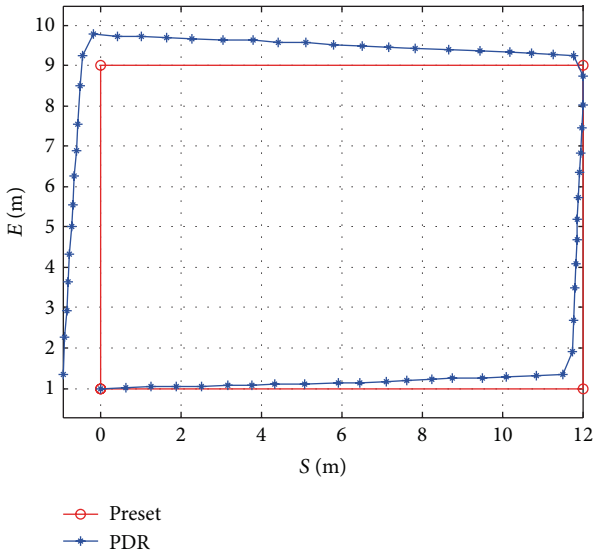

Figure 19: PDR walking route.

gait parameters analysis algorithm; the result reveals an obvious advantage in PDR navigation. Three points contribute to the navigation.

Point 1. In heading estimation, the heading singularities are eliminated by axis-exchanged compensation factored quaternion algorithm. In the meantime, real-time heading direction is obtained by R-adaptive Kalman filter. They improve the accuracy and obtain a real-time heading without increasing the amount of computation.

Point 2. In cadence detection, algorithm of axis-exchanged compensation and gait parameters analysis improves the detection accuracy and robustness.

Point 3. In step length estimation, algorithm of axis-exchanged compensation and gait parameters analysis improves the estimation adaptability and accuracy.

In addition, in order to verify the application scope of axis-exchanged compensation and gait parameters analysis algorithm, different walking distances and time are tested; the results are shown in Table 5. According to Table 5, navigation

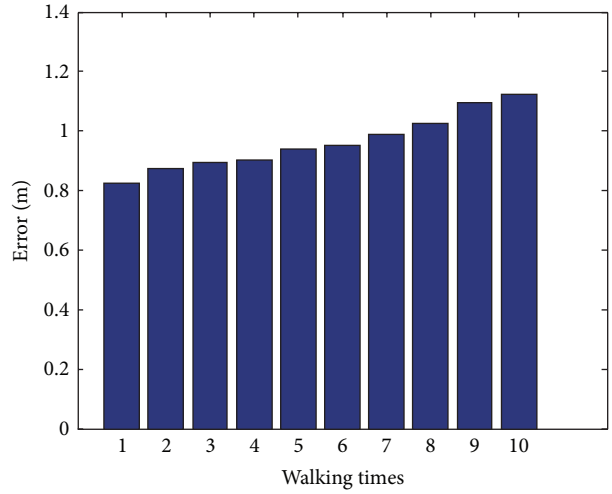

Figure 20: Navigation error.

error is accumulated with the increasing walking distance and time. When walking time approximately approaches 12 minutes or walking distance is about 500 meters, the navigation error RMS (root mean square) still remains less than 15 meters and the walking distance error is about 1%. However, when time or walking distance exceeded this range, single PDR navigation is needed to be considered before application. Therefore, axis-exchanged compensation and gait parameters analysis algorithm of PDR is more suitable for short-distance indoor navigation.

6. Conclusion

Based on the problem of accuracy in indoor PDR navigation, this paper proposed axis-exchanged compensation and gait parameters analysis algorithm of PDR in aspects of heading and walking distance. In heading estimation, axis-exchanged compensation factored quaternion algorithm is used to overcome the singularities; in performance, the heading fluctuation is eliminated without increasing the amount of computation. Subsequently, real-time heading is achieved by R-adaptive Kalman filter. In walking distance estimation, gait parameters analysis algorithm is used to improve the estimation accuracy in two steps: cadence and step length. In cadence detection, method of cadence classification and interval symmetry is presented. This method classifies cadence according to the walking speed; in the meantime, different detection thresholds are selected by classification. It improves the detection accuracy and robustness. Besides, in step length estimation, a step length model adjusted by cadence is established, which improves the estimation adaptability. And for further improving the accuracy among different people, parameters a, b, and c are personalized by brief calibration. And different parameters related to different step length for different people. Thus the axis-exchanged compensation and gait parameters analysis algorithm of PDR can suit the variation of people. Based on all the mentioned above, axis-exchanged compensation and gait parameters

Table 5: Error of different navigation.

Number	Walking times/s	Walking distance/m	Walking distance error/%	Navigation error RMS/m	Navigation error RMS/%	Maximum navigation error/m	Maximum navigation error/%
1	74.4	80	0.46	1.95	2.44	2.08	2.60
2	152.0	160	0.55	4.03	2.52	5.66	3.54
3	259.2	240	0.68	6.46	2.69	9.17	3.82
4	368.0	320	0.82	8.99	2.81	13.76	4.30
5	479.0	400	0.89	11.60	2.90	19.00	4.75
6	604.8	480	1.04	14.06	2.93	23.86	4.97
7	716.8	560	1.36	16.63	2.97	28.22	5.04
8	838.4	640	3.91	28.86	4.51	59.65	9.32
9	988.2	720	5.55	35.21	4.89	68.04	9.45
10	1124.0	800	7.88	45.76	5.72	79.60	9.95

analysis algorithm of PDR achieves high accuracy indoor navigation with MEMS-IMU, especially in short-distance navigation.

Conflict of Interests

The authors declare that there is no conflict of interests regarding the publication of this paper.

Acknowledgments

The authors would like to thank the reviewers for their detailed comments on earlier versions of this paper. This work was supported by a grant from the National High Technology Research and Development Program of China (863 Program) (nos. 2013AA03A1121 and 2013AA03A1122), the Leading Academic Disciplines Project of Shanghai Education Commission, China (no. J50104), and the China National Natural Science Fund under Grant no. 61376028.

References

[1] H. Zou, H. Jiang, X. Lu, and L. Xie, "An online sequential extreme learning machine approach to WiFi based indoor positioning," in *Proceedings of the IEEE World Forum on Internet of Things (WF-IoT '14)*, pp. 111–116, Seoul, Republic of Korea, March 2014.

[2] J.-Y. Zhang, J.-J. Zhang, R.-H. Li, D.-Z. Xu, and Q.-L. Xu, "Pipelined RFID indoor positioning based on locally-weighted regression," *Journal of Applied Sciences*, vol. 32, no. 2, pp. 125–132, 2014.

[3] J.-J. Li, J.-Y. Zhang, B.-Y. Zhang et al., "Fuzzy fingerprint location for bluetooth specification version 4.0," *Journal of Shanghai University (Natural Science)*, vol. 19, no. 2, pp. 126–131, 2013.

[4] L. Chen, H. Kuusniemi, Y. Chen, L. Pei, T. Kröger, and R. Chen, "Information filter with speed detection for indoor Bluetooth positioning," in *Proceedings of the International Conference on Localization and GNSS (ICL-GNSS '11)*, pp. 47–52, June 2011.

[5] Y. Wang, X. Yang, Y. Zhao, Y. Liu, and L. Cuthbert, "Bluetooth positioning using RSSI and triangulation methods," in *Proceedings of the IEEE 10th Consumer Communications and Networking Conference (CCNC '13)*, pp. 837–842, Las Vegas, Nev, USA, January 2013.

[6] J. Y. Zhang, S. Y. Duan, Y. J. Wu, C. H. Wang, and M. L. Ding, "Localization of collaboration ripples in wireless sensor network," *Journal of Applied Sciences*, vol. 30, no. 2, pp. 120–127, 2012.

[7] T. Judd and R. W. Levi, "Dead reckoning navigational system using accelerometer to measure foot impacts," U.S. Patent 5,583,776[P], 1996.

[8] F. A. Leve, "Evaluation of steering algorithm optimality for single-gimbal control moment gyroscopes," *IEEE Transactions on Control Systems Technology*, vol. 22, no. 3, pp. 1130–1134, 2014.

[9] J. Park and W.-K. Chung, "Geometric integration on Euclidean group with application to articulated multibody systems," *IEEE Transactions on Robotics*, vol. 21, no. 5, pp. 850–863, 2005.

[10] X. Yun, E. R. Bachmann, and R. B. McGhee, "A simplified quaternion-based algorithm for orientation estimation from earth gravity and magnetic field measurements," *IEEE Transactions on Instrumentation and Measurement*, vol. 57, no. 3, pp. 638–650, 2008.

[11] V. Renaudin, V. Demeule, and M. Ortiz, "Adaptative pedestrian displacement estimation with a smartphone," in *Proceedings of the International Conference on Indoor Positioning and Indoor Navigation (IPIN '13)*, pp. 1–9, IEEE, 2013.

[12] J. Wang, X. Lee, L. Yu, and L. Guo, "A method of walking parameters estimation via 3-axis accelerometer," in *Proceedings of the 1st International Conference on Orange Technologies (ICOT '13)*, pp. 298–301, IEEE, March 2013.

[13] W. A. Soehren, "Motion classification methods for personal navigation," U.S. Patent 7,561,960[P], 2009.

[14] S. Sabatelli, M. Galgani, L. Fanucci, and A. Rocchi, "A double-stage kalman filter for orientation tracking with an integrated processor in 9-D IMU," *IEEE Transactions on Instrumentation and Measurement*, vol. 62, no. 3, pp. 590–598, 2013.

[15] A. Correa, A. Morell, M. Barcelo, and J. L. Vicario, "Navigation system for elderly care applications based on wireless sensor networks," in *Proceedings of the 20th European Signal Processing Conference (EUSIPCO '12)*, pp. 210–214, IEEE, Bucharest, Romania, August 2012.

[16] J. H. Lee, B. Shin, S. L. J. H. Kim, C. Kim, T. Lee, and J. Park, "Motion based adaptive step length estimation using smartphone," in *Proceedings of the 18th IEEE International Symposium on Consumer Electronics (ISCE '14)*, pp. 1–2, JeJu Island, Republic of Korea, June 2014.

[17] M. R. Ahsan, M. I. Ibrahimy, and O. O. Khalifa, "EMG motion pattern classification through design and optimization of neural network," in *Proceedings of the International Conference on Biomedical Engineering (ICoBE '12)*, pp. 175–179, Penang, Malaysia, February 2012.

[18] H. Li and F.-L. Jian, "Human-induced vibration under walking-crowd excitation," *Journal of South China University of Technology (Natural Science)*, vol. 38, no. 4, pp. 125–130, 2010.

[19] Y.-K. Kim, S.-H. Choi, H.-W. Kim, and J.-M. Lee, "Performance improvement and height estimation of pedestrian dead-reckoning system using a low cost MEMS sensor," in *Proceedings of the 12th International Conference on Control, Automation and Systems (ICCAS '12)*, pp. 1655–1660, JeJu Island, The Republic of Korea, October 2012.

Hindawi Publishing Corporation
Journal of Sensors
Volume 2015, Article ID 382865, 9 pages
http://dx.doi.org/10.1155/2015/382865

Research Article

Study of Three-Component FBG Vibration Sensor for Simultaneous Measurement of Vibration, Temperature, and Verticality

Jiang Shan-chao, Wang Jing, Sui Qing-mei, Ye Qing-lin, and Wang Li-jun

School of Control Science and Engineering, Shandong University, Jinan 250061, China

Correspondence should be addressed to Wang Jing; wangjingkz@sdu.edu.cn

Received 5 October 2014; Revised 21 December 2014; Accepted 21 December 2014

Academic Editor: Fei Dai

To achieve simultaneous measurement of measurand vibration, temperature, and verticality, a three-component fiber Brag grating (TVFBG) vibration sensor is proposed in this paper. Polymer and metal diaphragm sensitization methods are utilized to improve this sensor measurement sensitivity. Project matrix theory is adopted to analyze this sensor. Theoretically, 9×9 nonsingular measuring coefficient matrix of this TVFBG sensor made up by three 3×3 measurand coefficient matrixes is established. In order to effectively extract measurand, Hilbert-Huang transform (HHT) is accepted to process this sensor's center wavelength signals. Calibration experiments are carried out to verify the performance of this TVFBG sensor. Experiment data confirm that this sensor has excellent frequency response and show good linearity at temperature and verticality measurement. Wrist rotation angle measurement experiment is also implemented to further identify this sensor practical value. Through analyzing by HHT, experiment results show that the angle measurement sensitivities of three fiber Brag gratings which are included in this sensor are separately 25.2 pm/°, 38.2 pm/°, and 38.3 pm/°.

1. Introduction

Simultaneous multiparameter measurement has provided one way which reduces the number of measuring sensors and cuts down detection cost to monitor the health status of engineering structure. Based on the characteristics of fiber Bragg grating (FBG), such as high accuracy, small size, immunity to electromagnetic interference, and multiplexing capacity, FBG sensors have been widely used in aerospace, energy industry, transportation, and geotechnical and civil engineering [1–8]. During the latest decades, there are many works about isochronous multiparameter measurement by FBG sensors have been down. Rao et al. [9] performed the simultaneous measurement of static strain, temperature, and vibration using a multiplexed in-FBG/fibre-F-P sensor. Zhang et al. [10] demonstrated an integrated inline microfiber sensor based on fiber Bragg gratings to simultaneously measure vibration and temperature information for state estimation of cable-stayed bridges.

Based on available research results, a three-component FBG vibration (TVFBG) sensor for synchronous measurement of vibration, temperature, and verticality is proposed in this paper. Due to the fact that axial strain sensitive coefficient of bare FBG is only 0.003 nm/MPa [11], many methods have been reported to improve its coefficient, such as polymer sensitization [12, 13], metal diaphragm sensitization [14, 15], and some other mechanical structures [1, 16]. Polymer and metal diaphragm sensitization methods are both used to improve measurement sensitivity of this TVFBG sensor.

According to project matrix theory, 9×9 nonsingular measuring coefficient matrix made up by three 3×3 measurand coefficient matrixes is established. All these 3×3 matrixes are deduced from this sensor theoretical model. Three fiber Bragg gratings (TFBGs) are included in this TVFBG sensor as the sensitive elements. All center wavelengths of TFBGs contain the information of vibration, temperature, and verticality. So as to effectively extract the measurand vibration, temperature, and verticality, Hilbert-Huang transform (HHT) is

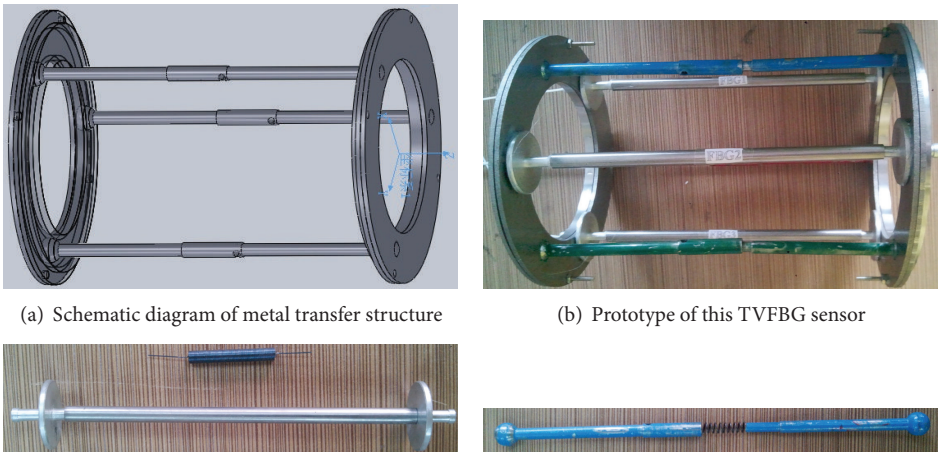

(a) Schematic diagram of metal transfer structure

(b) Prototype of this TVFBG sensor

(c) Sensing element component parts

(d) Components of link rob

Figure 1: Basic block diagram and prototype of this TVFBG sensor.

used to analyze the dynamic wavelength signals. Calibration experiment is carried out to test this sensor performance and wrist rotation angle measurement experiment further proves its practical value.

Generally speaking, in this sensor polymer and metal diaphragm sensitization methods are used to improve its measuring sensitivity. Theoretical calculation model based on project matrix theory is set up and HHT is utilized to extract and reconstruct the measurand. It realizes three-parameter measurement at the same time. Due to calibration and wrist rotation measurement experiment results, this TVFBG sensor possesses great potential in engineering application.

2. Structure of the TVFBG Sensor

Basic metal transfer structure and prototype of this TVFBG sensor are shown in Figure 1. This TVFBG sensor is composed of three sensing elements and one metal transfer structure. All these three sensing elements are equidistant distributed around the axial direction and the angle interval is 120° in the circumferential distribution. The sensing element which is shown in Figure 1(c) includes two connection terminals, one spring as the elastic element and one fiber Bragg grating as sensitive element.

Metal transfer structure shown in Figure 1(a) is made up by three link rods, upper fixed and lower free rings. Link rod exhibited in Figure 1(d) is composed of two omnidirectional wheels distributed at both ends and the middle elastic element. Basic geometric parameters of this metal transfer structure are presented in Table 1.

Table 1: Basic geometric parameters of metal transfer structure (unit: mm).

	Length	Height	Outer radius	Inner radius
The ring		7	110	70
Link rod	155		4	
Omnidirectional wheel			5	
Elastomer in the middle of link rod	2.5		5	4

3. Signal Analysis and Measurand Identification

Due to the advantages unlimited by fixed wavelet and adaptive signal processing, HHT [13, 17] is widely adopted as a powerful tool to deal with nonlinear and nonstationary signals. HHT is utilized to pick out three different signals $\Delta\lambda_{iV}$, $\Delta\lambda_{iT}$, and $\Delta\lambda_{iP}$ $(i = 1, 2, 3)$ from the original center wavelengths $\lambda_{\mathrm{FBG}i}$ $(i = 1, 2, 3)$. $\Delta\lambda_{iV}$, $\Delta\lambda_{iT}$, and $\Delta\lambda_{iP}$ are wavelength changes caused by external vibration, temperature, and verticality angle. Through analyzing by HHT, the original signals could be expressed as

$$\begin{aligned}
\lambda_{\mathrm{FBG1}} &= \lambda_{10} + \sum_{i=1}^{n} c_{1i}, \\
\lambda_{\mathrm{FBG2}} &= \lambda_{20} + \sum_{i=1}^{n} c_{2i}, \\
\lambda_{\mathrm{FBG3}} &= \lambda_{30} + \sum_{i=1}^{n} c_{3i},
\end{aligned} \tag{1}$$

where λ_{i0} $(i = 1, 2, 3)$ and c_{mi} $(m = 1, 2, 3)$ stand for residual signals and intrinsic mode functions of the original signals.

3.1. Vibration Identification. Because of middle elastic element, the external vibration signal induces axial dynamic strain on these TFBGs and further leads to the center wavelength changes. Relationship between axial strain ε and center wavelength shift $\Delta\lambda$ could be expressed as

$$\frac{\Delta\lambda}{\lambda} = (1 - p_e)\,\varepsilon, \tag{2}$$

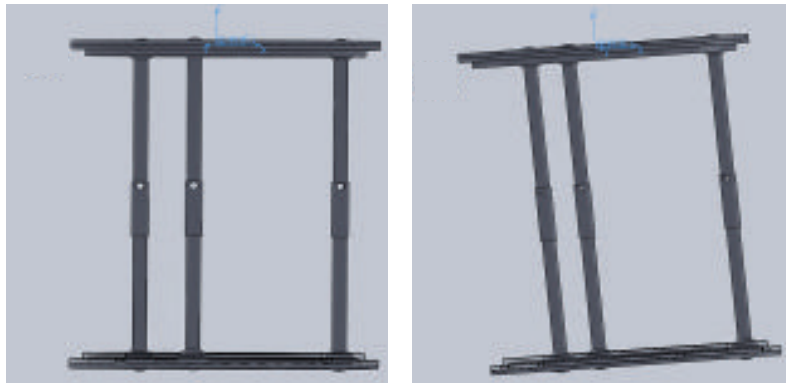

(a) (b)

Figure 2: (a) The fixed ring parallels the ground plane. (b) Verticality angle α between the fixed ring and the ground plane.

where p_e is the elastic-optic coefficient of optical fiber and its theoretical value equals 0.22. So, the efficiency of dynamic stress F worked on the optical fiber could be expressed as

$$F = E\varepsilon = k_e \cdot V(t), \tag{3}$$

where E is elasticity modulus of optical fiber, k_e is the elastic coefficient of elastomer in the link rob, and $V(t)$ represents the exterior dynamic signal.

Through (2) and (3), we could get that

$$\begin{aligned}
\Delta\lambda_{1V} &= \frac{(1-p_e)}{E} \cdot \lambda_{10} \cdot k_{e1} \cdot V_1(t), \\
\Delta\lambda_{2V} &= \frac{(1-p_e)}{E} \cdot \lambda_{20} \cdot k_{e2} \cdot V_2(t), \\
\Delta\lambda_{3V} &= \frac{(1-p_e)}{E} \cdot \lambda_{30} \cdot k_{e3} \cdot V_3(t) \quad \text{or} \\
\begin{bmatrix} \Delta\lambda_{1V} \\ \Delta\lambda_{2V} \\ \Delta\lambda_{3V} \end{bmatrix} &= \mathbf{V} \cdot \begin{bmatrix} V_1(t) \\ V_2(t) \\ V_3(t) \end{bmatrix},
\end{aligned} \tag{4}$$

where $V_1(t)$, $V_2(t)$, and $V_3(t)$ are exterior vibration signals and $\mathbf{V}$ represents the vibration coefficient matrix.

3.2. Temperature Identification. Temperature changes can be obtained by

$$\begin{aligned}
\Delta\lambda_{1T} &= \lambda_{10} \cdot (\alpha + \xi) \cdot T_1(t), \\
\Delta\lambda_{2T} &= \lambda_{20} \cdot (\alpha + \xi) \cdot T_2(t), \\
\Delta\lambda_{3T} &= \lambda_{30} \cdot (\alpha + \xi) \cdot T_3(t) \quad \text{or} \\
\begin{bmatrix} \Delta\lambda_{1T} \\ \Delta\lambda_{2T} \\ \Delta\lambda_{3T} \end{bmatrix} &= \mathbf{T} \cdot \begin{bmatrix} T_1(t) \\ T_2(t) \\ T_3(t) \end{bmatrix},
\end{aligned} \tag{5}$$

where α is thermal expansion coefficient, ξ is thermooptic coefficient of FBG, $T_1(t)$, $T_2(t)$, and $T_3(t)$ are the measured temperature, and $\mathbf{T}$ is the coefficient matrix of temperature.

3.3. Verticality Identification. While connecting line between upper and lower ring center points is not parallel with geodetic vertical line, the free ring could ceaselessly wiggle until the connecting line parallels the geodetic vertical line based on the function of omnidirectional wheel. The angle between geodetic vertical line and axis of this sensor metal transfer structure is selected as vertical evaluation standard and named as verticality angle α. When this sensor position changes from Figures 2(a) to 2(b), verticality angle α is generated by gravity.

Adding the Cartesian coordinate system to this sensor and assuming that the link rod with FBG1 is vertical orthogonal with x-axis, verticality calculation model is shown in Figure 3.

So, the length changes ΔL_i $(i = 1, 2, 3)$ of three link robs are expressed as

$$\begin{aligned}
\Delta L_1 &= r(1 + \cos\theta) \cdot \sin\alpha, \\
\Delta L_2 &= r\left[1 - \cos\left(\frac{\pi}{3} + \theta\right)\right] \cdot \sin\alpha, \\
\Delta L_3 &= r\left[1 - \cos\left(\frac{\pi}{3} - \theta\right)\right] \cdot \sin\alpha,
\end{aligned} \tag{6}$$

where r is radius of the upper fixed ring and θ is the directional angle between radius line ① and x axis in the XY plane.

Based on the above analysis, verticality calculation formula is expressed as

$$\begin{aligned}
\Delta\lambda_{1v} &= \lambda_{10} \cdot (1-p_e) \cdot r(1 + \cos\theta) \cdot \frac{\sin\alpha}{h}, \\
\Delta\lambda_{2v} &= \lambda_{20} \cdot (1-p_e) \cdot r\left[1 - \cos\left(\frac{\pi}{3} + \theta\right)\right] \cdot \frac{\sin\alpha}{h}, \\
\Delta\lambda_{3v} &= \lambda_{30} \cdot (1-p_e) \cdot r\left[1 - \cos\left(\frac{\pi}{3} - \theta\right)\right] \cdot \frac{\sin\alpha}{h} \quad \text{or} \\
\begin{bmatrix} \Delta\lambda_{1v} \\ \Delta\lambda_{2v} \\ \Delta\lambda_{3v} \end{bmatrix} &= \mathbf{V} \cdot \begin{bmatrix} P_1(t) \\ P_2(t) \\ P_3(t) \end{bmatrix},
\end{aligned} \tag{7}$$

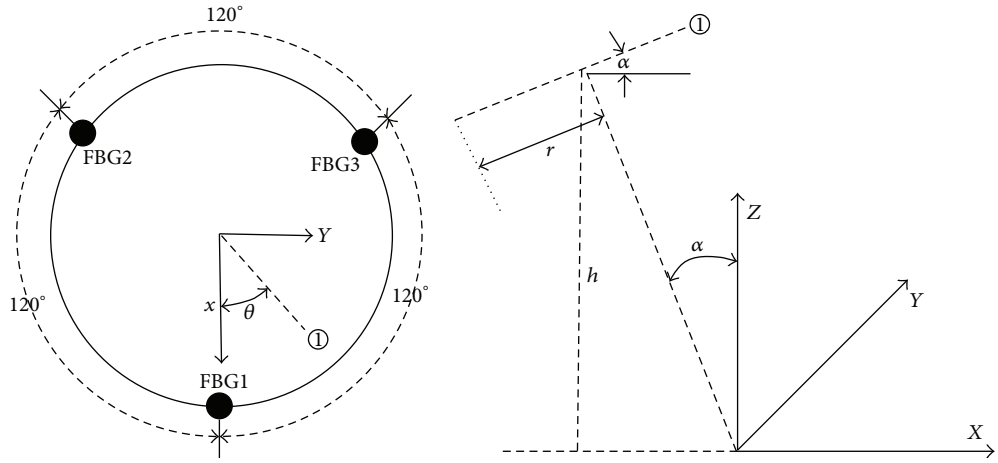

(a) Cross section of these three fiber Bragg gratings

(b) Geometry of verticality reconstruction based on the center wavelength changes

Figure 3: Verticality calculation model of this sensor.

where h is height of this sensor and $\mathbf{V}$ is the verticality coefficient matrix. Through (7), verticality angle α and directional angle θ are obtained.

The measurand identification could be concluded in four steps.

(1) Use HHT to extract different signals $\Delta\lambda_{iV}$, $\Delta\lambda_{iT}$, and $\Delta\lambda_{iP}$ $(i = 1, 2, 3)$ from the center wavelengths $\lambda_{\mathrm{FBG}i}$ $(i = 1, 2, 3)$.

(2) External dynamic signals $V_1(t)$, $V_2(t)$, and $V_3(t)$ are obtained by bringing $\Delta\lambda_{iV}$ $(i = 1, 2, 3)$ to (4).

(3) Environment temperatures $T_1(t)$, $T_2(t)$, and $T_3(t)$ are picked out by bringing $\Delta\lambda_{iT}$ $(i = 1, 2, 3)$ to (5).

(4) Verticality angle α and directional angle θ are calculated by bringing $\Delta\lambda_{iP}$ $(i = 1, 2, 3)$ to (7).

Therefore, the relationship between center wavelength changes and measurand could be expressed as

$$\begin{bmatrix} \Delta\lambda_{\mathrm{FBG1}} \\ \Delta\lambda_{\mathrm{FBG2}} \\ \Delta\lambda_{\mathrm{FBG3}} \end{bmatrix} \xrightarrow{\mathrm{HHT}} \begin{bmatrix} \Delta\lambda_{1V} \\ \Delta\lambda_{2V} \\ \Delta\lambda_{3V} \\ \Delta\lambda_{1T} \\ \Delta\lambda_{2T} \\ \Delta\lambda_{3T} \\ \Delta\lambda_{1P} \\ \Delta\lambda_{2P} \\ \Delta\lambda_{3P} \end{bmatrix}$$

$$= \begin{bmatrix} \mathbf{V} & & \\ & \mathbf{T} & \\ & & \mathbf{P} \end{bmatrix} \begin{bmatrix} V_1(t) & & \\ V_2(t) & & \\ V_3(t) & & \\ & T_1(t) & \\ & T_2(t) & \\ & T_3(t) & \\ & & P_1(t) \\ & & P_2(t) \\ & & P_3(t) \end{bmatrix}. \quad (8)$$

4. Calibration Experiment

For testing the performance of this TVFBG sensor, frequency response, temperature sensitivity, and verticality measuring experiment are all carried out. The basic instruments in these experiments are ASE broadband flattened light source, optical fiber circulator, and sense 20/20. Sense 20/20 is produced by Bay Spec, Inc., and acts as fiber dynamic demodulation instrument. Some other auxiliary equipment such as INV1601 vibration platform produced by Beijing Dongfang Vibration and Noise Technology Research Institute, thermostatic water tank, and protractor are also used in these experiments. The initial center wavelengths of FBG1, FBG2, and FBG3 are 1540.5533 nm, 1534.4096 nm, and 1530.7497 nm.

4.1. Frequency Response Experiment. Figure 4 shows diagram and basic instruments of frequency response experiment which is set up to simulate the exterior vibration environment. This sensor is adhered together with vibration platform through epoxy resin. Its status is kept vertical. In order to improve coupling coefficient, a thin layer ethyl α-cyanoacrylate is coated at the surface of simply supported

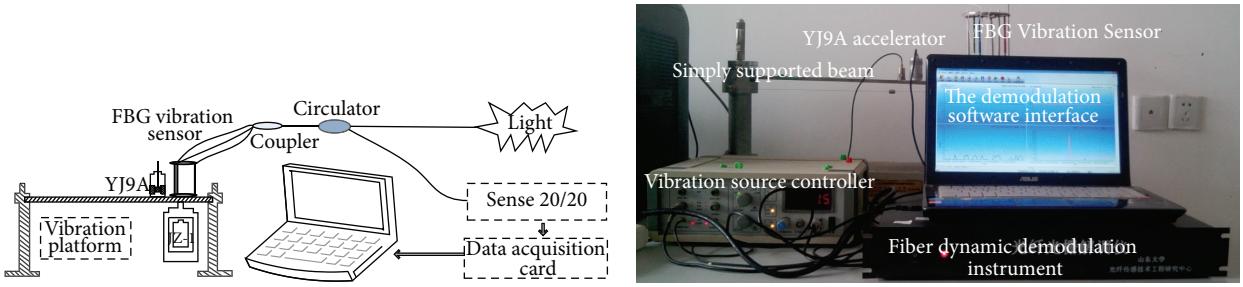

(a) Basic diagram of frequency response experiment

(b) Instruments in frequency response experiment

Figure 4: Frequency response experiment platform.

beam. Detection frequency ranges of sense 20/20 are 0–5 KHz and its frequency demodulation precision is 1 Hz. JZ-1 type vibration source included in the INV1601 vibration platform generates a series frequency from 100 Hz to 1 KHz in steps of 100 Hz with precision 0.1 Hz. The output amplitude is kept at 1.3 m/s^2 in the whole experiment. Comparative analysis data between detected data by this TVFBG sensor and generated data by JZ-1 are utilized as reference indicator to evaluate this sensor frequency response.

4.2. Temperature Sensitivity Experiment. Thermostatic water tank is utilized to change this sensor environment temperature. Diagram of temperature sensitivity experiment is shown in Figure 5. So as to avoid that the center wavelengths of TFBGs are influenced by exterior strain, this TVFBG sensor is statically placed at the bottom of the tank. SM125 (demodulation ranges 1510–1590 nm, demodulation precision 1 pm) is chosen as fiber interrogator. In this whole process, temperature variation ranges are 20°C–60°C and its step interval is 5°C. Water temperature is also measured by thermal resistance which is selected as contrastive data with this TVFBG sensor. Water temperature is remaining stable for almost one minute at each step. The heating and cooling processes are repeated twice.

4.3. Verticality Measuring Experiment. Protractor which is used in teaching acts as measure verticality angle measuring instrument and its precision is 1°. Instruments used in this experiment are shown in Figure 6. Achieving the purpose that data processing is more convenient, the axis of FBG1 is kept vertical orthogonal with zero depicting line at the beginning of this experiment. The manually controlled FBG1 axis rotates counterclockwise to change the verticality angle α. Due to metal transfer structure, center wavelength of FBG2 is increased and these other two wavelengths are both decreased. Limited by the theoretical maximum strain value of FBG which is 7860 $\mu\varepsilon$, small ranges verticality measuring experiment is carried out. The manually controlled verticality angle α increases from 0° to 5° with step interval 1°.

5. Data Analysis and Results

Analyzing the experiment data acquired in previous calibration experiment, the basic characteristics of the TVFBG sensor are identified in this section.

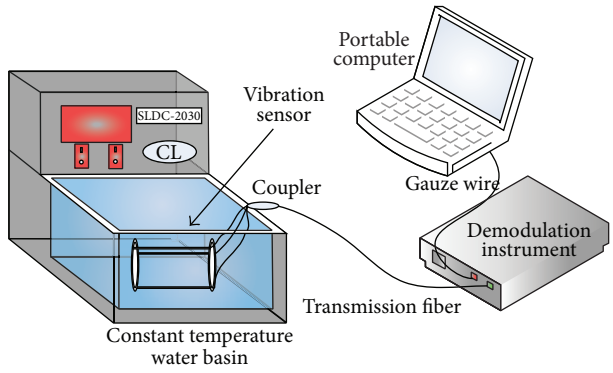

Figure 5: Diagram of temperature sensitivity experiment platform.

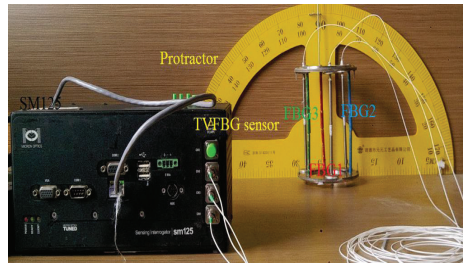

Figure 6: Instruments in the verticality response experiment.

5.1. Frequency Characteristic Analysis. Limited by length of this paper, Figure 7 just displays parts of sectional graphs of the demodulation software interface and the controller signals generated by JZ-1. These sectional graphs just display the frequency signals detected by FBG1.

Fast Fourier transform (FFT) is selected to extract frequency information of this TVFBG sensor in the frequency response experiment. The detected frequency data are shown in Table 2.

Formula of relative measuring error is expressed as

$$\delta_F = \frac{(F_{\mathrm{FBG}i} - F_{VS})}{F_{VS}} \cdot 100\%, \tag{9}$$

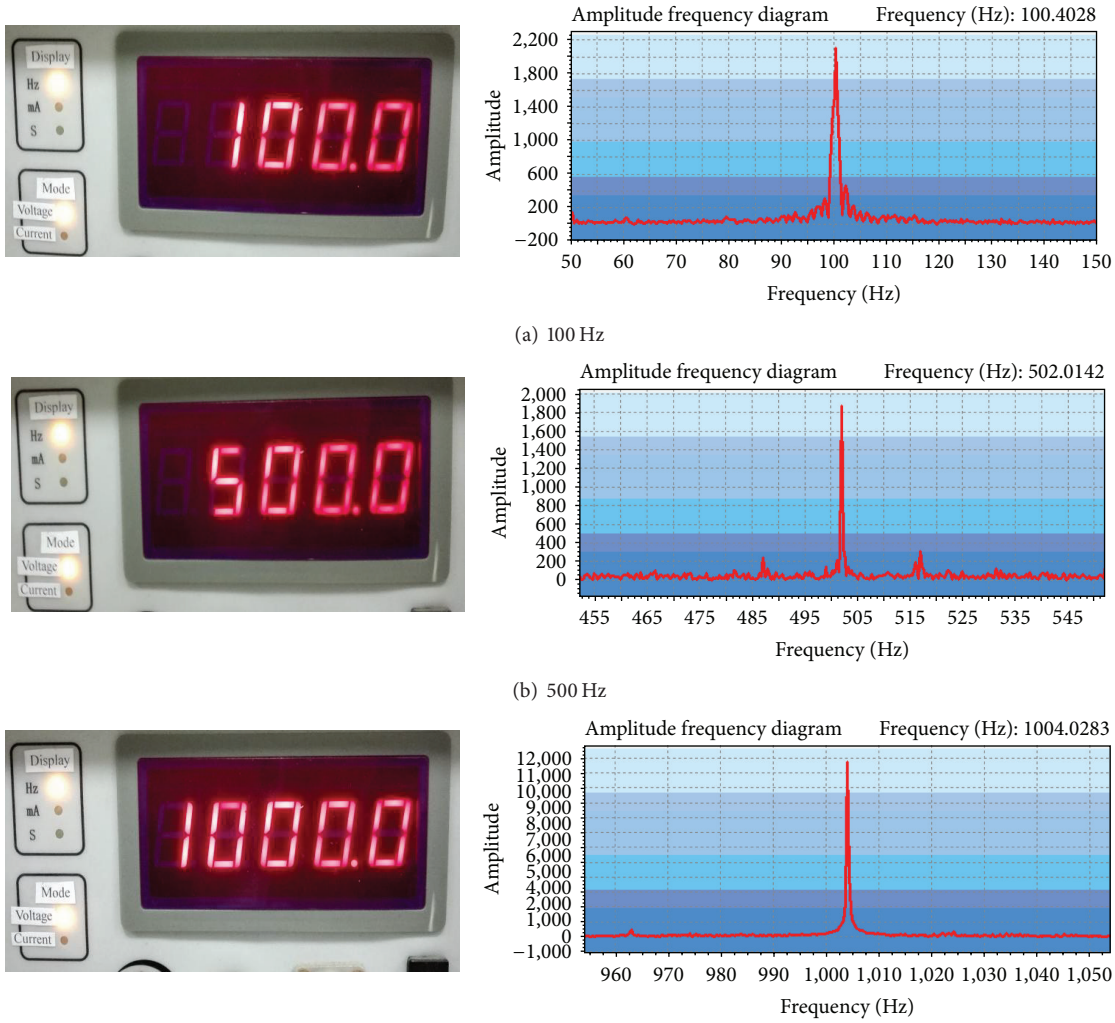

Figure 7: Left: front panel of vibration source controller. Right: demodulation software interface sectional graphs.

Table 2: Detected frequency data by this TVFBG sensor.

Generated frequency/Hz	Detected frequency/Hz		
	FBG1	FBG2	FBG3
100	100.4028	100.4028	100.4028
200	200.8057	200.8057	200.8057
300	301.2085	301.2085	301.2085
400	401.3062	401.6113	401.3062
500	502.0142	502.0142	502.0142
600	602.417	602.417	602.417
700	702.8198	702.8198	702.8198
800	803.2227	803.2227	803.2227
900	903.6255	903.6255	903.6255
1000	1004.0283	1004.0283	1004.0283

where F_{FBGi} $(i = 1, 2, 3)$ and F_{VS} represent detected frequency and the generated frequency, respectively.

Calculating the measuring error between generated and detected frequency through (9), its ranges are from 0.327% to 0.403%. Such data effectively prove that this TVFBG sensor has excellent frequency response.

5.2. Temperature Sensitivity Analysis. Data in the first heating process are displayed in Table 3 and Figure 8 shows changes of center wavelengths following the temperature variations in the whole temperature sensitivity experiment.

Figure 8 exhibits the fact that the relationship between temperature and center wavelengths has excellent linearity and reproducibility. Temperature sensitivities of FBG1 analyzed by least squares method are 0.0114 pm/°C, 0.0113 pm/°C, 0.0113 pm/°C, and 0.0113 pm/°C in the twice heating and cooling processes. Average value of these four sensitivities is selected as temperature sensitivity of FBG1 and its value is 11.3 pm/°C. Similarly, temperature sensitivities of FBG2 and FBG3 are 13.4 pm/°C and 11.2 pm/°C. Temperature sensitivities of TFBGs are all approximated to the bare FBG. Therefore, this sensor realizes precise temperature measurement.

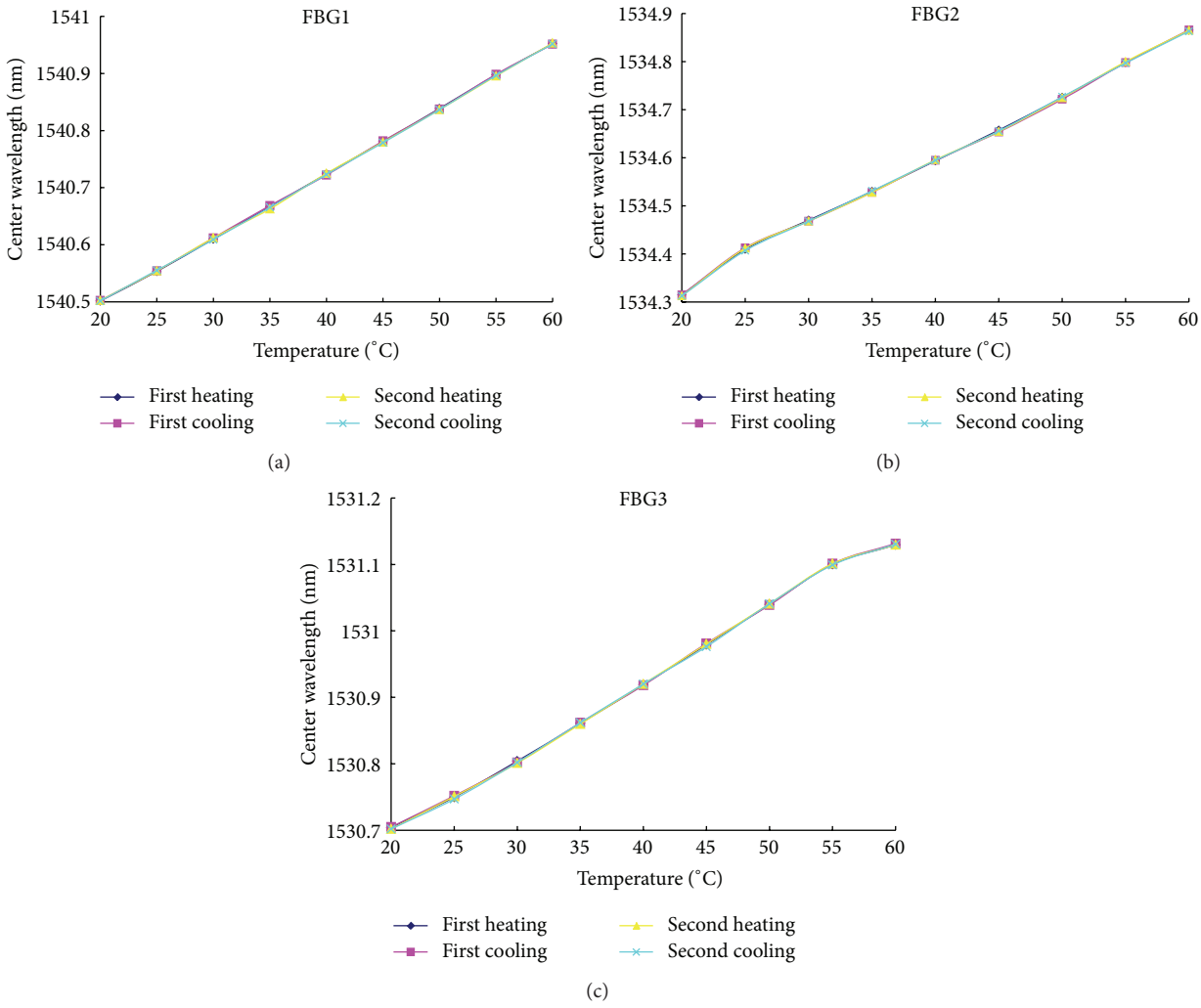

Figure 8: Fitting curves between center wavelengths and temperature.

Table 3: Experiment data in first heating procedure.

Temperature/°C	Center wavelength of FBG/nm		
	FBG1	FBG2	FBG3
20	1540.400517	1534.314647	1530.703881
25	1540.553308	1534.40965	1530.749724
30	1540.609982	1534.470089	1530.804002
35	1540.666616	1534.529987	1530.860776
40	1540.724015	1534.593595	1530.918992
45	1540.780719	1534.657476	1530.979152
50	1540.838631	1534.72566	1531.039742
55	1540.897591	1534.797819	1531.100086
60	1540.952174	1534.864976	1531.129372

5.3. Verticality Measuring Analysis. Table 4 gives the center wavelengths of this TVFBG sensor in the verticality measuring experiment.

Fitting curves between wavelength λ_B and verticality angle α are $\lambda_{FBG1} = -0.0267\alpha + 1540.3$ ($R^2 = 0.9969$), $\lambda_{FBG2} = 0.0407\alpha + 1535.3$ ($R^2 = 0.9935$), and $\lambda_{FBG3} = -0.0375\alpha + 1530.5$ ($R^2 = 0.9988$). Due to the fact that the verticality angle α is very small, its sine value equals itself. Relationship between λ_B and α presents excellent linearity and the verticality measuring sensitivities are 26.7 pm/°, 40.7 pm/°, and 37.5 pm/° severally. All these verticality coefficients are available just under calibration experiment conditions. So, this TVFBG sensor realizes verticality measuring

Table 4: Data of verticality measuring experiment.

Angle α/°	Center wavelength of FBG/nm		
	FBG1	FBG2	FBG3
0	1540.0843	1535.2864	1530.4722
1	1540.0578	1535.336	1530.4356
2	1540.0352	1535.3691	1530.3994
3	1540.0033	1535.4215	1530.3658
4	1539.9825	1535.4581	1530.3223
5	1539.9491	1535.4874	1530.2847

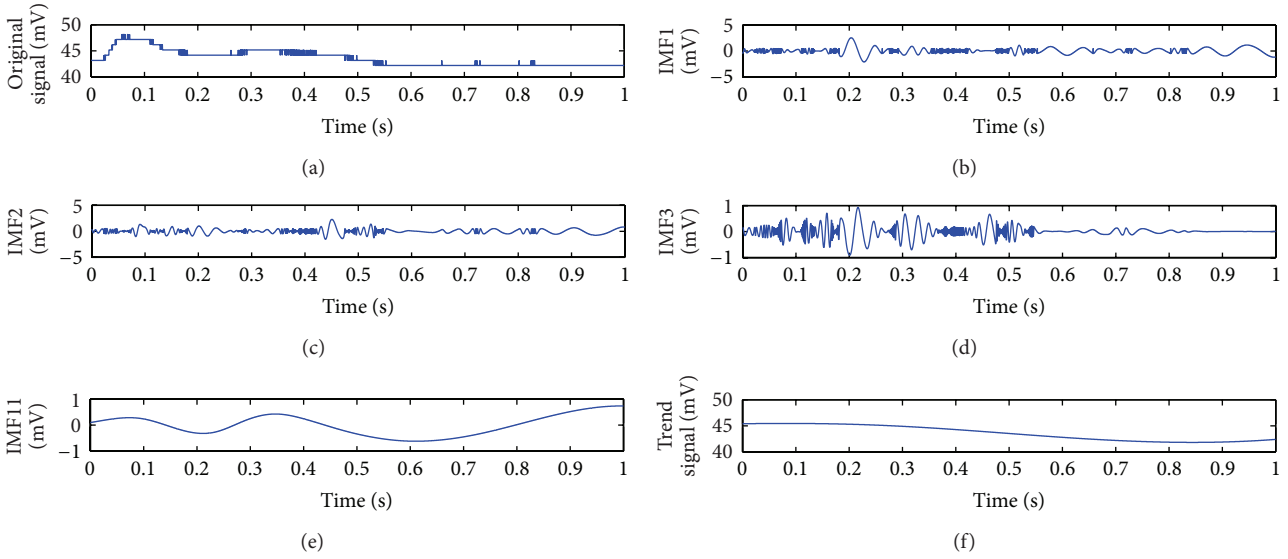

Figure 9: Sample data analyzed by HHT.

and shows excellent measuring linearity at small verticality angle ranges.

6. Wrist Rotation Angle Measurement Experiment

So as to verify the practical value of this TVEBG sensor, wrist rotation angle measurement experiment is implemented. Wrist rotation angle changes from −10° to 10° with step interval of 5° under the same condition in verticality measuring experiment. Sense 20/20 is chosen as the dynamic fiber interrogator. Wavelength data of FBG1 corresponding to angle 0° are selected as sample data to explain signal processing. The sample data processed by HHT is shown in Figure 9.

After HHT analysis, trend signals are chosen as the corresponding verticality angle data. Using the same signal processing methods, the extracted data are shown in Table 5.

Least squares method is used to acquire verticality measuring sensitivities and these values corresponding to TFBGs are 25.2 pm/°, 38.2 pm/°, and 38.3 pm/° separately. Hence, this sensor can be used in practical measurement.

Table 5: Extracted center wavelength data analyzed by HHT.

Wrist rotation angle α/°	Center wavelength of FBG/nm		
	FBG1	FBG2	FBG3
−10	1540.31	1534.899	1530.858
−5	1540.2125	1535.0854	1530.6487
0	1540.0843	1535.2864	1530.4722
5	1539.9491	1535.4874	1530.2847
10	1539.8126	1535.653	1530.082

7. Conclusion

A three-component FBG vibration sensor which could simultaneously measure vibration, temperature, and verticality is realized in this paper. Project matrix theory is chosen as basic theory to establish this sensor theatrical calculation model. HHT is used to analyze this sensor's wavelength signals and reconstruct measurand. Calibration experiments consisting of frequency response, temperature sensitivity, and verticality measuring experiment are carried out. Calibration experiments data confirm that this sensor could realize frequency, temperature, and verticality measurements with high precision. This TVFBG sensor's frequency measuring errors at ranges of 100–1000 Hz are all less than 1% and its temperature and verticality measuring sensitivities are 11.3 pm/°C, 13.4 pm/°C, 11.2 pm/°C, 26.7 pm/°, 40.7 pm/°, and 37.5 pm/°. In order to further verify this sensor practical value, wrist rotation angle experiment is also implemented. Wrist rotation experiment results show that this sensor realizes wrist angle measuring and its sensitivities are 25.2 pm/°, 38.2 pm/°, and 38.3 pm/°. All these experiment data prove that this sensor has certain practical value in engineering.

Conflict of Interests

The authors declare that there is no conflict of interests regarding the publication of this paper.

Acknowledgments

This work is cosupported by the National Natural Science Foundation of China under Grant nos. 61174018 and 41202206 and Independent Innovation Foundation of Shandong University under Grant no. yzc12081.

References

[1] T.-C. Liang and Y.-L. Lin, "Ground vibrations detection with fiber optic sensor," *Optics Communications*, vol. 285, no. 9, pp. 2363–2367, 2012.

[2] G. Wild, "Optical fiber bragg grating sensors applied to gas turbine engine instrumentation and monitoring," in *Proceedings of the 8th IEEE Sensors Applications Symposium (SAS'13)*, pp. 188–192, Galveston, Tex, USA, February 2013.

[3] R. Chintakindi and S. P. S. Rajesh, "Vital role of FBG sensors—2012 developments in electrical power systems," in *Proceedings of the International Conference Power, Energy and Control (ICPEC '13)*, pp. 478–483, Sri Rangalatchum Dindigul, February 2013.

[4] W. Ecke and M. W. Schmitt, "Fiber bragg gratings in industrial sensing," in *Proceedings of the Optical Fiber Communication Conference and Exposition and the National Fiber Optic Engineers Conference (OFC/NFOEC '13)*, pp. 1–67, March 2013.

[5] H.-H. Zhu, J.-H. Yin, L. Zhang, W. Jin, and J.-H. Dong, "Monitoring internal displacements of a model dam using FBG sensing bars," *Advances in Structural Engineering*, vol. 13, no. 2, pp. 249–261, 2010.

[6] H.-H. Zhu, J.-H. Yin, A. T. Yeung, and W. Jin, "Field pullout testing and performance evaluation of GFRP soil nails," *Journal of Geotechnical and Geoenvironmental Engineering*, vol. 137, no. 7, pp. 633–642, 2011.

[7] H.-H. Zhu, A. N. L. Ho, J.-H. Yin, H. W. Sun, H.-F. Pei, and C.-Y. Hong, "An optical fibre monitoring system for evaluating the performance of a soil nailed slope," *Smart Structures and Systems*, vol. 9, no. 5, pp. 393–410, 2012.

[8] H. H. Zhu, B. Shi, J. F. Yan, J. Zhang, C. C. Zhang, and B. J. Wang, "Fiber Bragg grating-based performance monitoring of a slope model subjected to seepage," *Smart Materials and Structures*, vol. 23, no. 9, Article ID 095027, 2014.

[9] Y. J. Rao, P. J. Henderson, D. A. Jackson, L. Zhang, and I. Bennion, "Simultaneous strain, temperature and vibration measurement using a multiplexed in-fibre-Bragg-grating/fibre-Fabry-Perot sensor system," *Electronics Letters*, vol. 33, no. 24, pp. 2063–2064, 1997.

[10] Q. Zhang, T. Zhu, J. D. Zhang, and K. S. Chiang, "Micro-fiber-based FBG sensor for simultaneous measurement of vibration and temperature," *IEEE Photonics Technology Letters*, vol. 25, no. 18, pp. 1751–1753, 2013.

[11] P.-F. Liu, G.-J. Liu, Q. Zhao, Y.-J. Wang, and F. Li, "A study of the development and application of fiber Bragg grating pressure sensors," in *Proceedings of the Academic International Symposium on Optoelectronics and Microelectronics Technology (AISOMT '11)*, pp. 232–235, October 2011.

[12] Z. X. Wei, D. C. Song, Q. M. Zhao, and H.-L. Cui, "High pressure sensor based on fiber bragg grating and carbon fiber laminated composite," *IEEE Sensors Journal*, vol. 8, no. 10, pp. 1615–1619, 2008.

[13] K. O. Lee, K. S. Chiang, and Z. Chen, "Temperature-insensitive fiber-Bragg-grating-based vibration sensor," *Optical Engineering*, vol. 40, no. 11, pp. 2582–2585, 2001.

[14] H. Tsuda, "Fiber Bragg grating vibration-sensing system, insensitive to Bragg wavelength and employing fiber ring laser," *Optics Letters*, vol. 35, no. 14, pp. 2349–2351, 2010.

[15] H.-K. Kang, H.-J. Bang, C.-S. Hong, and C.-G. Kim, "Simultaneous measurement of strain, temperature and vibration frequency using a fibre optic sensor," *Measurement Science and Technology*, vol. 13, no. 8, pp. 1191–1196, 2002.

[16] H. L. Bao, X. Y. Dong, L.-Y. Shao, C.-L. Zhao, and S. Jin, "Temperature-insensitive 2-D tilt sensor by incorporating fiber Bragg gratings with a hybrid pendulum," *Optics Communications*, vol. 283, no. 24, pp. 5021–5024, 2010.

[17] C. L. Xu, C. Liang, B. Zhou, and S. Wang, "HHT analysis of electrostatic fluctuation signals in dense-phase pneumatic conveying of pulverized coal at high pressure," *Chemical Engineering Science*, vol. 65, no. 4, pp. 1334–1344, 2010.

Hindawi Publishing Corporation
Journal of Sensors
Volume 2015, Article ID 376498, 7 pages
http://dx.doi.org/10.1155/2015/376498

Research Article

Application of R/S Method for Dynamic Analysis of Additional Strain and Fracture Warning in Shaft Lining

Guangsi Zhao,[1,2,3] Guoqing Zhou,[1] and Jianzhou Wang[1]

[1] *State Key Laboratory for Geomechanics and Deep Underground Engineering, China University of Mining & Technology, Xuzhou 221116, China*
[2] *Department of Civil and Environmental Engineering, The Hong Kong Polytechnic University, Hung Hom, Hong Kong*
[3] *School of Mechanics and Civil Engineering, China University of Mining & Technology, Xuzhou 221116, China*

Correspondence should be addressed to Guangsi Zhao; zgscumt@126.com

Received 15 October 2014; Revised 12 January 2015; Accepted 12 January 2015

Academic Editor: Fei Dai

In the past few decades, enormous losses have been induced by hundreds of vertical shafts collapse. This study is based on long-term in situ monitoring data of several mines with overburden soil layers in East China in the past six years. R/S modeling based on fractal theory was used to analyze the development of additional strains in shafts by using Hurst exponent. It can be found that from the monitoring results the Hurst effect is significant ranging from 0.5 to 1.0. Its trend also is in good agreement with forward-biased random distribution. Hence, R/S method can be used to predict the additional strain along the shaft lining. In this paper, Hurst exponent shows an irregular phenomenon before cracking. It is proved that Hurst exponent can be used to predicate the progressive failure of shaft lining from abnormal state to normal state. This paper presents the prediction of shaft lining failures using strains measured by embedded strain gauges in the thick overburden soil layers in east China.

1. Introduction

The disasters of shaft lining fracture have frequently occurred in China since 1987, which greatly threatened the production and safety of collieries. According to the data, there are more than 100 shaft linings with similar fracture, which has caused a large amount of property loss and a great deal of potential disaster [1]. So the present research focused on the causes, mechanism, and solving methods for these kinds of geotechnical calamities and the engineering projects have always been the hot topics in recent 20 years in the fields of shaft building, geology, and mining. The vertical additional stress theory on the shaft fracture put forward by China University of Mining and Technology (CUMT) can well describe the main characters of the shaft fracture and are gradually accepted by the experts and scholars both here and abroad because it has been supported by many results from theories, experiments, and practical researches [2, 3]. Most of the mines were completed in 1970s. The designers had not known the mechanism of shaft fracture. Now, in view of the broken shaft, researchers have developed several kinds of monitoring system for prediction of the fracture [4–9]. We still cannot predict the fracture of shaft lining for the stress history and current stress value having not been known.

The early warning of shaft lining fracture is a big issue. Nonlinear theory is becoming a hot issue for disaster prediction in recent years. Rescaled range analysis, as a nonlinear analysis method for time series, is presented by Hurst in 1965 [10, 11]. After that, there are more and more studies on self-affine fractal using this method [12–23].

The rescaled range is a statistical measure of the variability of a time series introduced by the British hydrologist Harold Edwin Hurst. Its purpose is to provide an assessment of how the apparent variability of a series changes with the length of the time-period being considered. The rescaled range is calculated from dividing the range of the values exhibited in a portion of the time series by the standard deviation of the values over the same portion of the time series. For example, consider a time series {2, 5, 3, 7, 8, 12, 4, 2} which has a range, R, of $12 - 2 = 10$. Its standard deviation, S, is 3.46, so

the rescaled range is $R/S = 2.71$. If we consider the same time series, but increase the number of observations of it, the rescaled range will generally also increase. The increase of the rescaled range can be characterized by making a plot of the logarithm of R/S versus the logarithm of n. The slope of this line gives the Hurst exponent, H. If the time series is generated by a random walk (or a Brownian motion process) it has the value of $H = 1/2$. Many physical phenomena that have a long time series suitable for analysis exhibit a Hurst exponent greater than 1/2. For example, observations of the height of the Nile River measured annually over many years give a value of $H = 0.77$ [12].

In the light of self-similarity of the fractal characteristics appearing in shaft lining fracture, rescaled range analysis method is applied to study the early warning of shaft lining fracture [10]. As strain is one of the most critical structural response parameters and plays an important role in structural health monitoring [19–23], an additional strain monitoring system was established [5]. A large amount of time series data are obtained using this system, which makes it possible that we study the evolution of additional strain and forecasting of shaft lining fracture. The additional strain during a shaft lining production run is studied in [13], using rescaled range analysis method. The value of Hurst exponent indicates that the method is feasible and effective. In this paper, additional strain data before fracture, obtained from a representative mine embedded in deep alluvium of east China, are studied using rescaled range analysis method. The result shows that Hurst exponent becomes abnormal before fracture. The evolution of Hurst exponent shows that it has anomalous change from 2 to 5 months before shaft lining fracture.

2. R/S Method [13]

The dynamic analyses process for additional strain is shown as follows: the corresponding time series is $\zeta_1, \zeta_2, \zeta_3, \ldots, \zeta_N$ at time of $t_1, t_2, t_3, \ldots, t_N$, and the time span of the mentioned time series is

$$\tau = t_N - t_1. \tag{1}$$

The average value of the time series within time span τ is

$$\overline{\zeta}_N = \frac{1}{N}\sum_{i=1}^{N}\zeta_i, \tag{2}$$

where N is the number of time series. The cumulative departure of ζ relating to their mean values at t_j can be written as

$$X\left(t_j, N\right) = \sum_{i=1}^{j}\left(\zeta_i - \overline{\zeta}_N\right). \tag{3}$$

The expression of $X(t, N)$ is not only related to t but also related to N. The difference between maximum $X(t)$ and minimum $X(t)$ at the similar N value is denoted as

$$R\left(t_N - t_1\right) = R\left(t\right) = \max X\left(t, N\right) - \min\left(t, N\right), \quad t_1 \le t \le t. \tag{4}$$

Hurst adopted the following standard departure:

$$S = \left[\frac{1}{\tau}\sum_{i=1}^{N}\left(\zeta_i - \overline{\zeta}_N\right)^2\right]^{1/2}, \quad t_1 \le t \le t_N. \tag{5}$$

Then introducing the dimensionless ratio R/S and rescaled R,

$$\frac{R}{S} = \frac{\max X\left(t, N\right) - \min X\left(t, N\right)}{\left[\left(1/\tau\right)\sum_{i=1}^{N}\left(\zeta_i - \overline{\zeta}_N\right)^2\right]^{1/2}}. \tag{6}$$

Hurst's relationship can be expressed as

$$\frac{R}{S} = a\tau^H, \tag{7}$$

where H is Hurst index, R/S is the rescaled range value of sequence ζ_i, and a is a constant. Hurst index can be obtained by

$$\lg\left(\frac{R}{S}\right) = \log a + H\lg\tau. \tag{8}$$

Hurst obtained the explanation to H based on a series of studies: (1) when $H = 0.5$, the sequence is Brownian motion, variables are independent, the corresponding coefficient is 0, variables will not affect the future, and, therefore, the time series is random. (2) When $0 \le H < 0.5$, it indicates that time series presents long-term correlation, but the future overall trend is contrary to the past; the process is antisustainability. (3) When $0.5 < H < 1$, it indicates that the time series present the characteristic of long-term correlation; that is to say, the process is sustainable.

Generally speaking, the shaft additional forces variation is consistent with the previous variation, and the maintenance is stronger as the increase of the H.

3. Dynamic Analysis of Additional Strain before the Fracture of Shaft Lining

The stress of shaft lining will change accompanied by the initiation of the shaft fracture. Therefore, the variation of additional strain is of great importance to the prediction of shaft lining fracture. Taking a mine as an example, dynamic analysis of the additional strain is presented before the fracture of shaft lining, which is used to provide scientific basis for the disaster forecasting of shaft lining fracture.

The thickness of alluvium over the shaft is 153.22 m. The shaft lining is built in 1977 with 400 mm thickness and 6000 mm diameter. It fractured on December 16, 2004, and was cured by cement grouting in around stratum from July 20, 2015, to June 26, 2006.

Figure 1 shows the variation of the additional strain at the depth of 145 m from January 1, 2004, to November 1, 2007. During the period of production and operation in a mine, the additional strain is increasing steadily. It presents a different phenomenon before fracture of shaft lining. The increasing rate becomes bigger than before. We calculate the average additional strain every 3 days as data of time series, $\zeta_1, \zeta_2, \zeta_3, \ldots, \zeta_N$. 100 pieces of information are obtained.

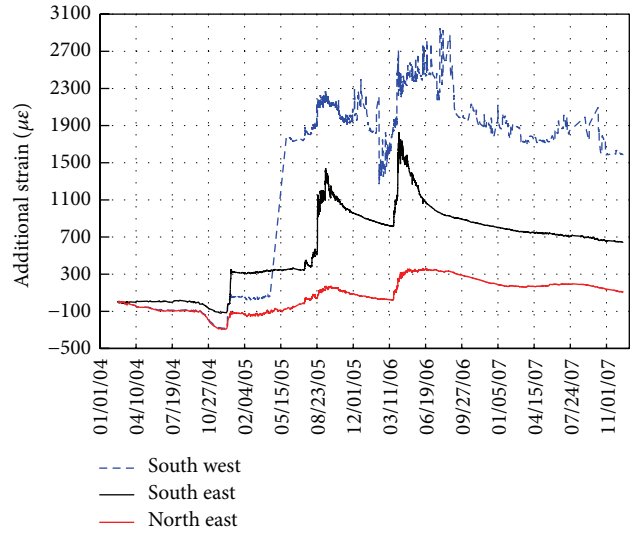

Figure 1: Monitoring data of shaft lining additional strain at 145 m.

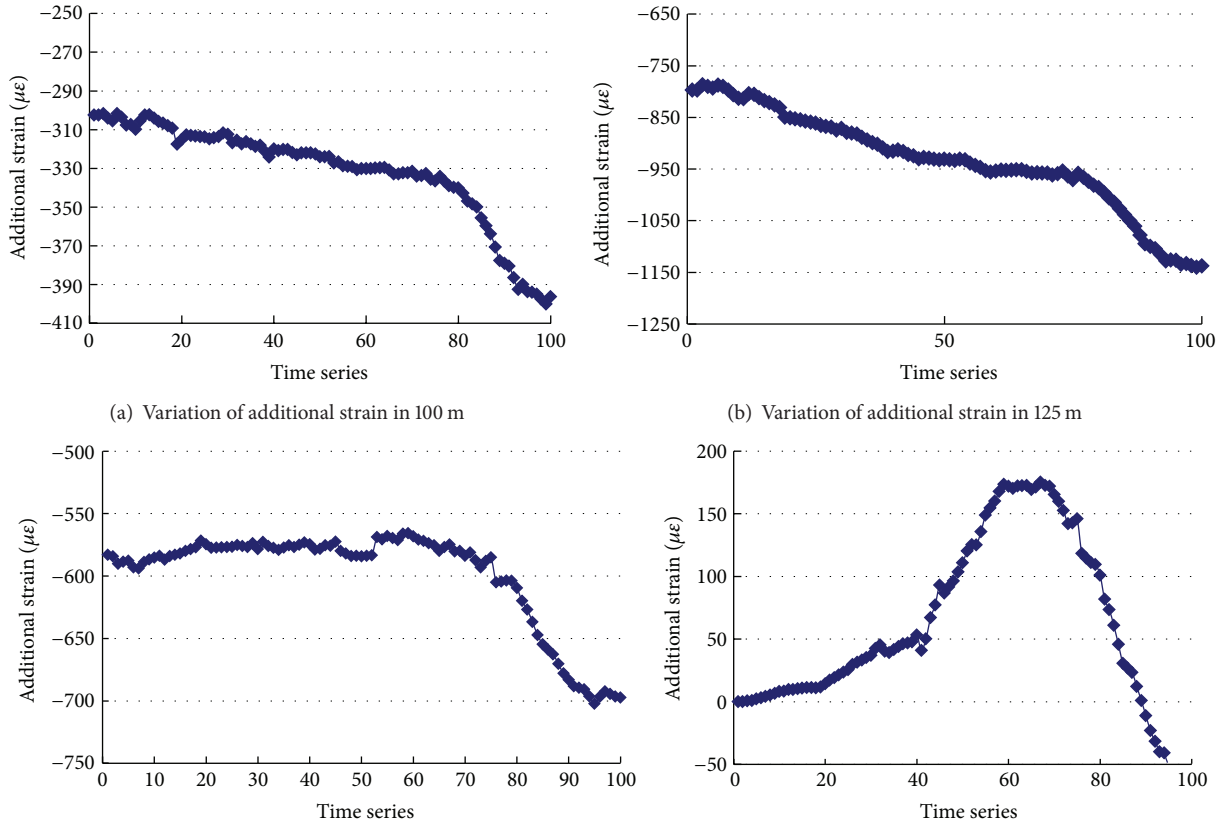

Figure 2: Monitoring data of additional strain of shaft lining.

Figure 2 shows the relationship between additional strain and time at different depths of 100 m, 125 m, 145 m, and 165 m. The monitoring record in ten months shows dynamic changes of the additional strains.

According to the above data, a series of $\lg(R/S)$ and $\lg N$ is obtained in log-log coordinate. It is easily seen that the slope and intercept are obtained through matching the curve, as is shown in Figure 3. Slope of the line is greater than 0.5 along with the increasing of the time scale. Analysis results are as follows.

(1) Because the time series of additional strain before fracture of shaft lining is not a pure random process, the in situ

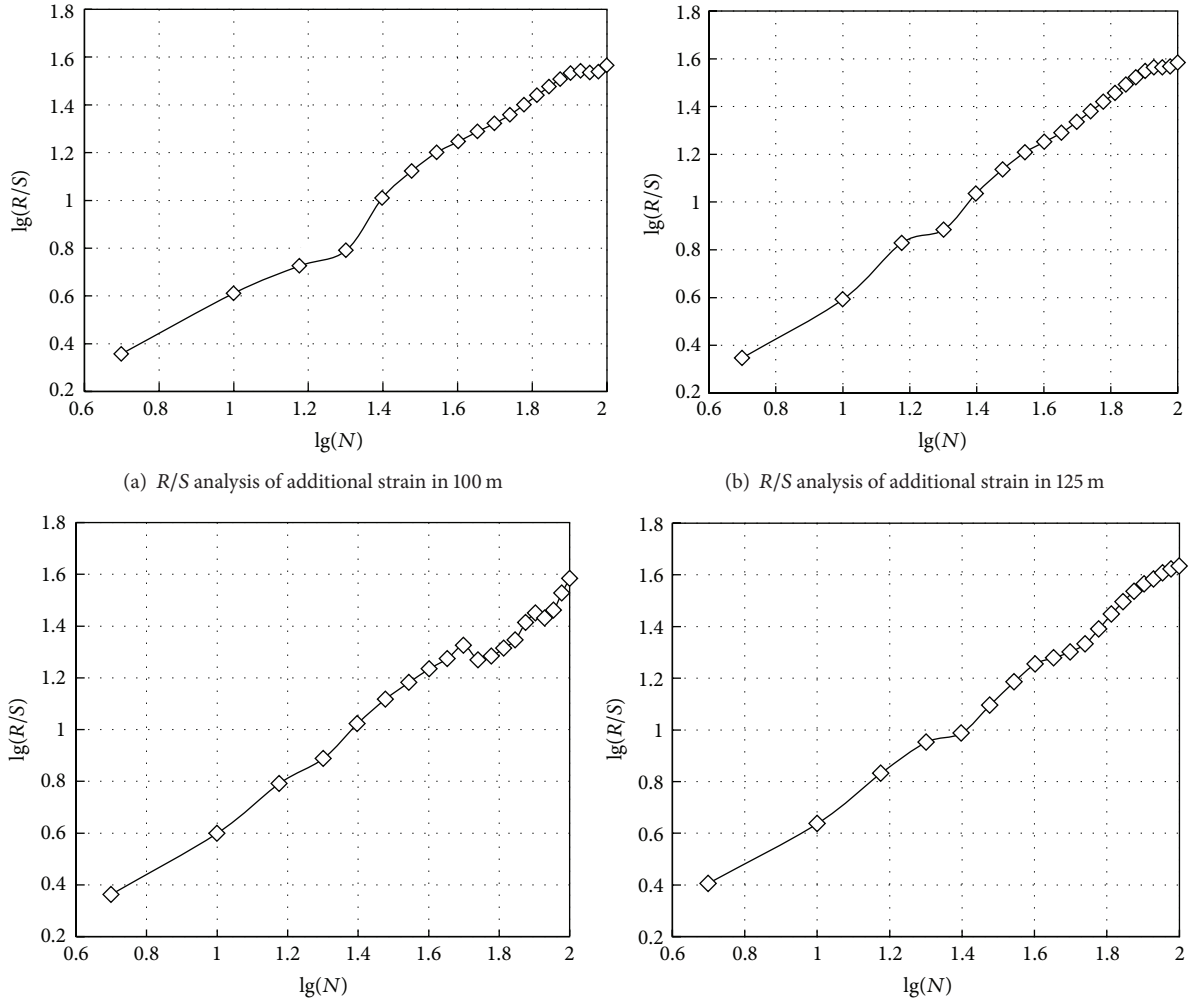

(a) R/S analysis of additional strain in 100 m

(b) R/S analysis of additional strain in 125 m

(c) R/S analysis of additional strain in 145 m

(d) R/S analysis of additional strain in 165 m

Figure 3: R/S results of additional strain.

measurement data are not independent. Dynamic changes of additional strain have long-term memory measurably.

(2) Hurst exponents are 0.9961, 0.9933, 0.8922, and 0.9795 at different depths 100 m, 125 m, 145 m, and 165 m. They are all greater than 0.5, which shows that the current trend of the additional strain exerts a tremendous influence on the next period of time. So we can draw the conclusion that the strain will continue to accumulate.

(3) Hurst exponent is changing with time scale especially at depth of 145 m.

It is easily seen from Figure 3(c) that there is an obviously inflection point when $N = 50$. In Figures 3(a) and 3(b), there are also inflection points when "N" equals 90 nearly though it is not obvious. It is necessary to make a deep analysis on the inflection point.

4. Hurst Exponent Study of Additional Strain before Fracture

In order to carry out Hurst exponent accumulative experiments, we should take actions as follows.

(1) We select the data from 30 May 2004 to 15 July 2004 as the initial window ($N = 35$~50) and then calculate Hurst exponent.

(2) Based on the initial window, we add the data from 16 July to 30 July ($N = 5$); the length of window data is 35 ($N = 35$~55); then we calculate Hurst exponent again. If the value changes, we consider that the change is caused by the new added data for the initial window data does not change.

(3) We can seek the inflection point of Hurst exponent through these accumulative experiments.

We choose the data at depth of 145 m, and the results are shown in Figure 4.

It is easily seen that Hurst exponent significantly reduced with the increase of sample data since 15 July 2004. It began to increase slowly after a period of months. The increasing rate was less than the decreasing rate.

Figure 5 shows the trend of Hurst exponent while adding the sample data every half a month until the fracture moment. The time process of Hurst exponent shows an unnatural variation before fracture (2~5 months). Before the shaft lining fracture, the abnormal feature of Hurst exponent appears to

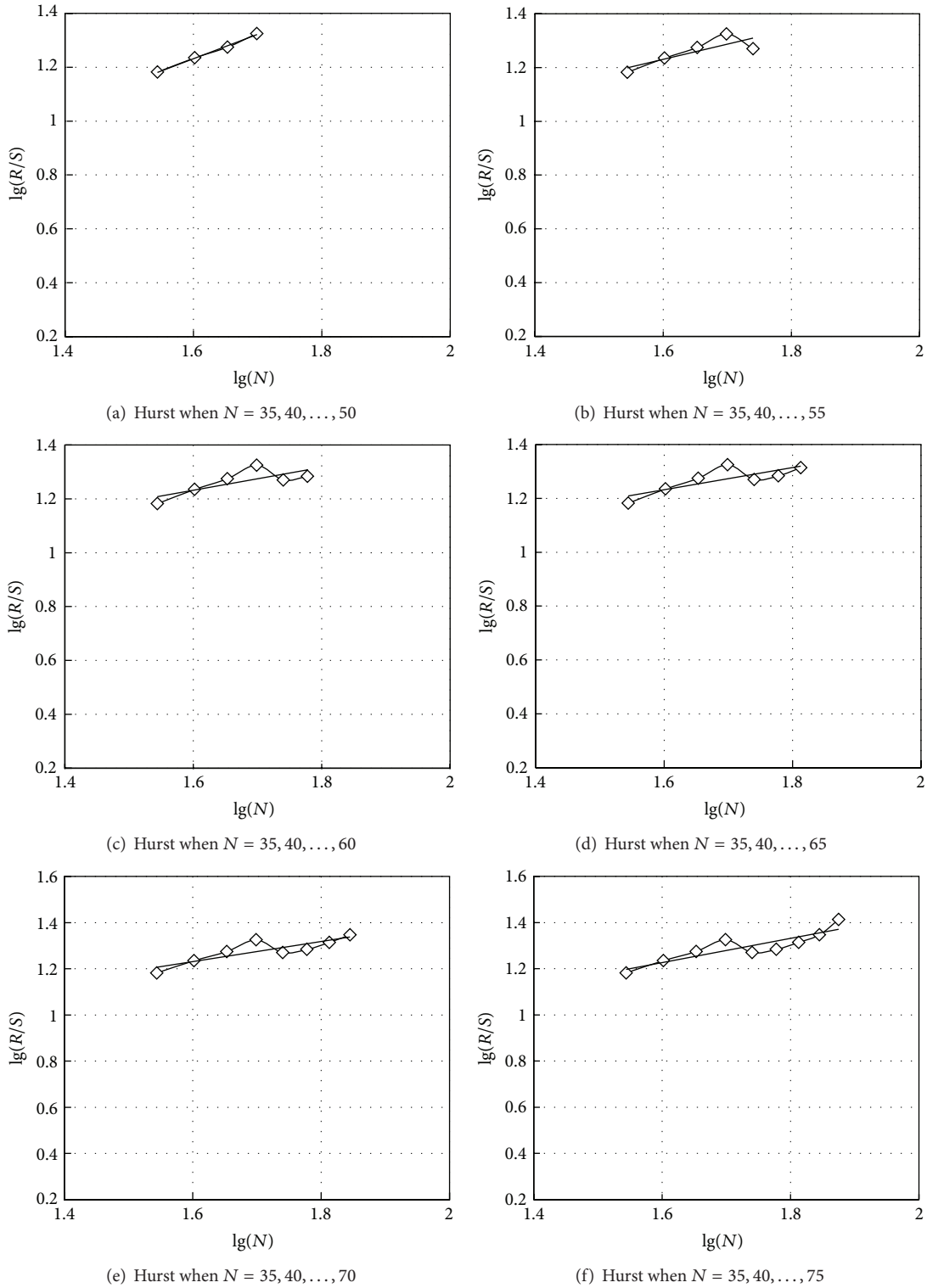

(a) Hurst when $N = 35, 40, \ldots, 50$

(b) Hurst when $N = 35, 40, \ldots, 55$

(c) Hurst when $N = 35, 40, \ldots, 60$

(d) Hurst when $N = 35, 40, \ldots, 65$

(e) Hurst when $N = 35, 40, \ldots, 70$

(f) Hurst when $N = 35, 40, \ldots, 75$

Figure 4: Results of accumulated experiments at depth of 145 m.

be a trend where there are 3 stages. In the first stage, the Hurst exponent declines until its value is less than 0.5. It maintains a lower value in the second stage. Some days later, the Hurst exponent begins to arise and it enters the third stage. The fracture takes place during the rising process. Hurst exponent is useful for forecasting of shaft lining fracture. It can be used to predicate the progressive failure of shaft lining from disorder state to order state.

When $H < 0.5$, the trend of additional strain in the future will change into a reversal. This heralds that shaft lining is

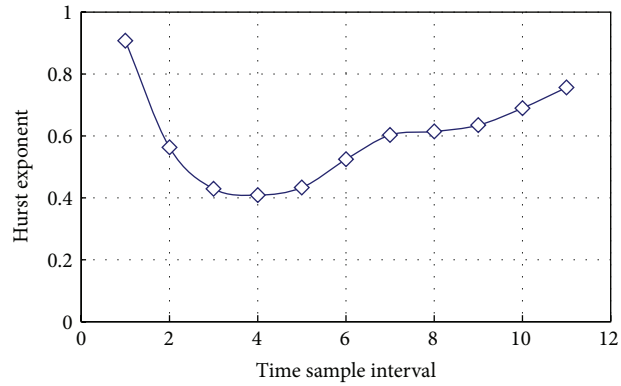

Figure 5: Variation of Hurst index before fracture.

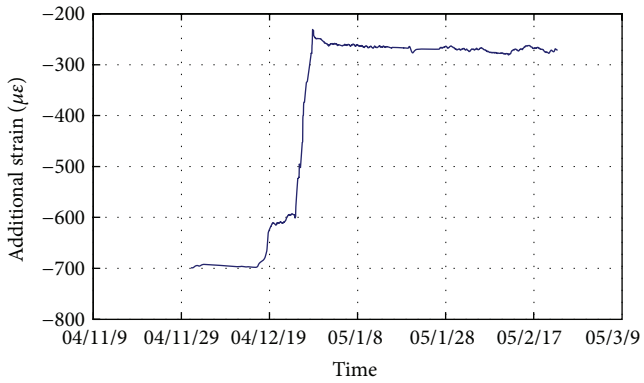

Figure 6: Variation of additional strain of depth of 145 m after fracture.

likely to fracture without the influence of external load, which causes stress release. As shown in Figure 6. The shaft lining fractured from 16 December to 18 December 2004. In situ measurement data at that time were shown in Figure 6.

5. Conclusions

The aim of this paper is to propose an effective method for predicting shaft lining fracture. According to the test results, the following conclusions can be drawn as follows.

(a) The R/S analysis method is applicable for studying the variation of additional strain of shaft lining.

(b) The Hurst exponent of additional strain is between 0.5 and 1. The sequence is positive biased random walk and presents a characteristic of strong positive correlation.

(c) Hurst exponent shows abrupt changes before fracture. It can be used to predict the progressive failure of shaft lining from disorder state to order state.

Conflict of Interests

The authors declare that there is no conflict of interests regarding the publication of this paper.

Acknowledgments

The financial supports from the Major State Basic Research Development Program of China (973 Program no. 2012CB026103), the National Natural Science Foundations of China (no. 51104149), and Postdoctoral Fund of China (no. 2013M541757) are acknowledged. This paper is also supported in part by the Fundamental Research Funds for the Central Universities (no. 2014QNB38), the Hong Kong Scholars Program (no. XJ2012043), and the China Postdoctoral Science Foundation funded project (no. 2012T50532).

References

[1] Z.-Q. Liu, G.-Q. Zhou, G.-S. Zhao, H.-C. Liang, and J.-S. Zhou, "Control method and its application about the soil grouting reinforcement process in vertical shaft," *Journal of the China Coal Society*, vol. 30, no. 4, pp. 472–475, 2005.

[2] X. L. Cheng and G. Q. Zhou, "Study on the stress calculation of shaft lining surrounded by special strata," in *Proceedings of the 2nd International Symposium on Mining Technology & Science*, Xuzhou, China, 1990.

[3] W. Yang, G. Cui, G. Zhou et al., "Fracture mechanism of shaft lining under special strata condition and the technique preventing the shaft from fracturing (part one)," *Journal of China University of Mining & Technology*, vol. 25, no. 4, pp. 1–5, 1996.

[4] T.-H. Yi and H.-N. Li, "Methodology developments in sensor placement for health monitoring of civil infrastructures," *International Journal of Distributed Sensor Networks*, vol. 2012, Article ID 612726, 11 pages, 2012.

[5] G. S. Zhao, H. F. Pei, and H. C. Liang, "Measurement of additional strains in shaft lining using differential resistance sensing technology," *International Journal of Distributed Sensor Networks*, vol. 2013, Article ID 153834, 6 pages, 2013.

[6] T.-H. Yi, H.-N. Li, and M. Gu, "Optimal sensor placement for structural health monitoring based on multiple optimization strategies," *Structural Design of Tall and Special Buildings*, vol. 20, no. 7, pp. 881–900, 2011.

[7] T.-H. Yi, H.-N. Li, and X.-D. Zhang, "Sensor placement on Canton Tower for health monitoring using asynchronous-climb monkey algorithm," *Smart Materials and Structures*, vol. 21, no. 12, Article ID 125023, 2012.

[8] H.-H. Zhu, J.-H. Yin, A. T. Yeung, and W. Jin, "Field pullout testing and performance evaluation of GFRP soil nails," *Journal of Geotechnical and Geoenvironmental Engineering*, vol. 137, no. 7, pp. 633–642, 2011.

[9] H.-H. Zhu, A. N. L. Ho, J.-H. Yin, H. W. Sun, H.-F. Pei, and C. -Y. Hong, "An optical fibre monitoring system for evaluating the performance of a soil nailed slope," *Smart Structures and Systems*, vol. 9, no. 5, pp. 393–410, 2012.

[10] H. E. Hurst, R. P. Black, and Y. M. Simaika, *Long-Term Storage: An Experimental Study*, Constable, London, UK, 1965.

[11] H. E. Hurst, "Long-term storage capacity of reservoirs," *Transactions of American Society of Civil Engineers*, vol. 116, pp. 770–808, 1951.

[12] B. Qian and K. Rasheed, "Hurst exponent and financial market predict ability," in *Proceedings of the IASTED Conference on Financial Engineering and Applications (FEA '04)*, pp. 203–209, 2004.

[13] G. Zhao, G. Q. Zhou, X. D. Zhao, Y. Z. Wei, and L. J. Li, "R/S analysis for stress evolution in shaft lining and fracture prediction Method," *Advanced Materials Research*, vol. 374–377, pp. 2271–2274, 2012.

[14] G. F. Yang, C. Li, and H. Yin, "Rescaled range analysis and its significance of climatic proxy in Lanzhou area," *Journal of Central China Normal University*, vol. 36, no. 3, pp. 394–396, 2002.

[15] X.-Z. Xue, Y.-J. Mi, Z.-L. Li, and Y.-N. Chen, "Long-term trends and sustainability analysis of air temperature and precipitation in the Hotan River Basin," *Resources Science*, vol. 30, no. 12, pp. 1833–1838, 2008.

[16] Y. Huang, Z. F. Zhou, J. G. Wang, and J. H. Wang, "Application of R/S method to dynamic groundwater analysis," *Journal of Hohai University*, vol. 30, no. 1, pp. 83–87, 2002.

[17] Y. Fan, J. Li, Y. J. Zhong, B. H. Yang, and K. Y. Guo, "Analysis on change trend of precipitation in Yunnan dry-hot valley region based on rescaled range analysis method," *Water Resources and Power*, vol. 26, no. 2, pp. 130–134, 2008.

[18] A. J. Cardini and J. T. DeWolf, "Long-term structural health monitoring of a multi-girder steel composite bridge using strain data," *Structural Health Monitoring*, vol. 8, no. 1, pp. 47–58, 2009.

[19] X. Weng, H.-H. Zhu, J. Chen, D. Liang, B. Shi, and C.-C. Zhang, "Experimental investigation of pavement behavior after embankment widening using a fiber optic sensor network," *Structural Health Monitoring*, vol. 14, no. 1, pp. 46–56, 2015.

[20] H.-H. Zhu, B. Shi, J.-F. Yan, J. Zhang, C.-C. Zhang, and B.-J. Wang, "Fiber Bragg grating-based performance monitoring of a slope model subjected to seepage," *Smart Materials and Structures*, vol. 23, no. 9, Article ID 095027, 2014.

[21] H.-H. Zhu, B. Shi, J. Zhang, J.-F. Yan, and C.-C. Zhang, "Distributed fiber optic monitoring and stability analysis of a model slope under surcharge loading," *Journal of Mountain Science*, vol. 11, no. 4, pp. 979–989, 2014.

[22] H.-F. Pei, J.-H. Yin, and W. Jin, "Development of novel optical fiber sensors for measuring tilts and displacements of geotechnical structures," *Measurement Science and Technology*, vol. 24, no. 9, Article ID 095202, 10 pages, 2013.

[23] H. F. Pei, J. H. Yin, H. H. Zhu, and C. Y. Hong, "Performance monitoring of a glass fiber-reinforced polymer bar soil nail during laboratory pullout test using FBG sensing technology," *International Journal of Geomechanics*, vol. 13, no. 4, pp. 467–472, 2013.

Hindawi Publishing Corporation
Journal of Sensors
Volume 2015, Article ID 987232, 11 pages
http://dx.doi.org/10.1155/2015/987232

Research Article

Microseismic Signal Characterization and Numerical Simulation of Concrete Beam Subjected to Three-Point Bending Fracture

Nuwen Xu,[1,2] Feng Dai,[1] Chun Sha,[3] Yingcheng Lei,[3] and Biao Li[1]

[1]*State Key Laboratory of Hydraulics and Mountain River Engineering, College of Water Resource and Hydropower, Sichuan University, Chengdu, Sichuan 610065, China*
[2]*College of Civil Engineering, Shandong University, Ji'nan, Shandong 250016, China*
[3]*Power China Chengdu Engineering Corporation Limited, Chengdu, Sichuan 610072, China*

Correspondence should be addressed to Feng Dai; fengdai@scu.edu.cn

Received 11 September 2014; Accepted 22 November 2014

Academic Editor: Fei Dai

To study the generation mechanism and failure mode of cracks in mass concrete, microseismic monitoring is conducted on the fracture processes of the three-point bending roller compacted concrete (RCC) beam of Guanyinyan hydropower station. The spectrum characteristics of microseismic signals in different deformation and failure stages of the concrete beam are analyzed, and the identification method of the fracture stages and crack propagation precursors of concrete beam is established. Meanwhile, the Realistic Failure Process Analysis code (RFPA) is adopted to simulate and analyze the entire failure processes of concrete beam from its cracks initiation, development, propagation, and coalescence, until macroscopic fractures formation subjected to three-point bending test. The relation curve of the load, loaded displacement, and acoustic emission (AE) of concrete beam in the three-point bending test is also obtained. It is found that the failure characteristics of concrete beam obtained from numerical experiments agree well with the field physical test results. The heterogeneity of concrete is the major cause of zigzag propagation paths of beam cracks subjected to three-point bending tests. The results lay foundation for further exploring the formation mechanism of dam concrete cracks of Guanyinyan hydropower station.

1. Introduction

In recent years, hosts of ultra-large hydropower projects are being constructed or to be completed and put into operation in the southwest of China. Therefore, the engineering sector has always attached great importance to and been committed to resolving the dam body security and stability problems [1, 2]. Most of these dams are located in western alpine valleys. The dam body is usually designed to be the concrete gravity dam or arch dam, which may lead to dam concrete cracking during construction of the concrete dam due to some factors including temperature control, grouting uplift, and structural distortion. The existence of cracks in the dam body not only worsens the appearance and damages the overall continuity of the dam but also weakens the stability and impermeability of the dam. The hydrostatic pressure in the crack (i.e., the horizontal crack) increases the displacement of the dam crest towards downstream, thus reducing the role of beams in the dam. Crack leakage makes calcium ion in concrete separate out and run away, may cause dam leakage and shorten the dam service life, and may even affect the dam security and restrict the later safe operation of the hydropower station [3]. Taking Xiaowan hydropower station arch dam for example, there are many arch cracks with about 1 mm average width in the middle of the dam body below an elevation of 1095.0 m, causing the failure to full reservoir and normal operation to the dam and serious economic loss [4]. Some arch dams also generate cracks after long-time running, such as Side arch dam and Shangbiao arch dam [5, 6]. Currently, extensive use of conventional measurement technology, such as multiple position extensometers, convergence meter, and surface subsidence monitoring, is found to be very useful in the surface deformation monitoring of concrete dam. However, it is unrealistic for them to monitor the occurrence of microfractures effectively in deep concrete of dam prior to the formation of a macroscopic fracture outside

the dam surface. With regard to concrete dams, these internal microfractures may often lead to macroscopic instability of dam. Consequently, there must be an intrinsic correlation between dam surface deformation and its internal microfractures (microseismicity). It is well known that brittle materials (i.e., rock or concrete) loaded in a testing machine and brittle structures that are stressed emit detectable acoustic or seismic signals. If these signals can be recorded sufficiently clearly as seismograms by a number of sensors, the original time of seismic event, and its location, source parameters such as source radius and dynamic stress drop can be estimated [7, 8]. Thus, microseismic monitoring technique has been attempted to locate such fractures in concrete engineering practices.

During the past two decades, microseismic monitoring technique emerged from a pure research means to a mainstream industrial tool for daily safety monitoring for various geotechnical engineering. It has wide engineering applications in South Africa, Canada, Japan, Australia, and America. Some achievements have been obtained in rock slopes [9–11], underground mining [8, 12–14], tunnels [15, 16], oil and gas exploration and development [17], and electricity generation by hot dry rock [18], and so forth. Dam concrete is brittle and the apparent displacement is usually small when a microfracture occurs internally. As the concrete microfracture constantly propagates, a large number of microfractures are usually formed around the fracture before a macroscopic crack zone is formed. Microseismic monitoring can capture signals during the process from initiation, development, propagation, and coalescence of these concrete microfractures in real time. Then, the occurrence time, position, and properties of the concrete microfractures can be obtained through back calculation. However, there is no precedent for monitoring cracks in the mass concrete dam by using the microseismic monitoring technology.

There are two kinds of methods to identify the concrete crack sign. One is to analyze hypocenter parameters of the microfracture, including the size, intensity, energy, magnitude, apparent stress, and stress drop, qualitatively deducing the development trend of the crack and macroscopic fracture, and then forecast the evolution rules of dam body concrete local failure or cracks. This kind of method has been successfully applied to engineering fields including the mine and hydropower projects [10, 19, 20]. The other is to reveal the microseismic signal characteristics in each stage of the concrete failure by using the modern digital signal processing and analyzing technologies such as time-frequency analysis, random signal analysis, Higher-Order Statistics (HOS) analysis, and fractal analysis. The concrete microseismic signal is nonstationary and random, which contains much information about the concrete fractures. Therefore, the conventional time-domain statistical parameters have some uncertainty. Many scholars [21–23] adopted the frequency spectrum analysis technology (Fourier transform) to analyze microseismic signals generated during rock fractures or frequency spectrum characteristics of AE signals and achieved some understandings. For instances, when the studied rock from small scale to a larger scale, AE signals shift from high frequency to low frequency. The time-frequency characteristics of microseismic signals during concrete failure are different from those during rock failure, which is mainly determined by the composition characteristics of concrete materials. Concrete is a brittle composite material formed by hardening a compound mixed with cementing materials, aggregate, water, required chemical admixture, and mineral admixture in a proper proportion. Studies show that the concrete failure process is composed of two processes: cement and cement or cement and aggregate falling off. The microseismic signals sent from these two processes can be effectively distinguished on the spectrogram.

This study attempts to analyze the spectrum characteristics of microseismic signals during the fracture processes of the concrete beam subjected to three-point bending test. The mechanical behavior of concrete beam fracture from microfracture initiation, development, and propagation until coalescence to form macroscopic cracks is revealed. Moreover, the entire fracture processes of concrete beam subjected to three-point bending tests using 3D numerical simulation are also reproduced, which lays foundation for studying the formation mechanism and evolution rules of cracks in mass concrete.

2. The Time-Frequency Analysis Principle of *S* Transform

S Transform is an overtime window Fourier transform method [24], proposed by Stockwell et al. in 1996. This method is the extension of continuous wavelet transform with Morlet wavelet as its basic wavelet. *S* Transform integrates the advantages of the short-time Fourier transform (STFT) and wavelet transform. It is mainly manifested as follows: its wavelet basis function adaptively reduces the analysis time width as the frequency increases and the time-frequency window is adaptive and does not need to meet wavelet admissible conditions.

In the geophysical prospecting field, *S* Transform has had many successful applications. For instances, Tan et al. [25, 26] applied *S* Transform to seismic data denoising and achieved better effect. Castagna et al. [27, 28] summarized the low frequency shadow rule on the oil-gas layer with *S* Transform and successfully guided petroleum exploration and production practices. Pinnegar and Mansinha [29] detected the arrival time of the longitudinal wave in the natural earthquake. Andria et al. [30] determined the thickness of the thin layer with *S* Transform in reservoir prediction, as well as detecting and identifying various transient signals.

S Transform can be expressed as phase correction of continuous wavelet transform. *S* Transform of function $h(t)$ is expressed as

$$S(t, f) = \int_{-\infty}^{\infty} h(\tau)\, w(\tau - t) \exp(-i2\pi f\tau)\, d\tau, \qquad (1)$$

where

$$w(\tau) = \frac{1}{\sigma\sqrt{2\pi}} \exp\left(-\frac{t^2}{2\sigma^2}\right), \quad \sigma(f) = \frac{1}{|f|}. \tag{2}$$

The following equation can be obtained after substituting (2) into (1):

$$S(t,f) = \int_{-\infty}^{\infty} h(\tau) \frac{|f|}{\sqrt{2\pi}} \exp\left(-\frac{(\tau-t)^2 f^2}{2}\right) \times \exp(-i2\pi f\tau)\, d\tau. \tag{3}$$

Set $W(v)$ to Fourier transform of $w(t)$; that is,

$$W(v) = \exp\left(-\frac{2\pi^2}{f^2} v^2\right). \tag{4}$$

In the preceding equation, v and f have the same unit.

The window function of S Transform must meet the following conditions:

$$\int_{-\infty}^{\infty} w(\tau - t, f)\, d\tau = 1. \tag{5}$$

Therefore, S Transform can be written as

$$\int_{-\infty}^{\infty} S(t,f)\, dt = \int_{-\infty}^{\infty} h(\tau) \exp(-i2\pi f\tau) \times \int_{-\infty}^{\infty} w(\tau - t, f)\, d\tau\, dt = \int_{-\infty}^{\infty} h(\tau) \exp(-i2\pi f\tau)\, dt = H(f). \tag{6}$$

Equation (6) actually provides the transformational relation between S Transform and Fourier transform. In addition, (6) can ensure the reversibility of S Transform.

Based on the mutual transformation process of STFT in the time domain and frequency domain, the following expression of S Transform in the frequency domain can be obtained:

$$S(t,f) = \int_{-\infty}^{\infty} H(v+f) W(v) \exp(i2\pi vt)\, dv = F^{-1}[H(v+f) W(v)]. \tag{7}$$

In the preceding equation, F^{-1} refers to Fourier inversion, $h(t)$ refers to the concrete microseismic signal to be analyzed, τ and f refer to time and frequency, respectively, and $S(t, f)$ is S matrix of one-dimensional concrete microseismic signals after S Transform. S matrix is obtained from concrete microseismic signals after S Transform. S modular matrix indicating the amplitude varying with time and frequency is obtained after a modulo operation on each element in S matrix. S modular matrix can be used to determine the distribution characteristics of concrete microseismic signals on the time-frequency plane.

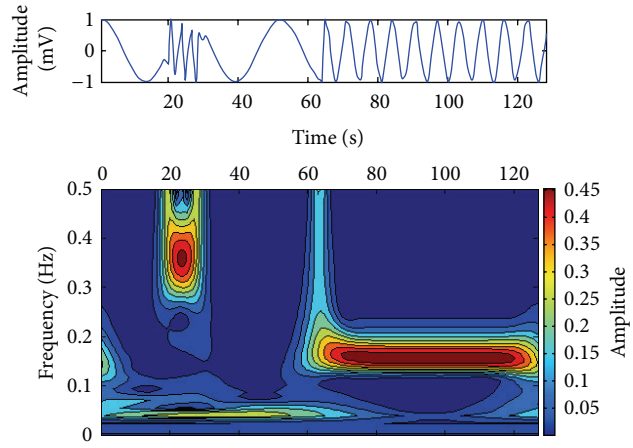

Figure 1: Spectrum characteristics of composite signal after S Transform.

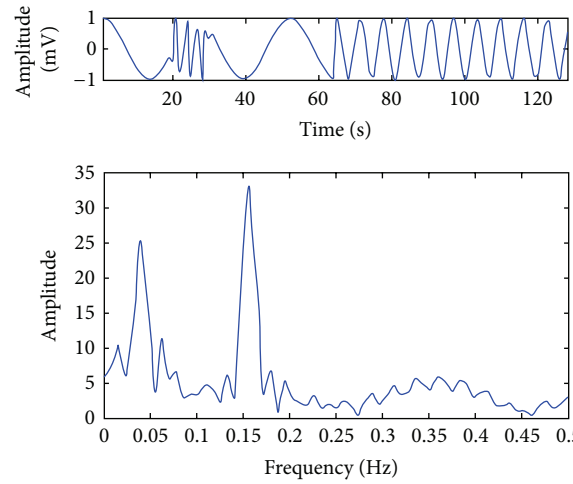

Figure 2: Spectrum characteristics of composite signal after Fourier transform.

Figure 1 shows one-dimensional composite signal $h(t)$ and its spectrum characteristics after S Transform. Figure 2 shows the spectrum characteristics of this signal after Fourier transform. A one-dimensional signal $h(t)$ contains three frequency components: the dominant frequency of 0~20 s and 32~64 s signal is 0.045 Hz; that of 20~30 s signal is 0.36 Hz; and that of 64~128 s signal is 0.16 Hz. According to Figures 1 and 2, S Transform spectrogram can effectively separate three dominant frequencies (0.045 Hz, 0.16 Hz, and 0.36 Hz) from each other with consistent time. Three dominant frequencies (obvious 0.045 Hz and 0.16 Hz and inconspicuous 0.36 Hz) rather than the occurrence time of each dominant frequency can be identified from Fourier transform spectrogram. Therefore, adopting S Transform can effectively analyze microseismic signals and obtain their dominant frequencies and occurrence times accurately.

Figure 3: Preparation of the concrete beam specimen.

3. Microseismic Signal Characteristics of Concrete Beam Subjected to Three-Point Bending Fracture

3.1. Concrete Beam Preparation. The concrete beam is cut and extracted from the RCC of the cast-in-place dam in Guanyinyan hydropower station. The dimensions of the beam model are 300 cm × 50 cm × 50 cm (length × width × height). The strength grade is designed to be C25 (90 days). The age of the model already exceeds 400 days when the three-point bending fracture test is conducted on the concrete beam, as shown in Figure 3.

The three-point bending failure test adopts the hierarchical load-keeping method. Hierarchical load complies with the following principles: (1) 20 kN is loaded each time on the 0~60 kN stage, stopped 5 minutes halfway. (2) 10 kN is loaded each time on the 60~140 kN stage, stopped 5 minutes halfway. (3) 5 kN is loaded each time on the 140~155 kN stage, stopped 10 minutes halfway. (4) The load is adjusted in real time according to microseismic monitoring data, and the next loading is performed until the changes of strain data and microseismic data keep stable.

3.2. Microseismic Monitoring System. The IHMS microseismic monitoring system produced by YueYang Aocheng Technology Co., Ltd. is used to monitor and analyze microseismic signals during the three-point bending fracture processes of the concrete beam in real time. This system is mainly composed of the data acquisition system, data remote transmission system, and data processing and analysis system. Figure 4 shows the layout of the microseismic monitoring system. The main parameters of the microseismic system include the sampling frequency (40 kHz), transducer sensitivity (30 V/g), and transducer threshold (20 mv). The P-wave velocity is 4800 m/s that is determined by acoustic wave tests. For details about the microseismic monitoring principles and parameters, refer to [10, 11] in References.

The microseismic monitoring transducers are installed on both ends of the concrete beam. The installation positions are ground flush with a polisher, and gypsum is used to fix the transducers. Figure 5 shows the installation positions of the transducers. A rectangular coordinate system as shown in Figure 5 is set up with the lower left corner as the origin of coordinates (0, 0, 0) to conduct positioning analysis on microseismic signals during the fracture processes of the concrete beam.

Figure 4: Microseismic monitoring system network.

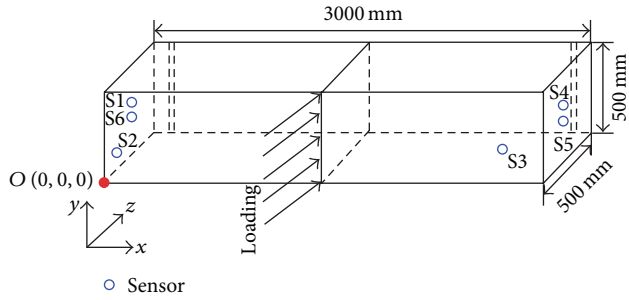

Figure 5: Layout of the microseismic monitoring transducers installed at the concrete beam.

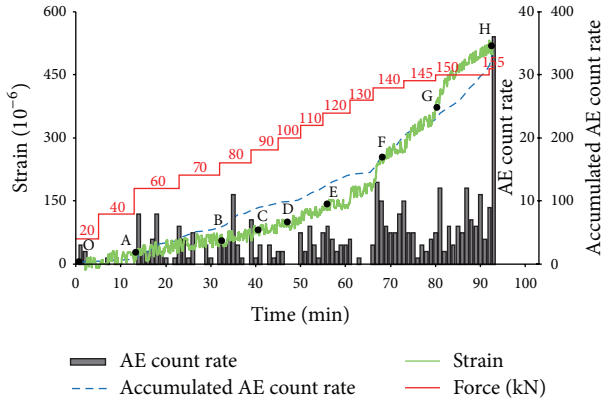

Figure 6: Characteristics of microseismic events during the failure processes of the concrete beam.

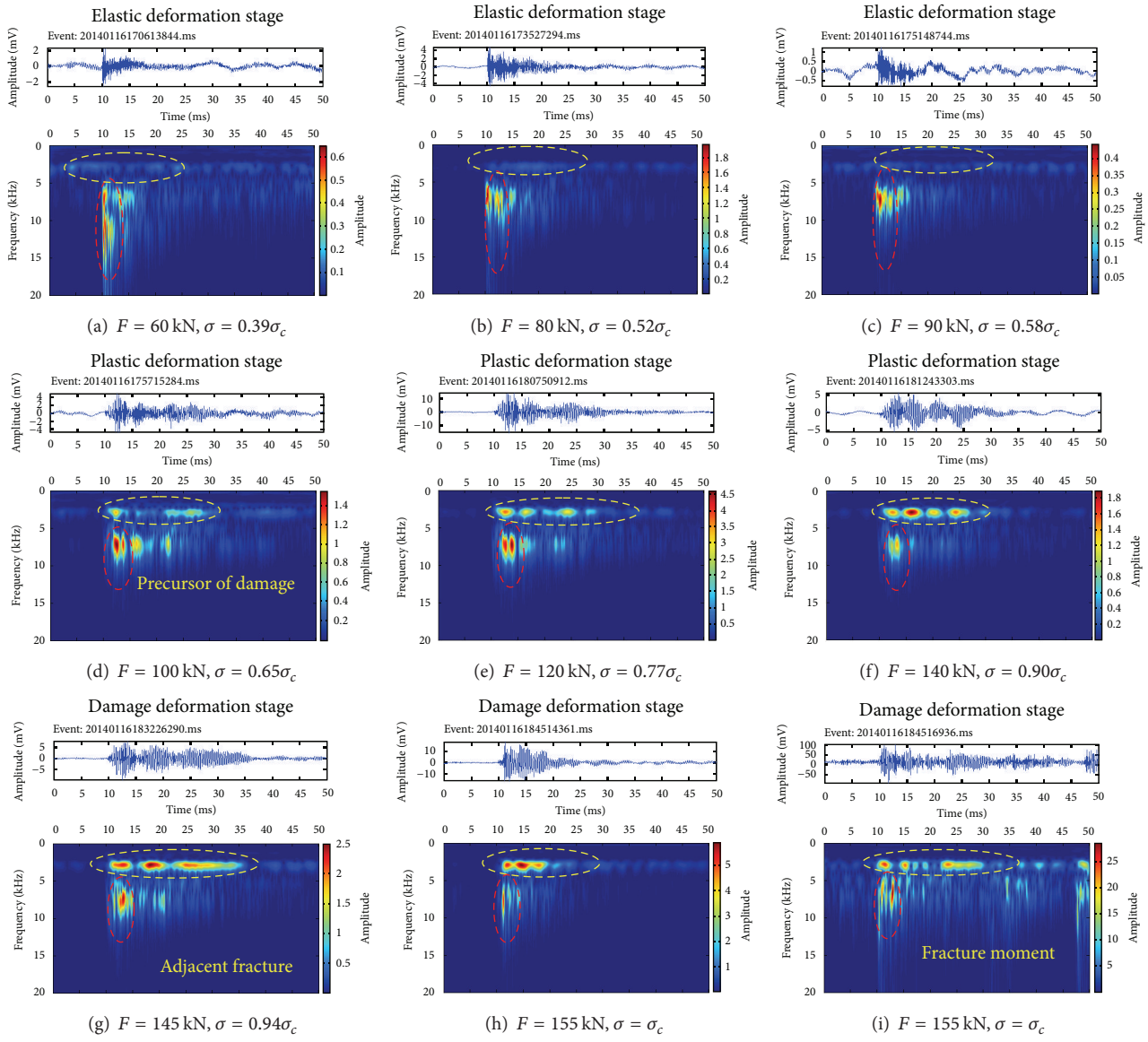

Figure 7: Microseismic signal spectrum characteristics of concrete beam during fracture processes.

3.3. Analysis on Microseismic Signal Characteristics during the Fracture Process of the Concrete Beam. Figure 6 shows the characteristic curve of microseismic events during the three-point bending fracture processes of the concrete beam. After comprehensive analysis on the curves of the loading process, microseismic events per unit time, accumulative microseismic events per unit time, and strain, the following results can be obtained. (1) The curve of the accumulative microseismic events per unit time of the concrete model has a basically consistent change trend with the strain curve. (2) In the single-stage load process, the number of microseismic events per unit time of the concrete beam shows a jump and then appears an attenuation trend. (3) Based on the slope change rules of the strain curve and the curve of the total number of microseismic events per unit time, the fracture process of the concrete beam can be divided into three stages: elastic deformation stage (OD), plastic deformation stage (DG), and failure deformation stage (GH).

Figure 7 shows the spectrum characteristics of some typical microseismic signals on each stage of the failure processes of the concrete beam. The spectrum characteristics in the three stages of the fracture processes of the concrete beam are as follows.

(1) Elastic deformation stage (OD): 0~90 kN load is imposed in this stage, with the corresponding stress $\sigma = 0 \sim 0.58\sigma_c$ (σ_c is the maximum normal stress when the concrete beam fractures). This process mainly shows that the initial cracks in the middle and on both sides of the beam are compacted or tensioned. The generated microseismic signal spectrum is as shown in Figures 7(a), 7(b), and 7(c). In the elastic deformation stage of the concrete beam, the microseismic signal is mainly single-shock and spreads about 5 ms on the time axis of the spectrogram, with frequency

ranging from 6 to 18 kHz and concentrating within 6 to 12 kHz range. The amplitude spectral value is small and the high frequency components of microseismic signals show a decay trend with increase of load and stress.

(2) Plastic deformation stage (DG): 90~140 kN load is imposed in this stage, with the corresponding stress $\sigma = 0.65 \sim 0.90\sigma_c$. This process shows that the initial cracks in the middle beam send microseismic signals after being compacted or tensioned; however, more microfractures in the middle gradually propagate and locally coalesce. The spectrum of the generated typical microseismic signal is as shown in Figures 7(d), 7(e), and 7(f). The microseismic signal in the plastic deformation stage of the concrete beam is multishock. It spreads about 15 ms on the time axis of the spectrogram. The signal has two dominant frequency bands: low frequency band around 3 kHz and middle and high frequency brand ranging from 6 to 10 kHz. As the load and stress increase, the middle and high frequencies of microseismic signals show a decay trend whilst the low frequency shows an increase trend. Compared with the elastic deformation stage, the low frequency (3 kHz) appears in this stage, which can be regarded as the precursor of concrete failure process.

(3) Failure deformation stage (GH): 145~155 kN load is imposed in this stage, with the corresponding stress $\sigma = 0.94 \sim 1.0\sigma_c$. This process shows that the initial cracks in the middle and on both sides of the beam send microseismic signals (relatively fewer and existing locally) after being compacted or tensioned. However, more microfractures in the middle beam gradually propagate and coalesce. The spectrum of the generated typical microseismic signal is as shown in Figures 7(g), 7(h), and 7(i). The microseismic signal in the failure deformation stage of the concrete beam is also multishock. It spreads about 15 to 20 ms on the time axis of the spectrogram. The signal has two dominant frequency bands: low frequency band around 3 kHz; middle and high frequency band ranging from 6 to 10 kHz (high frequency ranging from 6 to 18 kHz at the moment of failure). As the load and stress increase, the middle and high frequencies (6~10 kHz) of microseismic signals show a decay trend whilst the low frequency (3 kHz) shows an increase trend. When $\sigma = \sigma_c$, the low frequency is higher than the high frequency (as shown in Figure 7(h), the spectrogram is dominated by the low frequency). At the moment of the fracture of the concrete beam, the high frequency (6~18 kHz) components and low frequency components (3 kHz) obviously increase on the microseismic signal spectrogram (Figure 7(i)). When the spectrum of microseismic signals is dominated by low frequency (3 kHz) and high frequency (6~18 kHz) components, it can be regarded as the sign of concrete failure.

It can be seen that the spectrum characteristics of microseismic signals reproduce the three stages of concrete beam fracture and microseismic generation mechanism. To be specific, (1) the microscopic initial cracks of concrete are compacted or tensioned (cementing materials are compacted or tensioned); (2) concrete microfractures gradually propagate and locally coalesce under loading (cementing materials are compacted or tensioned; aggregate and cementing materials fall off); (3) concrete microfractures propagate, coalesce, and form macroscopic cracks under loading, thus causing concrete beam fracture.

3.4. Microseismic Evolution Rules during the Fracture Processes of the Concrete Beam. Figure 8 shows the spatial distribution evolution rules of microseismic events of the concrete beam under accumulated load. It intuitively reproduces the entire processes from microfractures initiation, development, propagation, and coalescence, until macroscopic fracture formation in the three-point bending test of the concrete beam. As shown in Figure 8, the evolution characteristics of microseismic events during the fracture process of the concrete beam can be summarized: (1) in the stage of crack initiation, when the force is exerted, the initial cracks in the middle and on both sides of the beam are compacted or tensioned, and microseismic events are randomly and discretely distributed on the concrete beam, as shown in Figures 8(a), 8(b), and 8(c); (2) in the stage of crack formation and propagation, as the load increases, microseismic events occur in the middle and on the right of the concrete beam but mainly concentrate in the middle and bottom of the beam, as shown in Figures 8(d) and 8(e); (3) in the crack coalescence stage, a large number of microseismic events mainly occur in the middle and bottom of the concrete beam, as shown in Figures 8(f), 8(g), and 8(h).

4. Numerical Simulation of Concrete Beam Subjected to Three-Point Bending Fracture

4.1. RFPA^{3D} Code. The RFPA code was developed by Tang et al. [31–33] considering the deformation of an elastic material containing an initial random distribution of microfeatures in order to simulate more clearly the progressive failure, including the failure process, failure induced seismic events, and failure induced stress redistribution. To include the statistical variability of the bulk failure strength in RFPA code, the mechanical parameters of the model elements are assumed to follow a Weibull distribution [34]:

$$W(x) = \frac{m}{x_0}\left(\frac{x}{x_0}\right)^{m-1} \exp\left[-\left(\frac{x}{x_0}\right)^m\right], \quad (8)$$

where m defines the shape of the Weibull distribution function, which can be referred to as the homogeneity index, x is the mechanical parameter of an element, and x_0 is the even value of the parameter of all elements. According to the Weibull distribution, the larger the m value, the more the elements with mechanical properties approaching the mean value, which depicts a more homogeneous rock specimen [35].

Compared with other numerical methods, the RFPA code features two merits [32]. One is that, by introducing heterogeneity of rock properties into the model, the code can simulate nonlinear deformation of a quasi-brittle behavior with an ideal brittle constitutive law at the local scale. The other is that, by introducing a reduction of material parameters after element failure, the RFPA code can simulate discontinuum mechanics problems in the frame of continuum mechanics. Details of the RFPA code can be seen in Tang and Kaiser [32].

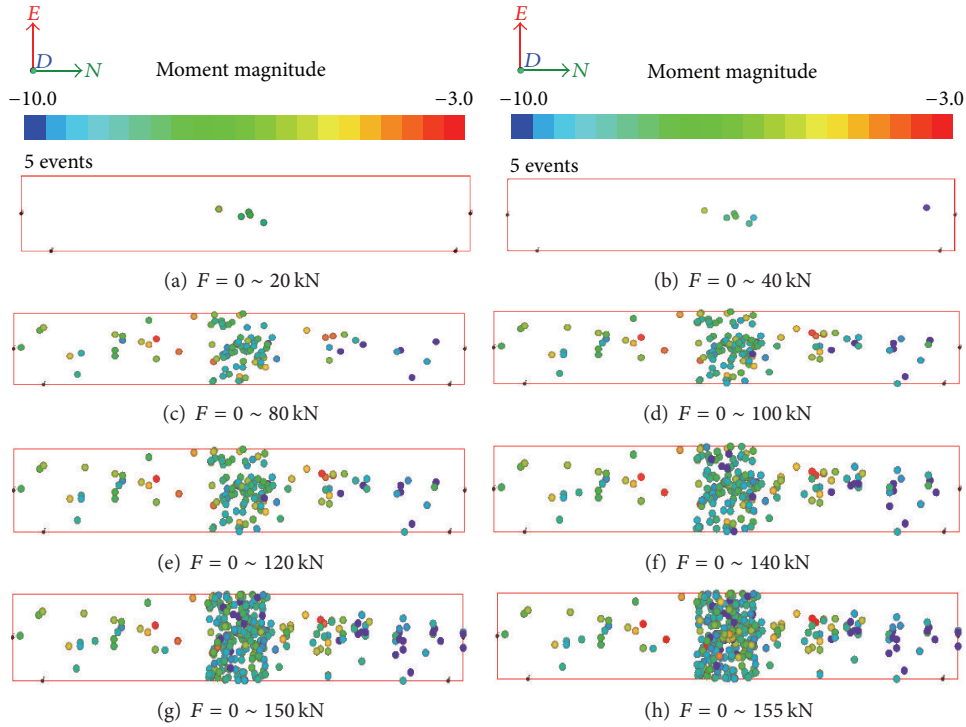

Figure 8: Spatial distribution evolution of MS events of concrete beam during loading stages (see from NE viewing).

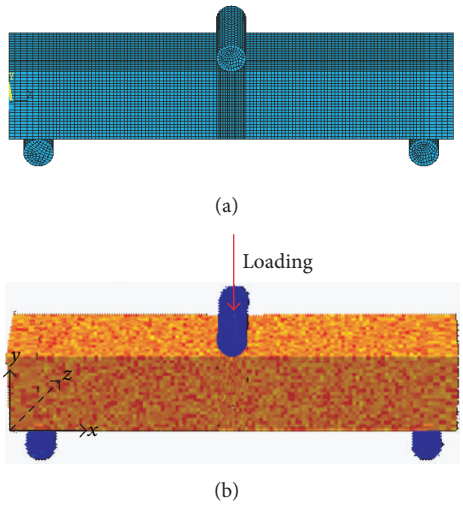

Figure 9: Calculation model (a) ANSYS model and (b) RFPA^{3D} model.

The robustness of RFPA and its 3D extension in simulating rock fracture has been evaluated by many scholars [10, 11, 31–33, 35].

4.2. Model Setup. Firstly, the ANSYS software is used to build a finite element model. The concrete beam has the cross section in dimensions of 500 mm × 500 mm and is 3000 mm long. Both the support and loading steel roller are cylinder with a 20 mm diameter. The distance between two supports is 2500 mm. Load transfer between the support, loading steel tube, and concrete beam is realized by a common node. The model is divided into 75049 hexahedral elements and mesh encryption is performed on the main force part of the concrete beam. Figure 9(a) shows mesh generation. Figure 9(b) shows the model after being imported to RFPA^{3D} considering concrete heterogeneity. The model constraint and load are imposed in the ANSYS. To be specific, the left support rebar is imposed with constraint in X and Y directions while the right support rebar is imposed with constraint in Y direction. Table 1 lists the material parameters of the finite element model. The concrete three-point bending test adopts the displacement-controlled stepwise loading mode, and the displacement loaded in each step is 0.02 mm.

Table 1: Macroscopic mechanical parameters of materials.

Materials	Elasticity modulus/MPa	Poisson's ratio	Compressive strength/MPa
Concrete	28000	0.2	25
Steel Roller	210000	0.3	600

After being imported to RFPA^{3D}, the mechanical parameters of the modeled material are converted from macroscopic parameters to microscopic parameters considering the material heterogeneity using the following equation:

$$\frac{f_1}{f_2} = 0.2602 \ln m + 0.0233,$$
$$\frac{E_1}{E_2} = 0.1412 \ln m + 0.6476. \quad (9)$$

Table 2: Mesoscopic mechanics parameters of materials in RFPA^{3D} model.

Materials	Elasticity modulus/MPa	Poisson's ratio	Compressive strength/MPa	Heterogeneity
Concrete	33200	0.2	65	4
Steel Roller	210000	0.3	600	100

In the preceding equation, m is the homogeneity; f_1 is the macroscopic strength; f_2 is the microscopic strength; E_1 is the macroscopic elastic modulus; E_2 is the microscopic elastic modulus. The homogeneity m of the concrete is set as 4 while that of the homogeneous support and loading steel roller is set to 100. The material mechanical parameters in Table 1 are converted to microscopic parameters in RFPA^{3D} by using (9), as listed in Table 2.

4.3. Numerical Simulation Results. Figure 10 shows the change rules of the loading force, loaded displacement, and AE of concrete beam during the three-point bending test. In RFPD^{3D} numerical simulation, the element failure is accompanied by AE, and the number of AEs is that of failed elements. Figure 10 shows the relation between the loaded displacement and AE, including the bar chart of AEs generated by the specimen in each loading and the total number of AEs during the entire loading processes.

Figure 11 shows the maximum principal stress and AE of the concrete beam during the three-point bending fracture process. The maximum principal stress figure shows a fixed section of the concrete beam while the blue spheres in the AE figure represent the tensile failure elements. It can be seen that, when it is loaded to step 7 (point A in Figure 10), the load reaches 48 kN; the specimen starts to initiate microfractures. As the loaded displacement constantly increases, microfractures gradually become more and the growth rate becomes faster and faster. When it is loaded to step 23, the load on the specimen reaches the peak value 148 kN (point B in Figure 10). Then, a large number of microfractures occur on mid-span of the bottom concrete beam (as shown on step 23 in Figure 11(b)) and a group of microfractures initiate on the bottom of concrete beam perpendicular to its axial direction (as shown on step 23 in Figure 11(a)). This is mainly because the maximum tensile stress occurs in the middle of the bottom beam during the three-point bending test, causing stress concentration. Before this, the concrete beam always shows linear elastic deformation (AB in Figure 10). When loading continues, the stress at the initial crack tip on the beam bottom is highly concentrated. Therefore, the main cracks start to initiate at the tip of microfractures and are on the same planes with the initial cracks. The bearing capacity of the beam reduces rapidly and shows its nonlinear characteristics (BC in Figure 10). A large number of tensile failure points continue to gather in the middle of the bottom concrete beam and gradually migrate and evolve to the beam top. When loading reaches step 30 (point C in Figure 10), the propagation length of the crack is about half of the beam height and the crack continues to propagate to the beam top in the vertical direction. According to Figure 10, when the test loading reaches step 40 (point D in Figure 10), the number of AEs hardly increases and those AEs form a vertical fracture band in the middle of the concrete beam (as shown on step 40 in Figure 11(b)). The cracks run through the concrete beam. The beam has almost no bearing capacity, and the specimen completely fails.

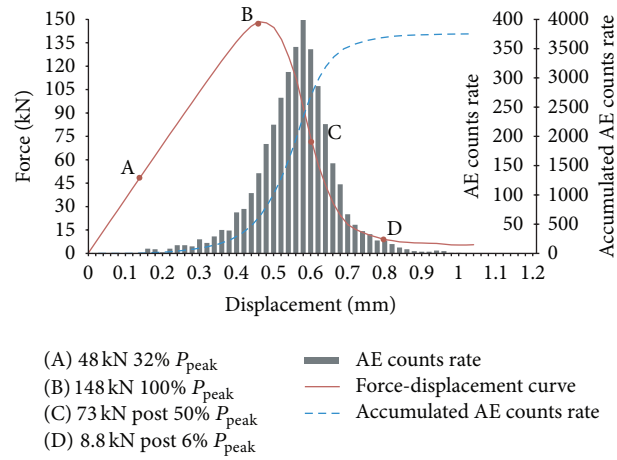

Figure 10: Variation of the test load, displacement, and AE of the concrete beam subjected to three-point bending.

It can be seen that numerical simulation used by RFPA^{3D} reproduces the entire processes of the concrete beam from its microfractures initiation, development, propagation, and coalescence, until macroscopic fracture band formation in the three-point bending tests. The numerical results reveal the failure modes and fracture mechanism of the concrete beam in different deformation stages.

5. Comparative Analysis of Field Test and Numerical Simulation Results

Figure 12 shows the AE from numerical simulation and field test. It can be seen that, when the load is started to be imposed, microfractures are randomly distributed on the beam model in the initial loading stage because the initial cracks in the middle and on both sides of the concrete beam are compacted or tensioned. When the specimen finally fractures, the AE obtained from numerical simulation agrees well with the accumulated spatial distribution of microseismic events obtained from field microseismic monitoring. That is, most microfractures concentrate in the middle of the concrete beam as shown in Figure 12.

Figure 13 shows the final fracture maps of the concrete beam obtained from numerical simulation and field test, respectively. It can be seen that, during the three-point bending fracture processes of the concrete beam, the cracks do not always initiate along the vertical direction. That is mainly because of the heterogeneity of concrete, which causes

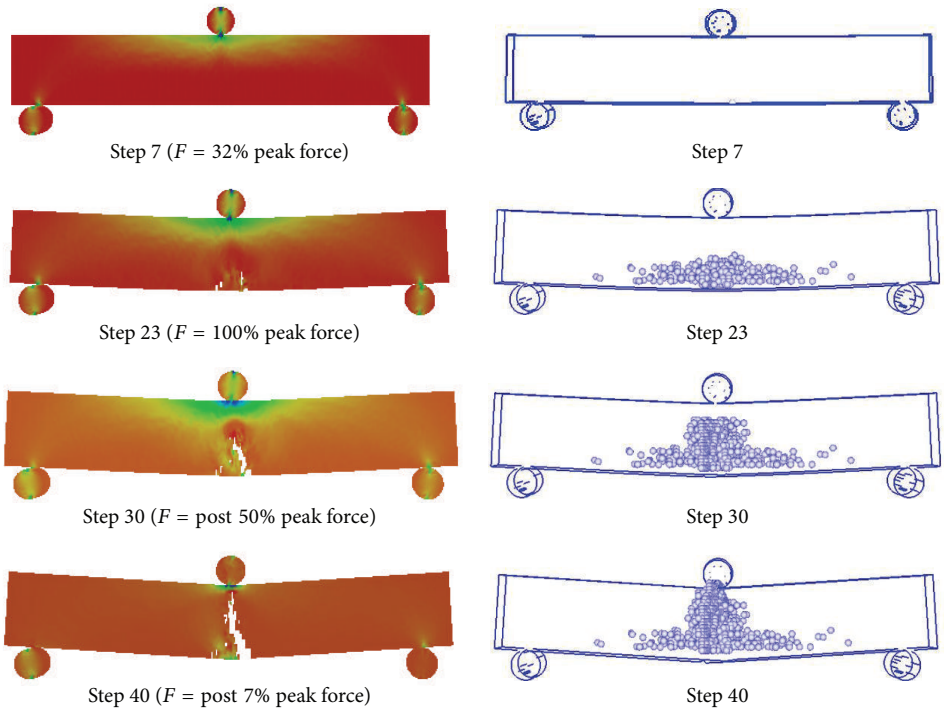

Figure 11: The failure processes of the concrete beam.

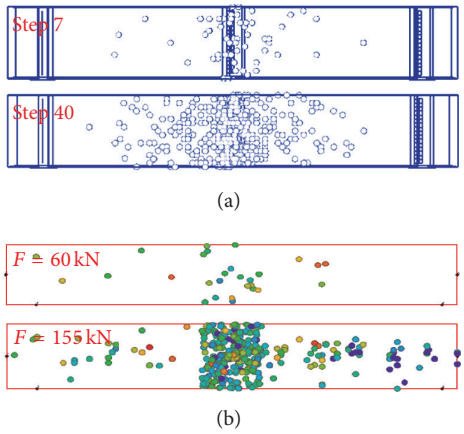

Figure 12: Comparison of spatial distribution of AE/MS between numerical simulation and microseismic monitoring results. (a) AE obtained from numerical simulation; (b) MS obtained from field test.

a zigzag propagation path of the cracks. The heterogeneity of concrete is taken into account during RPFA^{3D} numerical simulation for the fracture process of the concrete beam. The tough aggregates (elements with high strength in the numerical model) can prevent the cracks from propagating forwards. Instead, most cracks propagate along the cementing band around the aggregate, and therefore the crack propagation paths are zigzag. Numerical simulation results (Figure 13(a)) agree well with the field physical test results (Figure 13(b)). Consequently, the heterogeneity of concrete is the major cause of zigzag propagation paths of beam cracks subjected to three-point bending tests [36].

Furthermore, the bearing capacity of the concrete beam obtained from the field three-point bending test is 155 kN (as shown in Figures 6 and 8) while the bearing capacity obtained from numerical simulation is 148 kN (as shown in Figure 10), with a 4.5% relative error. It can be seen that the three-point bending fracture test results of the concrete beam obtained from numerical simulation are basically consistent with the field physical test results.

6. Conclusions

Microseismic monitoring is conducted on the three-point bending fracture processes of the field RCC beam. The spectrum characteristics of microseismic signals of concrete failure and its formation mechanism are revealed. The identification method of the fracture stages and crack propagation precursors of concrete is established. Numerical simulation reproduces the entire processes of the concrete beam rupture from microfractures initiation, development, propagation, and coalescence, until macroscopic fracture formation. The different failure modes and mechanism of the concrete beam rupture are thus revealed. The main conclusions are drawn as follows.

(1) When the specimen is under the plastic deformation stage, the microseismic signal is mainly multishock. The spectrum spreads about 15 ms on the time axis.

(a) Concrete beam rupture from numerical simulation

(b) Comparison map of concrete beam before and after rupture

Figure 13: Final rupture of the concrete beam.

The signal has two dominant frequency bands: low frequency band around 3 kHz and the middle and high frequency band ranging from 6 to 10 kHz. When the microseismic signal spectrum shows 3 kHz "low frequency shadow," it can be regarded as the precursor signal of the concrete failure. The microseismic signal at the moment of specimen failure is also mainly multishock. The spectrum spreads more than 20 ms on the time axis. The signal also has two dominant frequency bands: low frequency band around 3 kHz and high frequency band ranging from 6 to 18 kHz. The amplitude spectral value is relatively high. That is, when the spectrum shows that the microseismic signals are dominated by 3 kHz "low frequency shadow" and 6 to 18 kHz "high frequency shadow," concrete already fractures macroscopically.

(2) The RFPA^{3D} code is adopted to simulate the three-point bending test of concrete beam. The heterogeneity of concrete is taken into account. Numerical simulation reproduces the entire deformation and failure processes of the specimen subjected to three-point bending test. The relation between the load, displacement, and AE during the deformation and failure process of the specimen, as well as the cracks propagation processes and stress field distribution rules, is obtained.

(3) The fracture mode of the RCC beam revealed from numerical simulation agrees well with the field physical test results. During the loading processes, microfractures firstly initiate on the mid-span of the bottom concrete beam. Under loading, these microfractures constantly initiate, develop, gradually propagate along the vertical direction of the beam, coalesce, and form main failure fractures, finally causing macroscopic fractures of the concrete beam. The heterogeneity of concrete is the major cause of zigzag propagation paths of beam cracks subjected to three-point bending tests.

Conflict of Interests

The authors declare that there is no conflict of interests regarding the publication of this paper.

Acknowledgments

The authors are grateful for the financial support from the National Program on Key basic Research Project (no. 2015CB057903), National Natural Science Foundation of China (nos. 51209127 and 51374149), the Program for New Century Excellent Talents in University (NCET-13-0382), Sichuan Provincial Youth Science and Technology Fund (2014JQ0004), and the opening fund of State Key Laboratory of Hydrology-Water Resources and Hydraulic Engineering, Nanjing Hydraulic Research Institute (no. 2012491711).

References

[1] P. Lin, S. Kang, Q. Li, R. Wang, and Z. Wang, "Evaluation of rock mass quality and stability analysis of Xiluodu arch dam under construction phase," *Chinese Journal of Rock Mechanics and Engineering*, vol. 31, no. 10, pp. 2042–2052, 2012 (Chinese).

[2] S. Song and D. Cai, "Earthquake damage phenomena and deformation monitoring analysis for concrete faced rockfill dam at Zipingpu project during wenchuan earthquake," *Chinese Journal of Rock Mechanics and Engineering*, vol. 28, no. 4, pp. 840–849, 2009 (Chinese).

[3] F. W. Xu and B. Tian, "Analysis of contributing factors to cracks of high arch dam," *Hubei Water Power*, vol. 59, no. 2, pp. 14–17, 2005 (Chinese).

[4] Y. Liu, J. Wang, Q. Yang, R. Yang, and W. Zhou, "Research on influences of cracking of Xiaowan arch dam on its stress and stability," *Chinese Journal of Rock Mechanics and Engineering*, vol. 29, no. 6, pp. 1132–1139, 2010 (Chinese).

[5] Z.-Y. Shu, J. Xiong, and L.-G. Li, "Crack genetic analysis and countermeasure research of Si'de dam," *Journal of Sichuan University (Engineering Science Edition)*, vol. 39, no. 3, pp. 12–18, 2007 (Chinese).

[6] F. H. Ma, "Crack cause analysis of Shangbiao concrete arch dam," *Water Resources and Power*, vol. 19, no. 4, pp. 16–19, 2001 (Chinese).

[7] A. J. Mendecki, *Seismic Monitoring in Mines*, Chapman & Hall, London, UK, 1997.

[8] M. Cai, P. K. Kaiser, and C. D. Martin, "Quantification of rock mass damage in underground excavations from microseismic event monitoring," *International Journal of Rock Mechanics and Mining Sciences*, vol. 38, no. 8, pp. 1135–1145, 2001.

[9] R. A. Lynch, R. Wuite, B. S. Smith, and A. Cichowicz, "Microseismic monitoring of open pit slopes," in *Proceedings of the 6th*

Symposium on Rockbursts and Seismicity in Mines, Y. Potvin and M. Hudyma, Eds., pp. 581–592, ACG, Perth, Australia, 2005.

[10] N. W. Xu, F. Dai, Z. Z. Liang, Z. Zhou, C. Sha, and C. A. Tang, "The dynamic evaluation of rock slope stability considering the effects of microseismic damage," *Rock Mechanics and Rock Engineering*, vol. 47, no. 2, pp. 621–642, 2014.

[11] N. W. Xu, C. A. Tang, L. C. Li et al., "Microseismic monitoring and stability analysis of the left bank slope in Jinping first stage hydropower station in southwestern China," *International Journal of Rock Mechanics & Mining Sciences*, vol. 48, no. 6, pp. 950–963, 2011.

[12] M. Ge, "Efficient mine microseismic monitoring," *International Journal of Coal Geology*, vol. 64, no. 1-2, pp. 44–56, 2005.

[13] H. Wang and M. Ge, "Acoustic emission/microseismic source location analysis for a limestone mine exhibiting high horizontal stresses," *International Journal of Rock Mechanics and Mining Sciences*, vol. 45, no. 5, pp. 720–728, 2008.

[14] A. Leśniak and Z. Isakow, "Space-time clustering of seismic events and hazard assessment in the Zabrze-Bielszowice coal mine, Poland," *International Journal of Rock Mechanics and Mining Sciences*, vol. 46, no. 5, pp. 918–928, 2009.

[15] A. Hirata, Y. Kameoka, and T. Hirano, "Safety management based on detection of possible rock bursts by AE monitoring during tunnel excavation," *Rock Mechanics and Rock Engineering*, vol. 40, no. 6, pp. 563–576, 2007.

[16] C. A. Tang, J. M. Wang, and J. J. Zhang, "Preliminary engineering application of microseismic monitoring technique to rockburst prediction in tunneling of Jinping II project," *Joumal of Rock Mechanics and Geotechnical Engineering*, vol. 2, no. 3, pp. 193–208, 2011.

[17] S. L. Li, "Discussion on microseismic monitoring technology and its application to underground project," *Chinese Journal of Underground Space and Engineering*, vol. 5, no. 1, pp. 122–128, 2009 (Chinese).

[18] K. Tezuka and H. Niitsuma, "Stress estimated using microseismic clusters and its relationship to the fracture system of the Hijiori hot dry rock reservoir," *Engineering Geology*, vol. 56, no. 1-2, pp. 47–62, 2000.

[19] H.-H. Zhu, J.-H. Yin, L. Zhang, W. Jin, and J.-H. Dong, "Monitoring internal displacements of a model dam using FBG sensing bars," *Advances in Structural Engineering*, vol. 13, no. 2, pp. 249–261, 2010.

[20] H.-H. Zhu, J.-H. Yin, J.-H. Dong, and L. Zhang, "Physical modelling of sliding failure of concrete gravity dam under overloading condition," *Geomechanics and Engineering*, vol. 2, no. 2, pp. 89–106, 2010.

[21] J. Xu, R.-H. Yang, J.-G. Zhang, and Z.-Y. Xu, "A preliminary study on precursors of strong fracture in brittle material specimens," *Chinese Journal of Geophysics*, vol. 54, no. 9, pp. 2283–2292, 2011 (Chinese).

[22] Y. Gong, M. He, Z. Wang, and Y. Yin, "Research on time-frequency analysis algorithm and instantaneous frequency precursors for acoustic emission data from rock failure experiment," *Chinese Journal of Rock Mechanics and Engineering*, vol. 32, no. 4, pp. 787–799, 2013.

[23] C. Lu, L. Dou, X. Wu, Z. Mou, and G. Chen, "Experimental and empirical research on frequency-spectrum evolvement rule of rockburst precursory microseismic signals of coal-rock," *Chinese Journal of Rock Mechanics and Engineering*, vol. 27, no. 3, pp. 519–525, 2008 (Chinese).

[24] R. G. Stockwell, L. Mansinha, and R. P. Lowe, "Localization of the complex spectrum: the S-transform," *IEEE Transactions on Signal Processing*, vol. 44, no. 4, pp. 998–1001, 1996.

[25] Y.-Y. Tan, C. He, Y.-D. Wang, and Z. Zhao, "Ground roll attenuation using a time-frequency dependent polarization filter based on the S transform," *Applied Geophysics*, vol. 10, no. 3, pp. 279–294, 2013.

[26] Y. Z. Wang, J. T. Lan, and Y. S. Long, "The method for attenuating random noise based on S transform," *Progress in Geophys*, vol. 25, no. 2, pp. 562–567, 2010.

[27] J. P. Castagna, S. Sun, and R. W. Siegfried, "Instantaneous spectral analysis: detection of low-frequency shadows associated with hydrocarbons," *The Leading Edge*, vol. 22, no. 2, pp. 120–127, 2003.

[28] X. H. Chen, Z. H. He, D. J. Huang, and X. T. Wen, "Low frequency shadow detection of gas reservoirs in time-frequency domain," *Chinese Journal of Geophysics*, vol. 52, no. 1, pp. 215–221, 2009 (Chinese).

[29] C. R. Pinnegar and L. Mansinha, "The S-transform with windows of arbitrary and varying shape," *Geophysics*, vol. 68, no. 1, pp. 381–385, 2003.

[30] G. Andria, M. Savino, and A. Trotta, "Application of Wigner-Ville distribution to measurements on transient signals," *IEEE Transactions on Instrumentation and Measurement*, vol. 43, no. 2, pp. 187–193, 1994.

[31] C. A. Tang, "Numerical simulation of progressive rock failure and associated seismicity," *International Journal of Rock Mechanics and Mining Sciences*, vol. 34, no. 2, pp. 249–261, 1997.

[32] C. A. Tang and P. K. Kaiser, "Numerical simulation of cumulative damage and seismic energy release during brittle rock failure—part I: fundamentals," *International Journal of Rock Mechanics and Mining Sciences*, vol. 35, no. 2, pp. 113–121, 1998.

[33] C. A. Tang, H. Liu, P. K. K. Lee, Y. Tsui, and L. G. Tham, "Numerical studies of the influence of microstructure on rock failure in uniaxial compression. Part I. Effect of heterogeneity," *International Journal of Rock Mechanics and Mining Sciences*, vol. 37, no. 4, pp. 555–569, 2000.

[34] W. Weibull, "A statistical distribution functions of wide application," *Journal of Applied Mechanics*, vol. 18, pp. 293–297, 1951.

[35] Z. Z. Liang, H. Xing, S. Y. Wang, D. J. Williams, and C. A. Tang, "A three-dimensional numerical investigation of the fracture of rock specimens containing a pre-existing surface flaw," *Computers and Geotechnics*, vol. 45, pp. 19–33, 2012.

[36] W. C. Zhu, S. H. Wang, and C. A. Tang, "Computer simulation on the three-point bending test of concrete specimen," *Journal of Northeastern University (Natural Science)*, vol. 20, no. 5, pp. 533–535, 1999 (Chinese).

Hindawi Publishing Corporation
Journal of Sensors
Volume 2015, Article ID 281538, 6 pages
http://dx.doi.org/10.1155/2015/281538

Research Article

Blind Source Separation Model of Earth-Rock Junctions in Dike Engineering Based on Distributed Optical Fiber Sensing Technology

Huaizhi Su,[1,2] Meng Yang,[1,2] Kunpeng Zhao,[3] and Zhiping Wen[4]

[1] *State Key Laboratory of Hydrology-Water Resources and Hydraulic Engineering, Hohai University, Nanjing 210098, China*
[2] *College of Water Conservancy and Hydropower Engineering, Hohai University, Nanjing 210098, China*
[3] *National Engineering Research Center of Water Resources Efficient Utilization and Engineering Safety, Nanjing 210098, China*
[4] *Department of Computer Engineering, Nanjing Institute of Technology, Nanjing 211167, China*

Correspondence should be addressed to Huaizhi Su; su_huaizhi@hhu.edu.cn

Received 17 October 2014; Accepted 2 March 2015

Academic Editor: Zhenhua Zhu

Distributed temperature sensing (DTS) provides an important technology support for the earth-rock junctions of dike projects (ERJD), which are binding sites between culvert, gates, and pipes and dike body and dike foundation. In this study, a blind source separation model is used for the identification of leakages based on the temperature data of DTS in leakage monitoring of ERJD. First, a denoising method is established based on the temperature monitoring data of distributed optical fiber in ERJD by a wavelet packet signal decomposition technique. The temperature monitoring messages of fibers are combined response for leakages and other factors. Its character of unclear responding mechanism is very obvious. Thus, a blind source separation technology is finally selected. Then, the rule of temperature measurement data for optical fiber is analyzed and its temporal and spatial change process is also discussed. The realization method of the blind source separation model is explored by combining independent component analysis (ICA) with principal component analysis (PCA). The practical test result in an example shows that the method could efficiently locate and identify the leakage location of ERJD. This paper is expected to be useful for further scientific research and efficient applications of distributed optical fiber sensing technology.

1. Introduction

China is a country affected by monsoons significantly. Floods and other natural disasters are often caused for rainy season. A large number of dikes are built in order to reduce the loss caused by flooding and invasion of storm tide. However, the integrity and safety of dike projects are objectively undermined by crossing culverts and other hydraulic structures, especially earth-rock junctions [1]. The operating experience of hydraulic structures of dikes indicated that strengthening real-time location and identification of leakage hazards for the earth-rock junctions of dike projects (ERJD) had special significances to ensure the safety of entire culverts and dike projects [2]. Research and analysis of high-tech leakage monitoring in ERJD have gotten more and more attention in engineering and academia during improvement and optimization of traditional monitoring techniques and methods [3]. The temperature tracing technology is a geophysical technique based on geophysics and it has broad application prospects in seepage monitoring [4]. Compared to the traditional leakage monitoring technology, such as piezometer tubes and osmometers, the early temperature tracing technology was more sensitive and effective and had lower unit acquisition cost. However, the early temperature tracing method was still a point-monitoring technology. The singular area of internal temperature in buildings would not be detected inevitably because of a large layout spacing of thermistor thermometers and other reasons [5].

DTS, as a new approach, was produced by combination of optical fiber sensing technology and leakage risk monitoring technique [6, 7]. The new leakage monitoring method, DTS, provides a possible way to the distributed, long-distance, and

large-scale monitoring [8, 9]. In general, the use of distributed fiber sensing technology in leakage monitoring of buildings is still in its infancy stage for theoretical research, experimental simulation, and engineering application research, especially for monitoring the combination between two mediums in ERJD. The consequent analysis of temperature monitoring data and processing aspects still need more studies. Therefore, an experimental model of ERJD was established and the distributed fiber leakage monitoring technology was developed according to the working features of ERJD. In-depth studies of models and methods for leakage identification of ERJD have important science and engineering applications based on features of monitoring data.

2. Denoising Research of DTS Monitoring Data with Wavelet Packet

Wavelet transform method was proposed by Morlet in the early 1980s, and then it changed rapidly to be a very powerful tool for digital signal processing, image processing, data compression, data denoising, and so forth.

Wavelet is a breakthrough to Fourier transform analysis. It is a time-frequency analysis method with fixed window size and changeable shape, time window and frequency window. Local features signal can be well characterized in both time domain and the frequency domain.

Its main advantage is the ability to do local refinement and analysis for signal, which overcomes the difficulties of not processing the nonstationary signals for Fourier transform technique and short-time Fourier transform method.

During practical applications, wavelet transform will disperse the stretching factor a and translation factor τ in order to adapt to the computer calculation. a takes $a_0^0, a_0^1, a_0^2, \ldots, a_0^j$. The sampling interval of displacement amount τ is $\Delta\tau = a_0^j \tau_0$. Thus, wavelet function is

$$\phi_{a,\tau}(t) = a_0^{-j/2} \phi\left(a_0^{-j}\left(t - k a_0^j \tau_0\right)\right), \tag{1}$$

where j and k are positive integers.

Taking $a_0 = 2$ and $\tau_0 = 1$ in practical operation, wavelet basis function, $\phi_{a,\tau}(t)$, can be expressed as follows:

$$\phi_{j,k}(t) = 2^{-j/2} \phi\left(2^{-j} t - k\right). \tag{2}$$

Corresponding discrete wavelet transform is

$$\mathrm{WT}_x(j,k) = \left\langle x(t), \phi_{j,k}(t) \right\rangle = \int_R x(t) \overline{\phi_{j,k}(t)} dt. \tag{3}$$

The signal can be decomposed into a high frequency portion named D and a low frequency part marked A by wavelet transformation. Compared to the wavelet transform, wavelet packet decomposition analysis is a more sophisticated approach, which well disassembles the high and low frequency parts of each layer simultaneously. It greatly improves the resolution of signal and overcomes the insufficient of wavelet decomposition in "low-resolution of high-frequency." The wavelet packet decomposition has more broad application prospects and the 3-layer wavelet packet decomposition process was expressed in Figure 1.

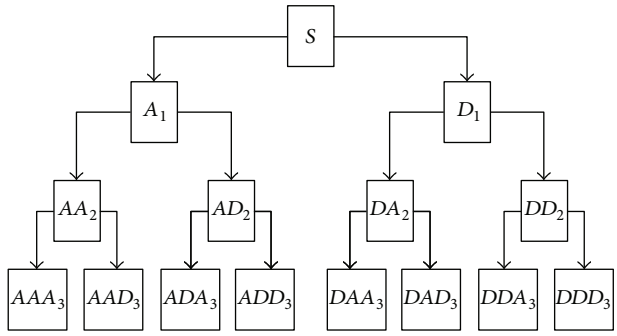

Figure 1: Transform decomposition process of wavelet packet.

As shown in Figure 1, the decomposition relationship of 3-layer wavelet packet is as follows:

$$\begin{aligned} S = {} & AAA_3 + AAD_3 + ADA_3 + ADD_3 \\ & + DAA_3 + DAD_3 + DDA_3 + DDD_3. \end{aligned} \tag{4}$$

The denoising procedure of wavelet packet for DTS leakage measurement data is summarized as below.

(1) Wavelet packet decomposition. Select wavelets and determine the decomposition level N then decompose N-layer wavelet packet for original signal S. During data processing, the wavelet packet decomposition level is determined by the wavelet packet noise reduction effect.

(2) Thresholds quantization. Select the appropriate threshold quantization method to quantify treatment for each wavelet packet coefficients decomposed.

(3) Reconstruction of wavelet packet. Reconstruct the low-frequency coefficients of wavelet packet N-layer and its corresponding high-frequency coefficients.

Among the previous steps, the keys are selection of the wavelet packet decomposition level and approach to the threshold quantization. Wavelet packet decomposition level is generally not more than 5-layer. The threshold quantization can be processed by denoising with the soft threshold and hard threshold method.

Coefficient of wavelet packet of hard threshold estimated is

$$\overline{w}_{j,k} = \begin{cases} w_{j,k}, & \left|w_{j,k}\right| \geq \lambda \\ 0, & \left|w_{j,k}\right| < \lambda. \end{cases} \tag{5}$$

Coefficient of wavelet packet built for soft threshold is given:

$$\overline{w}_{j,k} = \begin{cases} \mathrm{sign}\left(w_{j,k}\right)\left(\left|w_{j,k}\right| - \lambda\right), & \left|w_{j,k}\right| \geq \lambda \\ 0, & \left|w_{j,k}\right| < \lambda. \end{cases} \tag{6}$$

For (5) and (6), $w_{j,k}$ represents wavelet packet coefficient and λ is preset threshold or threshold value, which is calculated in the form

$$\lambda = \frac{\sigma\sqrt{2\lg N}}{\lg(j+1)}, \tag{7}$$

where σ is noise variance, j is decomposed scale, and N is signal length.

Signal to noise ratio (SNR) and root mean square error (RMSE) are usually selected as a signal denoising performance evaluation, which are calculated by following equations:

$$\begin{aligned} \mathrm{SNR} &= 10\lg\left(\frac{\sum_{n=1}^{N} s^2(n)}{\sum_{n=1}^{N}\left[s(n)-\bar{s}(n)\right]^2}\right), \\ \mathrm{RMSE} &= \sqrt{\frac{1}{N}\left[s(n)-\bar{s}(n)\right]^2}, \end{aligned} \tag{8}$$

where $s(n)$ is original signal, $\bar{s}(n)$ represents signal after denoising by wavelet packet, and N is signal length.

3. Blind Source Separation Models and Methods of DTS Temperature Monitoring Data

Seepage will lead to a change in the stability temperature field in the media and a partial volatile region can be generated [10, 11]. However, the temperature field distribution of structure body is affected not only by leakage field, but also soil characteristics, natural phenomena, optical fiber laying elevation, cross artificial cavities, and other factors. Further, the measured value of the optical fiber temperature sensing system is affected. Therefore, the temperature field of structure body is a result caused by multiple-factor under the combined effects. The positioning of leakage points inside ERJD under national condition can be attributed to the blind source separation problem for the influence of multiple-factor [12].

Leakages, soil characteristics or other factors causing changes in temperature monitoring data unit have a corresponding source component which is a function of the distance between the sampling point and the starting point. Soil characteristics, natural phenomena, and other factors should be possibly separated out of the temperature data except for the leakage factor. The separated data can be a result of temperature field change only affected by the leakage factor as much as possible. And the leakage factor is just the final concern.

The effects of leakage factor, soil characteristics, or other factors on the measured temperature data can also be considered to be independent units. The temperature data in most regions along fiber are not affected by leakages, gutters, and other factors, which are small probability events on time and space. Based on non-Gaussian distribution and statistical independent of the source signal, ICA is selected in blind source separation technique. In addition, PCA is determined as a pretreatment method for ICA technique in order to reduce the computational complexity and effective multiple-variable correlation.

The key of PCA is the certain degree of relevance and redundancy of information between the variables. At the same time, adjacent sampling points have similar work environment and strong correlation, which provide a possibility to the use of PCA. The mathematical model of PCA can be obtained by the following process. First, a p dimensional random vector is consisted by p scalars and it is expressed as $X = (X_1, \ldots, X_p)'$. p is defined as an arbitrary number. X is used for orthogonal transformation, ordering $Y = T'X$, and T is orthogonal matrix. Each component of Y is not relevant, and the variance of the first variable of Y is the largest, the second variable coming after. This process can be represented by the following matrix:

$$\begin{aligned} Y_1 &= t_{11}X_1 + t_{12}X_2 + \cdots + t_{1p}X_p = T_1'X, \\ Y_2 &= t_{21}X_1 + t_{22}X_2 + \cdots + t_{2p}X_p = T_2'X, \\ &\vdots \\ Y_p &= t_{p1}X_1 + t_{p2}X_2 + \cdots + t_{pp}X_p = T_p'X. \end{aligned} \tag{9}$$

The definition of singular value decomposition (SVD) of PCA can be described: M represents a matrix with m rows and n columns, whose elements belong to the field of real numbers or complex field. There is the following decomposition:

$$M = USV^T, \tag{10}$$

where U represents a unitary matrix with $m \times m$ order and is called left singular matrix of M, V is a unitary matrix with $n \times n$ order and is named right singular matrix of M, V^T is transpose of matrix V, the same bellow, S represents a positive semidefinite diagonal matrix with $m \times n$ order, and elements on the diagonal matrix are singular values of M, which are equal to the square root of eigenvalues of $M^T * M$. It is orthogonal matrix as the elements of unitary matrix are real numbers. Relationship between the main component of Y and monitoring data matrix X can be obtained by

$$Y = XT. \tag{11}$$

Thus,

$$X = YT', \tag{12}$$

where matrix of T is constituted by eigenvectors of diagonal matrix and X^TX is orthogonal matrix.

From the theory of SVD, it can be obtained that

$$X = USV'. \tag{13}$$

Comparing formula (12) with (13), it can be known that $T = V$; then, $Y = US = XV$.

Therefore, the main component of matrix is the product of left singular matrix and its corresponding singular values and is also equal to the product of monitoring data matrix and the right singular matrix. The number of principal components can be determined through the cumulative variance contribution rate. Variance contribution rate and cumulative variance contribution rate are described follows:

$$\begin{aligned} \varphi_k &= \frac{\lambda_k}{\sum_{k=1}^{p}\lambda_k}, \\ \psi_m &= \frac{\sum_{k=1}^{m}\lambda_k}{\sum_{k=1}^{p}\lambda_k}, \end{aligned} \tag{14}$$

where λ_k represents the eigenvalues of covariance matrix and φ_k and ψ_m are, respectively, called variance contribution rate and cumulative variance contribution rate.

In order to avoid inconsistencies between dimensions and units of data, the data is typically normalized:

$$X_i^* = \frac{X_i - E(X_i)}{\sqrt{D(X_i)}}. \tag{15}$$

The mathematical model of ICA can be expressed by

$$\begin{aligned} x_1 &= a_{11}s_1 + a_{12}s_2 + \cdots + a_{1n}s_n, \\ x_2 &= a_{21}s_1 + a_{22}s_2 + \cdots + a_{2n}s_n, \\ &\vdots \\ x_n &= a_{n1}s_1 + a_{n2}s_2 + \cdots + a_{nn}s_n, \end{aligned} \tag{16}$$

where $x_1, x_2, \ldots, x_n$ represent n random variables, named mixed signals; $s_1, s_2, \ldots, s_n$ are n independent components, called source signals; a_{ij} $(i, j = 1, 2, \ldots, n)$ is mixing coefficient.

Parallel algorithm calculation steps of several independent components are described as follows:

(1) standardize the data so that the mean and variance of each column are, respectively, 0 and 1;

(2) data whitened of z is gotten from the data obtained from Step (1);

(3) m is selected as the number of independent component to be estimated;

(4) the mixing coefficient of w_i is initialized, $i = 1, 2, \ldots, m$, and every w_i is changed to be a unit 2-norm; then, matrix W is orthogonalised by the method of Step (6);

(5) update each w_i, $w_i \leftarrow E\{zg(w_i^T z)\} - E\{g'(w_i^T z)\}w_i$; the function of g can be selected from formula (17) to formula (19);

(6) matrix $W = (w_1, \ldots, w_m)'$ is orthogonalised, $W \leftarrow (WW')^{-1/2}W$;

(7) return to Step (5) if the result is not converged.

The function of g can be selected from the following functions:

$$g_1(y) = \tanh(a_1 y), \tag{17}$$

$$g_2(y) = y \exp\left(-\frac{y^2}{2}\right), \tag{18}$$

$$g_3(y) = y^3. \tag{19}$$

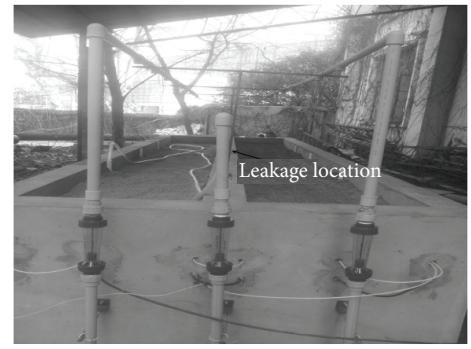

Figure 2: Model experiment of ERJD.

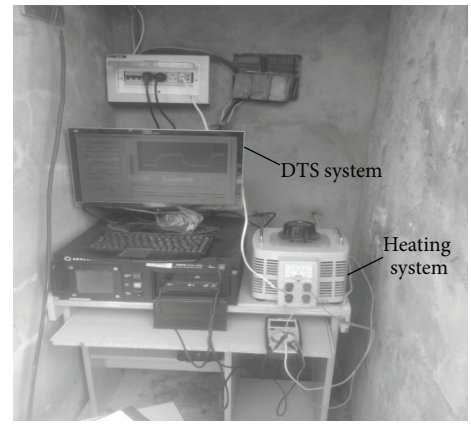

Figure 3: DTS monitoring and heating system.

The corresponding derivative functions are described as follows:

$$\begin{aligned} g_1'(y) &= a_1\left(1 - \tanh^2(a_1 y)\right), \\ g_2'(y) &= \left(1 - y^2\right)\exp\left(-\frac{y^2}{2}\right), \\ g_3'(y) &= 3y^2, \end{aligned} \tag{20}$$

where a_1 is a constant, valuing in [1, 2], and the value is usually taken as 1; $\tanh(x)$ represents hyperbolic tangent function.

4. Application Case Analyses

A model experiment platform was formed and shown in Figure 2 to simulate the existence of leakages for ERJD. The DTS monitoring system of Sentinel DTS-LR produced by Sensornet was applied. The DTS monitoring and heating system was shown in Figure 3. A schematic diagram of the model was given in Figure 4. Multimode four core armored cable of 50/125 um was used as the monitoring optical cable with a type of ZTT-GYXTW-4A1a.

The ZTT-GYXTW-4A1a was a special optical cable which could be used to be heated. And its structure section was drawn in Figure 5.

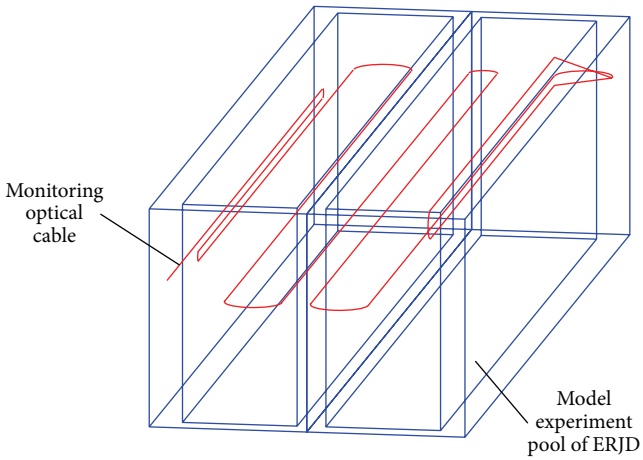

Figure 4: Schematic diagram of the model.

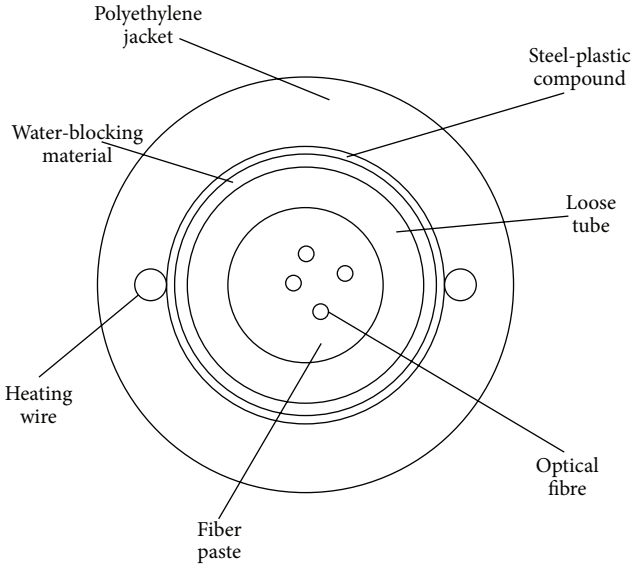

Figure 5: Structure section of ZTT-GYXTW-4A1a.

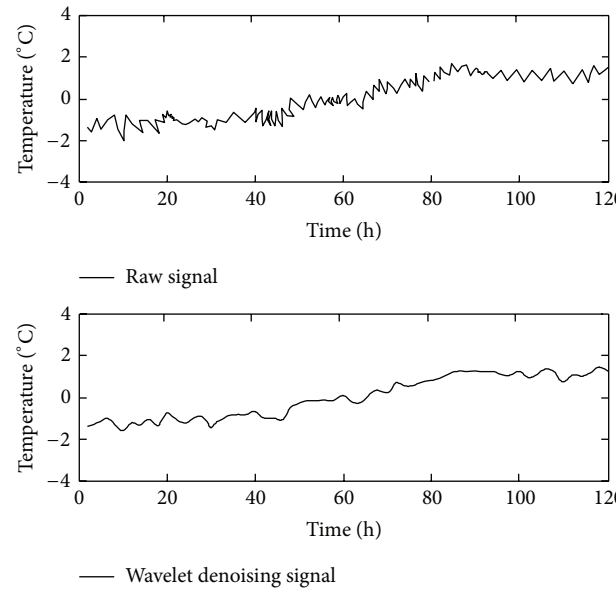

Figure 6: Comparative diagram between raw signal and the wavelet denoising signal.

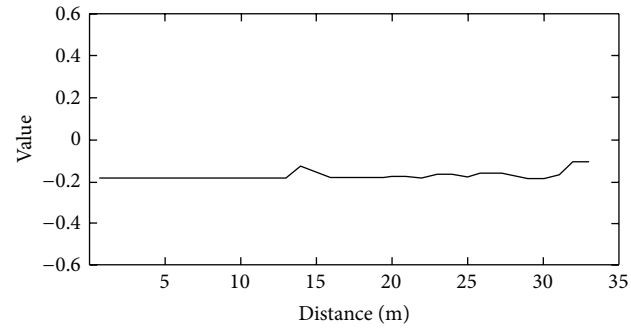

Figure 7: Result diagram after PCA method.

The leakage location was washed by a water pipe and the velocity of seepage was controlled. The monitoring data was noted as the stable velocity was formed.

For simplicity, just one leakage point was introduced in the model, and the sampling distance was 1 m and the sampling interval was 2 hours for 5 days. Thus, each measuring point obtained 60 groups of data. First, the original temperature data should be denoised and a typical point was selected as an example analyzed. After calculation, the decomposition levels of the wavelet packet were 3-layer. Figure 6 was shown to compare the raw signal with the wavelet denoising signal.

The first principal component was calculated and listed in Figure 7.

The corresponding variance contribution rate of the first principal component, $\sigma_1 / \sum \sigma$, was 87.21%, and it could be concluded that the contribution of the first principal component to information was larger. The difference of the principal component value between the leakage point presented and other points was much larger than the one of the first principal component. Therefore, the second and third principal components were selected to the next ICA, which meant $i = 2$. One of the two principal components was used to construct a separate component of the signal space, and the other one was made to build a separate part of the salvage space. The difference of the separate component 1 in the leakage point was more evident than the one of other points whose distribution was more stable. Thereby, the separate component 1 was considered to establish a salvage space. The separate component 2 constructed a separate component signal space. The corresponding grey-scale map of residual space was shown in Figure 8.

From the result of data processing, it can be known that the problem of the optical fiber temperature monitoring data could be analyzed by the blind source separation and ICA was used to process data. In Figure 8, the leakage area of 14 m was larger than the area of 32 m. And the test distance of the model was less than 32 m. Therefore, the area of 32 m

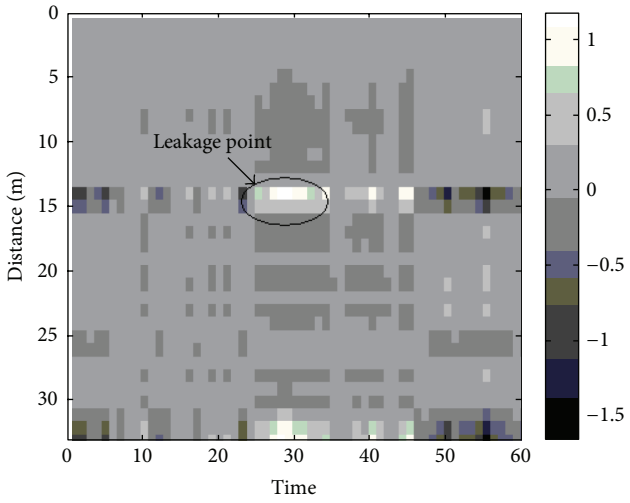

Figure 8: Grey-scale map of residual space.

was not considered. Finally the leakage location could be well implemented.

5. Conclusions

In this paper, ERJD was the studied object and its leakage identification was for the research emphasis. Based on leakage characteristics of monitoring ERJD by DTS, the affecting factors of optical fiber temperature monitoring data were analyzed. The wavelet packet denoising method and threshold determining method were also studied. A blind source separation model of optical fiber temperature data was finally built and the corresponding temperature change process of the leakage source was extracted. The implementation method of blind source separation technique was discussed. In-depth research on characteristics of optical fiber temperature data was carried out and optimal applicable conditions for realization method of the blind source separation techniques were also analyzed. The blind source separation technique implementation combining ICA with PCA was finally proposed. With leakage fiber-optic model experiment of ERJD, the reliability of optical fiber temperature measuring data based on the blind source separation method is validated.

Conflict of Interests

The authors declare that there is no conflict of interests regarding the publication of this paper.

Acknowledgments

This research has been partially supported by Jiangsu Natural Science Foundation (SN: BK2012036), the National Natural Science Foundation of China (SN: 51179066, 51139001, 41323001, and 51409167), the Specialized Research Fund for the Doctoral Program of Higher Education of China (SN: 20130094110010), the Nonprofit Industry Financial Program of MWR (SN: 201301061 and 201201038), the Open Foundation of State Key Laboratory of Hydrology-Water Resources and Hydraulic Engineering (SN: 20145027612), the Research Program on Natural Science for Colleges and Universities in Jiangsu Province (SN: 14KJB520016), the Priority Academic Program Development of Jiangsu Higher Education Institutions (SN: YS11001), and the Scientific Innovation Research Scheme for Jiangsu University Graduate (SN: 2013B25514).

References

[1] H.-H. Zhu, A. N. L. Ho, J.-H. Yin, H. W. Sun, H.-F. Pei, and C.-Y. Hong, "An optical fibre monitoring system for evaluating the performance of a soil nailed slope," *Smart Structures and Systems*, vol. 9, no. 5, pp. 393–410, 2012.

[2] B. Shi, C.-S. Tang, L. Gao, C. Liu, and B.-J. Wang, "Observation and analysis of the urban heat island effect on soil in Nanjing, China," *Environmental Earth Sciences*, vol. 67, no. 1, pp. 215–229, 2012.

[3] J. F. Yan, B. Shi, D. F. Cao, H. H. Zhu, and G. Q. Wei, "Experiment study on carbon coated heating optical fiber for sand leakage monitoring based on distributed temperature system," in *Proceedings of the 6th International Conference on Structural Health Monitoring of Intelligent Infrastructure*, Paper no. MS03-06, Hong Kong, 2013.

[4] S. Johansson, "Localization and quantification of water leakage in ageing embankment dams by regular temperature measurements," in *Proceedings of the 17th International Congress on Large Dams (ICOLD '91)*, pp. 991–1005, Vienna, Austria, 1991.

[5] O. Kappelmeyer, "The use of near surface temperature measurements for discovering anomalies due to causes at depths," *Geophysical Prospecting*, vol. 5, no. 3, pp. 239–258, 1957.

[6] A. H. Hartog, "Distributed fiber-optic temperature sensors: principles and applications," in *Optical Fiber Sensor Technology*, K. T. Grattan and B. T. Meggitt, Eds., pp. 241–301, Kluwer Academic Publishers, New York, NY, USA, 2000.

[7] H. Z. Su, J. Y. Li, J. Hu, and Z. Wen, "Analysis and back-analysis for temperature field of concrete arch dam during construction period based on temperature data measured by DTS," *IEEE Sensors Journal*, vol. 13, no. 5, pp. 1403–1412, 2013.

[8] S. Yin, "Distributed fiber optic sensors," in *Fiber Optic Sensors*, F. T. Yu and S. Yin, Eds., pp. 201–229, Marcel Dekker, New York, NY, USA, 2000.

[9] A. D. Kersey, "Optical fiber sensors for downwell monitoring applications in the oil and gas industry," in *Proceedings of the 13th International Conference on Optical Fiber Sensors (Ofs-13 '99)*, pp. 326–331, 1999.

[10] S. Grosswig, A. Graupner, and E. Hurtig, "Distributed fiber optical temperature sensing technique—a variable tool for monitoring tasks," in *Proceedings of the 8th International Symposium on Temperature and Thermal Measurements in Industry and Science*, pp. 9–17, 2001.

[11] S. A. Wade, K. T. V. Grattan, B. McKinley, L. F. Boswell, and C. D'Mello, " Incorporation of fiber optic sensors in concrete specimens: testing and evaluation," *IEEE Sensors Journal*, vol. 4, no. 1, pp. 127–134, 2004.

[12] H.-H. Zhu, L.-C. Liu, H.-F. Pei, and B. Shi, "Settlement analysis of viscoelastic foundation under vertical line load using a fractional Kelvin-Voigt model," *Geomechanics and Engineering*, vol. 4, no. 1, pp. 67–78, 2012.

Hindawi Publishing Corporation
Journal of Sensors
Volume 2015, Article ID 246480, 6 pages
http://dx.doi.org/10.1155/2015/246480

Research Article

A Practical Method for Grid Structures Damage Location

Zhefu Yu[1] and Linsheng Huo[2]

[1]*Transportation Equipment and Marine Engineering College, Dalian Maritime University, Dalian, Liaoning 116026, China*
[2]*Dalian University of Technology, Linggong Road No. 2, Integrated Building 4, 219-B, Dalian, Liaoning 116024, China*

Correspondence should be addressed to Zhefu Yu; yuzf629@sina.com

Received 29 September 2014; Revised 29 January 2015; Accepted 9 February 2015

Academic Editor: Christos Riziotis

A damage location method based on cross correlation function, wavelet packet decomposition, and support vector machine was proposed for grid structure. The approximate damage positions in grid structures could be determined through the peak abrupt changes of the cross correlation function that was produced by two vibration responses of adjacent measuring points. The vibration response was decomposed into eight bands by wavelet packet in order to accurately locate damage rods. The energy distribution in eight bands was used as a feature vector. SVM is trained to locate damaged bar elements in grid structures. Numerical analysis results showed that this method had good accuracy.

1. Introduction

Grid structures suffer from all kinds of damage during service, due to environmental effects, natural disasters, and human factors. For the maintenance of grid structures, accurately locating damage position is very critical.

The traditional methods of damage location are based in displacement measurement and strain measurement, but they are damaging to the structures [1]. According to the theory of structural dynamics, structural damage can affect the dynamic characteristics of structures. Therefore, damage location methods based on vibration analysis have attracted much attention in the past twenty years [2]. The modes of structural damage could be identified by analyzing modal parameters. The modal parameters include natural frequencies [3], vibration modes [4, 5], and other parameters [6, 7]. For a complex structure, the high natural frequencies are difficult to be measured. Precise measurement of vibration modes requires more measuring sensors [8]. The modal parameters are affected easily by signal noise, structure characteristics, and human factors. The damage location methods based on modal parameters cannot reach the expected result.

Despite the fact that the damage detection methods integrated signal processing [9], pattern recognition and artificial intelligence [10, 11] are the developing direction in recent years; such methods were only applied to some of simple structures. Because the number of bar element in grid structure is huge, and the number of damage mode is enormous, to get the damage location of grid structure, a larger number of damage mode samples are required to train classifier, which will bring huge workload for building samples with finite element methods.

This paper proposed a damage location method which integrated the cross correlation function of the random vibration, wavelet packet decomposition, and SVM. The proposed method includes two steps. The first step is the approximate damage location. The damaged basic units were found through the peak abrupt changes of the cross correlation function [12]. In the second step, wavelet packet and support vector machines are used in determining the damaged bars in the basic units.

2. Cross Correlation Function, Wavelet Packet Decomposition, and SVM

2.1. The Conception of Cross Correlation Function. Cross correlation function can reflect the correlation between two random vibration signals. The correlation changes with the time interval of the two signals. If a structure is subjected to

a random excitation, the response of two adjacent measuring points can be regarded as two stationary random processes x_1 and x_2. The cross correlation function is shown as

$$\varphi_{x_1x_2}(\tau) = E\left[x_1(t)\, x_2(t+\tau)\right] = \iint x_1 x_2 p(x_1 x_2)\, dx_1 dx_2, \quad (1)$$

where $\phi_{x_1x_2}$ is the cross correlation function; τ is the time interval; $E[\cdot]$ means the expecting value; $p(x_1x_2)$ denotes joint probability distribution function.

If the random vibration responses are ergodic, the cross correlation function can be derived through the time-history of one random process. It is shown as

$$\varphi_{x_1x_2}(\tau) = \lim_{T\to\infty} \lim \frac{1}{T} \int_0^T x_1(t)\, x_2(t+\tau)\, dt. \quad (2)$$

In the numerical analysis, the vibration response in each measuring point is a discrete time series. The integral of cross correlation function can not be acquired by (2). It can be replaced by the summation formula as shown in

$$\varphi_{x_1x_2}(k) = \frac{1}{N} \sum_{i=1}^{N-k} x_1(i)\, x_2(i+k), \quad (k = 0, 1, \ldots, N), \quad (3)$$

where N is the number of sampling points.

In a cross correlation function, the largest amplitude as shown in (4) is defined as peak in this paper:

$$r_{l,l+1} = \left|\varphi_{x_l x_{l+1}}(\tau)\right|_{\max} = \left|\varphi_{x_l x_{l+1}}(k)\right|_{\max}. \quad (4)$$

According to the characteristics of grid structures, measuring points are arranged on the bottom nodes uniformly. Cross correlation functions can be acquired by adjacent measuring points. Every cross correlation function has a peak. Thence, a peak matrix for the entire grid structure can be derived [12]. By introducing the peak matrix, the influence of noise pollution in measurement signals can be reduced [13, 14]. In case of one damage mode of a grid structure, the peak matrixes obtained from same spectrum vibrations are highly similar. After normalizing treatment, they are almost identical. Different damage modes produce different peak matrixes. By comparing the peak matrix of the damaged structure with the peak matrix of the intact structure, the approximate damage position would be determined.

2.2. Wavelet Packet Decomposition. Wavelet packet decomposition is derived from the wavelet analysis, which is a tool for multilevel band analysis and signal reconstruction. Wavelet packet decomposition can decompose the high-frequency portion of a signal more narrowly than the wavelet analysis. The different bands of a signal have different energy. The energy distribution of the vibration responses in grid structure may reflect the damage position.

2.3. SVM. SVM proposed by Vapnik is a machine learning algorithm based on statistical learning theory [15]. It minimizes actual risk through seeking minimal structural risk.

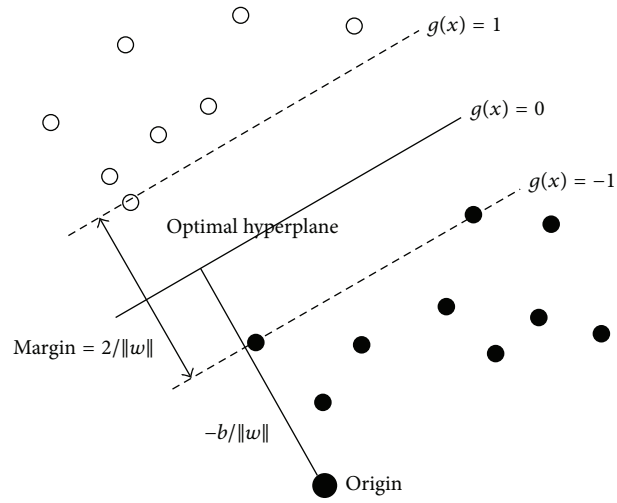

Figure 1: Support vector machine.

It can get a good learning result in the case of small sample size. Since the SVM algorithm is a quadratic optimization problem, the resulting solution is globally optimal.

The explanation of SVM starts with a set of training data $(x_1, y_1), \ldots, (x_l, y_l)$, where $x_i \in R^n$ is an n-dimension vector and $y_i \in \{-1, +1\}$ is the class label of the ith sample. The optimal hyperplane $(w \cdot x) + b = 0$ divides the training data into two classes. The basic idea of SVM is to maximize the margin between the positive samples and the negative samples. Figure 1 shows that the training examples can be linearly separated into two classes. In general, it is not necessary to separate training examples into each class without error. The variable $\xi_i \geq 0$ is introduced for misclassification errors; $C > 0$ is a constant. Then, this optimization problem is defined as follows:

$$\min_w \phi(w) = \|w\|^2 + C \sum_1^l \xi_i \quad (5)$$

$$\text{s.t.: } y_i (w \cdot x_i + b) \geq 1, \quad i = 1, \ldots, l. \quad (6)$$

In (5), the first term $\|w\|^2$ specifies the size of the margin, and the second term $C\sum_1^l \xi_i$ represents the cost of the misclassification. The decision function $f(x)$ can be written as

$$f(x) = \operatorname{sgn}\left(\sum_i \alpha_i y_i (x_i \cdot x) + b\right), \quad (7)$$

where $\alpha_i \geq 0$ are Lagrange multipliers. α_i corresponds to the ith sample. When the maximal margin hyperplane is found in feature space, the α_i corresponding to the points close to the hyperplane are greater than zero, and these points are called the support vectors. The α_i corresponding to other points are equal to zero, which means that the representation of the hyperplane is solely given by the support vectors.

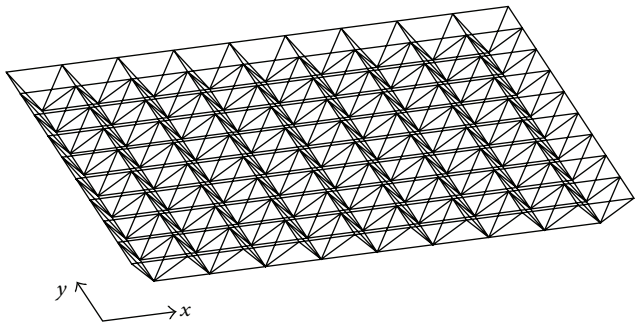

Figure 2: The grid structure.

The kernel function is defined as $\Phi(u) \otimes \Phi(v) = K(u, v)$ for a non-linear SVM classifier. After using a kernel function, (7) can be rewritten as

$$f(x) = \operatorname{sgn}\left(\sum_i \alpha_i y_i K(x_i, x) + b\right). \quad (8)$$

Classical SVM algorithm is only a two-class classifier, but general problems need multiclass classifiers. It was solved by combining multiple two-class classifiers. There are many combination methods, such as one to all, one to one, and decision tree. In this paper, the combination method of one to one is used to realize the multiclass classification.

3. Damage Location of Grid Structure

3.1. Grid Structure. A double square pyramid grid was chosen to verify the damage location method proposed in this paper. The grid is square with the side length of 30 m and height of 1.5 m. The bars are seamless steel pipe with the cross-sectional dimension of 40 mm. In the case of support, there is fixed hinge bracket in the four corners of the grid, which is shown in Figure 2. The SAP2000 software was applied for FEM analysis.

Excitation is an important part of the dynamic analysis. It is directly related to the analysis accuracy. Excitation can be divided into artificial excitation and environmental pulsation. Because the damage location indicator proposed in this paper is the peak of cross correlation function, the noise control in the acceleration response signal of measuring point is unimportant [6, 7]. So this method uses environmental pulsation as the signal source. In the process of finite element calculation, an acceleration signal source is a white noise signal generated by MATLAB. The acceleration amplitude delivered to the grid network through fixed hinge bracket is 2×10^{-3} m/s^2. The sampling interval is 0.01 s, and the sampling time is 10 s.

The bar damage was generated by reducing the elastic modulus in the analysis. Two kinds of damage are considered in the paper, in which the elastic modulus was, respectively, reduced 40% and 80%.

3.2. The Layout Scheme Measuring Point. After selecting excitation method, we should determine the number and the position of the measuring point. Because the upper chords are covered with roofing material, the acceleration response sensors were placed on bottom chord nodes. This was shown in Figure 3. Every sensor was fixed in x-axis direction.

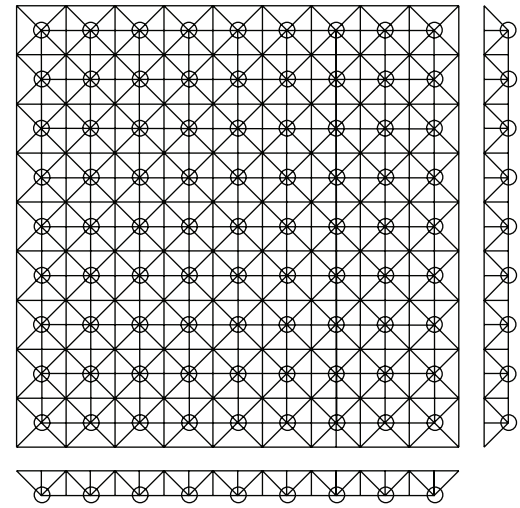

Figure 3: The layout of acceleration sensor.

The cross correlation function was calculated by using the responses of two adjacent acceleration sensors. The peaks of cross correlation functions formed a matrix as shown in (9). $r_{1,1\text{-}2}$ means a cross correlation function peak obtained from the sensor 1 and the sensor 2 in the first row. Consider

$$R = \begin{vmatrix} r_{1,1\text{-}2}, r_{1,2\text{-}3}, \ldots, r_{1,8\text{-}9} \\ r_{2,1\text{-}2}, \ldots \\ \vdots \\ r_{9,1\text{-}2}, r_{9,2\text{-}3}, \ldots, r_{9,8\text{-}9} \end{vmatrix}. \quad (9)$$

The environment pulsation is a stationary signal. Its spectrum is almost unchanged. For the same damage, the peak matrixes obtained at different time are highly similar. By placing measuring points in different zones at different time, we can also get the whole peak distribution. When the grid size is very large, and the number of sensor is limited, the layout scheme as shown in Figure 4 can be used. The accelerometers were placed on the bottom nodes, evenly placed first, and then subregionally placed in the damage zone.

3.3. Damage Location. The damaged positions can be acquired through the abrupt changes of the peak matrix. Figure 5 shows the peak distribution of an intact grid. Figure 6 shows the peak distribution of a damaged grid. If the areas where the peak changes occur can be seen, the damage positions can be found.

In order to find the peak abrupt changes easily, the peak matrix could be processed as follows. After the matrix of a damaged grid subtracted the matrix of an intact grid, an abrupt change matrix was obtained as shown in Figure 7. We can more easily identify the damage positions from Figure 7.

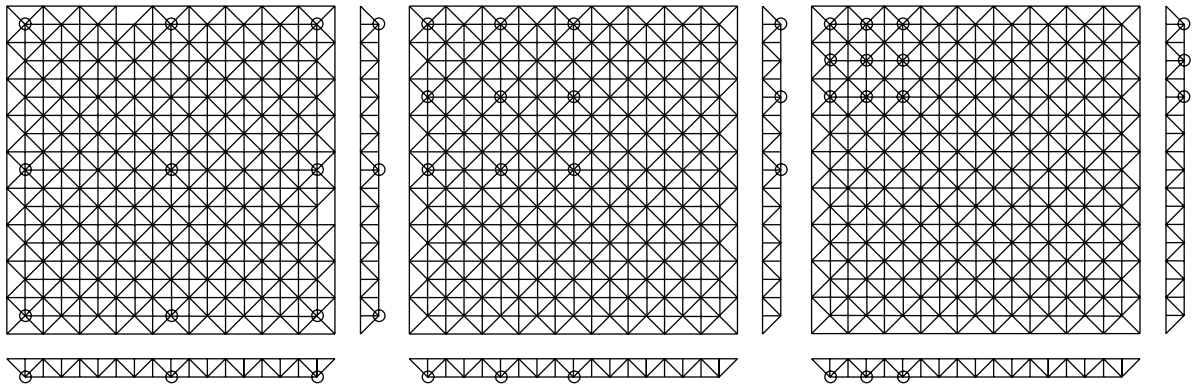

Figure 4: The subregional layout of acceleration sensor.

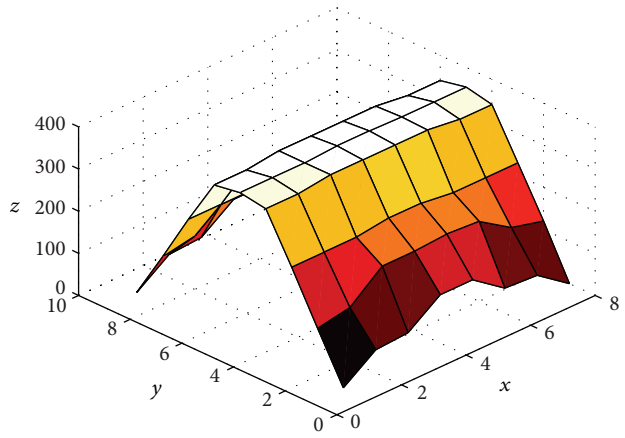

Figure 5: The peak distribution of an intact grid.

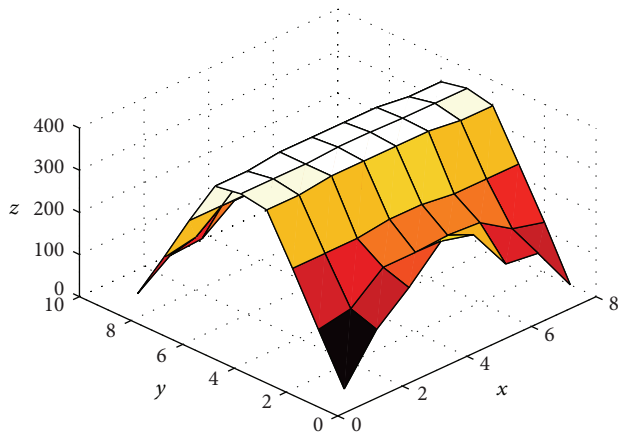

Figure 6: The peak distribution of a damaged grid.

If the sensors were fixed in every bottom node along y direction, we could obtain another matrix shown as (10). $r_{1\text{-}2,1}$ means a cross correlation function peak obtained from the sensor 1 and the sensor 2 in the first column. Consider

$$R' = \begin{vmatrix} r_{1\text{-}2,1}, r_{1\text{-}2,2}, \ldots, r_{1\text{-}2,9} \\ r_{2\text{-}3,1}, \cdots \\ \vdots \\ r_{8\text{-}9,1}, r_{8\text{-}9,2}, \ldots, r_{8\text{-}9,9} \end{vmatrix}. \quad (10)$$

Combining the distribution maps of abrupt changes derived from two directions, we can determine which quarter of the basic unit (as shown in Figure 8) involves damaged bars. Considering the case of node failure, each quarter has five damage modes: (1) the bottom chord along x direction was damaged or off node; (2) the bottom chord along y direction was damaged or off node; (3) the diagonal chord was damaged or off node; (4) the upper chord along x direction was damaged or off node; (5) the upper chord along y direction was damaged or off node.

3.4. Wavelet Packet Decomposition. The acceleration responses in damaged basic units were decomposed into 8 frequency components from low to high. After calculating the energy of every band, an 8-dimensional feature vector can be acquired and should be normalized, as shown in

$$S = [E_0, E_1, E_2, \ldots, E_7]. \quad (11)$$

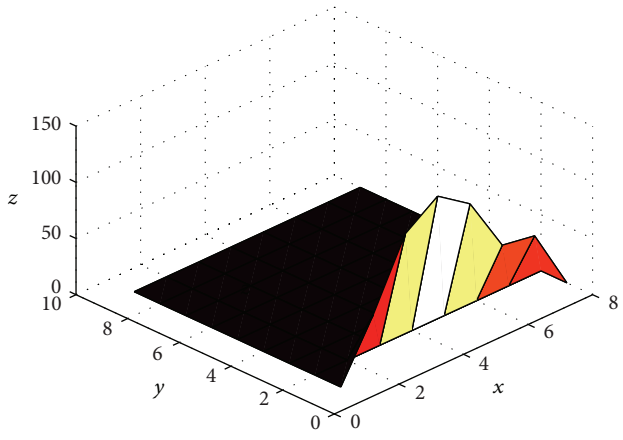

Figure 7: The abrupt change distribution of a damaged grid.

Table 1: Test accuracy.

Damage mode	The bottom bar element along x-axis	The bottom bar element along y-axis	The diagonal bar element	The bottom bar element along x-axis	The bottom bar element along y-axis
Accuracy	100%	70%	90%	50%	50%

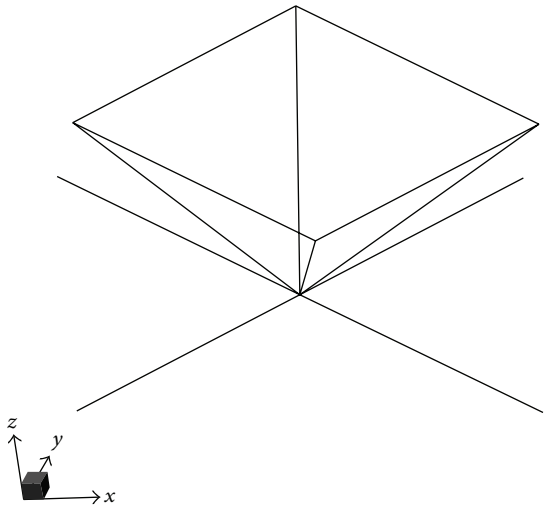

Figure 8: The grid structure module.

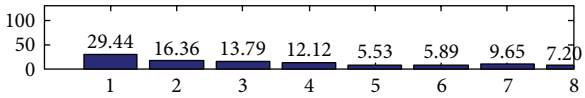

Figure 9: The energy distribution of intact base unit.

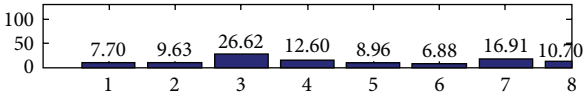

Figure 10: The energy distribution of bottom damaged chord in the x direction.

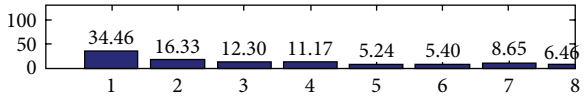

Figure 11: The energy distribution of bottom damaged chord in the y direction.

For each basic unit, different damaged bars will produce different 8-dimensional feature vectors. The energy distribution of the intact mode is shown in Figure 9. The energy distributions of the 5 damage modes are shown in Figures 10–14. A training sample of SVM was composed of the feature vector and the corresponding damage mode, while a test sample includes the feature vector only.

We collected 100 acceleration response signals as samples, which include five damage modes as samples. Every damage mode has 20 samples. Ten samples in each damage mode are

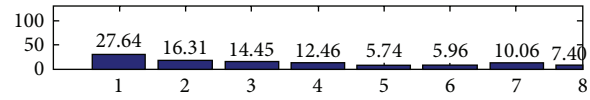

Figure 12: The energy distribution of damaged chord in the diagonal direction.

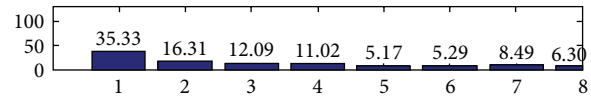

Figure 13: The energy distribution of upper damaged chord in the x direction.

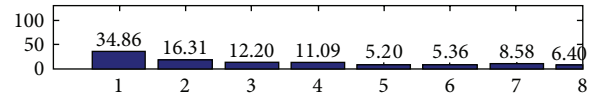

Figure 14: The energy distribution of upper damaged chord in the y direction.

randomly selected as the training set. In the SVM, the kernel function is Radial Basis Function. The optimal C and gamma were obtained by 5-fold cross validation. The remaining 50 samples were used as test set. The accuracy of the test is shown in Table 1. As seen from the above results, the accuracy of the bottom bars is higher than the accuracy of the upper bars. The sensors are placed in the lower nodes; therefore, they are more sensitive to the damage of lower bars.

4. Conclusion

This paper established a damage location method which integrated a cross correlation function, wavelet packet decomposition, and support vector machine. The method was applied to a grid structure. The results show that the damaged bar elements in grid structures can be recognized accurately at controllable computation cost, which means less finite element calculation and less measuring points.

Conflict of Interests

The authors declare that there is no conflict of interests regarding the publication of this paper.

References

[1] D. J. Pines and A. E. Aktan, "Status of structural health monitoring of long-span bridges in the United States," *Progress*

in Structural Engineering and Materials, vol. 4, no. 4, pp. 372–380, 2002.

[2] H. S. Sohn, C. R. Farrar, F. M. Hemez et al., *A Review of Structural Health Monitoring Literature 1996–2001*, Los Alamos National Laboratory, San Francisco, Calif, USA, 2003.

[3] S. Chen and G. Li, "Artificial neural networks in structural damage identification," *Vibration, Test and Damage*, vol. 21, no. 2, pp. 116–124, 2001.

[4] M. Kaouk, D. C. Zimmerman, and T. W. Simmermacher, "Assessment of damage affecting all structural properties using experimental modal parameters," *Journal of Vibration and Acoustics*, vol. 122, no. 4, pp. 456–463, 2000.

[5] S.-L. J. Hu, H. Li, and S. Wang, "Cross-model cross-mode method for model updating," *Mechanical Systems and Signal Processing*, vol. 21, no. 4, pp. 1690–1703, 2007.

[6] A. Dixit and S. Hanagud, "Damage localization by isolating the part of the response due to the damage only," *Journal of Applied Mechanics*, vol. 80, no. 1, Article ID 011015, 8 pages, 2012.

[7] M. R. Hernandez-Garcia, S. F. Masri, R. Ghanem, E. Figueiredo, and C. R. Farrar, "An experimental investigation of change detection in uncertain chain-like systems," *Journal of Sound and Vibration*, vol. 329, no. 12, pp. 2395–2409, 2010.

[8] A. Alvandi and C. Cremona, "Assessment of vibration-based damage identification techniques," *Journal of Sound and Vibration*, vol. 292, no. 1-2, pp. 179–202, 2006.

[9] J.-G. Han, W.-X. Ren, and Z.-S. Sun, "Wavelet packet based damage identification of beam structures," *International Journal of Solids and Structures*, vol. 42, no. 26, pp. 6610–6627, 2005.

[10] E. Figueiredo, M. D. Todd, C. R. Farrar, and E. Flynn, "Autoregressive modeling with state-space embedding vectors for damage detection under operational variability," *International Journal of Engineering Science*, vol. 48, no. 10, pp. 822–834, 2010.

[11] L. Liu and G. Meng, "Vector regression algorithm applied research in the beam structural damage diagnosis support," *Shock and Vibration*, vol. 25, no. 3, pp. 99–100, 2006.

[12] Y. Zhefu, H. Linsheng, and Z. Lei, "Grid structure damage location base on cross-correlation function," in *Proceedings of the 4th International Conference on Civil Engineering, Architecture and Building Materials*, pp. 1083–1086, May 2014.

[13] R. J. Allemang and D. L. Brown, "A correlation coefficient for modal vector analysis," in *Proceedings of the 1st International Modal Analysis Conference & Exhibit (IMAC '82)*, pp. 110–116, November 1982.

[14] L. Jiayan, Y. Qianfeng, L. Ying et al., "Experimental analysis of structural damage identification based on random vibration response of the cross-correlation function," *Vibration and Shock*, vol. 30, no. 8, pp. 221–224, 236, 2011.

[15] V. N. Vapnik, *The Nature of Statistical Learning Theory*, Springer, New York, NY, USA, 1995.